



HAL
open science

Ligand effects on the properties of ultra-small platinum-based nanoparticles

Nataliia Marchenko

► **To cite this version:**

Nataliia Marchenko. Ligand effects on the properties of ultra-small platinum-based nanoparticles. Organic chemistry. INSA de Toulouse, 2023. English. NNT : 2023ISAT0061 . tel-04659361

HAL Id: tel-04659361

<https://theses.hal.science/tel-04659361>

Submitted on 23 Jul 2024

HAL is a multi-disciplinary open access archive for the deposit and dissemination of scientific research documents, whether they are published or not. The documents may come from teaching and research institutions in France or abroad, or from public or private research centers.

L'archive ouverte pluridisciplinaire **HAL**, est destinée au dépôt et à la diffusion de documents scientifiques de niveau recherche, publiés ou non, émanant des établissements d'enseignement et de recherche français ou étrangers, des laboratoires publics ou privés.



THÈSE

En vue de l'obtention du
DOCTORAT DE L'UNIVERSITÉ DE TOULOUSE
Délivré par l'Institut National des Sciences Appliquées de
Toulouse

Présentée et soutenue par
Nataliia MARCHENKO

Le 11 juillet 2023

**Effets de ligand sur les propriétés de nanoparticules ultra-petites
à base de platine**

Ecole doctorale : **SDM - SCIENCES DE LA MATIERE - Toulouse**

Spécialité : **Chimie Organométallique et de Coordination**

Unité de recherche :

LPCNO-IRSAMC - Laboratoire de Physique et Chimie des Nano-Objets

Thèse dirigée par
Simon TRICARD

Jury

M. Laurent PICCOLO, Rapporteur
M. Jean-Cyrille HIERSO, Rapporteur
Mme Karine PHILIPPOT, Examinatrice
M. Stéphane CAMPIDELLI, Examinateur
M. Simon TRICARD, Directeur de thèse
M. Alexis BORDET, Invité

Acknowledgements

I would like to acknowledge the jury members that kindly accepted to review my work and give valuable suggestions: Dr. Laurent PICCOLO, Prof. Jean-Cyrille HIERSO, Dr. Karine PHILIPPOT, and Dr. Stephane CAMPIDELLI. I believe that in the scientific society, it is highly important to share knowledge from different fields, so I am happy to be evaluated by the experts in diverse areas, from organometallics to electrochemistry.

I express my deepest gratitude to my supervisor Dr. Simon TRICARD. You always believed in me and cheered me up; you gave me a lot of freedom to choose and manage the projects I wanted to do, you encouraged me to try new things; your guidance and expertise were essential in this research. During my PhD time, I gained confidence and learned how to work independently, thank you for this. You were always kind and helped me with everything, even if it was some administrative staff or other things not related to work which shows you as a caring and warmhearted person.

Special thanks to Alexis BORDET and his team who hosted me at MPI CEC in Mülheim an der Ruhr, Germany. Alexis was very reactive and helped me to find a solution to every little issue I had in the laboratory; I could come to discuss the science with him anytime. As a result, we completed an interesting project in the short term, I learned how to work really efficiently!

I would like to acknowledge our collaborators who made this work possible: Dominique ARMSPACH and Sebastian JUNG from Strasbourg University, Claire KAMMERER and Seifallah ABID from CEMES Toulouse, thank you for the ligands which you kindly provided and for our scientific discussions; Piet W.N.M. van Leeuwen, thank you for the valuable suggestions about SPO ligands. Many thanks to the engineers who characterized my samples: Yannick COPPEL for NMR experiments, Delphine LAGARDE and Charles-Louis SERPENTINI for TRPL measurements, Marine TASSE for CAFM analysis, Jerome ESVAN for XPS data, and Alain MOREAU for ICP analysis.

I am extremely thankful to our NCO team, in particular to Adeline PHAM who helped me with the projects, especially with TEM and SEM characterization; to Lise-Marie Lacroix for VSM measurements and scientific discourse, to Simon CAYEZ, who trained me for XRD, TEM, and SEM-EDX; to Francis CHOUZENOUX for TGA analysis, and to Angelique GILLET who quickly resolved any equipment issues. I thank my teammates for sharing with me their knowledge, being always there for me in the lab, and having fun together! It was a pleasure to work in such a friendly and supportive environment with kind and funny mates whom I call friends now.

I thank my parents for the trust and letting me leave the nest to pursue my dream job in another country. Although they wanted me to become a “real doctor” I hope to make them proud with a PhD title. Last but not least, I would like to thank my husband Serge for fighting my imposter syndrome and supporting me in the difficult times when science refused to work.

The path I went through to write the present thesis work was not always easy, but all the people I acknowledged and many more whom I forgot to mention, made my PhD journey better than I could ever imagine. I thank all of the participants in my study for their time and willingness to share their knowledge with me.

Abstract

Ultra-small metal nanoparticles (NP) have unique properties originating from their size such as a high surface-to-volume ratio and a quantization of their physical properties. These characteristics make them a popular object of investigation in catalysis, self-assembly (SA), photophysics or charge transport. Stabilizing ligands that are generally used to preserve the small size and the dispersion of NPs can also influence their functional properties. In this thesis, we investigate how ligands can modulate the intrinsic properties of platinum NPs and how this knowledge can be applied in different spheres, from self-assembly to catalysis. This manuscript consists of five chapters: a literature review and four experimental studies that cover independent projects, where ultra-small platinum-based NPs are the main object of investigation.

Chapter 1 gathers representative examples of ligand influence on the synthesis, SA, and catalytic properties of metal-based NPs. In the first part, classical organic ligands like thiols or polymers are considered, while the second part covers examples of so-called “hybrid systems” where metal complexes interact with NPs.

Chapter 2 reports synthesis, characterization and catalytic properties of Pt NPs stabilized with pyranose macrocycles - *cyclodextrins* (CD). The influence of the functional group of the CD (thiol or secondary phosphine oxide moieties) and the effect of the ligand relative quantity on hydrogenation performance of Pt NPs are discussed.

Chapter 3 is dedicated to FePt NPs immobilized on silica-based supported ionic liquid phases (*SILP*). In this chapter, the importance of the Fe content modulation as well as the role of the ionic liquid-modified support are demonstrated in selective catalytic hydrogenation and hydrodeoxygenation of ketones and aldehydes.

Chapter 4 describes hybrid systems made of Pt NPs and functionalized *porphyrins* or *metal porphyrins*. Particularly, the formation of SAs of different shapes and obvious changes in the photophysical properties of the systems are rationalized and correlated to the strength of interactions between the Pt NP and the porphyrins.

Chapter 5 describes the synthesis and the characterization of hybrid systems containing Pt NPs and covalently attached *ruthenium(II) bipyridyl complexes modified with imidazolium fragments*. The prepared NP-antenna systems are promising candidates in photocatalysis.

In conclusion, this thesis demonstrates valuable findings about ligand control of the synthesis, SA, and catalytic properties of ultra-small Pt NPs. This study highlights the importance of a thorough ligand choice to produce stable and active NPs. The results of this research can serve as a guideline for a rational design of nanocomposites to form self-assembled systems or selective catalysts.

Résumé

Les nanoparticules (NP) métalliques ultra-petites possèdent des propriétés uniques en raison de leur taille : un rapport surface sur volume élevé et une quantification de leurs propriétés physiques. Ces caractéristiques en font des objets d'étude populaires en catalyse, en auto-assemblage (AA), en photophysique ou en transport de charge. Des ligands stabilisants sont généralement utilisés pour préserver la petite taille et la dispersion des NP, en plus d'influencer leurs propriétés fonctionnelles. Dans cette thèse, nous étudions comment les ligands peuvent moduler les propriétés intrinsèques des NP de platine et comment ces connaissances peuvent être appliquées dans différentes sphères, de l'auto-assemblage à la catalyse. Cette thèse est composée de cinq chapitres : une revue de la littérature et quatre études expérimentales qui couvrent des projets indépendants, où les NP ultra-petites à base de platine sont l'objet principal de la recherche.

Le chapitre 1 regroupe des exemples représentatifs de l'influence des ligands sur la synthèse, l'AA et les propriétés catalytiques de NP à base de métal. Dans la première partie, les *ligands organiques* classiques tels que les thiols ou les polymères sont pris en compte, tandis que la deuxième partie couvre des exemples de ce que l'on appelle les "systèmes hybrides" où des *complexes métalliques* stabilisent ou interagissent avec les NP.

Le chapitre 2 présente la synthèse, la caractérisation et les propriétés catalytiques des nanoparticules de platine stabilisées par des macrocycles de pyranose - les *cyclodextrines* (CD). L'influence du groupement fonctionnel de la CD (motifs thiol ou oxyde de phosphine secondaire) et l'effet de la quantité relative de ligand sur la performance d'hydrogénation des NP de Pt sont discutés.

Le chapitre 3 est consacré à la synthèse de NP de FePt immobilisées sur des *phases liquides ioniques supportées* (SILP) à base de silice, et à leur utilisation en tant que catalyseurs. Dans ce chapitre, l'importance de la modulation de la teneur en Fe ainsi que le rôle du support modifié par le liquide ionique sont démontrés en hydrogénation et l'hydrodésoxygénation catalytiques sélectives de cétones et d'aldéhydes.

Le chapitre 4 décrit des systèmes hybrides composés de NP de Pt et de *porphyrines* ou de *porphyrines métalliques* fonctionnalisées. En particulier, la formation d'AA de différentes formes et les changements évidents dans les propriétés photophysiques des systèmes sont rationalisés et corrélés à la force des interactions entre les NP de Pt et les porphyrines.

Le chapitre 5 décrit la synthèse et la caractérisation de systèmes hybrides contenant des NP de Pt UP et des complexes de *ruthénium(II) bipyridyle modifiés par des fragments imidazolium* attachés de manière covalente. Les systèmes NP-antennes préparés sont des candidats prometteurs pour la photocatalyse.

En conclusion, cette thèse présente des résultats de valeur sur le contrôle par les ligands de la synthèse, de l'AA et des propriétés catalytiques des NP de Pt ultra-petites. Cette étude souligne l'importance d'un choix minutieux des ligands pour produire des NP stables et actives. Les résultats de cette recherche peuvent servir de ligne directrice pour la conception rationnelle de nanocomposites afin de former des systèmes auto-assemblés ou des catalyseurs sélectifs.

Table of content

Acknowledgements.....	I
Abstract.....	II
Résumé.....	III
Table of content.....	IV
List of abbreviations.....	VI
General introduction.....	1
CHAPTER 1. Ligand effects on the properties of metal nanoparticles.....	4
1.1. Nanoparticles stabilized by molecular species	5
1.1.1. Capping ligands in colloidal synthesis	5
1.1.2. Ligand-mediated self-assembly.....	10
1.1.3. Ligand role in catalysis	21
1.2. Hybrid systems of type “nanoobject-metal complex”	46
1.2.1. Synthesis of hybrid systems	46
1.2.2. Complexation-mediated self-assembly.....	49
1.2.3. Hybrid systems in catalysis.....	52
1.3. Conclusions	60
CHAPTER 2. Platinum nanoparticles stabilized by functionalized cyclodextrins for selective hydrogenation	61
2.1. NPs stabilized with CD-SH: catalytic performances regulated by the ligands.....	62
2.1.1. General synthetic procedure for the Pt-CD systems	64
2.1.2. Pt-b2 catalyst: optimization of the synthetic procedure	66
2.1.3. Pt-0.5CD catalysts: biphasic catalysis.....	72
2.1.4. Pt-b1 catalyst: influence of the ligand ratio on the catalytic activity	79
2.2. NPs stabilized with alfa-CD-SPO: introduction of an activation moiety	88
2.2.1. Synthesis and characterization of the systems	89
2.2.2. Identification of active species in selective cinnamyl alcohol formation	92
2.3. Conclusions and perspectives.....	95
2.4. Experimental part	95
CHAPTER 3. FePt NPs immobilized on supported ionic liquid phases – a catalytic study.....	99
3.1. FePt@SILP in the context of bimetallic NP catalysts for selective hydrogenation.....	100
3.2. Synthesis of Fe _x Pt _{100-x} nanoparticles on imidazolium-based SILP.....	101
3.2.1. Synthetic optimization	101
3.2.2. Optimized synthetic procedure.....	103
3.3. Characterization of the catalytic materials.....	104

3.4. Catalytic performance of Fe _x Pt _{100-x} @SILP	110
3.4.1. Benzylidene acetone hydrogenation	110
3.4.2. Acetophenone hydrogenation and hydrodeoxygenation.....	111
3.4.3. Selective hydrogenation of unsaturated aldehydes	115
3.4.4. Hydrogenation of other substrates.....	117
3.5. Conclusions	117
3.6. Experimental part	119
CHAPTER 4. Platinum-porphyrin photoactive nanomaterials.....	121
4.1. Introduction to energy transfer in NP-porphyrin hybrid systems	122
4.2. Building blocks	125
4.3. Synthesis of the Pt NP-porphyrin systems.....	127
4.4. Influence of the porphyrin structure on the SA of NPs	127
4.5. Photophysical response	131
4.5.1. Absorption and emission of the porphyrins	131
4.5.2. PL quenching mechanisms	133
4.5.3. Dynamic quenching.....	134
4.5.4. Static quenching.....	137
4.5.5. Electrical properties of the hybrid systems	138
4.6. Conclusions	139
4.7. Experimental part	140
CHAPTER 5. Platinum-ruthenium antenna hybrid systems	143
5.1 Model compound - ruthenium(II) trisbipyridyl complex	144
5.2 Synthesis of ruthenium bipyridyl imidazolium complexes	146
5.3 Characterization of the complexes	147
5.4 Deprotonation of the L1 complexes	149
5.5 Synthesis of Pt NPs stabilized with L1Cl.....	151
5.6 Conclusions	153
5.7 Experimental part	154
5.8 Appendix to Chapter 5	161
Conclusions and perspectives.....	169
Résumé de la thèse.....	171
Reference list	192

List of abbreviations

A	acceptor
AcN	acetonitrile
ATR-FTIR	attenuated total reflectance - Fourier transform infrared spectroscopy
bpy	bipyridyl
CAFM	conductive atomic force microscopy
CD	cyclodextrin
D	donor
dba	dibenzylidene acetone
DFT	density-functional theory
DOSY	diffusion-ordered NMR spectroscopy
ee	enantiomeric excess
Eq	equivalent
ESI MS	electron spray ionization mass spectrometry
fcc	face-centered cubic
FRET	Förster resonance energy transfer
HAADF-STEM	high-angle annular dark-field scanning transmission electron microscopy
HDO	hydrodeoxygenation
HER	hydrogen evolution reaction
(HR)TEM	high resolution transmission electron microscopy
IL	ionic liquid
MC	metal complex
MC	metal complex
nbe	norbornene
NHC	N-heterocyclic carbene
NO	nanoobject
NP	nanoparticle
NR	nanorods
OER	oxygen evolution reaction
ORR	oxygen reduction reaction
PDT	photodynamic therapy
PL	photoluminescence
PS	photosensitizer
PTT	photothermal therapy
ref	reference
SA	self-assembly
SEM-EDX	scanning electron microscopy - energy-dispersive X-ray spectroscopy
SILP	supported ionic liquid phases
SPO	secondary phosphine oxide
TGA	thermogravimetric analysis
US	ultra-small
UV-Vis	ultra-violet - visible spectroscopy
XPS	X-ray photoelectron spectrometry

General introduction

Nowadays it is hard to overestimate the value and potential of nanoscience. It is blooming for over three decades and has found applications in electronics, optics, catalysis, and medicine. Researchers all over the globe continue working on control of the structure and ordering of nanoparticles (NPs) to afford high performance in the abovementioned fields of science. One possible way of controlling the properties of NPs is by introducing ligands of a specific function. In early studies, ligands served solely as capping agents; strongly interacting thiols were used to stabilize metal NPs for physical studies, whereas weaker interacting stabilizers such as citric acid or cetyltrimethyl ammonium bromide were preferred to stabilize metal NPs for catalytic applications. Nowadays it is accepted that stabilizers inevitably alter the properties of NPs; however, the global view on the benefits which ligands can bring is still lacking. To our mind, it is of high importance to generalize the knowledge from different nanoscience fields and to share the experience of the experts in these specific fields. For example, researchers from the catalytic field use organic molecules to influence the electron density and crowdedness of the NPs surface inducing selectivity of the nanocatalysts towards desired products¹; energy transfer from ligands to NPs is used in photothermal therapy to treat cancer²; in nanoelectronics by adjusting stabilizers structure, the modulation of electron transport properties of NPs can be achieved³. Sometimes ligands can even act as independent reactive species. To name some, in biomedicine, NPs serve as delivery systems for the ligands that are applied in cell imaging and anti-cancer therapy⁴; in photocatalysis, semiconductor NPs are used to transfer electrons to the attached ligands that act as molecular catalysts⁵.

In this PhD work, we decided to investigate the influence of ligands on the synthesis and properties of ultra-small (US) Pt NPs (<3 nm). Pt NPs have a wide range of applications due to their high stability and conductivity, and excellent catalytic properties. They are applied as catalysts in fuel cells and lithium-oxygen batteries, or as catalytic converters in cars⁶⁻⁸. Thanks to their relatively low toxicity and high biocompatibility, Pt NPs are used as drug delivery systems, contrast agents or in the selective treatment of cancer cells^{9,10}. However, the limited resources and high cost of Pt require the development of efficient protocols of the NPs synthesis and functionalization to achieve high performance in the selected applications. Thus, using the organometallic approach, we decided to synthesize US Pt NPs stabilized by *cyclodextrins (CD)*, *porphyrins*, *ruthenium(II) bipyridyl complexes* or *supported ionic liquids (IL)*. Stability on air and the possibility of facile functionalization make Pt NPs a convenient object of investigation of ligand effects.

In CHAPTER 1 the role of ligands in the synthesis, self-assembly (SA), and catalysis with NPs is discussed. This chapter provides examples where ligands are used to enhance the catalytic properties of the NPs or to directly participate in catalysis or SA. The first part of the literature review provides various roles of organic ligands, while the second part reports applications of NP-metal complex hybrid systems. Separate sections devoted to NP-CD and NP-IL systems are also provided.

CHAPTER 2 investigates the synthesis and catalytic properties of Pt NPs stabilized with CD. Precisely, the first part describes NPs capped with thiolated α/β -CD (CD-SH), whereas the second part discusses Pt NPs stabilized with α -CD bearing a secondary phosphine oxide moiety (CD-SPO). An easy size modulation of US Pt NPs was demonstrated by adjusting the CD-SH/Pt ratio from 0.05 to 0.5, resulting in NPs of 1.1-2.0 nm. Pt NPs do not lose their hydrogenation catalytic activity by stabilization with thiols, although the activity increases with the decrease of the CD-SH content. With Pt-CD-SPO NPs, a peculiar activity of selective hydrogenation of C=O double bonds was observed, when synthesized in the presence of an acid. Overall, CD ligands served as efficient stabilizers which allowed to perform biphasic catalysis in water-organic substrate medium at mild reaction conditions with the possibility of catalyst reuse.

CHAPTER 3 presents the effect of Pt "dilution" by a non-precious iron metal with the formation of bimetallic $\text{Fe}_x\text{Pt}_{100-x}$ alloys of different compositions. The stability of the alloys was assured by an imidazolium-based ionic liquid-modified silica, commonly called supported ionic liquid phases (SILP). $\text{Fe}_x\text{Pt}_{100-x}$ @SILP materials showed high catalytic activity and selectivity in double C=O and C=C bonds hydrogenation and C-O deoxygenation, while preserving aromatic rings. Moreover, by controlling the Fe/Pt ratio it was possible to reach tailor-made selectivity towards specific moieties in a molecule. Similar $\text{Fe}_x\text{Pt}_{100-x}$ @SiO₂ materials showed unreproducible results pointing out the importance of additional stabilization by ionic liquids.

In CHAPTER 4 the synthesis, photophysical and electric properties of Pt NP-porphyrin hybrid systems are presented. Porphyrins and metal porphyrins having different functional groups were used to stabilize US Pt NPs so that two parts of the hybrid system interact through non-covalent interactions or through a coordination bond. This chapter illustrates how the strong interactions between the NP and the porphyrin can originate in new properties, like energy transfer or formation of SAs of defined shapes. Also, the structure-property relations of the hybrid systems in electron transport are discussed.

CHAPTER 5 describes the synthesis and properties of hybrid NP-antenna systems containing Pt NPs and functionalized ruthenium complexes. The ruthenium complexes were synthesized using

a multi-step protocol which yielded complexes of highly photoactive $(\text{Ru}(\text{bpy})_3)^{2+}$ where one bipyridyl ligand contained an aliphatic chain with imidazolium in the end. Imidazolium moiety is essential for the stability of the Pt NPs since after imidazolium deprotonation the formed N-heterocyclic carbene (NHC) can strongly bind to Pt. NHC complexes can be applied directly as stabilizers during the synthesis of Pt NPs or they can be used in a post-synthetic functionalization. In this chapter, the first way was used to yield US Pt NPs. In future, we plan to test the hybrid systems in model hydrogenation and dehydration reactions and to apply the optimized system in important photocatalytic transformations like biomass photodegradation or water splitting reactions.

Altogether, this thesis presents the results of four distinct projects where the ligand's role on the properties of the NPs is investigated. By systematically studying the effects of various stabilizers on the US Pt NPs we show that the choice of a ligand can have a significant impact on the properties and applications of NPs. The present study not only expands our fundamental understanding of ligand-nanoparticle interactions but also provides valuable insights and practical guidance for nanoscientists seeking for the ways to modulate the performance of nanomaterials.

CHAPTER 1. Ligand effects on the properties of metal nanoparticles

1.1. Nanoparticles stabilized by molecular species	5
1.1.1. Capping ligands in colloidal synthesis	5
1.1.1.1. As stabilizing agents.....	5
1.1.1.2. As size and shape regulators	7
1.1.2. Ligand-mediated self-assembly.....	10
1.1.2.1. Partial ligand replacement	11
1.1.2.2. Solvent influence	12
1.1.2.3. Strongly coordinating crosslinking ligands	14
1.1.2.4. Photoresponsive ligands.....	15
1.1.2.5. pH-responsive ligands.....	17
1.1.2.6. Thermoresponsive polymers.....	18
1.1.2.7. Addition of external linkers	19
1.1.3. Ligand role in catalysis	21
1.1.3.1. Electronic effects of ligands.....	22
1.1.3.2. Steric effects of ligands.....	26
1.1.3.3. Ligand-substrate interactions.....	29
1.1.3.4. Dual catalysis	35
1.1.3.5. Case of cyclodextrins	36
1.1.3.6. Case of Ionic liquids	40
1.2. Hybrid systems of type “nanoobject-metal complex”	46
1.2.1. Synthesis of hybrid systems	46
1.2.1.1. Direct synthesis.....	46
1.2.1.2. Post-functionalization.....	47
1.2.2. Complexation-mediated self-assembly.....	49
1.2.3. Hybrid systems in catalysis.....	52
1.2.3.3. Complex as a photosensitizer	52
1.2.3.4. Complex as an active center.....	56
1.3. Conclusions	60

Nanochemistry is a fascinating field of science, which found many applications. However, even if it is a 40-year-old field, a lot of discoveries still have to be done. NPs present unique properties comparing to the bulk materials, which allows specific applications in catalysis, electronics, medicine, etc. There are lots of reviews dedicated to the exceptional properties of NPs, but *what makes them so special? What keeps them small? How can we control their unique behaviors?* In this chapter, we would like to shift our attention to invisible entities (at least by TEM) which are always there for colloidal NPs – surface ligands. The aim of this chapter is to focus on the various effects arising from NP-ligand interaction, starting from the influence of a stabilizer during the synthesis of NPs, the essential role in the self-assembly of NPs and finishing with application of the ligand effects in catalysis. In the first part of the review multiple roles of classical *molecular* stabilizing agents are discussed whereas the second part reports the recent achievements in the domain of *hybrid systems* in which *organometallic complexes* are attached to the surface of NPs. In both sections we review the cases where the ligand serves as a modifier of the active sites of the NP and as an active site itself, while the NP acts rather as a vector directing the overall performance.

1.1. Nanoparticles stabilized by molecular species

1.1.1. Capping ligands in colloidal synthesis

1.1.1.1. As stabilizing agents

NPs have a high surface energy due to the low-coordinated surface atoms. To compensate it capping ligands interact with surface sites thus preserving the small sizes of the NPs. Another function of ligands is to prevent NPs from agglomeration. The plot of the total interaction potential vs. the interparticle distance is presented in Figure 1.1.1 a. At short interparticle distances, van der Waals (vdW) forces are dominant; they lead to irreversible aggregation of NPs (a primary minimum in Figure 1.1.1 a). Thus, capping ligands must be used to prevent the NP approaching to each other, providing the repulsive forces (Figure 1.1.1 b) which keep NPs either in a secondary minimum (reversible aggregated state) or in a free kinetically stable state where NPs are separated.

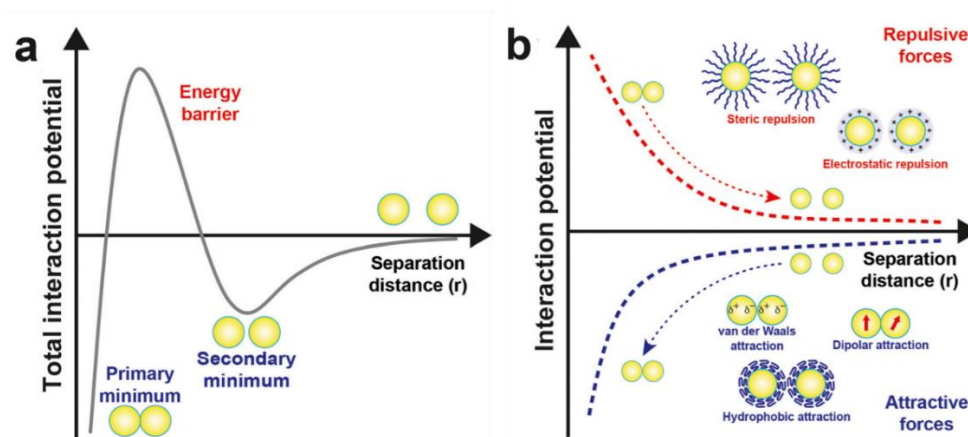


Figure 1.1.1 a) A plot of a total interaction potential of interactions of two particles taking into account attractive and repulsive forces from extended DLVO theory; b) plots of repulsive and attractive forces. Reproduced from ref¹¹.

Several strategies of NP stabilization exist, namely, steric, electronic, and electrosteric stabilization (Figure 1.1.2).

- In the *steric* approach, long chain or bulky molecules as well as polymers are adsorbed on the surface of the NPs. While the NPs approach each other, interactions of adsorbed molecules will lead to entropy decrease due to the steric hindrance, which will unfavor NP aggregation. On another side, an increase of local concentration of ligands will induce osmotic repulsion. As a result, the solvent will reestablish the equilibrium by diluting the macromolecules and will result in separating the particles. The strength of stabilization depends on the type of the interaction between the stabilizer and the metal. Thus, it is not always necessary to have bulky functional groups or long chains if a strong covalent bond is formed. For example, small molecules like mercaptobenzoic acid or ethylenediamine can protect NPs from aggregation.
- In the *electrostatic* approach, adsorption of charged ligands will cause a double electric layer formation. In this case, electrostatic repulsion between two approaching electric double layers will prevent NP aggregation.
- *Electrosteric* stabilization combines both approaches. For instance, cetyltrimethyl ammonium bromide (CTAB) is a charged ligand with a long chain that induces both electrostatic and steric repulsion.

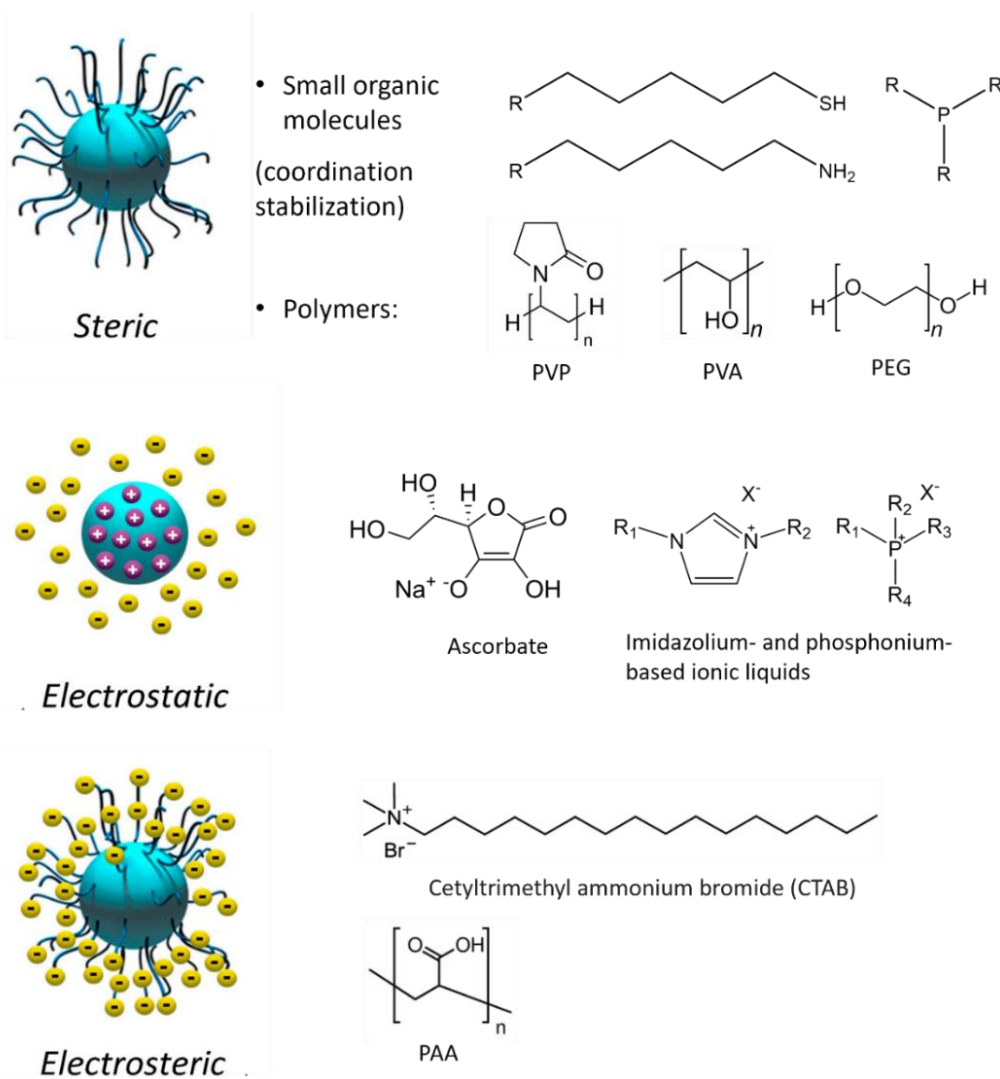


Figure 1.1.2 Types of stabilization of NPs with examples of stabilizers.

1.1.1.2. As size and shape regulators

Effect on the size of the NPs

Each ligand has its own binding strength, diffusion rate and packing modes on the surface of the NPs. All these parameters influence the size and the shape of the NPs. If we consider the parameter of binding strength, the stronger-interacting capping ligand will better passivate the surface, resulting in NPs of smaller sizes. A classic example is the synthesis of Au NPs. With strongly coordinating thiols (126–167 kJ/mol), the size of the NPs may range from 2 to 10 nm¹² while synthesis with weakly interacting ascorbic acid (7 kJ/mol) leads to bigger NPs, reaching sizes of more than a hundred nm^{13,14}.

The amount of a ligand added to the solution of a precursor and a reductant is also important. In a simple case, bigger amount of a stabilizer will lead to higher surface coverage of nuclei and thus will reduce their growth rate resulting in smaller particles. Hussain and coworkers¹⁵ synthesized ultra-small near-monodispersed Au NPs stabilized with water-soluble alkyl thioether

end-functionalized poly(methacrylic acid). They reported that the size of the NPs decreased from 4 to 1.5 nm by increasing the amount of a stabilizer from 0.006 mM to 3.6 mM (Figure 1.1.3). The researchers suggested that the ligand creates a coating on Au nucleus that allows other monomers to approach but prevents fusion of few nuclei, which results in a high degree of monodispersity.

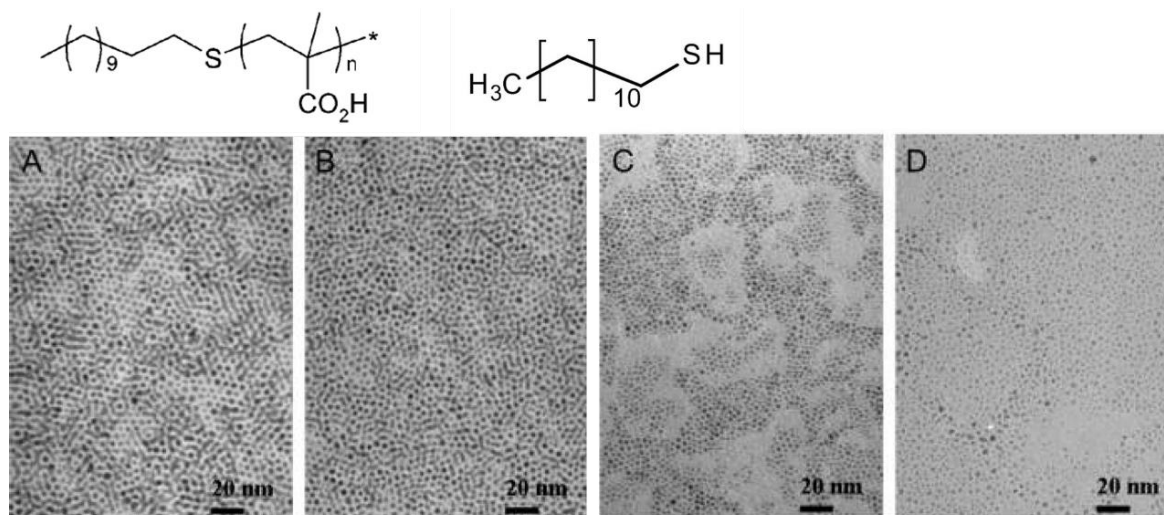


Figure 1.1.3 Structures of alkyl thioether end-functionalized poly(methacrylic acid) and of 1-dodecylthiol used for a phase transfer; TEM images of Au NPs synthesized in a) 0.006 mM (4.0 ± 0.1 nm); b) 0.03 mM (3.0 ± 0.1 nm); c) 0.6 mM (2.0 ± 0.2 nm); d) 3.6 mM (1.50 ± 0.2 nm) of the polymer after the ligand exchange with dodecyl thiol with phase transfer to hexane Adapted from ref¹⁵.

Xian et al. synthesized Pd NPs stabilized with PVP capping agent (Figure 1.1.4)¹⁶. Depending on the ratio of the metal precursor/PVP monomer Pd NPs of mean sizes between 4.4 nm (PVP/Pd = 1-20) and 16.4 nm (PVP/Pd = 0.005) were obtained. Interestingly, the coordination mode of PVP depended on the crowdedness on the surface of the NPs. In case of small NPs PVP was coordinated through oxygen while on big NPs capped with small amount of PVP, coordination through both O- and N-sites was detected. Based on IR results author suggested that bidentate coordination may even lead to the pyrrolidone ring opening.

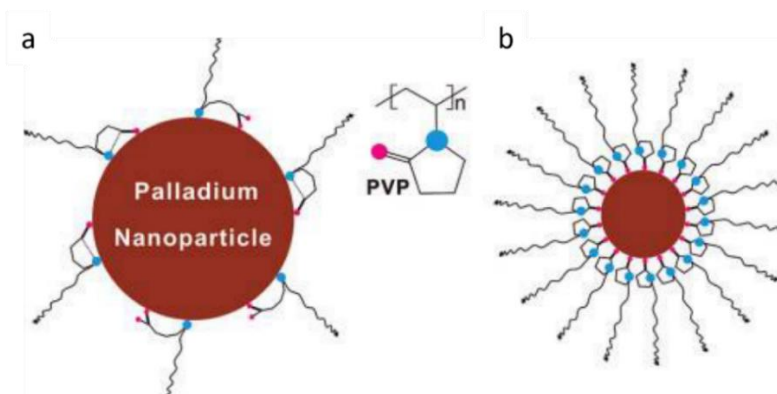


Figure 1.1.4 a) Illustrations of bidentate and b) monodentate coordination of PVP to the surface of Pd NPs. Reproduced from ref¹⁶.

Effect on the shape of the NPs

Noble metal NPs usually form *fcc* structures, since the formation of cuboctahedrons or truncated octahedrons (near spheric shape) enclosed by (111) and (100) facets most efficiently minimizes surface energy. However, if capping ligands have different affinity to facets presented in a single crystal seed, it will affect the final shape of the NP. More precisely, if the ligand is preferentially adsorbed on one of the facets, it will slow down its growing comparing to other facets since its surface energy is lower than the energy of uncovered facet. Thus, the shape with maximal expression of this type of facet will be formed. On the Figure 1.1.5, the influence of two ligands on the final shape of the NP is illustrated. Starting from a seed of *fcc* shape, a capping ligand that prefers to interact with (100) facets will lead to the formation of a nanocube shape, while a capping ligand that binds to (111) facets will provoke formation of octahedron shape (Figure 1.1.5). An example of such system is Ag NPs synthesized from the seeds with PVP which preferentially interacts with (100) surfaces with formation of cubes or with sodium citrate which mostly interacts with (111) surfaces with formation of octahedral NPs¹⁷.

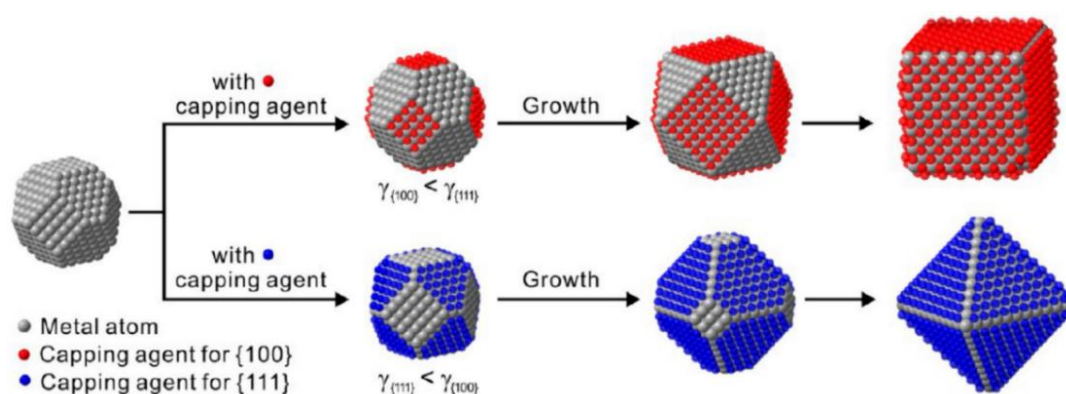


Figure 1.1.5 Illustration of the role of a capping agent in directing the shape of the NP. Reprinted from the ref¹⁸.

In another example by Lim and colleagues the concentrations of metal precursor and ligand could regulate the shape of final NPs (Figure 1.1.6)¹⁹. Citric acid (CA) has three carboxylic acid groups that match well with the hexagonal symmetry of (111) surface of *fcc* metals. Therefore, it preferentially interacts with (111) face slowing down its growth. As a result, by adjusting concentration of a precursor PdCl_4^{2-} (5.8–17.4 mM) and CA (28–84 mM) various shapes were obtained: octahedra, icosahedra, decahedra, which are all dominated by (111) facets.

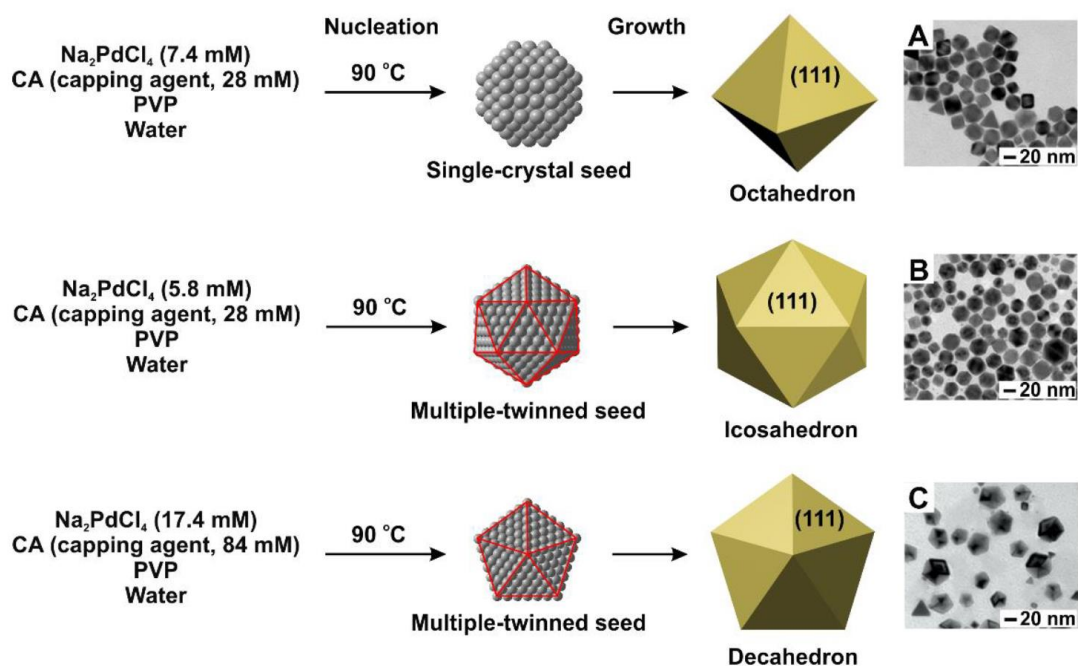


Figure 1.1.6 Schemes of synthesis and TEM images of (A) octahedra, (B) icosahedra, (C) decahedra shapes obtained by varying concentrations of Pd precursor and citric acid. Reprinted from ref²⁰.

By adjusting the reaction conditions and carefully choosing the capping agent, it is possible to synthesize clearly anisotropic nanoobjects. The most famous example is a seed-mediated growth of Au nanorods (NR). In this synthesis, Au seeds are added to the solution containing gold precursor, a weak reducing agent, like an ascorbic acid, and a capping agent - cetyltrimethylammonium bromide (CTAB). CTAB binds preferentially to the (100) crystal plane on the side of the NR decreasing its growth rate and promoting an anisotropic crystal growth on the (111) facets at the tips that leads to formation of Au nanorods.

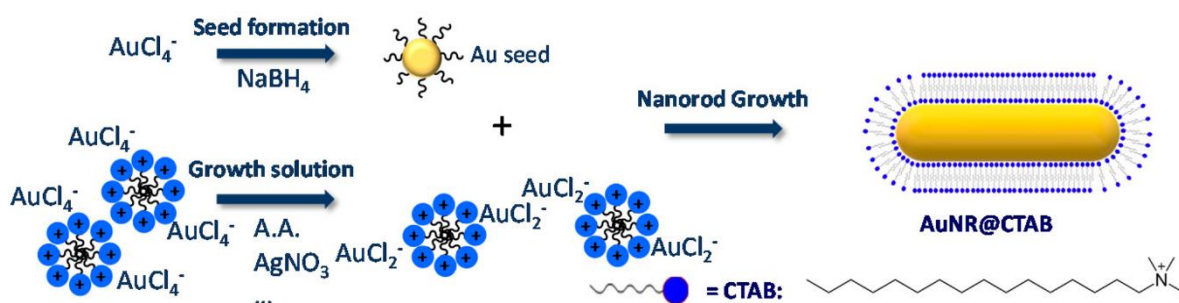


Figure 1.1.7 Illustration of seeded-growth of Au nanorods. Adapted from ref²¹.

1.1.2. Ligand-mediated self-assembly

As it was discussed in the previous section, ligands are used to preserve NPs in their dispersed state. However, by precise modulation of attractive-repulsive forces between ligands, it is possible to keep NPs on the distances that correspond to the secondary minimum on the Figure 1.1.1 a, that is in the self-assembled state. From the secondary minimum, it is possible to go back to the dispersed state

by applying energy equal to k_bT , by tuning the entropy-enthalpy factors, nature of the ligands and their attracting-repulsive interactions or by adding external compounds. In this section, such examples of SA of monometallic NPs stimulated by external stimuli (pH, light, solvent etc) will be discussed. Most of the studies use Au NPs due to the well-defined procedures of a size-controlled synthesis and ligand exchange, as well as due to the possibility of a simple characterization of the aggregated and dispersed states by UV-Vis following surface plasmon resonance (SPR) signal of Au NPs.

1.1.2.1. Partial ligand replacement

Regarding the dominant forces that influence NP dispersion, repulsive electrostatic and steric interactions contribute to the NPs dispersed state while dipolar, hydrophobic and van der Waals interactions contribute to aggregation of NPs. While vdW interactions are mostly due to the intrinsic core properties, the other forces can be modulated by attaching additional ligand on the surface of the NPs. Gentili and coworkers showed that citrate-capped Au NPs could form reversible SA by changing the amount of a second ligand - (11-mercaptoundecyl)hexa-(ethylene glycol) (MUHEG)²². At around 50% of MUHEG on the surface of Au, NPs chain-like SAs were formed due to the replacement of citrate ions which display repulsive electrostatic and steric forces by MUHEG with attractive dipolar and repulsive steric forces ($[V_{vdW} + V_{dip}] > [V_{ele} + V_{ste}]$) (Figure 1.1.8 a, b). However, upon further increase of the MUHEG content, the repulsive steric interactions of the hydrophilic ethylene glycol chains became dominant, which lead to the disassembly ($[V_{vdW} + V_{dip}] < [V_{ele} + V_{ste}]$). Interestingly, by addition of citrate-capped Au NPs to the solution of dispersed Au NPs with 80% of MUHEG, the SA structures began to appear, suggesting interparticle ligand exchange. This work showed an importance of an interplay between electrostatic, dipolar, and steric interactions to obtain stable reversible SAs.

Controlled formation of vesicles was performed with Au NPs covered with a mix of hydrophobic (1-dodecanethiol (DT)) and hydrophilic ligands (11-mercapto-1-undecanol (MUL))²³. With more DT in the system, hydrophobic interactions led to a thicker membrane of nanovesicles (Figure 1.1.8 e). This observation and supporting MD calculations suggested a phase segregation of the ligands where outer shell was formed with the alcohol ligands while between the nanoparticle layers hydrophobic ligands induced attractive interactions (Figure 1.1.8 d). The authors used this assemblies for a controllable dye release. They prepared dye-loaded vesicles of a defined thickness by varying ligands ratio. With the thinnest shell after some time an increase in fluorescence was observed in accordance with breaking the SA and emission of a free dye. Meanwhile, vesicles with

thicker shell were stable upon irradiation. Thus, the dye release could be controlled by the thickness of vesicles membrane.

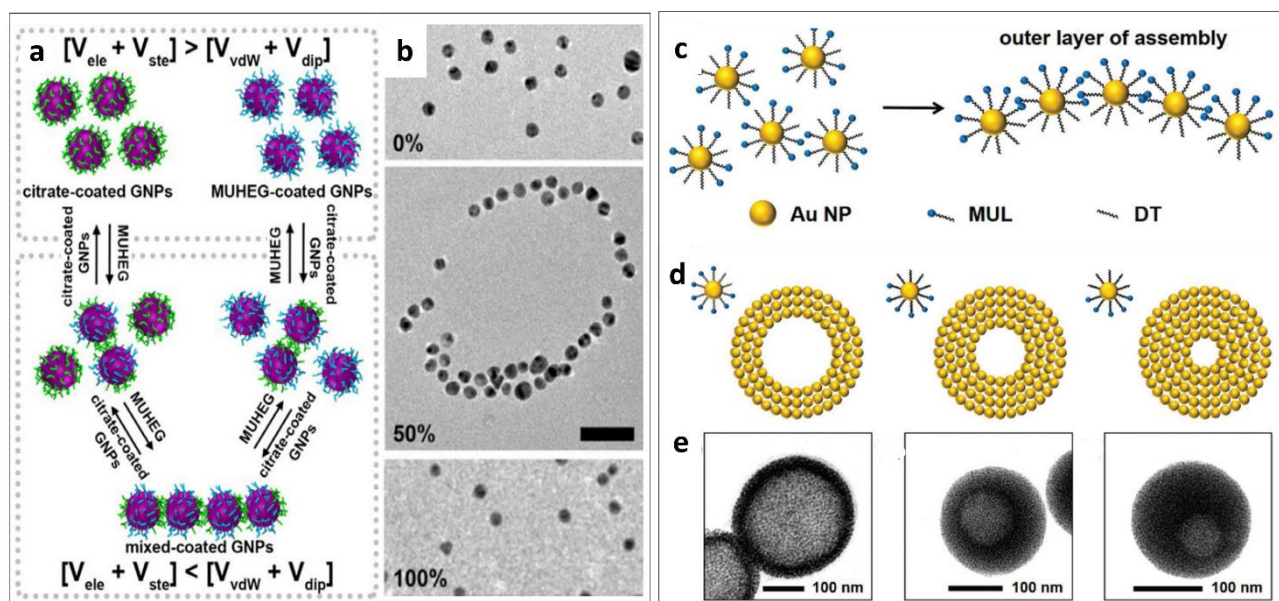


Figure 1.1.8 a) Scheme of assembly-dissassembly processes depending on the ligand ratio and the forces involved; b) TEM images of Au NPs with 0%, 50%, and 100% of MUHEG. Adapted from ref²². c) scheme of phase segregation on Au NPs; d) illustration of dependence of the shell thickness on ligands ratio with corresponding TEM images e). Adapted from ref²³.

1.1.2.2. Solvent influence

Hydrophobic interactions are important non-covalent interactions that can provoke assembly of NPs stabilized with hydrophobic ligands upon addition of a poor solvent. However, it is important to develop methods to control these interactions in order to avoid complete aggregation and sedimentation.

Sanchez-Iglesias and coworkers used water as a poor solvent to induce SA of Au NPs stabilized with polystyrene in THF²⁴. One day after water addition, complete sedimentation of the NPs was observed. To control aggregation, they added a polymeric surfactant together with water, which resulted in encapsulation of aggregates. Further evaporation of THF lead to rearrangement of the NPs in the capsule and preserved the stability of the assemblies in water solutions (Figure 1.1.9 a, b). Importantly, upon readdition of THF, the NPs could be redispersed (Figure 1.1.9 c).

A bright example of using the quality of the solvent to design various SA structures of Au nanorods (NRs) was reported by Nie and colleagues²⁵. In their study, Au NRs were covered with cetyltrimethylammonium bromide (CTAB) on long sides and with thiol-terminated polystyrene (PS) on the ends. By the addition of H₂O the DMF or THF solution of NRs SAs were formed. Precisely, end-to-end nanochain SAs (Figure 1.1.10 a,b) were obtained by water addition to the DMF solution

of NRs since water is a poor solvent for polystyrene; bigger content of water stimulated the formation of longer chains. In THF Au NRs stabilized with CTAB were poorly soluble. So, in THF with 6% of water content side-to-side interactions of CTAB were favored which led to the formation of NRs bundles (Figure 1.1.10 c). By increasing water content hydrophobic interactions between polystyrene resulted in the SA of nanospheres (Figure 1.1.10 d). By using three solvents together all the abovementioned interactions were favored resulting in the bundled chains of NRs (Figure 1.1.10 e).

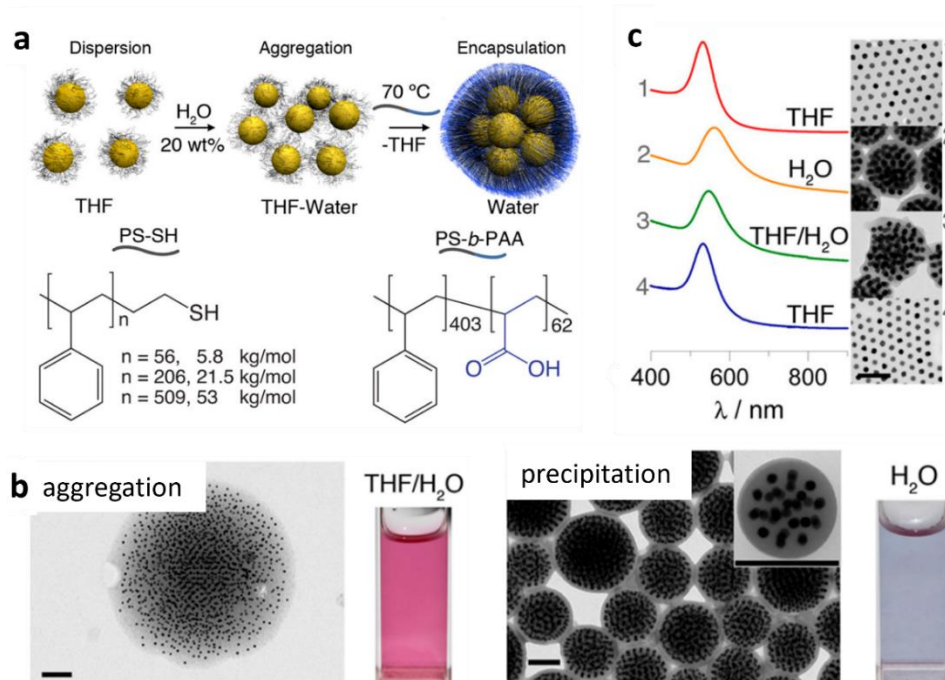


Figure 1.1.9 a) Scheme of polymer-controlled structural transitions of Au NPs with corresponding TEM pictures b); c) Surface plasmon resonance bond of Au NPs and TEM images at different steps of assembly-disassembly process. Adapted from ref²⁴.

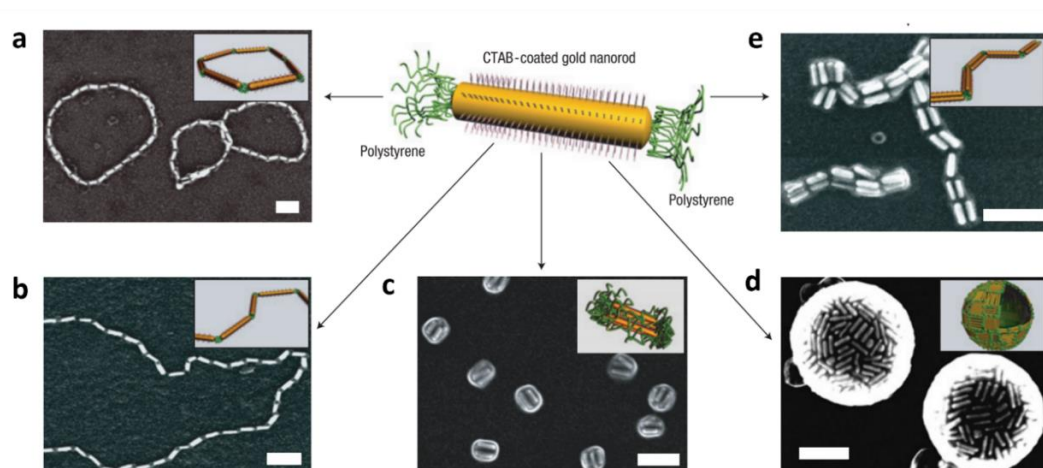


Figure 1.1.10 Structure of an Au NR stabilized with CTAB and polystyrene ligands and the corresponding SEM images of SAs: a), b) chains in DMF/ H₂O at H₂O contents of 6 and 20 wt%, respectively, c) bundles and d) nanospheres in the THF/H₂O at H₂O contents of 6 and 20 wt%, respectively, e) bundled chains obtained in DMF//THF/ H₂O mixture at a weight ratio of liquids 42.5:42.5:15. The scale bars correspond to 100 nm. Adapted from ref²⁵.

1.1.2.3. Strongly coordinating crosslinking ligands

Ligands that have few strong binding entities are used to create stable irreversible short- or long-range ordered NP networks for electronic or catalytic applications. A binding strength to Au (111) surface increases in a row $-\text{COOH}$ (Au–O, 8.4 kJ/mol), $-\text{NH}_2$ (Au–N, 65 kJ/mol), $-\text{SH}$ (Au–S, 167 kJ/mol)²⁶, so thiols can be used to directly stabilize NPs and form rigid superstructures or to partially cover the surface through post-synthetic ligand exchange. Nasrallah and colleagues used small adamantane derivatives functionalized with two thiols (1,1'-bisadamantane-3,3'-dithiol and diamantane-4,9-dithiol) to stabilize Au NPs and create rigid NP assemblies²⁷. The systems showed narrow size distribution with sizes below 3 nm (Figure 1.1.11 a). Short-range order in these systems was confirmed by SAXS where the interparticle distance almost perfectly corresponded to the theoretically calculated distances between two nanoparticles separated by a corresponding linker (Figure 1.1.11 b,c). These systems were successfully applied as a precatalyst in cascade reactions: dimethyl allyl(propargyl)malonate cyclization – Diels-Alder cyclization with maleic anhydride, and outperformed commercial gold catalysts.

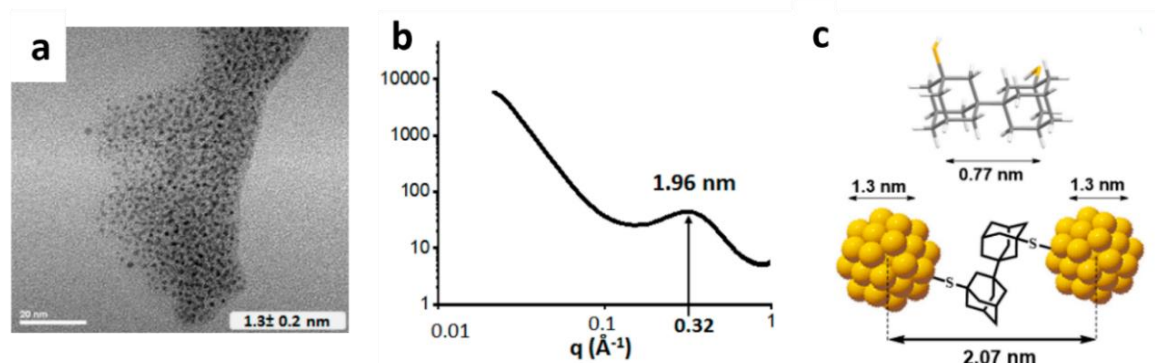


Figure 1.1.11 a) TEM image of Au NPs stabilized with 1.5 eq of 1,1'-bisadamantane-3,3'-dithiol; b) SAXS analysis indicating short order arrangement; c) scheme of the network local dimension. Adapted from ref²⁷.

Klajn and colleagues used 4,4'-bis(11- mercaptoundecanoxy)azobenzene (ADT) (Figure 1.1.12 a) to partially replace dodecylamine (DDA) from the surface of Au NPs²⁸. Depending on the ratio ADT/DDA and the ratio of methanol/toluene solvents, different superstructures could be obtained under UV irradiation (Figure 1.1.12 b). While under visible irradiation, azobenzene is present as a trans-isomer, under UV irradiation, it isomerizes into a more polar cis-isomer (dipolar moments are approximately 1 debye for the trans-isomer and 5 debye for the cis-form). Thus, strong dipole interactions and thiol linkers participate in SA formation (Figure 1.1.12 c). With a low amount of ADT and a low content of methanol, reversible crystals could be obtained, which were stable only upon continuous UV irradiation. However, in the regime of high ADT content, the authors reported the formation of irreversible highly-ordered *hcp* crystals of the sizes up to 0.8 μm . The formed

crystals were stable upon visible light, thermal heating up to 100 °C, sonication or addition of other thiol linkers. Interestingly, the size of the SA could be controlled either by the content of ADT or by the time of UV irradiation (Figure 1.1.12 d-g).

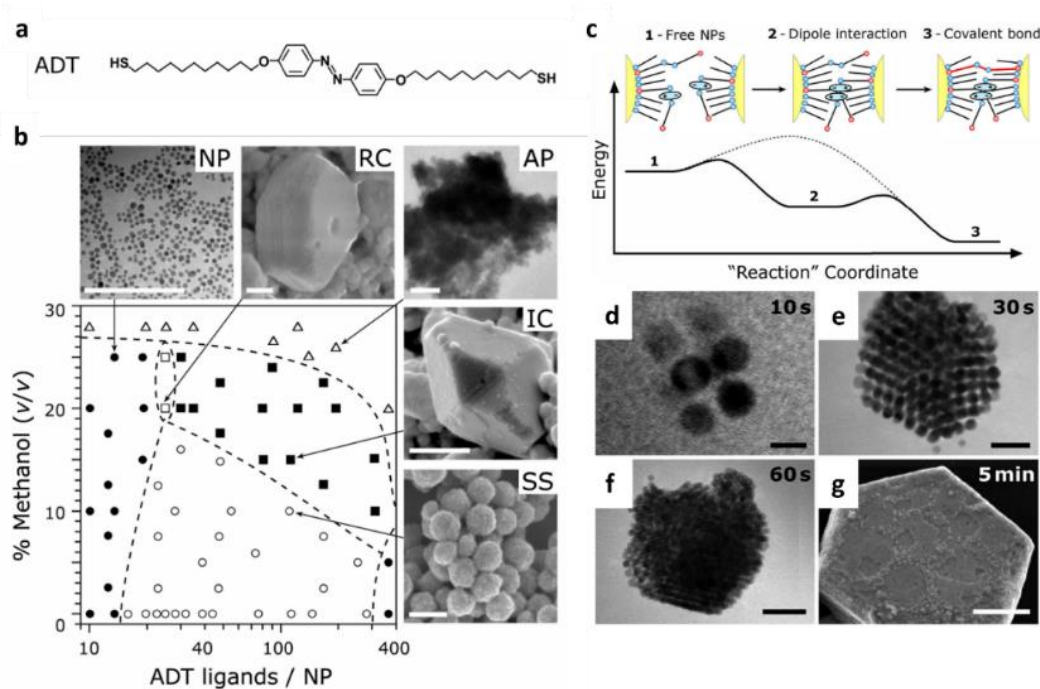


Figure 1.1.12 a) structure of ADT ligand; b) Phase diagram showing formation of various superstructures depending on the content of ADT ligand and methanol (NP - dispersed NPs, RC - light-reversible crystals, AP - amorphous precipitate, IC - irreversible crystals, SS - supraspheres). Scale bars: 100 nm. c) Energy diagram representing energy gain by light-induced dipole interaction of cis-ADT ligands and covalent cross-linking of the assembled particles. Dashed line shows qualitatively an energy barrier for cross-linking in the absence of dipole-dipole interactions. d)-g) TEM images of NP SAs with high ADT content upon different time of UV irradiation. Scale bars: d - 5 nm, b - 20 nm, c - 50 nm, d - 200 nm. Adapted from ref²⁸.

1.1.2.4. Photoresponsive ligands

Some molecules can undergo simple reversible transformations under light irradiation like isomerization or dimerization. For instance, in the previous example an azobenzene derivative was responsible for dipole-dipole attractive forces which lead to SA of NPs. In this part we would like to illustrate few more examples of a reversible light-induced SA.

The Klajn group specializes on a light-responsive NP SA. In one of their studies, they attached thiol-functionalized azobenzene ((11-mercaptoundecyloxy)azobenzene, MUA) to Au and Ag NPs (Figure 1.1.13)²⁹. Under UV a more polar cis-isomer was formed leading to dipole-dipole interactions and consequent formation of spheric self-assemblies. Under visible light or upon mild heating trans-isomer was formed and disaggregation took place. UV irradiation time influenced the proportion of aggregated NPs, which induced color change from red to violet in case of Au NPs and from yellow

to violet with Ag NPs. The simplicity and reversibility of the system allowed to insert the NPs in a gel matrix and to use the material as self-erasing inks (Figure 1.1.13, d).

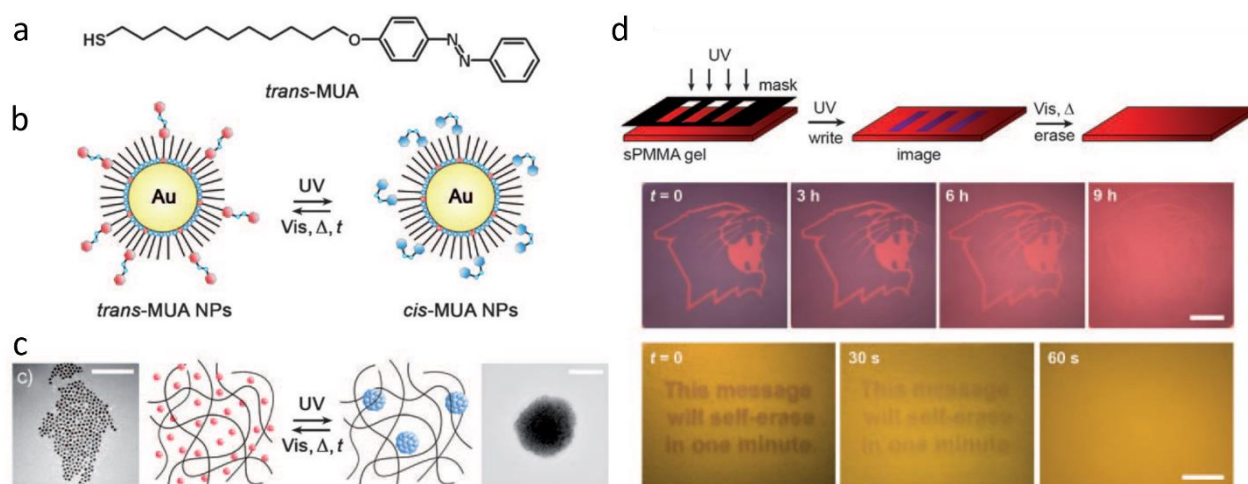


Figure 1.1.13 a) Structure of (11-mercaptoundecanoxy)azobenzene; b) scheme of isomerization of MUA attached to Au NPs and c) corresponding TEM images; d) scheme of applying image on the film containing Au@MUA with UV light through mask and photographs of resulting images that are erased under visible light and heating. Adapted from ref²⁹.

Another interesting application for reversible azobenzene-based NP SA systems is using the aggregated state as a nanoflask³⁰. The researchers proposed that upon SA of NPs, polar reagents could be trapped within the NP aggregate (Figure 1.1.14 a, c). This, in turn, would increase their local concentration and consequently the reaction rate. Importantly, products can be conveniently released upon SA disaggregation. Indeed, reaction acceleration was observed for hydrolysis (Figure 1.1.14 b) and dimerization reactions.

Spirofurans (SF) is another molecule that upon UV irradiation can undergo chemical transformation, namely, ring opening with formation of merocyanine (MC). Nanoparticles coated with SF under UV formed strongly interacting aggregates due to electrostatic and π - π interactions between MC (Figure 1.1.14 d)³¹. These aggregates could keep their sizes in the dark for prolonged period of time and disassemble under visible light. In this way the size of the aggregates could be tuned by modifying the irradiation time (Figure 1.1.14 e, f).

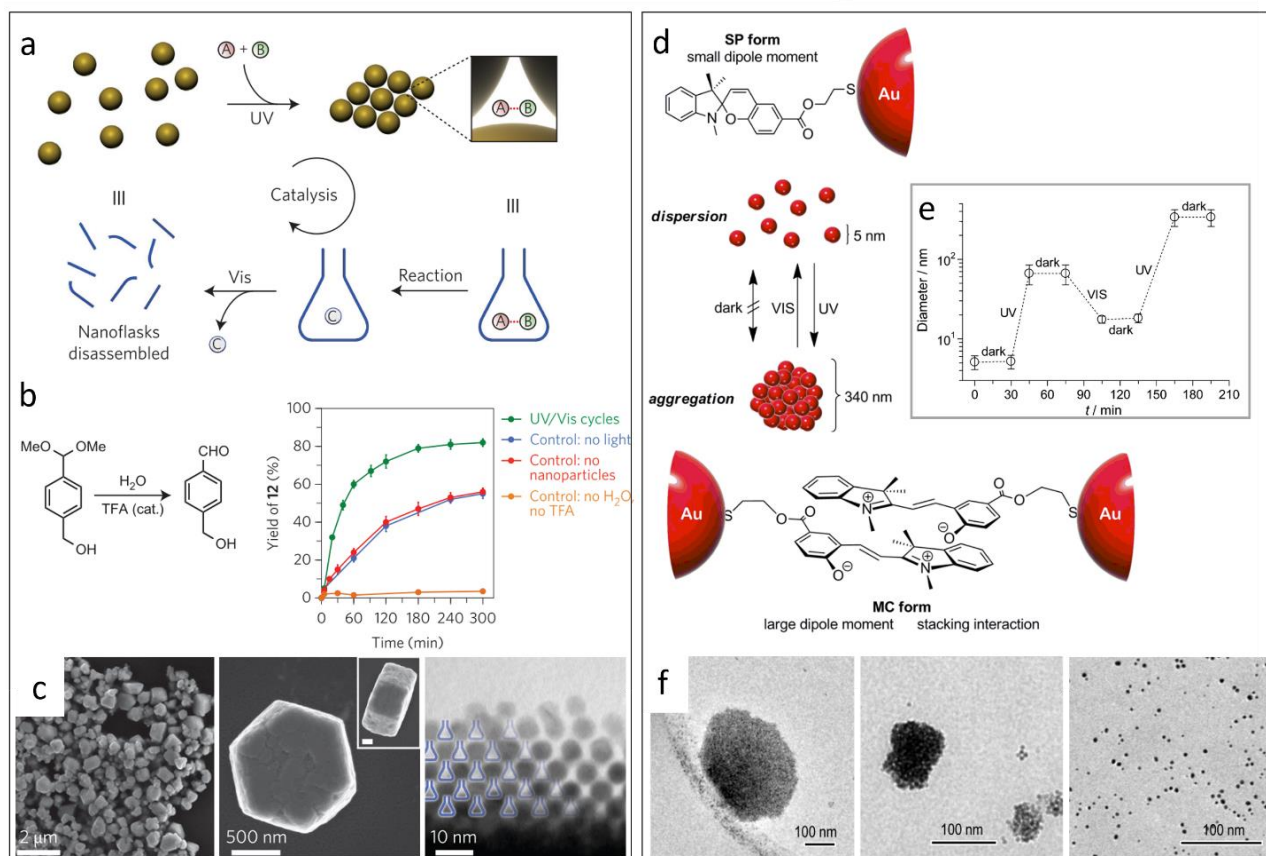


Figure 1.1.14 a) Scheme of a reaction between reagents confined in space inside the NP aggregate; b) example of accelerated reaction due to the confinement inside the aggregates; c) SEM and TEM images of SA crystals. Adapted from ref³⁰. d) Scheme of a reversible SA of Au NPs stabilized with a thiolated spirofuran; e) plot of the size modification of the aggregates induced by UV or Vis irradiation time; f) TEM images of the aggregates after 30 min of UV irradiation 0 min of Vis irradiation; 30 min of UV and 60 min of Vis; 30 min of UV and 90 min of Vis. Adapted from ref³¹.

1.1.2.5. pH-responsive ligands

pH-responsive capping ligands like acids or amines can be used as a driving force of SA. By adjusting the pH of the solution, it is possible to influence on deprotonation degree of ligands. In these conditions, acids in protonated form can interact through hydrogen bonds forming SA, while deprotonation provokes disassembly due to electrostatic repulsion.

This approach was employed by Fan and coworkers to form Au NPs vesicles (Figure 1.1.15 a-c)³². Firstly, oleylamine-capped NPs were synthesized, then a partial ligand exchange with mercaptobenzoic acid was performed. Upon sonication in water Au NPs capped with hydrophobic and hydrophilic ligands rearranged in vesicles in order to minimize contact of oleylamine with water. When increasing pH from initial 4.8 to 11.7, the aggregates disassembled and only well-dispersed individual NPs were observed. The reason was that at high pH, acid was deprotonated, which induced electrostatic repulsion and increased hydrophilicity of the system. The authors showed that the SA process was fully reversible, performing five assembly-disassembly cycles.

With zwitterionic ligands, the situation is even more interesting since both electrostatic attracting and repulsive interactions can take place depending on deprotonation degree. Such transformations provide dual pH response of the NPs showing disassembly-assembly-disassembly behavior by increasing pH level. He and colleagues prepared Au NPs stabilized with thiolated guanidiniocarbonyl pyrrole carboxylate zwitterion (GCPZ) (Figure 1.1.15 d)³³. At pH of 5-8, GCPZ in zwitterionic state forms strong dimers; this behavior was responsible for Au NPs SA formation in DMSO/H₂O =10/1 solvent. Meanwhile, after addition of acid or base only well-dispersed NPs were found due to the corresponding protonation or deprotonation of the ligand and losing its zwitterionic form (Figure 1.1.15 e-h). Interestingly, the authors found that in the medium with 30% of H₂O and more, the SA was stable even in a protonated state. They assumed that with increasing the water content, hydrophobic interactions between ligands became dominant which kept the system in an assembled state.

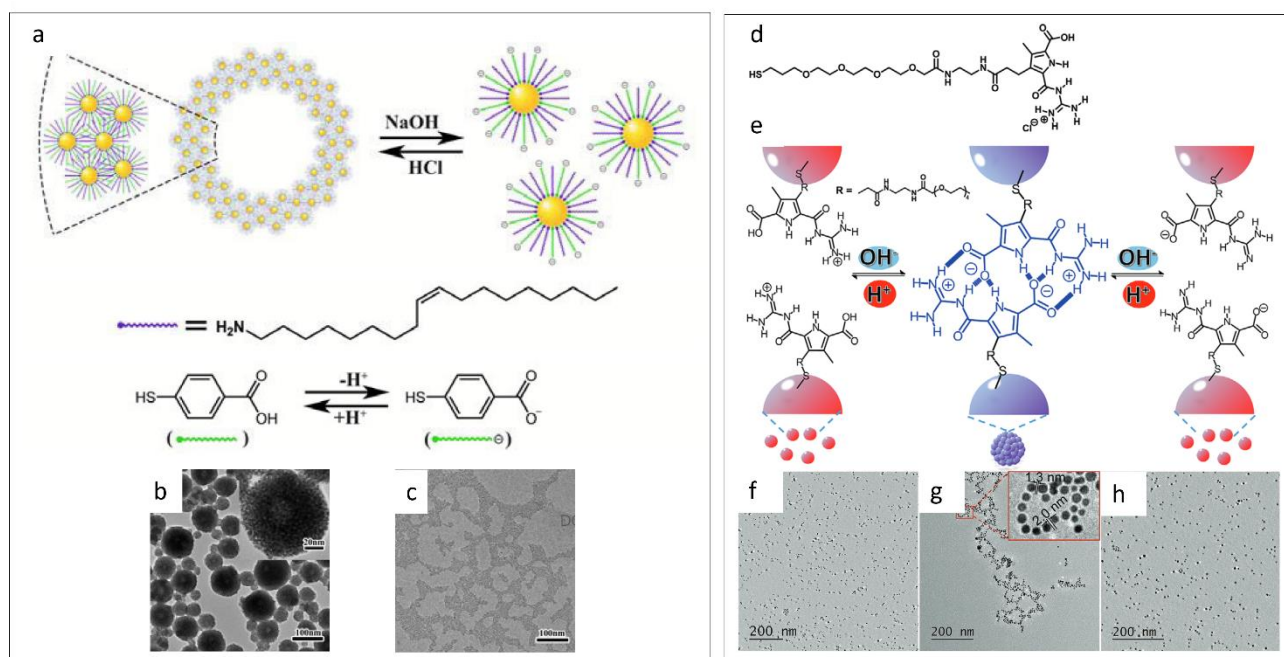


Figure 1.1.15 a) Illustration of vesicle SA of Au NPs and its disassembly upon base addition; b), c) corresponding TEM images in assembled and dispersed state. Adapted from ref³². d) structure of a zwitterionic ligand; e) a scheme of disassembly-assembly-disassembly of Au NPs with pH increase with corresponding TEM images in each state (f-h). Adapted from ref³³.

1.1.2.6. Thermoresponsive polymers

Thermoresponsive SA of polymer protected NPs rely on the property of the ligand to have hydrophilic-hydrophobic transition when temperature reaches a limit of lower critical solution temperature (LCST). One of the most studied thermoresponsive polymers - poly(N-isopropylacrylamide) (PNIPAM) undergoes coil-to-globule transition at the temperature as low as 32°C. At this temperature hydrogen bonds between amide moieties and water molecules break and

hydrophobic interactions between isopropyl groups become dominant leading to transformation into a globular structure.

Balasubramaniam and colleagues synthesized oleylamine-capped Fe_3O_4 NPs which were further functionalized with a bis(phosphonate)-PNIPAM polymer (Figure 1.1.16 a)³⁴. While having a hydrodynamic diameter of 38 nm upon reaching LCST and higher temperatures, the diameter drastically increased (Figure 1.1.16 b) indicating the loss of steric stabilization of NPs due to the coil-to-globule transition. At $t = 40^\circ\text{C}$ flocculation of NPs took place (Figure 1.1.16 c), however a decrease of temperature allowed their redispersion. The authors showed that the size of the aggregates could be conveniently tuned with the temperature control.

A photothermal approach to assemble NPs was applied by Fava and coworkers³⁵. In their study, gold nanorods (Au NRs) were coated by CTAB on the long sides and by PNIPAM on the corners (Figure 1.1.16 d, e). Upon irradiation surface plasmon resonance of Au NRs resulted in plasmonic heating. The heating provoked a collapse of polymer structure into globular shape and an end-to-end assembly of the NRs (Figure 1.1.16 d, f).

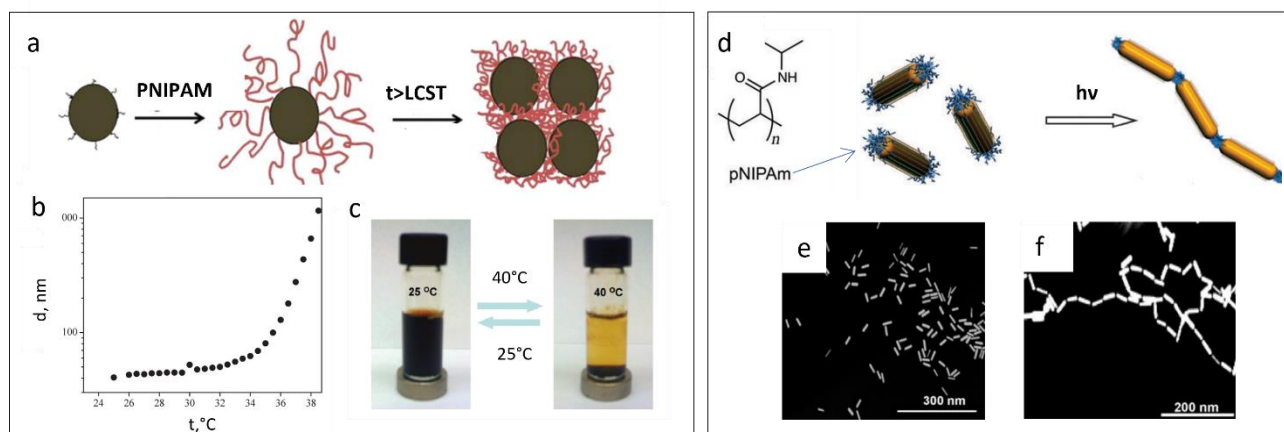


Figure 1.1.16 a) Scheme of temperature induced SA of Fe_3O_4 -PNIPAM NPs; b) dependence of diameter of particles on a temperature. Diameter was measured by DLS; c) photos of Fe_3O_4 -PNIPAM-Nile Red NPs at 25°C and at 40°C . Adapted from ref³⁴. d) Scheme of SA of Au-PNIPAM NRs; e) TEM image in dispersed and f) assembled states. Adapted from ref³⁵.

1.1.2.7. Addition of external linkers

Inclusion complexes with cyclodextrines

Cyclodextrins (CD) are macrocycles that are known to create strong inclusion complexes with unipolar molecules of suitable sizes. This type of supramolecular interactions was used by some scientists to create NP SAs^{36,37}. Liu and colleagues synthesized Au NPs stabilized with thiol-modified β -CD³⁸. Au NPs while being well-dispersed in solution, upon addition of diazo linker aggregated due to the interaction of two phenyl rings of the linker with CDs of two NRs (Figure 1.1.17 c,d). The

aggregation can be followed by change of the solution color from pink to purple (Figure 1.1.17 a). It was possible to redisperse NPs by addition of α -CD which forms stronger inclusion complexes with phenyl rings (Figure 1.1.17 b).

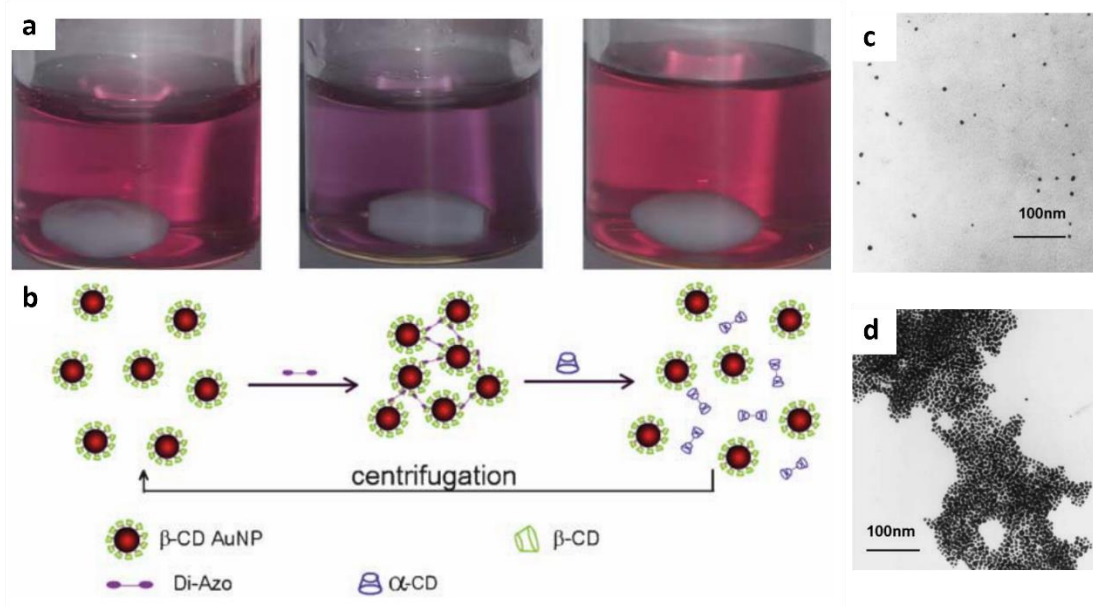


Figure 1.1.17 a) Color change of Au-CD NPs solution upon addition of a di-azo dye and after addition of α -CD; b) a schematic representation of assembly-disassembly reactions; c) TEM images before and d) after the linker addition. Adapted from ref³⁸.

Halogen bonding

Previously we showed examples of SA induced by electrostatic, dipolar, hydrophobic or hydrogen bond interactions. Halogen bonds, although rarely applied, can also be used to form strong interactions. The concept of halogen bonds formation was used to induce a SA in a study of Shirman and colleagues³⁹. Au NPs capped with TOAB underwent ligand exchange with halogenated N-oxide (**1** in Figure 1.1.18) which served as a donor of halogen bond (XB). Consequently, upon addition of a bifunctional XB accepting linker (1,4-bis((E)-2-(pyridin-4-yl)vinyl)benzene, BPEB) NPs formed chain-like SAs or dense aggregates depending on the concentration of BPEB (Figure 1.1.18 c, d). Interestingly, when using the ligand without iodine sites (**2** in Figure 1.1.18) no SA was formed indicating that halogen bonding was a driving force of SA and that XB bond was only formed with iodine which is a stronger halogen bond donor.

In summary, NP SA process can be controlled by an interplay of repulsive-attractive forces of surface ligands. The reversibility of these assemblies was shown to be tuned by various parameters like solvent polarity, light, heating and others. The resulting self-assembled materials can find various applications in nanotechnology and biomedicine.

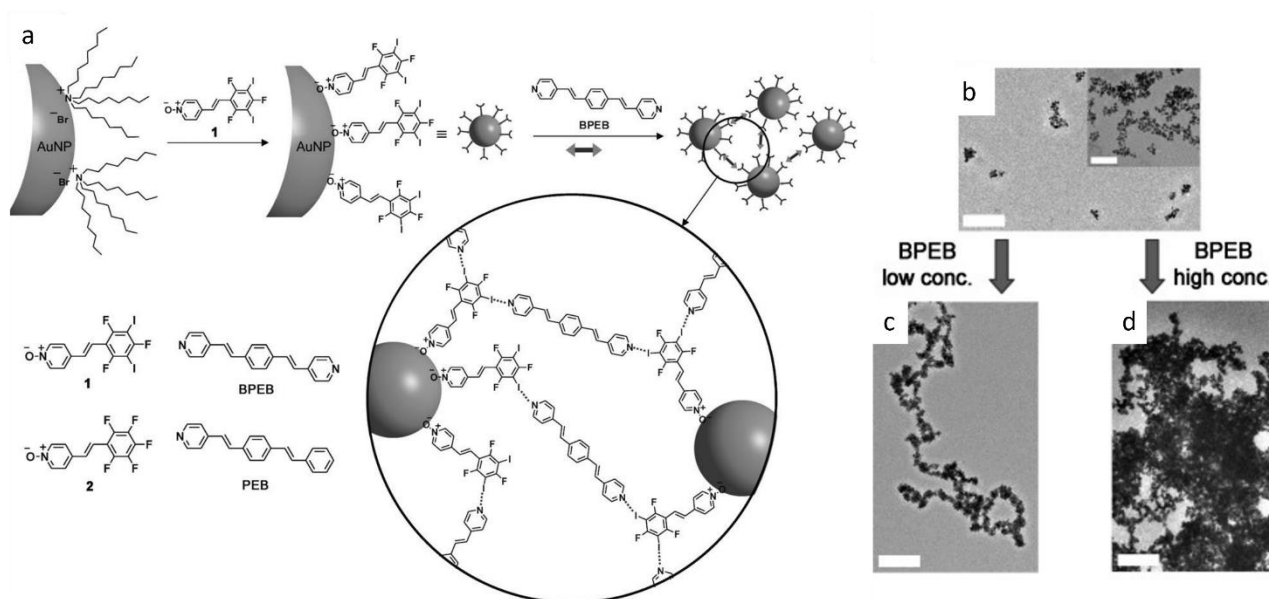


Figure 1.1.18 a) Scheme of a functionalization and SA formation upon addition of a halogen bond acceptor BPEB; TEM images of b) dispersed NPs; c) NP SA at low concentration of BPEB d) NP SA at high concentration of BPEB. The scale bars correspond to 200 nm. Adapted from ref³⁹.

1.1.3. Ligand role in catalysis

Ligand is an essential component in controllable synthesis and SA of NPs. However, for catalytic applications, most of the time ligands are considered as undesirable species since they can compete with substrates for the active catalytic sites. As a matter of fact, numerous papers report poisoning behavior of thiol species on reduced metal surfaces in hydrogenation and dehydration reactions. Here, the ligand influences both geometry and electronic properties of the surface that leads to deactivation of NPs in catalysis. However, in the last decade, a strategy of surface modification with ligands attracted a lot of attention due to the possibility of improving the selectivity of the reaction. Indeed, small additions of ligands that can selectively block reactive sites on the surface of a metal NP (MNP) will beneficially influence on the selectivity of the reaction without significant deterioration of the activity. One of the pioneering works in this regard is a work of Lindlar on a supported Pd catalyst named after him (10.15227/orgsyn.046.0089). Lindlar catalyst is used in selective hydrogenation of alkynes to alkenes. Overhydrogenation to alkanes is stopped due to the surface poisoning with quinoline, tin, or sulfur compounds. In addition to blocking of active sites, other beneficial effects can take place, like electron enrichment of the metal surface, ligand interaction with a substrate (molecular recognition), substrate confinement and others that will be explained in this section. Apparently, not only one but rather a combination of these effects controls the selectivity of the reaction. Nevertheless, most of the times researches try to experimentally confirm at least one of them, so in this chapter the examples will be distributed accordingly. Examples of both colloidal and supported NPs will be discussed; however, the focus will be on the

ligand influence and not on the metal-support interaction. The issues related to surface modification such as chemical stability of the ligands upon the reaction conditions or stability during recycling will be also addressed.

1.1.3.1. Electronic effects of ligands

Interaction of ligand with metal surface may result in electron transfer from the ligand to the NP or vice versa. Particularly strong sigma donors are phosphines and N-heterocyclic carbenes while thiols can act as acceptors of electron density. Modification of electronic density on the surface of NPs leads to changes in adsorption energy of substrates, which can be estimated by DFT. In such conditions, competitive adsorption can take place. In other words, ligand may have weaker adsorption energy than a reagent but stronger than a primary product. This, in turn, prevents primary product from further transformations on the surface which increases the selectivity of the reaction towards the primary product.

Chen and coworkers investigated how the modification of platinum nanowires (Pt NWs) with ethylenediamine (EDA) (Figure 1.1.19 a) influences their performance in the catalytic hydrogenation of nitrobenzene⁴⁰. Interestingly, while non-modified wires allowed an aniline formation, the addition of EDA resulted in the selective formation of hydroxylamine. DFT calculations revealed that the strong interaction of EDA with the Pt surface modifies the adsorption energies of reactants and intermediates. Precisely, adsorption free energies of nitrobenzene, nitrosobenzene, and N-hydroxylaniline on unmodified Pt surface were calculated to be -1.27, -1.48, and -0.89 eV, respectively, while upon addition of EDA the adsorption energies changed to -0.55, -0.87, 0.41 eV, respectively, meaning that the adsorption of the hydroxylamine was strongly disfavored (Figure 1.1.19 b). Experimental data obtained from adsorptive stripping voltammetry with CO confirmed electron density increase on Pt sites. Concerning theoretical calculations and experimental data, possible explanation can be that electron-rich platinum sites interact strongly with relatively electron-poor systems like nitro- and nitrosobenzene through d- π^* donation, whereas interaction with electron-rich hydroxylaniline is disfavored.

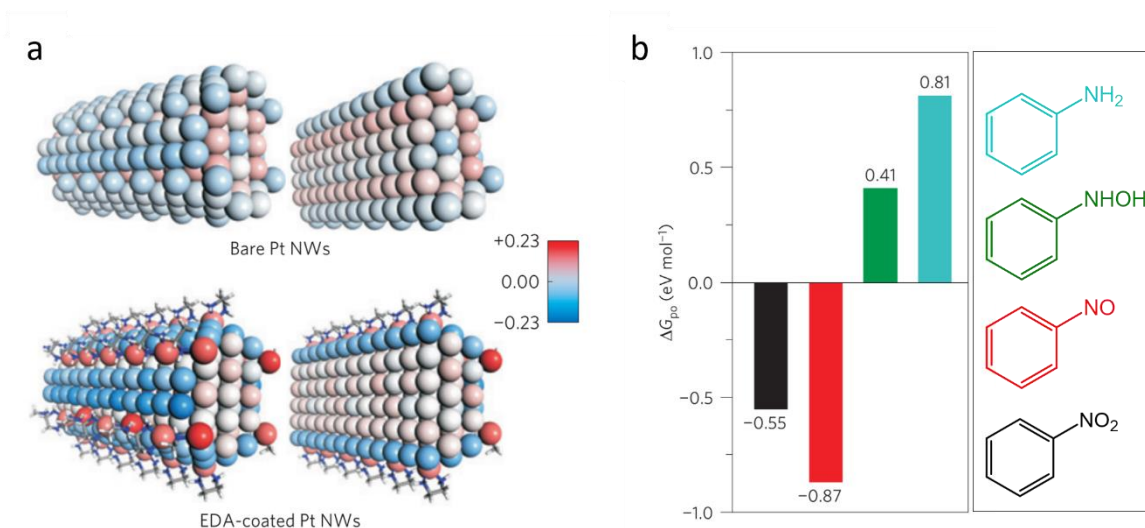


Figure 1.1.19 a) Constructed models of bare Pt NW and EDA-Pt NW. The colours in Pt NWs indicate the Bader charge of each atom; b) Free energies (ΔG_{po}) for the adsorption of N-containing aromatics over EDA pre-coated Pt NWs. Reprinted from ref⁴⁰.

Kwon and coworkers have systematically checked the influence of different ligands (primary amines, trioctylamine, trioctylphosphine (TOP), trioctylphosphine oxide (TOPO), oleic acid, 1-dodecanethiol (DDT) on Pt NPs and CoPt₃ NPs performance in catalytic hydrogenation of alkynes to alkenes (Figure 1.1.20 a)⁴¹. They found that while with unmodified NPs overhydrogenation to alkanes was observed, the influence of additions of the ligands on the selectivity correlated well with the adsorption energies of these ligands predicted by DFT calculations. Namely, it was found that for ligands that did not influence catalyst performance, like trioctylamine, oleic acid, and TOPO, adsorption energies were lower than for reagents and products so they could be readily replaced by alkenes and hydrogenation to alkanes took place. In the case of strongly bonded ligands like TOP or DDT, adsorption energies were higher than for reagents and products which resulted in low activity with these modifiers. Meanwhile, primary amines, regardless the carbon chain length of an amine, afforded high selectivity toward alkenes. Interestingly, DFT results showed that the adsorption energy of adsorbents could be regulated by the surface coverage of primary amines. When the concentration of amines on the surface was sufficient enough amine adsorption energy becomes higher than that of alkenes, which hampers alkenes further hydrogenation (Figure 1.1.20 b). This study shows that careful choice of a ligand with suitable energy of interaction, neither too strong nor too weak, can greatly improve the selectivity of a reaction.

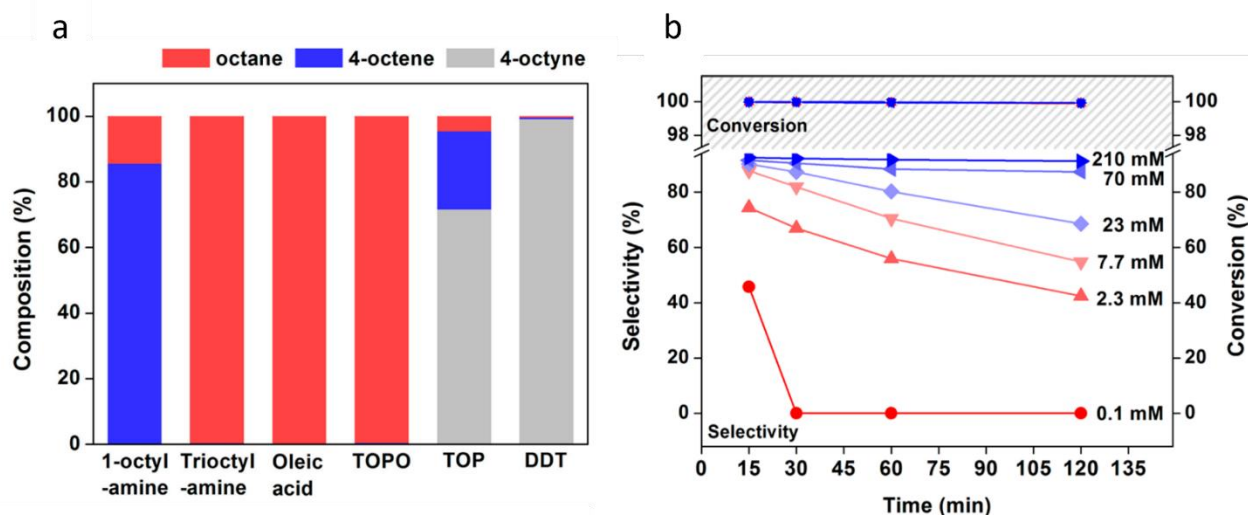


Figure 1.1.20 a) Effect of different capping ligands on activity and selectivity of 3.5 nm Pt NPs in hydrogenation reaction of 4-octyne. The concentration of all ligands was ~ 23 mM; b) kinetic data demonstrating the conversion (upper section, 100% in all the cases) and the selectivity (lower section) of 4-octyne hydrogenation using 3.5 nm Pt NPs as a function of octylamine concentration (shown on the right). The concentration of Pt was 2.6 ± 0.5 mM in all experiments. The data points shown in blue and red represent high and low selectivity regimes towards 4-octene, respectively. Reprinted from ref⁴¹.

In another combined experimental theoretical study, Kaeffer and colleagues used Cu/ SiO₂ catalyst for the semihydrogenation of alkynes⁴². DFT calculations showed that on a “clean” surface, adsorption energy of alkynes was higher than that of alkenes, meaning that the interaction of alkyne with the surface was favored so it got easily hydrogenated. However, further alkene hydrogenation occurred and the resulting product was an alkane. Kinetic studies showed that upon the addition of a phosphine (Cy₃P), alkene hydrogenation slowed down, while with an NHC (IMes) as a ligand, alkene hydrogenation almost stopped. It was explained by the strength of interaction between metal and ligand, particularly by electron donation to the surface, which was confirmed following CO adsorption with IR. Experimental findings supported theoretical explanations that in general, an NHC is a better sigma-donor than a phosphine.

Strong sigma donation of NHC that results in electron enriched surfaces was widely applied in different fields of catalysis⁴³. In particular, our group use NHCs to stabilize MNPs (Ru, RuPt, Ni, PdNi etc) and provide their water-solubility with sulfonated NHC to use them in hydrogenation^{44–47} and H/D exchange^{48–50} reactions.

A peculiar example of catalysis improved with NHC was provided by Ernst and colleagues⁵¹. They discovered that Pd/Al₂O₃, which is usually inactive in Buchwald–Hartwig amination of aryl halides, could efficiently catalyze it by catalyst modification with various NHC ligands. The binding to the surface through carbonic carbon was shown with solid-state NMR, meanwhile donation of electron density from NHC to Pd sites was confirmed with XPS. DFT calculations revealed a decrease

in the activation barrier for cleavage of Ar-Br bond in the presence of coordinated NHC. Moreover, a smaller activation barrier was found with electron-rich NHC bearing aromatic rings (IMes, IPr) than with NHC modified with alkyl fragments (IMe, ICy), well in accordance with the observed activity of the modified catalysts.

Au and Pd NPs stabilized with NHC-containing polymers showed higher stability in reductive conditions of electrocatalytic CO₂ reduction, compared to the Pd NPs stabilized with conventional ligands like thiols and amines⁵². In addition, higher selectivity towards CO₂ reduction over proton reduction was observed (Figure 1.1.21). Using CO stripping voltammetry, researchers suggested that electron donation from NHC to the surface of NPs resulted in an increased selectivity.

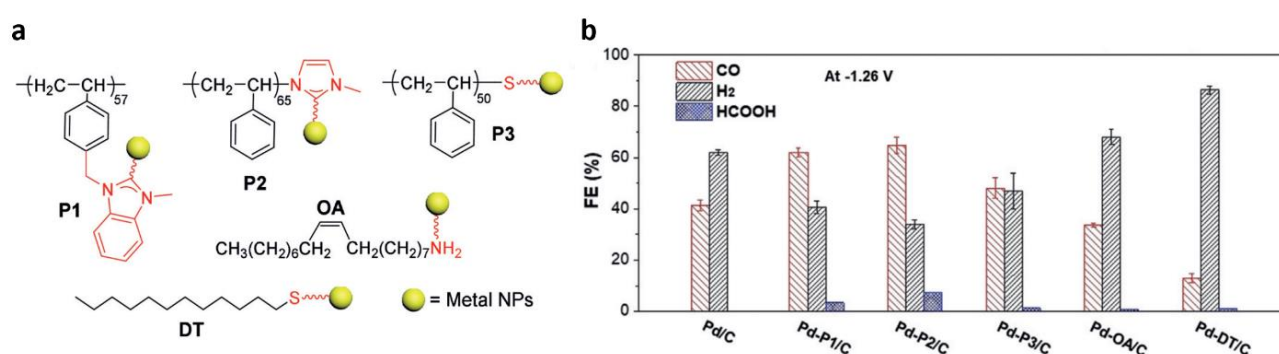


Figure 1.1.21 a) Structure of the ligands used to stabilize Pd NPs; b) Product analysis of CO₂ reduction using different Pd catalysts at -1.26 V. Reprinted from ref⁵².

Usually, thiols are considered to be too strong stabilizing agents that block activity of the NPs in catalysis⁵³, however a few studies could show that controllable addition of thiols can be beneficial^{54,55}. For instance, in the study of Marshal *et al.* self-assembled monolayers (SAMs) of thiols were used to cover Pd/Al₂O₃ and this material was used in the hydrogenation of epoxy alkenes (Figure 1.1.22)⁵⁶. It was found that electron-withdrawing thiols decrease electron density on Pd sites. This interaction favors the binding and hydrogenation of electron-rich C=C bonds and disfavors cycle-opening that requires breaking a C–O or C–C bond. Temperature-programmed desorption studies on single-crystal Pd surfaces confirmed that the barrier for epoxide ring opening increased significantly in the presence of the SAM. These findings suggested that electron depletion on Pd sites induced by thiols favored bond-making over bond-breaking reactions and thus preserved the epoxide ring from hydrogenolysis.

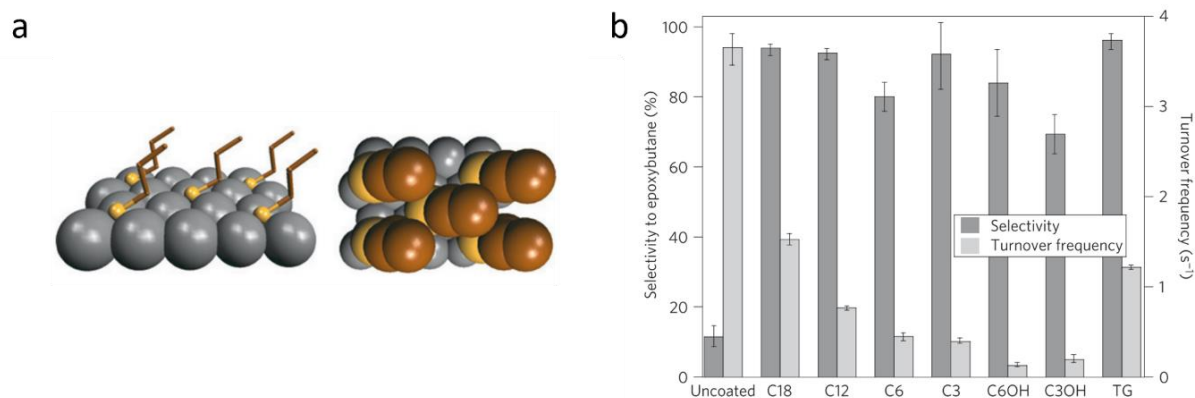


Figure 1.1.22 a) structure of a propanethiol SAM on Pd(111); b) epoxybutane selectivity and formation rate for different thiol coatings at 313 K. epoxybutane conversion was $5 \pm 2\%$ in all cases. (C3: propanethiol, C6: hexanethiol, C12: dodecanethiol, C18: octadecanethiol, C3OH: 1-mercapto-3-propanol, C6OH: 1-mercapto-6-hexanol, TG: thioglycerol) Reprinted from ref⁵⁶.

1.1.3.2. Steric effects of ligands

1.1.3.2.1. General crowding effect

The above-discussed study by Marshal and colleagues⁵⁶ also serves as a good example of steric effects induced by SAMs. Particularly, they found that a shorter chain of alkanethiols resulted in less ordered SAMs, which was confirmed following the IR signal of methylene stretch. SAMs exhibit a greater number of gauche defects with increasing disorder, causing the methylene stretching mode at $\sim 2,920 \text{ cm}^{-1}$ (value for crystalline alkane structures) to shift to a higher wavelength at $\sim 2,928 \text{ cm}^{-1}$ (value for liquid- or solution-phase with lower degree of order). Disordered tails may physically block adsorption sites, as well as may decrease the entropic barrier of adsorption of reagents. As a result, the activity of the catalyst decreased with decreasing length of the side chain (Figure 1.1.22 d). The best results were obtained with C18 chain, where the reaction rate was 40% of the rate on an uncoated catalyst.

A contrasting trend was found in a study by Wu and coworkers, who used Pt₃Co nanoparticles capped by different amines in cinnamaldehyde (CAL) hydrogenation⁵⁷. A longer-chain capping amine offered lower activity in hydrogenation but higher selectivity towards unsaturated alcohol. The explanation, corroborated with DFT calculations, was that on the surface covered with long chain amines, the most stable adsorption mode was upstanding sigma-O mode that lead to selective C=O hydrogenation. DFT-D studies showed that amines with shorter chain length had slightly lower adsorption energy and a lower rotational barrier. Authors suggested that the higher freedom of movement of short-chain ligands could lead to easier diffusion of CAL molecules onto the catalytic metal surface and thus to more efficient catalysis.

In a study by Pérez-Ramírez and coworkers, the influence of the ligand amount was studied⁵⁸. Pd NPs were stabilized with different amount of hexadecyl(2-hydroxyethyl)dimethylammoniumdihydrogen-phosphate (HHDMA) and deposited on titanium silicate (TiSi_2O_6). They were tested in hydrogenation of different substrates, like acetylenes, nitriles, and carbonyls. Interestingly, it was found that on the surface, ligands behaved like SAMs that changed their configuration depending on the ligand concentration (Figure 1.1.23). Based on TEM analysis and combined MD-DFT calculations it was proposed that at low coverage, the organic layer lied almost flat on the surface of the metal nanoparticle blocking a large number of metal sites and thus lowering overall activity. At the same time, high HHDMA coverages favored an ordered 3D configuration of the alkyl chain, which lead to a lower steric hindrance of active Pd sites and to an increase in overall reaction rate.

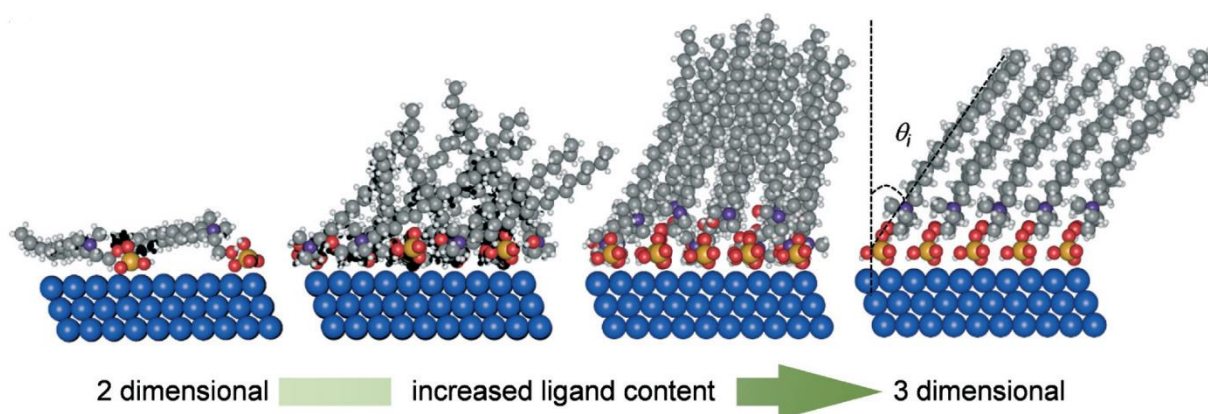


Figure 1.1.23 Schematic representation of the catalyst structures with variable ligand concentration. Reprinted from ref⁵⁸.

An example of a drastic selectivity change induced by a ligand is a study by Makosch and coworkers⁵⁹. They used uncoated and thiol-coated Pt/ TiO_2 catalyst in 4-nitrostyrene hydrogenation. With an unmodified catalyst at 100% of conversion a mix of 4-ethylnitrobenzene and 4-ethylaniline was formed, whereas modification with thiols (thioglycerol, 1,6-dithiolhexane, α -lipoic acid, 1-dodecanethiol) resulted in the formation of a nitrostyrene as a primary reaction product at almost 100% of conversion. Authors speculated that the sterically hindered surface prohibited the flat mode of adsorption of 4-nitrostyrene that could lead to side reactions, while a preferential interaction of the nitro-group with the TiO_2 lead to its activation and dictated the selectivity of the reaction.

A dynamic ligand layer reconstruction upon hydrogenation conditions was studied by Schroeder *et al*⁶⁰. In their detailed mechanistic study, they used Pd (111) functionalized with allyl cyanide for selective hydrogenation of unsaturated aldehyde acrolein. Combination of operando IR

and STM results suggested that under reacting conditions, the allyl cyanide ligand transformed to N-butylimine, which formed more densely packed ordered layers with ligands in standing-up position. This ligand arrangement allowed standing-up adsorption of acrolein and its selective hydrogenation to propenol (Figure 1.1.24).

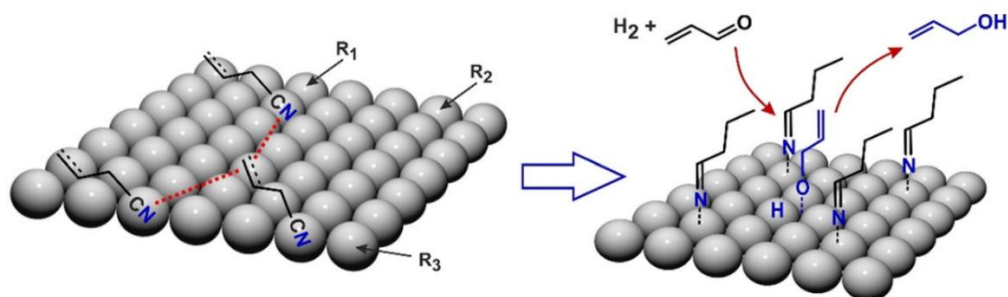


Figure 1.1.24 Illustration of ligand layer reconstruction and acrolein hydrogenation under reacting conditions. Reprinted from ref⁶⁰.

1.1.3.2.2. Active site selection

As it was discussed in the section 1.1.1 ligands preferentially adsorb on specific surfaces. It affects the adsorption of reagents, that is, reagents adsorb less on the parts occupied by ligands than on other parts. Randomness in the geometry of the substrate approach to active site decreases, which enhances the selectivity of the reaction.

In a study by Pang and coworkers, Pd/Al₂O₃ catalysts modified with thiol ligands were tested in the hydrogenation of furfural⁶¹. SAMs of octadecanethiol (C18) with a nearest neighbour distance of 4.7 Å on Pd *fcc* (111) surfaces and SAMs of 1-adamantanethiol (AT) with a nearest neighbour distance of 6.4 Å were chosen to see the influence of a steric difference on catalysts performance. Using more densely packed C18 SAMs, decarbonylation of furfural was efficiently inhibited while modification with AT SAMs barely influenced the rate of decarbonylation reaction (Figure 1.1.25). Following IR study with CO adsorption it was shown that on the C18-coated surface CO adsorbed only on threefold hollow (1,885 cm⁻¹) and top sites at step edges and defects (2051cm⁻¹), whereas on AT-coated Pd sites CO had additional access to terraces which was confirmed by appearing of the additional signals attributed to CO adsorption on terrace via bridging (1919cm⁻¹) and linear mode (2,077cm⁻¹). This result corroborated experimental data where decarbonylation that is known to proceed on (111) faces was disfavored, while hydrogenation that happens on coordinatively unsaturated sites still occurred. Similarly, in the study of Campisi and coworkers⁶² benzyl alcohol oxidation reaction was investigated on Pd/Al₂O₃ catalyst. They found that catalysis with an uncovered Pd surface resulted in a mixture of oxidation and decarbonylation products. However, when PVA was used to cover the surface, selectivity towards benzaldehyde significantly increased

due to a decrease in the rate of further decarbonylation. Using operando ATR-IR and DRIFTS spectroscopy with CO as an adsorbent, it was postulated that PVA interacts stronger with Pd (111) planes that are active in decarbonylation. Thus, due to the selective poisoning of (111) facets, decarbonylation was strongly disfavored.

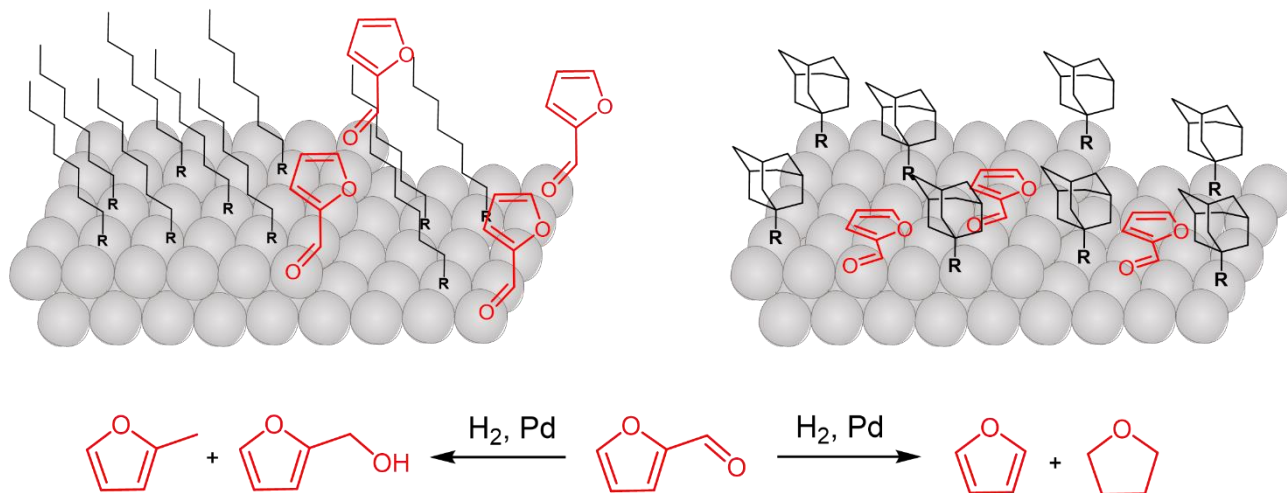


Figure 1.1.25 Illustration of selectivity switch in furfural hydrogenation on Pd surface covered with ordered layer of octadecanethiol that preferentially coordinates to the terrace atoms and with less dense layer of adamantanethiol.

1.1.3.3. Ligand-substrate interactions

Intermolecular interactions between ligand and reactant or so-called *molecular recognition effects* are rather rarely described in the literature since they are specific for each substrate-ligand pair. However, a few astonishing examples of selectivity and activity improvement due to hydrophobic, π - π , or H-bond interactions are discussed in this section.

1.1.3.3.1. π - π stacking

One of the most cited examples of molecular recognition is a work by Kahsar and colleagues⁶³. They were applying different thiol SAMs to coat Pt/Al₂O₃ catalyst which was used in the hydrogenation of conjugated aldehydes – cinnamaldehyde and prenal (Figure 1.1.26 a, b). They found that the activity and selectivity towards C=O hydrogenation of cinnamaldehyde with phenylalkylthiols depended on the position of the phenyl ring. Authors suggested that cinnamaldehyde can interact with thiols bearing a phenyl ring through π - π stacking interactions. The highest selectivity (more than 90%) with 3-phenylpropanethiol was associated with an alkyl chain length that was the same for the thiol and cinnamaldehyde. This allowed cinnamaldehyde to have a π - π stacking of phenyl rings while interacting with a surface in a η^1 σ -O (standing-up) adsorption mode. Polarization modulation reflection-absorption infrared spectroscopy (PM-RAIRS) proved the η^1 configuration of cinnamaldehyde on Pt surface covered with 3-phenylpropanethiol. Having a shorter alkyl chain like for 2-phenylethylthiol resulted in a little lower selectivity, whereas having one methyl longer chain

like in the case of 4-phenylbutanethiol stacking that occurred far from the surface and hindered interaction with the metal surface that resulted in lower conversion. To prove the hypothesis, prenal hydrogenation was performed with the coated catalysts since this substrate does not contain an aromatic ring. The selectivity in prenal hydrogenation was found to be independent to the presence of a phenyl group in the SAM, as it was comparably increasing with alkanethiol SAMs as with phenylalkylthiol SAMs (Figure 1.1.26 c). Thus, π - π stacking interactions between cinnamaldehyde and phenylalkane thiols allowed an increase of selectivity in cinnamyl alcohol formation, while in the hydrogenation of prenal an unspecific non-tunable increase of selectivity was observed.

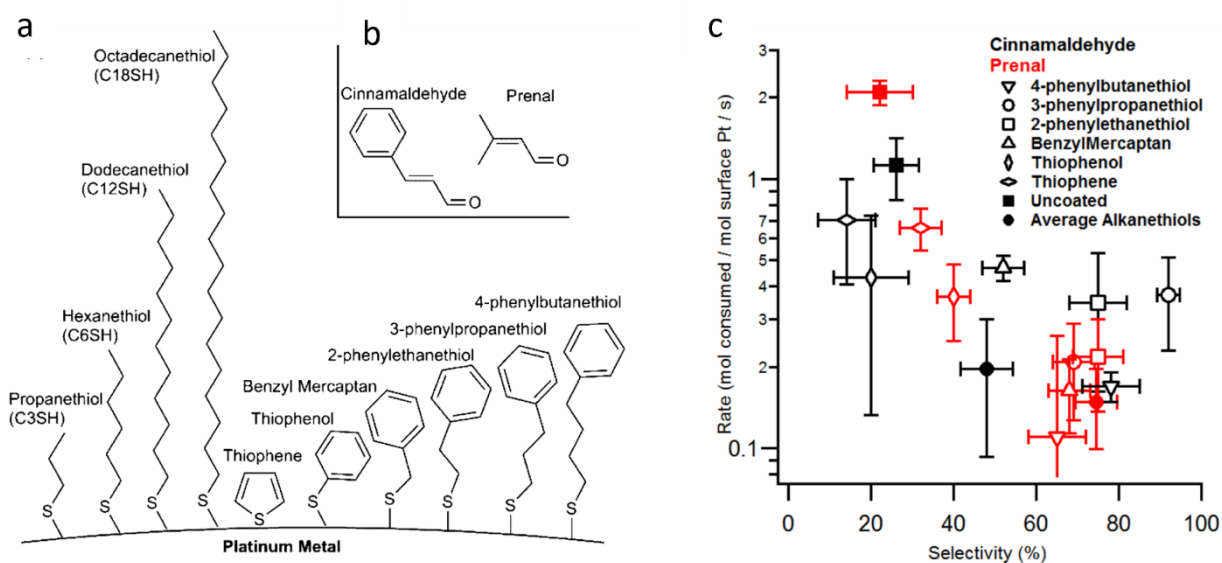


Figure 1.1.26 Structure of a) ligands used to cover Pt/Al₂O₃ surface and b) substrates used in selective hydrogenation; c) plot of rate versus selectivity to unsaturated alcohol for uncoated and thiol-coated Pt/Al₂O₃ catalytic materials. Rates are calculated as the moles of reactant consumed per moles of surface platinum per second. Reprinted from ref⁶³.

1.1.3.3.2. H-bond interactions

Another work of the same team highlights selectivity enhancement due to the H-bonding of the substrate and a ligand. In a study by Coan and colleagues, they found that Pd/Al₂O₃ catalyst modified with a phosphonic acid showed high activity in furfuryl ring hydrogenation⁶⁴. DFT studies showed that strong H-bond interaction between furfuryl alcohol and phosphonic acid leads to the beneficial adsorption of a reagent on the surface with further ring hydrogenation. Remarkably, when a high concentration of phosphonic acid was used, the reaction rate increased more than twice compared with the unmodified catalyst. Such ligand acceleration effects are commonly used in homogeneous catalysis with organometallic complexes. However, nowadays coordination chemistry of metal surfaces becomes more and more popular, although the characterization of these systems remains challenging and often DFT calculations are used to confirm a hypothesis. A remarkable activity increase with modification of Pt surface was observed in a study by Schrader and coworkers⁶⁵. Here,

“naked” Pt NPs derived from polyol synthesis were stabilized with L-proline and used in the hydrogenation of acetophenone. Total selectivity towards phenyletanol and higher reaction rate was observed for Pt NPs modified with proline compared with unmodified Pt NPs. While enhanced selectivity was attributed to steric effects, an increase in activity was attributed to a hydrogen bonded to the nitrogen of proline that becomes acidic upon coordination to the surface of Pt. The authors proposed a mechanism where the acidic proton coordinates to the oxygen of the carbonyl group, activating it whereas another hydrogen forms a bond with the carbon atom of the carbonyl resulting in phenyl ethanol (Figure 1.1.27 a). As a proof, authors conducted a test with a tertiary amine, N-methylproline, and confirmed that in absence of an amine proton the rate of hydrogenation decreased.

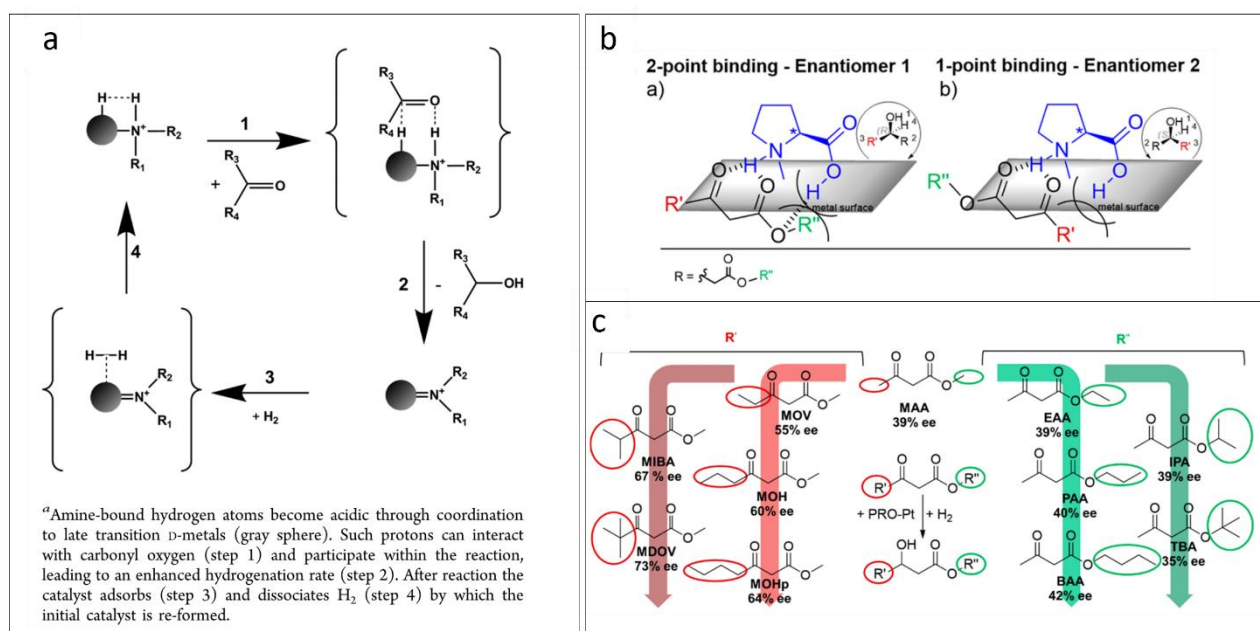


Figure 1.1.27 a) Proposed mechanism of ligand accelerated hydrogenation of acetophenone with Pt NPs stabilized with L-proline. Adopted from ref⁶⁵; b) illustration of two-point binding (major) and one-point binding (minor) interactions of L-proline with a substrate; c) Structure-stereoselectivity dependence in hydrogenation of beta-ketoesters. Adopted from ref⁷¹

Enantioselective catalysis

Interestingly, while in the last example only modest stereoselectivity was achieved in acetophenone hydrogenation (14% of ee) the same team successfully applied this system in asymmetric hydrogenation of alpha-ketoesters and reached values of 39 – 74 % of ee depending on the structure of the compound. The suggested explanation of such behavior laid in the formation of two H-bonds between the substrate and L-proline that directs the stereoselectivity of the reaction (Figure 1.1.27b). Depending on the geometry of the compound these interactions were more or less pronounced and lead to a different degree of ligand-controlled enantioselectivity (Figure 1.1.27 c).

Indeed, the adsorption behavior of the ligand and reactant, their conformation, and their intermolecular interactions are the key parameters, which determine the enantioselectivity of a chemical reaction on the surface, similar to asymmetric homogeneous catalysis. The most investigated well-performing system for enantioselective heterogeneous catalysis is the Pt-cinchona alkaloids system for the hydrogenation of α -ketoesters^{66,67}. The widely accepted model of the reaction is an adsorption model. According to this model the cinchona-type modifier is adsorbed by the aromatic rings on the metal surface where the interaction between the chiral modifier and the substrate occurs. The cinchona alkaloids are big enough to provide by themselves the chiral local environment required to direct the hydrogenation. Initially, it was proposed by Baiker and colleagues that interaction between cinchona modifier and substrate proceeds via formation of one hydrogen bond⁶⁸ (Figure 1.1.28 a). Later, a two-point activated model was suggested by McBreen and coworkers (Figure 1.1.28 b) which was supported by their STM and DFT results^{69,70}. In both cases activation of a substrate via hydrogen bonding creates more confined geometry, resulting in the preferential formation of one enantiomer. However, the exact mechanism of asymmetric hydrogenation is still a question of debate.

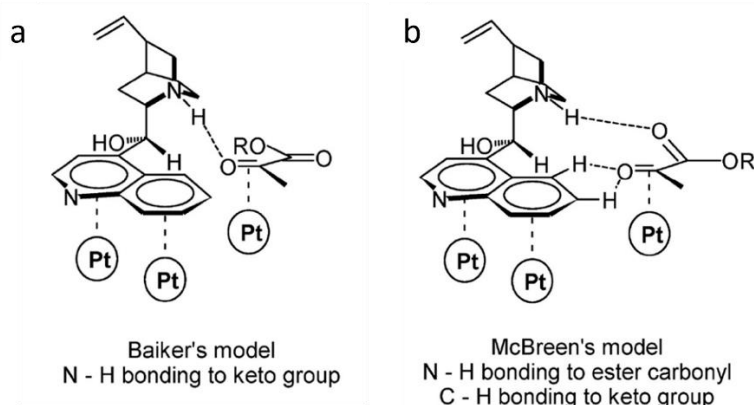


Figure 1.1.28 Illustration of activated a) one-point and b) three-point chiral modifier-substrate complexes. Reprinted from ref⁶⁶.

In the first studies, cinchonidine (Cd) was added as a modifier in the solution containing Pt catalyst that drastically increased the enantiomeric excess of formed α -hydroxy esters (up to 94% ee)⁷². However, to preserve the same level of selectivity Cd needed to be continuously injected to the reaction mixture. Also, separation of Cd presented similar issues as in homogeneous catalysis. Hong *et al.* developed a protocol of Cd tethering on Pt/SiO₂ catalyst via carbamate- or mercapto-linkers distributed randomly on the surface of the support or in a correlated way around the Pt NPs (Figure 1.1.29 a)⁷³. They found that stereoselectivity of ethyl pyruvate hydrogenation with the

system containing Cd well-distributed around Pt NPs was higher than with randomly distributed Cd, although it was smaller than with free Cd in solution (Figure 1.1.29 b).

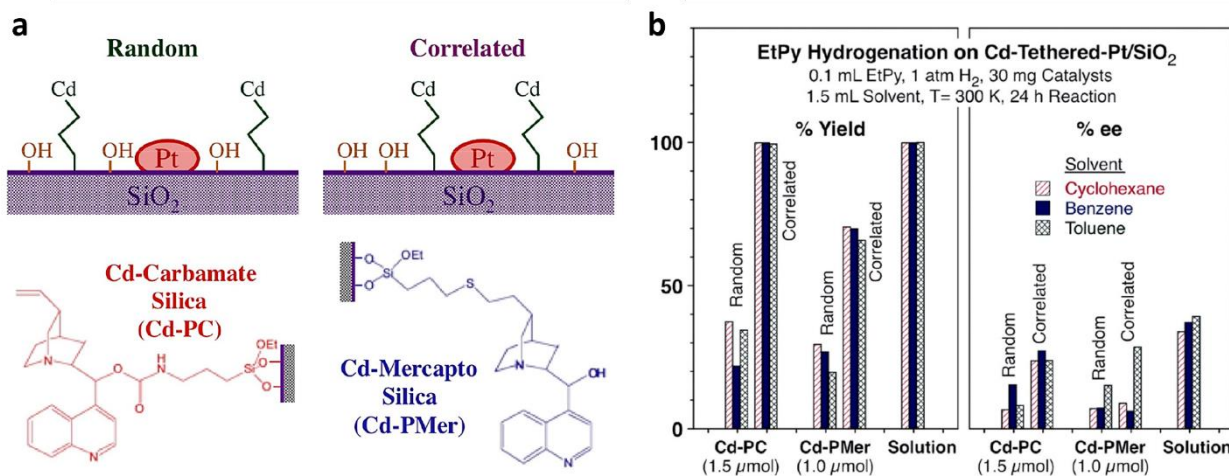


Figure 1.1.29 a) Illustration of cinchonidine grafted to the surface of silica via carbamate and mercapto-linkage; b) yield and selectivity of ethyl pyruvate hydrogenation reaction with correlated and randomly distributed Cd. Reprinted from ref⁷³.

Nevertheless, with the development of new modifiers, high enantioselectivities were reached by some groups. For example, secondary amide-substituted chiral diene-modified Rh/Ag NP systems were applied in asymmetric 1,4-addition of arylboronic acids to α,β -unsaturated carbonyl compounds where excellent selectivity towards arylated products was achieved with activities higher than for a homogeneous catalyst (Figure 1.1.30)⁷⁴. It was suggested that the diene parts of the chiral modifier could coordinate to Rh, and, at the same time, the secondary amide group could form hydrogen bonds with an α,β -unsaturated ester. Researchers proved that the nature of species was not homogeneous, however, they did not discard the possibility of the formation of small clusters that can reprecipitate on the support.

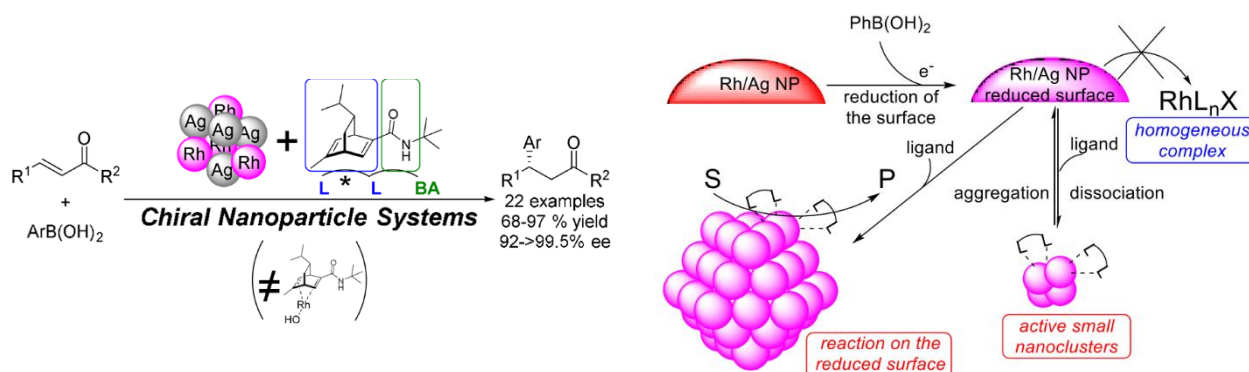


Figure 1.1.30 Illustration of reaction catalyzed by Rh/Ag NP modified with a chiral ligand with proposed mechanism of the reaction. Reprinted from ref⁷⁴.

1.1.3.3.3. Ligand-assisted H_2 activation

In hydrogenation reaction, a mode of hydrogen dissociation (homolytic or heterolytic) is one of crucial factors of selectivity of the reaction. In general, it is considered that homolytically cleaved hydrogen, that is a common dissociation mode on noble metal surfaces, is suitable for hydrogenation of unpolar bonds while heterolytically dissociated hydrogen preferentially interacts with polar bonds. An example of ligand-assisted heterolytic hydrogen cleavage was provided in studies by Cano *et al.*^{75–77}. Secondary phosphine oxides (SPO) were used as ligands for Au NPs and later for Ir NPs since SPO ligands are known to participate in a heterolytic cleavage of hydrogen. The obtained systems were used in the selective hydrogenation of conjugated aldehydes. Remarkably, high activity and very high selectivity in the hydrogenation of a rich scope of unsaturated aldehydes were observed. Usually, Au NPs are considered as weak hydrogen activators; however, ligand-metal cooperative effects promoted catalytic performance of Au. Based on DFT calculations authors suggested that the SPO ligand acted as a heterolytic activator for H_2 through a metal-ligand concerted mechanism (Figure 1.1.31)⁷⁸.

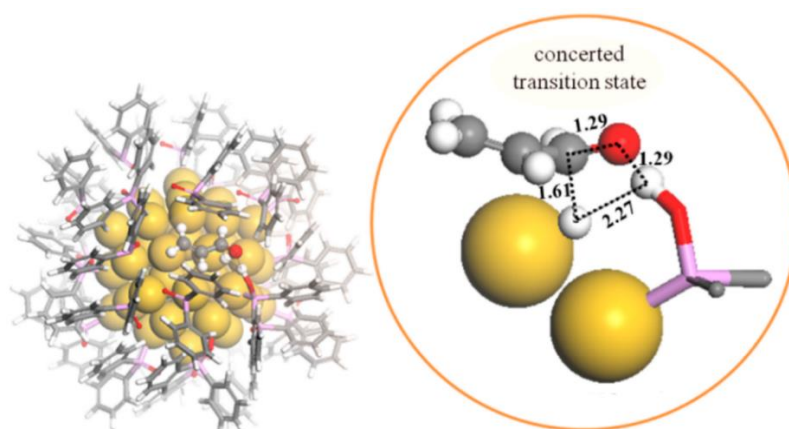


Figure 1.1.31 Structure of the concerted transition state in the hydrogenation of the acrolein carbonyl bond on Au NPs stabilized with an SPO ligand. The inset illustrates four-membered cycle with distances. Yellow – gold, pink – phosphorus, red – oxygen, grey – carbon, white – hydrogen. Reprinted from ref ⁷⁸.

An example of equal importance is a ligand-assisted heterolytic H_2 cleavage provided by Fiorio *et al.*⁷⁹. Among different nitrogen-containing molecules (Figure 1.1.32 a), they found that additions of piperazine provided high activity in alkynes hydrogenation with excellent selectivity toward alkenes. The universality of the catalyst was proved with a big scope of molecules having different functional groups. Only aldehydes, ketones, and carboxylic acids could not be selectively hydrogenated due to side reactions with the ligand. In analogy to homogeneous catalysis, where primary and secondary amines act as promoters of H_2 heterolytic cleavage to give metal hydride species, the researches confirmed with DFT calculations that the presence of piperazine on the

surface of Au lowers the dissociation energy barrier of H_2 while piperazine gets protonated. In this case a stepwise mechanism of hydrogen addition to the alkyne is proposed (Figure 1.1.32 b).

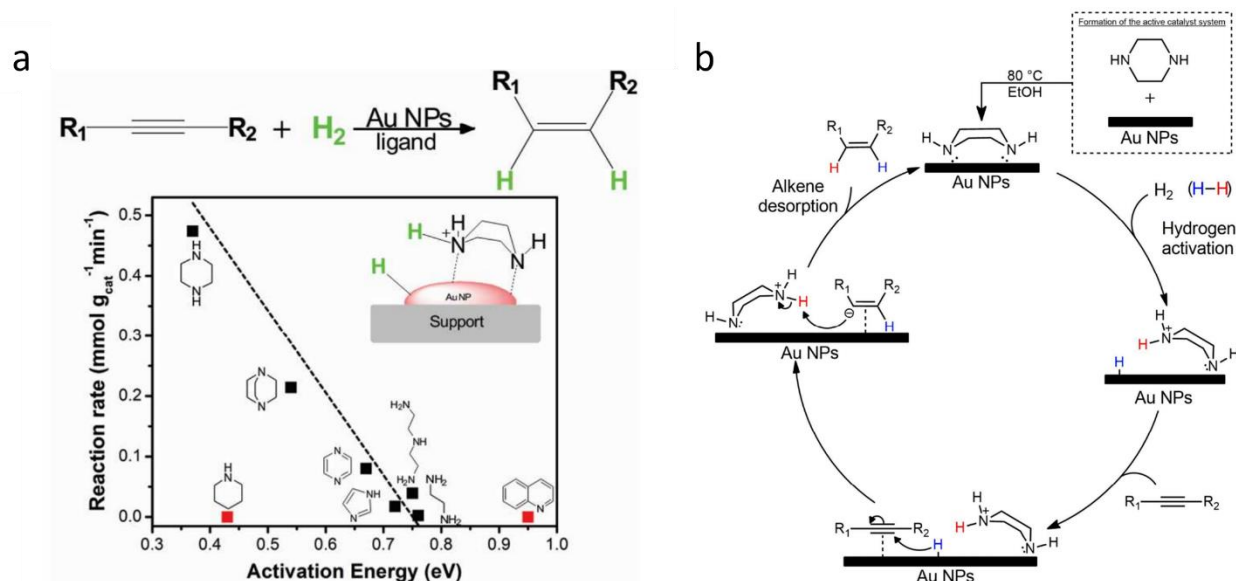


Figure 1.1.32 a) Nitrogen-containing bases used as ligands for supported Au NPs; b) Proposed mechanism of ligand-assisted selective hydrogenation of alkynes to alkenes. Reprinted from ref⁷⁹.

1.1.3.4. Dual catalysis

Dual catalysis is a particularly attractive approach since there few reaction steps can proceed in one pot with one multifunctional catalyst. Such system optimization or simplification is even more important in industrial scale, where complex multi-step procedures are used in chemicals synthesis. A widely used combination is a metal catalyst for hydrogen activation with acid-base catalyst for substrate activation. In these systems, either the support itself or a surface modifier/ligand can activate the substrate. Among the most popular examples, zeolites, metal organic frameworks (MOFs), covalent organic framework (COFs), or reducible oxide supports can be used as sources of acid-basic sites⁸⁰. Alternatively, immobilization of desired functionalities on the support can be performed. In a study of Zhang and colleagues phosphonate-coated Al_2O_3 was synthesized and used to accommodate Pt or Pd NPs⁸¹. Modification with methylphosphonic acid (MPA) increased the stability of the catalyst on stream (Figure 1.1.33 b). Depending in the structure of phosphonic acid (Figure 1.1.33 c), the acid strength could be modified which was used to control hydrodeoxygenation (HDO) performance of the catalyst (Figure 1.1.33 d).

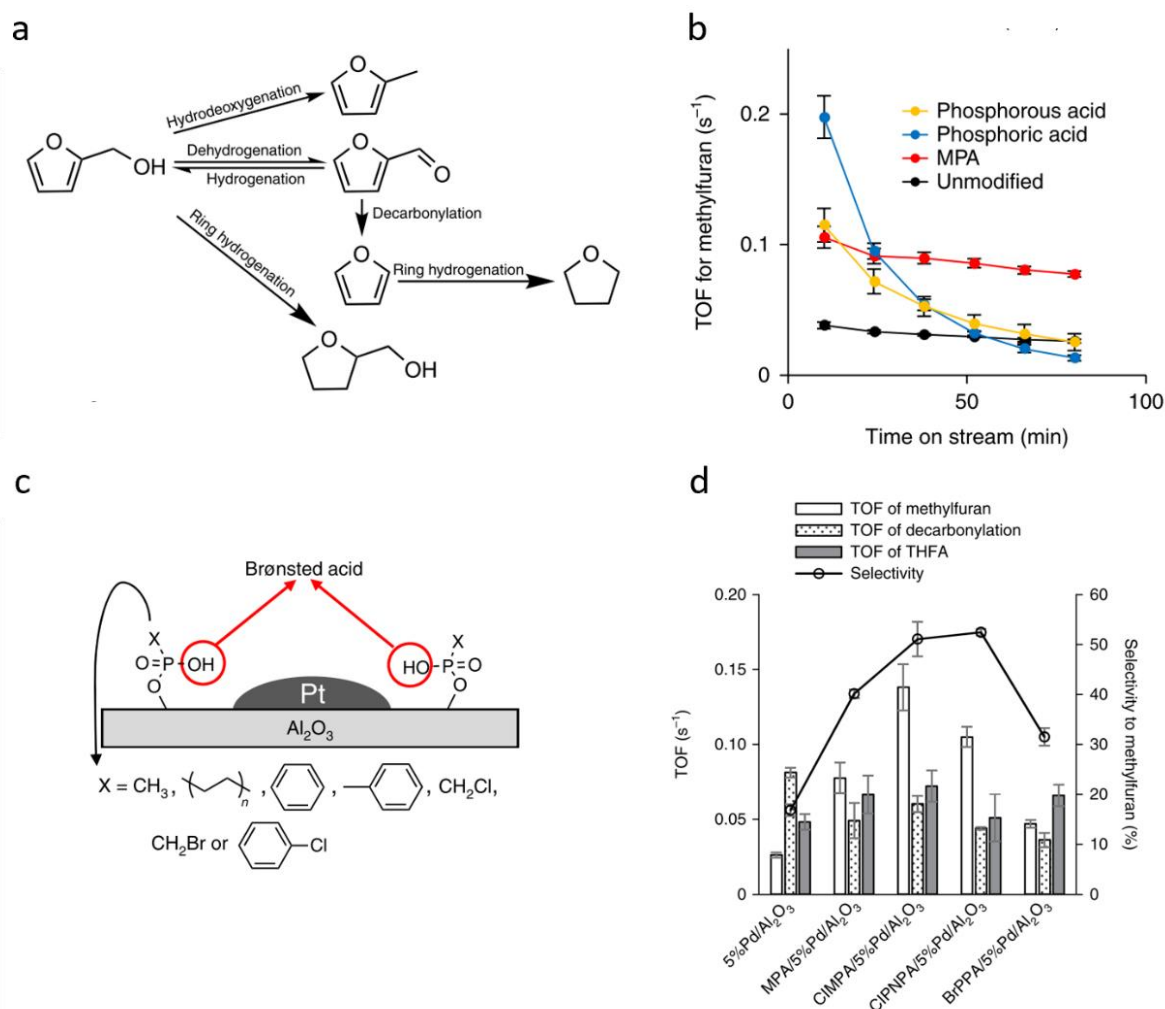


Figure 1.1.33 a) Furfuryl alcohol transformation pathways; b) 2-Methylfuran turnover frequency using different catalysts; c) moieties used to modify phosphonic acid sites; d) TOF and selectivities in furfuryl alcohol hydrogenation with unmodified and modified Pd/Al₂O₃ catalyst. Adopted from ref⁸¹.

1.1.3.5. Case of cyclodextrins

In this section, special attention will be paid to cyclodextrins (CD) since these compounds have been used in the frame of this PhD work (Chapter 2). These supramolecular cyclic compounds can interact with substrates by accommodating them in their cavity which might be interesting for catalytic applications. Cyclodextrins are cyclic oligosaccharides containing glucose units linked by α -1,4 bonds (Figure 1.1.34). Typical CDs contain six (alfa-CD), seven (beta-CD), or eight glucose units (gamma-CD) in a cycle with a mean diameter of the cavity equal to 5 Å, 6.3 Å, and 7.8 Å respectively. The CD has a toroidal shape where secondary hydroxyl groups are situated on the bigger ring opening (secondary face) while the primary hydroxyls form a smaller opening (primary face) since the free rotation of the latter reduces the effective diameter of the cavity. Thus, outside the molecule, hydroxyl groups give a hydrophilic character to the molecule. Meanwhile, the cavity has a more

hydrophobic character since it is lined by carbon and hydrogen atoms together with glycosidic oxygen bridges.

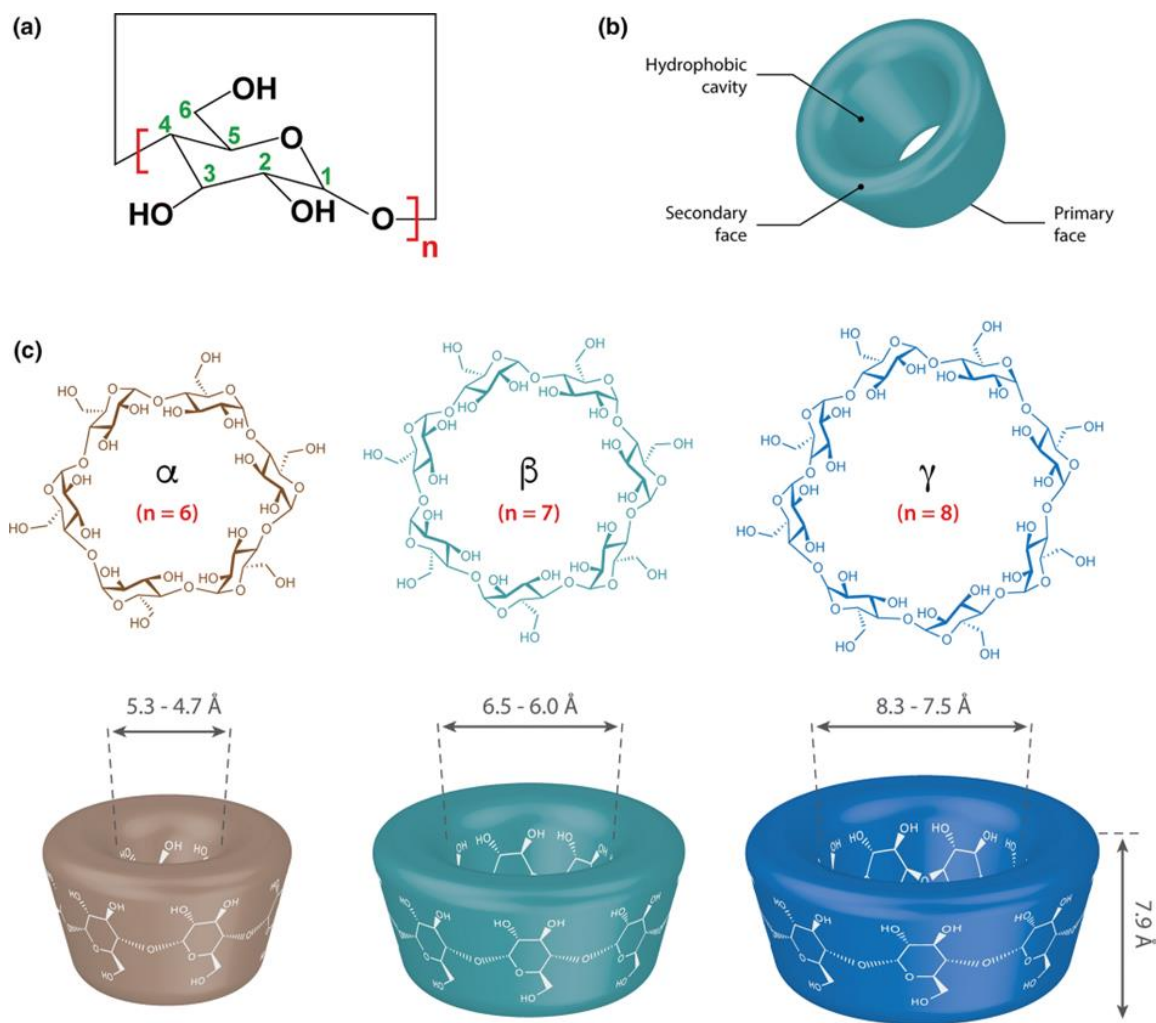


Figure 1.1.34 Illustration of a) the general chemical structure and b) the tridimensional structure of cyclodextrins, and c) chemical structure and dimensions for α -, β - and γ -cyclodextrin ($n = 6, 7$ and 8 , respectively). Reprinted from ref⁸².

The presence of both hydrophobic and hydrophilic regions allows a high solubility in water together with the possibility of the formation of inclusion complexes with hydrophobic molecules hosted inside the cavity. Formation of inclusion complexes is energetically favored since it causes a release of water molecules from the apolar cavity, together with the inclusion of the hydrophobic guest. This phenomenon contributes favorably to the enthalpy of the whole system due to the formation of hydrogen bonds and van der Waals interactions between the host and the guest⁸³.

The ability of CD to incorporate molecules makes them appealing ligands for NPs. In this way, biphasic catalysis can take place, where water-soluble NPs stabilized with CDs form a hydrophilic phase and organic substrates form a hydrophobic phase. Due to the constant dynamic ligand exchange on the surface of NPs, CD inclusion complexes can efficiently deliver substrates to the catalytic surface, which contributes to the efficiency of the selected transformation. Additionally,

the strength of the interactions between the CD and the host molecule can regulate the selectivity of the reaction. The affinity depends on the size and the polarity of the guest. It is assumed that more polar substrates have weaker affinity to the cavity and can be released more easily from it. Another important property of CD is the size of the cavity which allows only specific geometry and adsorption mode of the reagents. In this way the selectivity of the reaction can be sterically controlled. To further improve the performance of CD, the hydroxyls of the macrocycles can be selectively replaced by the substituents of choice. Chemical modification of cyclodextrins affects their physical properties as well as their association constants with reactants or their binding strength to the NPs. The most popular strategy includes substitution with the formation of methoxy and isopropoxy groups. However, CD modified with thiols, phosphines, chiral moieties and other functionalities were also employed in catalysis.

There are many examples of excellent selectivity control with homogeneous catalysts attached to CD, like Au-catalyzed intramolecular cyclisation where the size of the resulting cycle was sterically controlled by the cavity size resulting in 5-member cycles with alfa-CD and mostly in 6-member cycle with beta-CD (Figure 1.1.35 a)⁸⁴ or hydroformylation with Rh complex grafted inside the CD where high regio- and enantioselectivity were achieved (Figure 1.1.35 b)⁸⁵. So, it is not surprising that inspired with these results NPs stabilized with CDs were synthesized to use in catalysis.

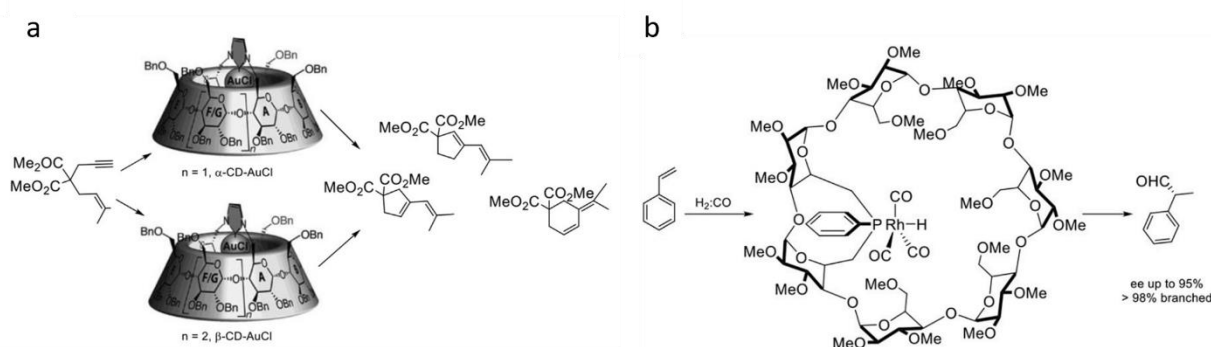


Figure 1.1.35 a) Confined in CD Au catalyst for sterically-controlled cyclization reaction; b) confined in a CD rhodium catalyst in the asymmetric hydroformylation of styrene. Reprinted from ref⁸⁶.

The first example of NPs stabilization with native CD was published in 1983 by Komiyama and Hirai⁸⁷. They obtained small Rh NPs (2.8 nm) stabilized with alfa- or beta-CD that showed to be active in catalytic hydrogenation. However, most of the time, functionalized CDs show better performance in stabilizing NPs and in catalysis. For instance, Monflier's group used Pd/C NPs with the addition of native and functionalized alfa- and beta-cyclodextrins such as methylated CD, hydroxypropylated CD, cationic ($R = \text{CH}_2\text{CH}(\text{OH})\text{-CH}_2\text{-N}(\text{CH}_3)_3\text{Cl}$) and anionic ($R = (\text{CH}_2)_4\text{-SO}_3\text{Na}$)

CDs⁸⁸. Among them, the best activity in Suzuki-Miraya couplings was showed by methylated beta-CD, going from 10 % to 62% of conversion, where the efficacy strongly depended on the substitution degree of the CD. Researchers suggested that such an increase in activity was mainly due to two effects: phase transfer properties of CD and improved dispersion of Pd/C catalyst in water due to CD adsorption on carbon. The same group applied Pd/C with methylated CD in Heck cross-coupling⁸⁹. As previously, they observed an increase in overall catalytic performance in presence of CD. Interestingly, an increase in stereoselectivity was also observed. Usually, Z-alkene is the major product formed with heterogeneous catalysts, however, in this case, an increase of E-isomer was attributed to steric hindrance of the CD cavity that favored E-alkene formation. However, special attention must be paid to a Pd state in cross-coupling reactions. It was shown by Senra and coworkers that CD can stabilize Pd clusters formed from heterogeneous Pd/CaCO₃⁹⁰. The combination of atomic absorption spectroscopy and leaching experiments confirmed that the homogeneous mechanism of catalytic cross-coupling was dominant. In this sense supported Pd NPs served mainly as a reservoir of active species rather than a real heterogeneous catalyst.

Hydrogenation was intensively investigated as another model reaction catalyzed by NP-CD systems. Using methylated cyclodextrins, a moderate increase in activity and no big influence on the selectivity was commonly observed, which was attributed to weak interactions of methylated CD with NPs. Chau and colleagues confirmed with DOSY NMR that methylated CD mostly served as a dispersing agent, which prevent agglomeration of NPs rather than a strongly interacting ligand⁹¹. Denicourt-Nowicki and coworkers showed that ratios [CD]/[Ru] lower than 10 were not sufficient to preserve the stability of Ru NPs, which again suggests weak interactions between ligand and Ru⁹². Nevertheless, a clear effect of ring size was shown in this study. Researchers observed that the hydrogenation of the aromatic ring of benzene and styrene was suppressed using alfa-Me-CD whereas the size of the cavity of gamma-Me-CD allowed the hydrogenation of aromatic rings. In the case of beta-Me-CD, the hydrogenation of an aromatic ring depended on the substitution degree by a methyl group. The authors proposed that CDs with a higher methylation degree became more hydrophobic and thus stronger interacted with a benzene ring, which preserved it from hydrogenation. However, for more polar substrates like anisole, ring hydrogenation was observed regardless of the substitution degree. Similar reactivity was observed in the previously discussed study by Chau *et al.*⁹¹ as well as in our investigations (Chapter 2). It is possible that oxygen-containing substrates have a lower association constant with cyclodextrin, so they may be adsorbed directly on the surface of NPs in the mode which allows ring hydrogenation.

Modification of methylated CD with chiral amino acids like L-alanine (Ala) and L-leucine (Leu) was performed by Chau and others for stabilization of Ru NPs⁹³. During the hydrogenation of prochiral substrates high activity and selectivity but modest enantiomeric excess was observed. In another study of Noël and colleagues, cinchonidine (CN) fragment was used to modify CD (Figure 1.1.36, a)⁹⁴. Pt NPs stabilized by these CDs were used in the hydrogenation of ethyl pyruvate and showed excellent activity and good enantiomeric excess – 63%. Importantly, the physical mixture of a CD and cinchonidine led to poor *ee* values – 15%, most probably due to the instability of the colloidal dispersion. Unfortunately, poor recyclability was observed for Pt NPs stabilized with CN-modified beta-CD due to the hydrogenation of the ligand and agglomeration of Pt NPs (Figure 1.1.36, b).

To sum up, NPs stabilized with CD show significant improvement in catalysis in terms of activity mainly due to mass transfer properties of CD^{95–99}. Regarding the selectivity improvement, some promising results were obtained as well, however it seems that there is still plenty of space for improvement which can be done by modification of the CD structure and wise choice of the reaction according to the affinity of the reagents and products to the cavity.

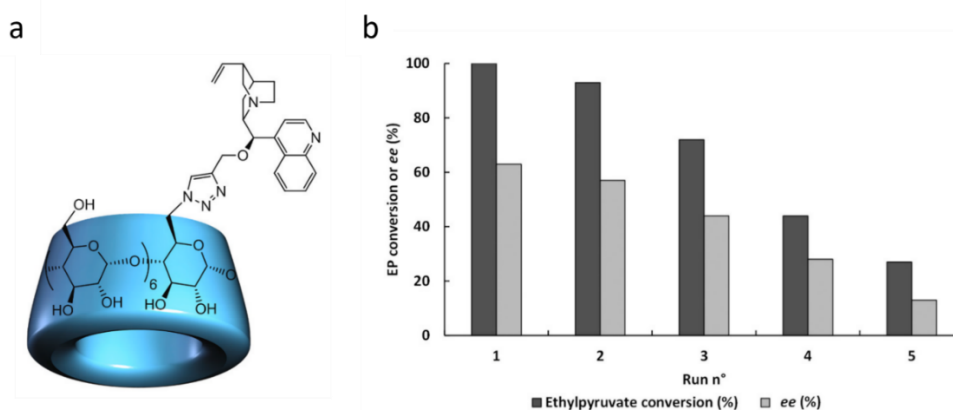


Figure 1.1.36 a) Structure of cinchonidine-modified cyclodextrin; b) Reusability of Pt-CD-CN in the hydrogenation of ethyl pyruvate. Reprinted from ref⁹⁴.

1.1.3.6. Case of Ionic liquids

In this section, NPs stabilized with ionic liquids (IL) or NPs supported on surfaces containing IL will be briefly reviewed, since they are the subject of the work described in Chapter 3. It was shown that modification of each component of IL-based catalytic systems has a direct influence on the catalyst performance. Therefore, such catalysts can be purposefully modified in order to reach desired selectivity in catalysis.

ILs are salts that usually contain a bulky organic cation and weakly coordinating anion (Figure 1.1.37). Their melting point is low so a large number of them are in a liquid state at room temperature. ILs are widely applied as protective agents due to the high rotational freedom of the ligands which provides an access to the entire NP surface. In addition, ILs can be used as solvents and in multifunctional catalysis as co-catalysts¹⁰⁰.

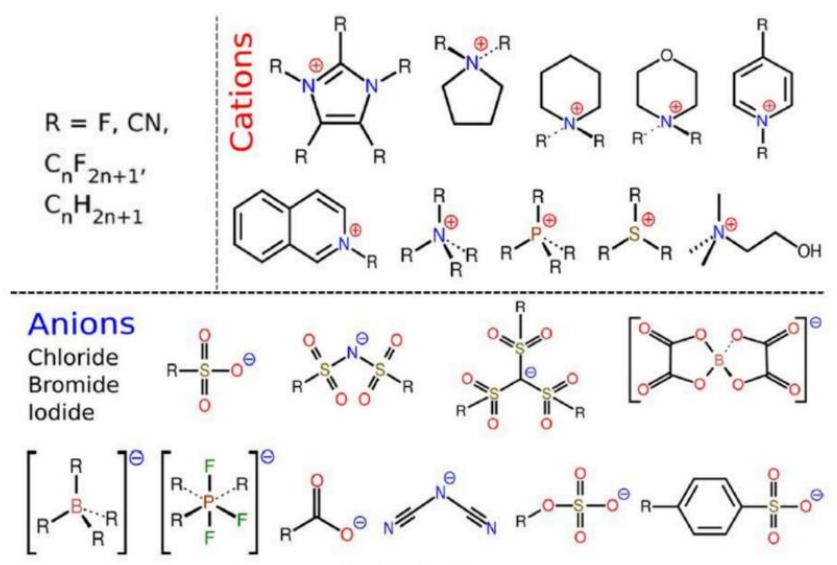


Figure 1.1.37 Commonly used cations and anions of ILs. Adapted from ref¹⁰¹.

In a study of Prechtl and coworkers, Ru NPs stabilized by nitrile-functionalized ionic liquids were used in hydrogenation of benzonitrile¹⁰². NPs showed to be selective towards the formation of N-benzylidene-1-phenylmethanamine coupling product, while uncommonly for Ru hydrogenation of an aromatic ring did not occur (Figure 1.1.38 a). Authors speculated that IL adsorption through the nitrile group is stronger than that of aromatic ring and thus ring is not hydrogenated.

Karakulina et al. stabilized Rh NPs with chlorozincate IL. They found that the catalytic materials were selective in hydrogenation of a broad scope of heteroaromatic polycycles, where only a heterocycle was hydrogenated (Figure 1.1.38 b)¹⁰³. Authors did not propose a mechanism, but we can assume that interactions between basic nitrogen of the heterocycle and Lewis acidic sites of IL direct the selectivity of the hydrogenation.

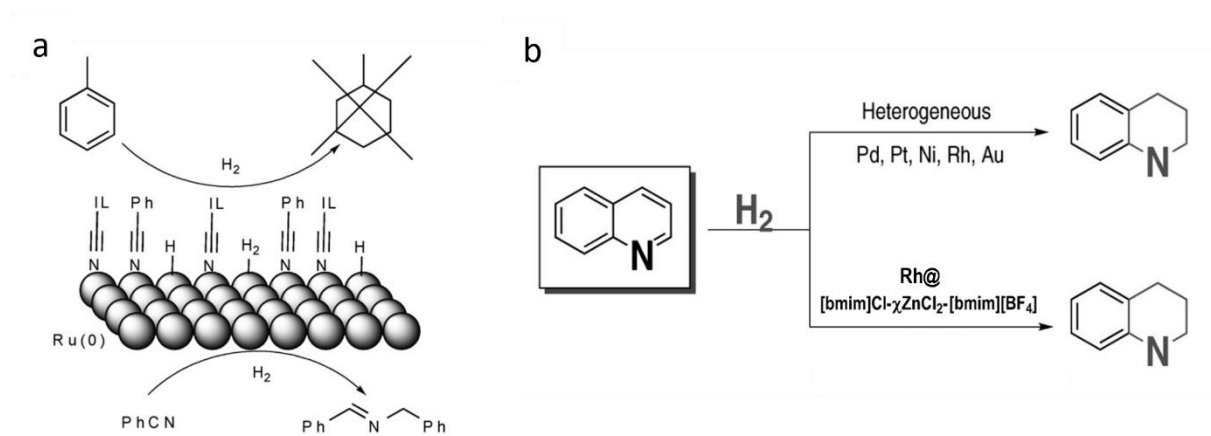


Figure 1.1.38 a) selective hydrogenation over Ru NPs stabilized with nitril-modified IL. Reprinted from ref¹⁰²; b) selective hydrogenation over Rh NPs stabilized with chlorozincate-modified IL. Reprinted from ref¹⁰³.

Although ILs can stabilize well NPs, this system presents a few drawbacks, such as high viscosity and high price, which limit their use¹⁰⁴. With the development of surface functionalization techniques, it became possible to immobilize molecules^{105,106}, polymers¹⁰⁷ or ILs^{108,109}. In these systems, mass transfer and cost are not issues anymore as only a small amount of IL is used and catalyst can easily be recovered.

Firstly, ILs were used in heterogeneous catalysis as solid catalysts with ionic liquid layers (SCILL) where the catalyst is covered with a thin layer of an IL. They showed high performance in reactions where selectivity can be achieved by difference in solubility of primary/final products and ionic liquids¹¹⁰. For example, Friedrich and colleagues used a SCILL that consisted of Pd/Al₂O₃ covered by a film of ionic liquid in hydrogenation of propyne (Figure 1.1.39 a)¹¹¹. Presence of the IL on the surface resulted in excellent selectivity towards propene (>95%) as well as in decreased formation of side products that poison the catalytic surface. Additionally, it was proposed that IL could selectively poison catalysts active sites, thus improving selectivity of a reaction¹¹². With different SCILL systems, selective hydrogenation of unsaturated aldehydes like citral¹¹³ or hydrocarbons like 1-octyne¹¹⁴ and butadiene¹¹⁵ was achieved. However, the main issue of the SCILL system is IL leaching, which restricts potential applications.

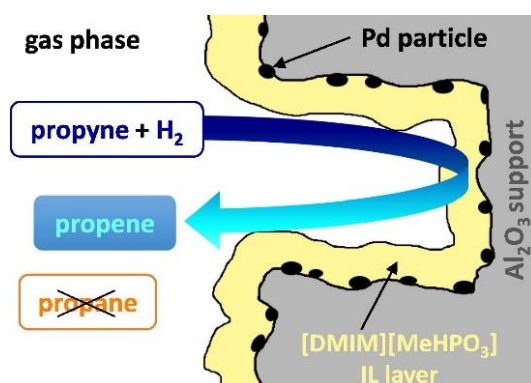


Figure 1.1.39 Illustration of selective propyne hydrogenation with SCILL catalyst. Reprinted from ref¹¹¹.

Addressing to mass transfer and stability issues of IL and SCILL, supports with covalently grafted ILs can be used^{109,116}. Catalysts immobilized on such supports, so-called supported ionic liquid phases (SILP), seem to be appealing materials due to the big variety of building blocks and the easy modification of each part of the system: catalyst (complex or metal nanoparticle), support (commonly used silica, alumina or carbon), and IL structure (mostly imidazolium and phosphonium IL) (Figure 1.1.40). SILP catalyst was firstly employed by Mehnert in hydroformylation¹¹⁷. Since then, big progress was done in this field, and SILP catalysts were employed in a variety of reactions such as water-gas shift reaction, selective hydrogenation, coupling reactions and others which are well-described in a book edited by Fehrman *et al.*¹¹⁸. Some of the representative examples are discussed below.

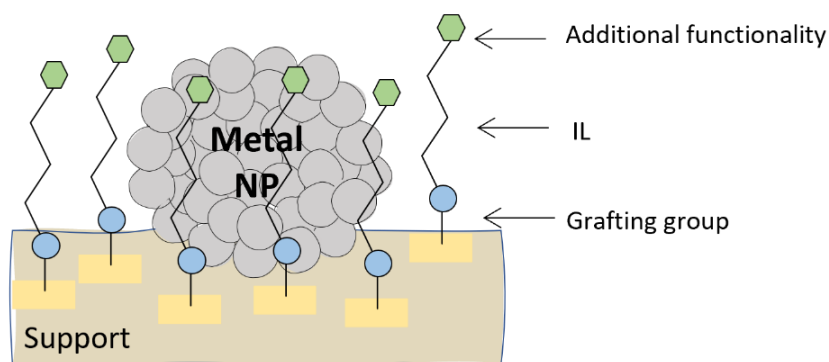


Figure 1.1.40 Illustration of NP@SILP concept.

In a comprehensive study, Bordet and colleagues¹¹⁹ investigated how the structure of covalently linked imidazolium ionic liquid (Figure 1.1.41) influences the synthesis of Rh@SILP and catalytic hydrogenation. Firstly, they showed that Rh-NPs stabilized by SILP are more active than the ones stabilized with unmodified silica or octyl chain-modified silica. They found that among NTf_2^- , OTf^- , and Br^- anions the bulkiest and the least coordinating NTf_2^- anion led to a significant increase of activity in furfural acetone hydrogenation (TOF are 127; 5; and 13 h^{-1} respectively). The selectivity modulation was possible by changing the carbon chain length between the imidazolium and the

substrate as well as by changing the N-alkyl chain length. However, the results could be influenced by different NPs sizes from 1.2 to 2.0 nm, so it was not possible to distinguish which effect contributed the most.

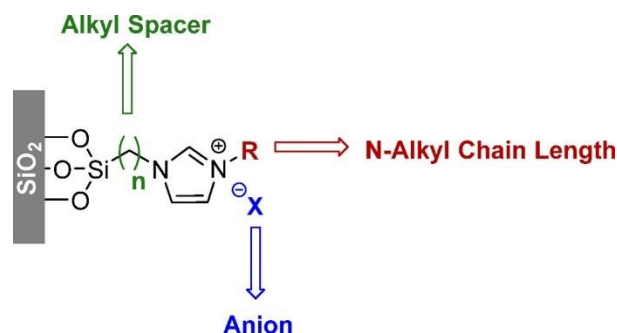


Figure 1.1.41 Illustration of the tunable parameters of an imidazolium-based supported ionic liquid phase (SILP) used for the organometallic synthesis of rhodium nanoparticles (Rh@SILP). Reprinted from ref¹¹⁹.

Recently another study by Moos *et al.*¹²⁰ highlighted a non-innocent role of a counteranion of IL in catalysis. They found that Rh NPs stabilized with a phosphonium-based SILP with an NTf₂⁻ anion (Figure 1.1.42 a) provided hydrodeoxygenation of acetophenone with formation of ethylcyclohexene; on the contrary, changing an anion to BPh₄⁻ allowed solely hydrogenation with formation of a cyclohexylethanol. The authors assume that acidic rhodium fluoride species formed due to partial decomposition of NTf₂⁻ catalyze deoxygenation reaction.

An interesting hybrid material was obtained by Abu-Reziq and others by surface modification of magnetite nanoparticles with an imidazolium- or dihydroimidazolium-based IL¹²¹. The modified Fe₃O₄ NPs served as a support for Pt-NPs (Figure 1.1.42 b). This catalytic material showed high selectivity in hydrogenation of a diphenylacetylene to a cis-stilbene. The authors suppose that steric hindrance caused by IL complicates alkene adsorption on the NP surface and thus prevents overhydrogenation of an alkene to an alkane. Using the same catalyst, it was possible to selectively hydrogenate cinnamaldehyde to cinnamyl alcohol. In this case, authors speculate that the magnetite NPs to some extent can polarize the Pt MNP surface allowing a preferable coordination and subsequent hydrogenation of the polar carbonyl group.

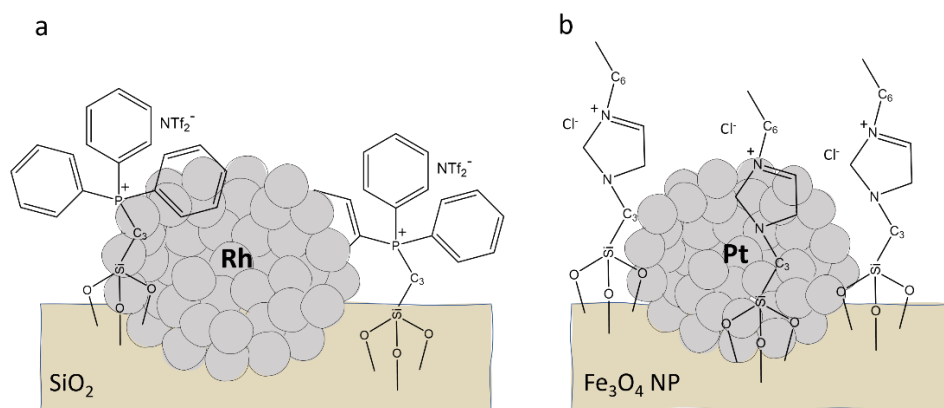


Figure 1.1.42 Illustration of a) Rh@SILP and b) Pt@Fe₃O₄-SILP systems.

A combination of Ru NPs and a silica support with ionic liquid phases (SILP) partially functionalized with sulphonate moieties was applied by Luska *et al.* in HDO of biomass-derived substrates (Figure 1.1.43 a)¹²². In this dual catalyst (Ru@SILP-SO₃H) Ru was responsible for hydrogenation of unsaturated bonds, whereas the IL activated hydrogenated molecules in deoxygenation reaction. As a result, high deoxygenation activity was achieved, with a possibility of selectivity control by adjusting the number of acidic sites and reaction conditions (Figure 1.1.43 b).

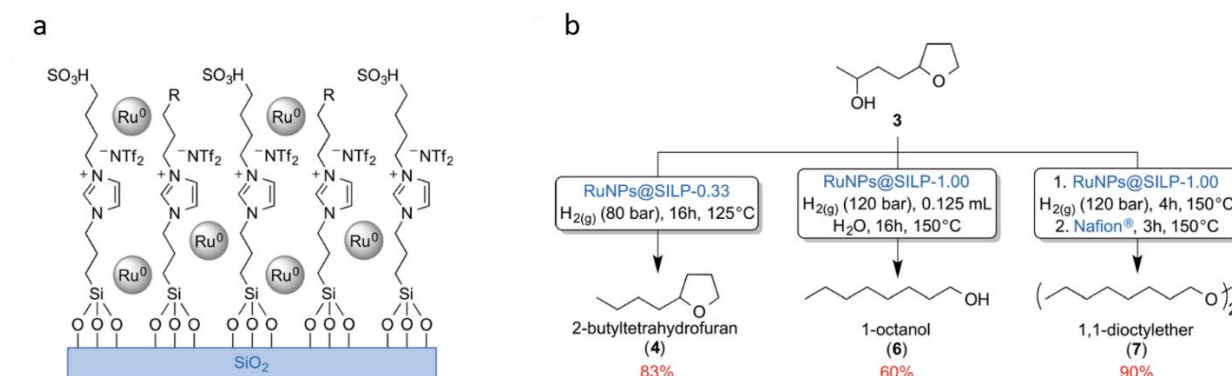


Figure 1.1.43 a) structure of Ru@SILP-SO₃H; b) control of selectivity in deoxygenation of 4-(2-tetrahydrofuryl)-2-butanol by adjusting acidity and reaction conditions. Reprinted from ref¹²².

Going further, researchers from the same group synthesized bimetallic iron-ruthenium nanoparticles supported on SILP with physisorbed acidic IL (Fe₂₅Ru₇₅@SILP+IL-SO₃H). Applying this system in catalysis, non-benzylic and benzylic ketones could be hydrodeoxygenated while the aromaticity of the ring was preserved¹²³. According to the authors, the deoxygenation pathway included the following steps: ketone hydrogenation with formation of alcohol; alcohol dehydration; alkene hydrogenation. Interestingly, the conversion of diphenylketone to diphenylmethane was also quantitative, indicating that the formation of an alkene intermediate is not required if sufficiently stable carbocations can be formed.

1.2. Hybrid systems of type “nanoobject-metal complex”

In this section we use the term “hybrid systems” to describe the systems that consist of a material part, a nanoobject (NO) (metal NP, quantum dot, carbon nanotube, *etc*), and a molecular part, a metal complex (MC). So, in this concept molecular and material chemistry are combined in order to exhibit unique properties that are distinct from those of the individual components. For instance, the NP can provide stability or dispersibility to the MC while the MC can modify electronic, photophysical or catalytic properties of the NP. The resulting hybrid material can be applied in catalysis, sensing, biomedicine, electronics, *etc*^{26,124,125}. Meanwhile, we will focus solely on catalytic applications. In addition, we will only cover the hybrid systems where the two parts are relatively strongly attached to each other, *e.g.* by covalent grafting or by electrostatic interactions. In this way we can compare effects of organic ligands that were discussed in the previous sections with the effect of metal complexes.

1.2.1. Synthesis of hybrid systems

There are two main methodologies to synthesize covalently attached hybrid systems, namely using a complex with anchoring groups as a stabilizer directly during the synthesis of NOs^{126,127}, or by a post-functionalization on the NO surface^{128–130}. To covalently bind an MC to a semiconductor, mostly carboxyl and phosphonate linkers are used, however, stability of other anchors such as hydroxyamic acid or silantrane have been also reported¹³¹. Strong electrostatic interactions between two parts of a hybrid system can be achieved by interactions of a charged complex with an oppositely charged ligand grafted to the surface of a NO^{132,133}.

1.2.1.1. Direct synthesis

In the early studies of the hybrid systems Mayer and colleagues synthesized gold and silver NPs in the presence of sodium borohydride as a reductant and Ru(II) polypyridyl complexes bearing bidentate phenanthroline, monodentate pyridine or monodentate thiophene functions, which can coordinate to the surface of the NPs (Figure 1.2.1 a)^{134,135}. The weakest interactions were observed for thiophene-functionalized Ru(II) complex, where NPs were polydisperse, while phenanthroline and pyridine functions could better stabilize NPs. Similar to NPs covered with molecular stabilizers, the size control by tuning the Me/Ru ratio was also demonstrated (Figure 1.2.1 b).

In a recent study by Martin Morales and coworkers, Ru NPs were synthesized in the presence of H₂ as a reductant and a cationic organophosphorus ruthenium(II) polypyridyl complex as a capping agent (Figure 1.2.1 c,d)¹³⁶. Combining NMR and DFT experiments, the authors

suggested that the complex was covalently attached to the surface of Ru through Cl ligand while an outer shell made of the same complex was formed due to the electrostatic interactions with counterions from the inner layer.

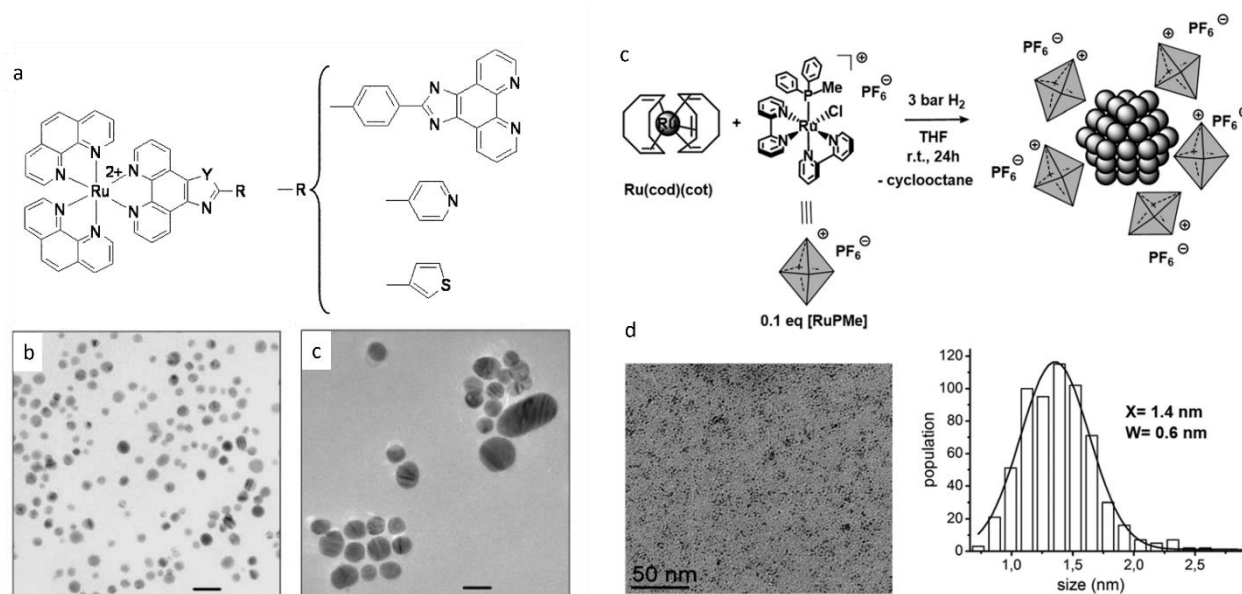


Figure 1.2.1 a) illustration of Ru(II) polypyridyl complexes; b) Ag NPs stabilized with pyridine-functionalized complex with ratios Ag/ Ru equal to 2 and c) equal to 10. Scale bar 20 nm. Reproduced from refs^{134,135}. c) Scheme of the synthesis of a Ru NP-Ru(II) polypyridyl hybrid system; d) TEM image and size distribution diagram of as-obtained NPs. Reproduced from ref¹³⁶.

1.2.1.2. Post-functionalization

When direct stabilization with a complex is not possible a post-functionalization procedure may be a solution. Three main ways of a post-synthetic functionalization are illustrated in Figure 1.2.2. Namely, ligand attachment can be achieved through a direct ligand-exchange procedure, chemical functionalization of the ligands, and by electrostatic interactions.

Friederici and coworkers applied methods of ligand exchange and ligand functionalization in their study about the synthesis of Pd NP-MC hybrid systems¹²⁸. The authors prepared hexanethiol-capped Pd NPs (2 nm) which were consequently functionalized with phosphine-modified thiols. The ligand-exchange strategy was applied in this case because direct synthesis of NPs with phosphine-functionalized thiols caused the formation of new complexes instead of NPs. Based on NMR and FTIR experiments, the authors suggested that the functionalized ligands were attached to Pd NPs through the SH moieties thus providing phosphine functions to form strong bonds with various metals. As a result, a facile organometallic functionalization with metal complexes containing Pd, Rh, Ir, and Ru metal centers could be performed to achieve hybrid systems of interest (Figure 1.2.3).

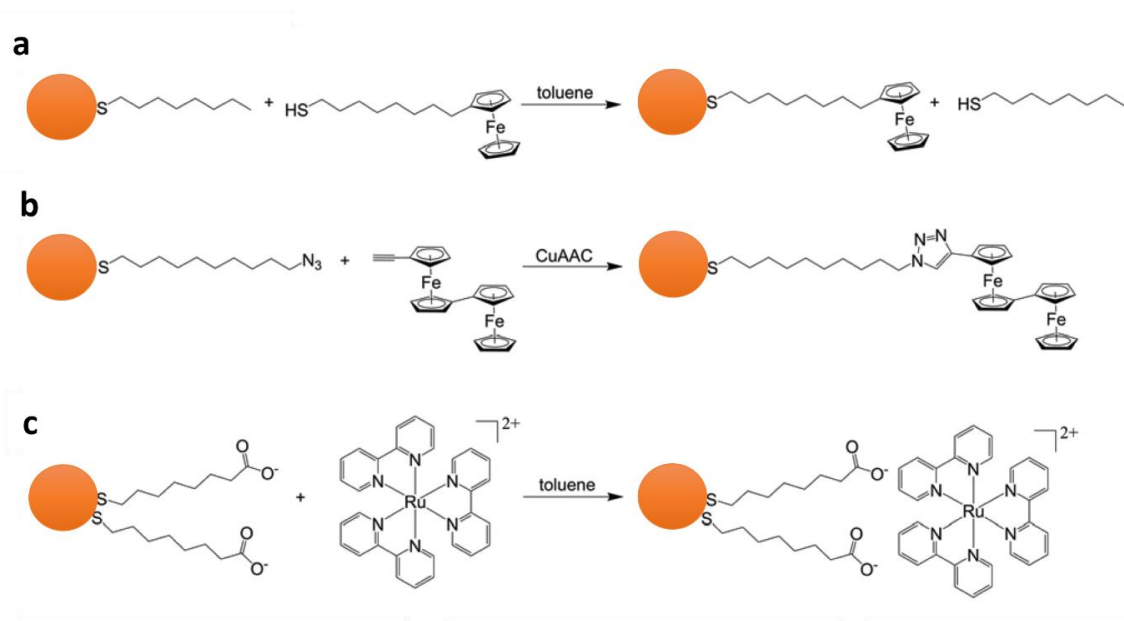


Figure 1.2.2 Post-synthetic functionalization of NPs to form hybrid NP-MC systems. a) ligand exchange; b) chemical functionalization of the ligand; electrostatic attachment of the MC. Adapted from ref²⁶.

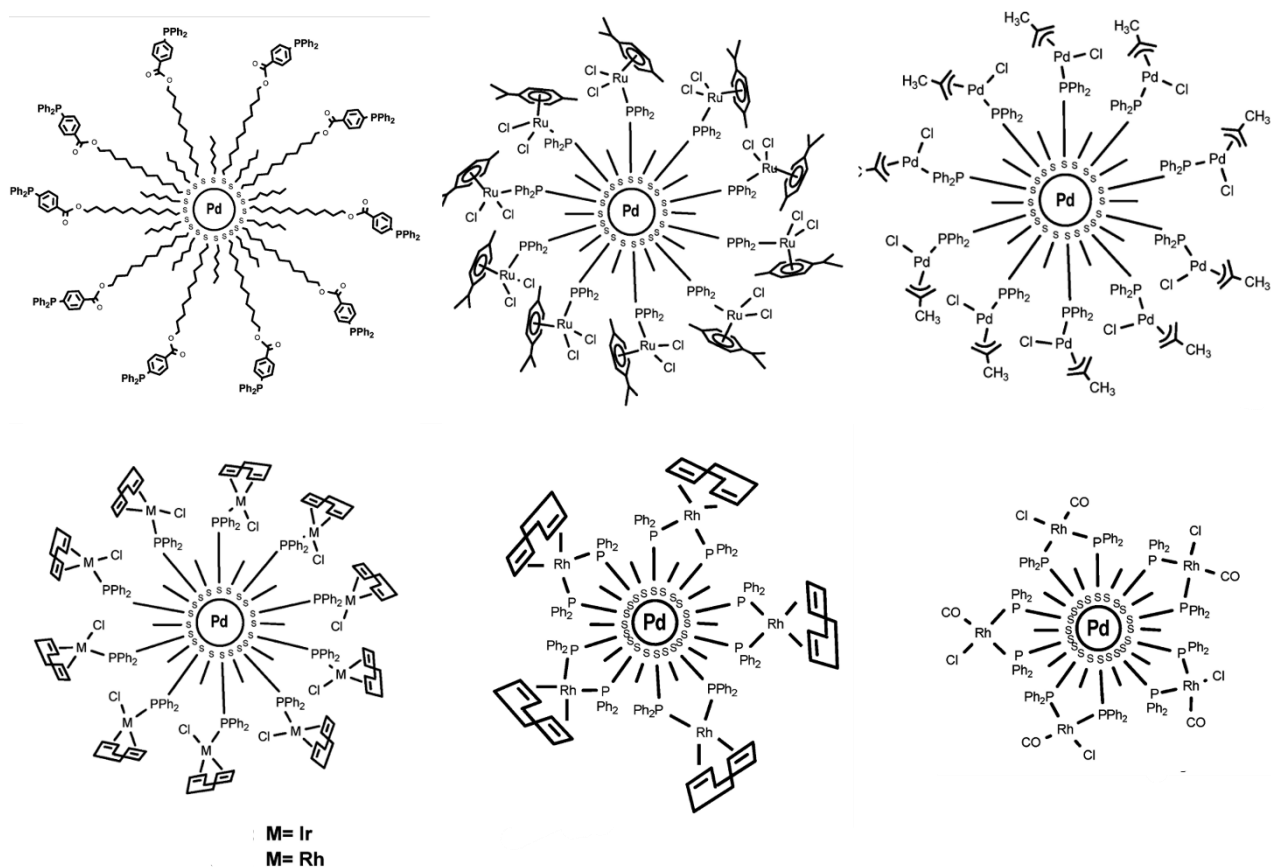


Figure 1.2.3 Illustration of Pd NPs functionalized with phosphine-bearing thiol and different hybrid materials synthesized by organometallic functionalization of the NPs. Adapted from ref¹²⁸.

1.2.2. Complexation-mediated self-assembly

SAs with MCs can be formed by addition of metal ions to the NPs stabilized with chelating ligands that will lead to in-situ complexation. Mostly SAs induced by complexation are used as sensors or trapping agents to remove toxic cations from the solution. Some representative examples are provided in this section.

SA produced through complexation were reported by Zhang and colleagues¹³⁷. In this study, Au NPs were stabilized with a thiol-modified terpyridine to assure coordination through sulfur, leaving terpyridine on the free end (Figure 1.2.4 a). While big shapeless aggregates were observed for the as-prepared Au-NPs, the addition of $\text{Co}(\text{NO}_3)_2$ resulted in direct transformation into another spherical 3D aggregates of smaller sizes, due to the strong binding of terpyridine to Co center (Figure 1.2.4 b,c). A similar approach was used by Zhu and coworkers, but in this case Au NPs were stabilized by poly(acrylic acid)-1-dodecanethiol¹³⁸. Upon addition of coordinating metal ion (Pb^{2+} , Hg^{2+} , Cd^{2+} , Ba^{2+} , Zn^{2+}) chain-like SAs were formed (Figure 1.2.4 e,f). SAs were observed only at neutral pH. In acidic conditions metal ions (shown on example of Pb^{2+}) could not efficiently coordinate protonated acid, whereas in basic conditions Pb was precipitating in the form of $\text{Pb}(\text{OH})_2$. Importantly, SA could break upon addition of a stronger chelating agent – ethylenediaminetetraacetate (EDTA) (Figure 1.2.4 g). To explain the observed 1D assembly, the authors proposed to consider each NP with coordinated metal cations as a dipole where the negatively charged carboxylates and the chelated ones can rearrange on the surface to form a chain-like SA.

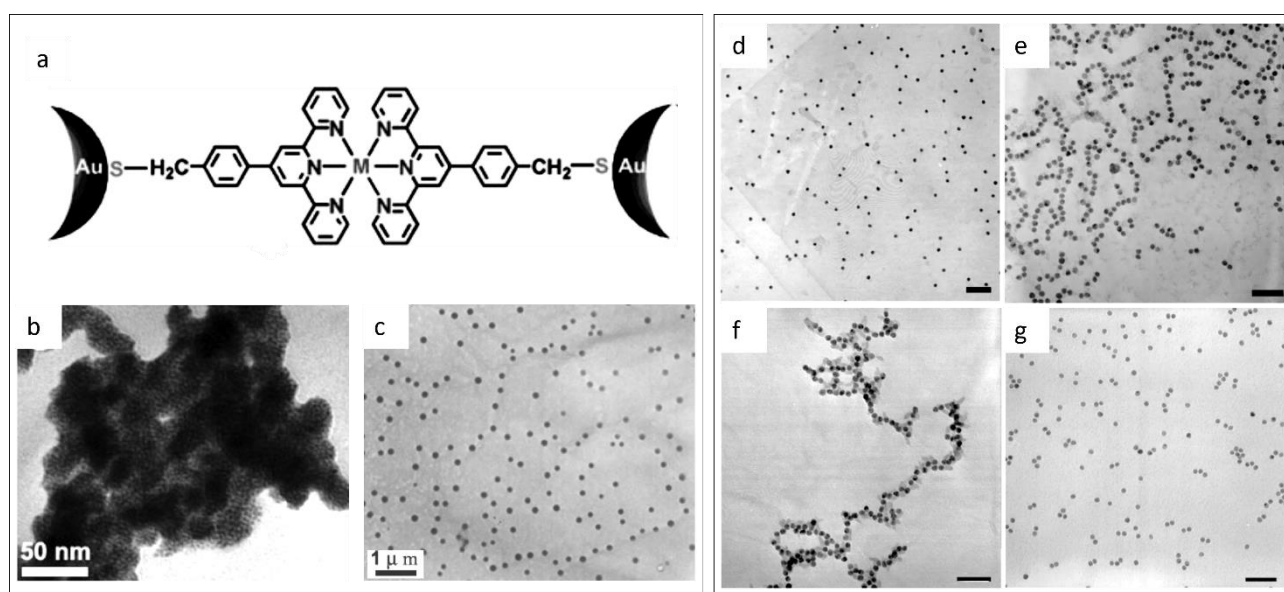
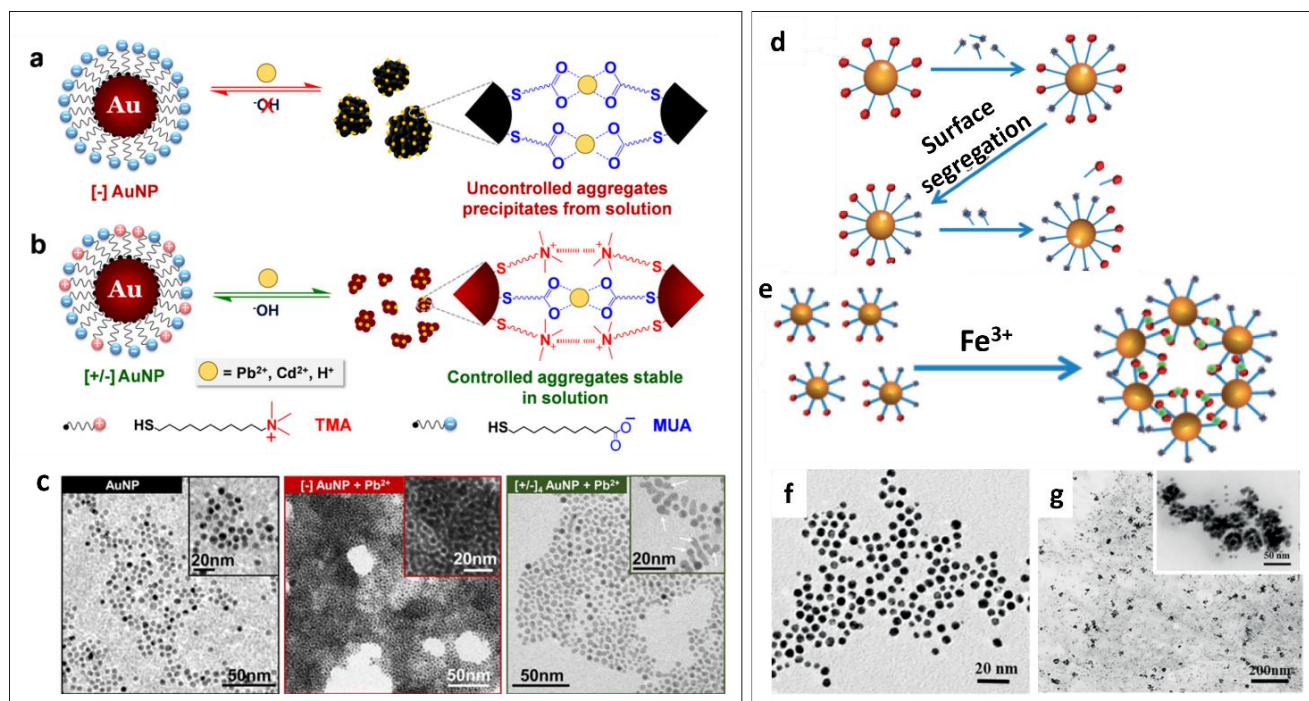


Figure 1.2.4 a) Illustration of complexation induced SA of terpyridine-capped Au NPs; TEM images of Au NPs b) big shapeless aggregates once prepared; c) smaller spherical aggregates after addition of Co^{2+} . Adapted from ref¹³⁷. TEM images of polyacrylic acid-capped Au NPs with d) 0; e) 22; f) 36 μM of Pb^{2+} ; g) with 36 μM of Pb^{2+} and 100 μM of EDTA. Scale is 100 nm. Adapted from ref¹³⁸.

The importance of the equilibrium between attracting and repulsive forces provided by ligands was shown by Rao and colleagues (Figure 1.2.5 a-c)¹³⁹. In their study Au NPs stabilized with 11-mercapto-undecanoic acid (MUA) formed irreversible precipitating aggregates upon chelation of Pb^{2+} . However, when a positively charged ligand (N,N,N-trimethyl(11-mercapto-undecyl) ammonium chloride (TMA) was attached to the surface the interplay between negatively and positively charged ligand allowed formation of smaller aggregates which preserved the system from precipitation and allowed disassembly upon addition of NaOH.

Another work where a mix of ligands was used to tune SA properties is a study of Su and colleagues (Figure 1.2.5 d-g)¹⁴⁰. In their work, Au nanoparticles stabilized with citrate and tannic acid ligands could form self-assemblies upon addition of Fe^{3+} . Interestingly, the SA shape was different from that formed by addition of Fe^{3+} to Au NPs capped with tannic acid alone. With a mixture of ligands, SAs of controlled sizes (50 nm) were achieved and no cross-linking with the formation of bigger aggregates was observed. The authors suggested that the ligands could undergo a surface segregation favored by π - π interactions between tannic acid ligands (Figure 1.2.5 d). This arrangement would lead to iron ions coordination by tannic acid inside the aggregates (Figure 1.2.5 e, g).



Interesting application of complexation-driven SA was developed by Liu and coworkers¹⁴¹. They stabilized AuNPs with an alkanethiol terminated in photoactive spiropyran (SF) responsible for chelation and an alkanethiol terminated in triethylene glycol used to induce water-solubility and to dilute an active ligand. Spirofurane was used because under UV irradiation it isomerizes to merocyanine (MC) which contains a chelating phenolate group (Figure 1.2.6 a). This system was used as logic gates where UV light (input 1) and Cu^{2+} (input 1) were used as inputs and a complexation-induced SA was used as an output (output 1). Output could be monitored by UV/Vis spectroscopy, zeta potential, DLS, or eventually, by a naked eye. Few logics operations were performed by this system based on the simple algorithm where combination of two inputs lead to output while no response was caused by either of inputs (1/0 or 0/1) (Figure 1.2.6 b).

Formation of well-defined crystalline phases of NP SAs is also possible. Wang and coworkers showed that trioxalatocobaltate(III) complex (TOC) (Figure 1.2.6 c) could induce an SA of AuNPs co-stabilized with (11-mercaptoundecyl)-N,N,N-trimethylammonium bromide (TMA) and 1-hexanethiol through electrostatic interactions with ammonium head¹⁴². Firstly, amorphous aggregates were formed (Figure 1.2.6 e) which could be transformed into *fcc* crystals (Figure 1.2.6 f) upon addition and consequent decomposition of a volatile salt $(\text{NH}_4)_2\text{CO}_3$ (Figure 1.2.6 d). Interestingly, upon light irradiation this complex could disproportionate releasing oxalate which was oxidized to CO_2 and reducing Co(III) to Co(II) (Figure 1.2.6 c). Formation of dianionic complex caused disassembly. Authors explained this behavior by the Hardy–Schulze rule, which postulates that the coagulating ability of oligo-ions toward oppositely charged colloids is strongly influenced by the charge of the oligo-anions.

To sum up, SAs with complexes can be synthesized by in-situ complexation or by the complex addition as an external agent that can induce SA through attractive interactions. These SAs can be disordered or crystalline, they can be applied as metal sensors, components of logical gates or serve as potential candidates for controllable delivery systems.

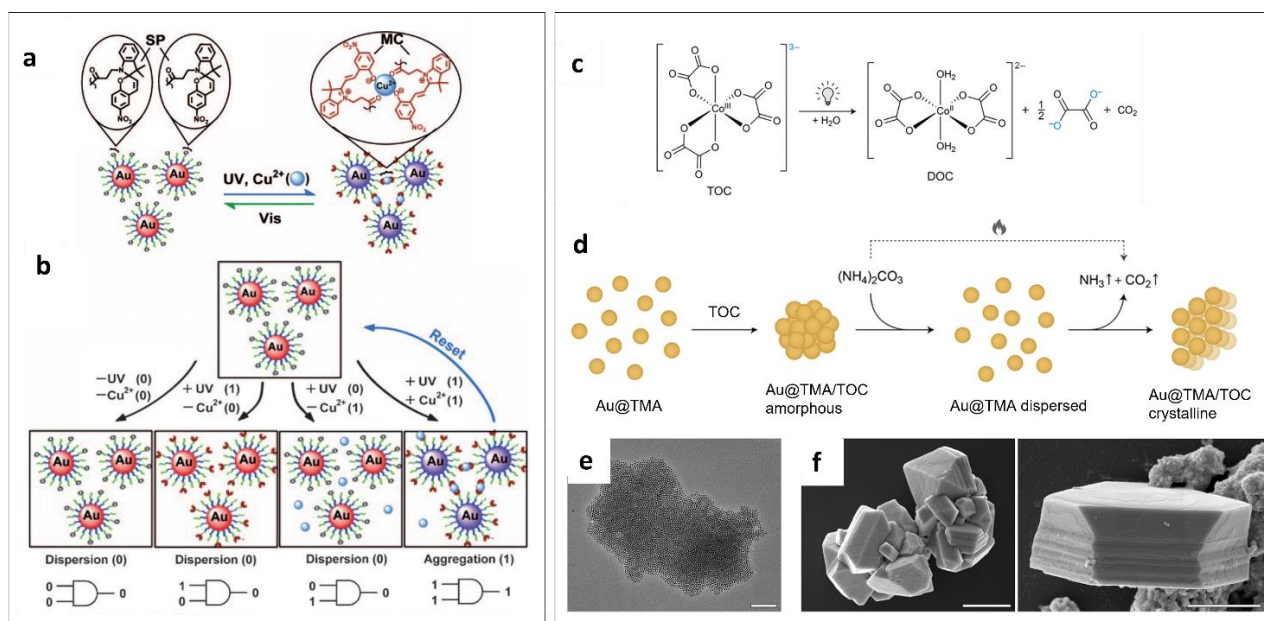


Figure 1.2.6 a) Scheme of UV and Cu^{2+} induced SA of Au NPs; b) scheme of logic gates concept where in the absence of both inputs (0/0) or in the presence of either input (1/0, 0/1), the AuNPs@SF solutions stay red (output=0); in the presence of both inputs (1/1), the AuNP solutions change color to purple. Adapted from ref¹⁴¹. c) Scheme of trioxalato-cobaltate(III) complex disproportionation; d) scheme of formation of an amorphous SA with consequent redispersion and formation of a crystalline SA; e) TEM image of amorphous SA; f) SEM images of crystalline SA. Adapted from ref¹⁴².

1.2.3. Hybrid systems in catalysis

1.2.3.3. Complex as a photosensitizer

One of the first comprehensive studies explaining the mechanism of heterogeneous photocatalysis was a study of Goodeve and Kitchener on catalytic photobleaching of dyes by TiO_2 catalyst in 1938¹⁴³. Since then, plenty of heterogeneous photocatalysts were developed with the aim to create an efficient system utilizing a green source of energy - light, which can be used to solve energetic (water splitting for hydrogen production) and environmental (pollutants decomposition, CO_2 conversion) problems.

A semiconductor photocatalyst in excited state can generate an exciton (electron-hole pair) that allows to participate in redox reactions, namely with the valence band (V.B.) holes in oxidation processes and with the conduction band (C.B.) electrons in reduction processes. In addition, attachment of co-catalytic sites can bring a few benefits to the system. In particular, it promotes charge-carrier separation and a decrease in electron-hole recombination; a co-catalyst provides reaction sites; also it can minimize the overpotential (Figure 1.2.7)^{124,144}. For example, Pt showed to significantly improve activity of TiO_2 in hydrogen evolution reaction, because Gibbs free adsorption energy of hydrogen on Pt is close to the thermoneutral state.

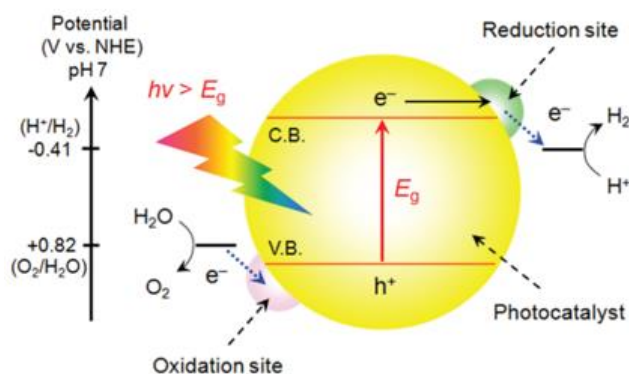


Figure 1.2.7 Scheme of photocatalytic water splitting using semiconductor/co-catalyst system. Reprinted from ref¹⁴⁵.

The main limitation of the semiconductors with wide band gap like TiO₂ is that UV irradiation is required, thus the system is not efficient while using white light. As a possible solution Gerischer presented a concept of spectral sensitization - using redox complexes as photosensitizers (PS) for a semiconductor¹⁴⁶. There, a complex gets excited under visible light irradiation and transfers its electrons to the conduction band of the semiconductor ($E(\text{LUMO}) > E(\text{C.B.})$) where they are further transported to the active catalytic sites; meanwhile, the oxidized complex gets reduced by a sacrificial electron donor. Each element of this elegant hybrid system plays a crucial role in the activity of the system: a PS allows to use a visible light, a semiconductor serves as an efficient electron mediator (and often as a catalyst), and co-catalyst directly interacts with the substrates during catalysis. The efficiency of this system mainly depends on two events: the speed of electron transfer from an excited PS to a semiconductor and the electron-hole recombination effects. To further improve the electron transfer, strong interactions like covalent grafting of a PS to the semiconductor or electrostatic interactions are used. Therefore, in this section, the most attention will be devoted to the systems where a complex strongly interacts with a catalyst.

1.2.3.3.1. Case of Ru(II) polypyridyl complexes

Ru(II) polypyridyl complexes are a popular choice for a PS due to their appealing photophysical and redox properties¹⁴⁷. For example, the [Ru(bpy)₃]²⁺ complex in the excited state is better electron-donor and electron-acceptor than in the ground state, which allows fast electron transfer from/to the excited complex. It is also easy to functionalize the complex if modification of the absorption wavelength or addition of extra functionalities, or covalent anchors are needed.

Li and coworkers used carboxylic acid-functionalized Ru(II) polypyridyl complex (**RuC**) to covalently bind to small TiO₂ NPs (Figure 1.2.8)¹⁴⁸. At prolonged irradiation time, they found partial detachment of **RuC** complex in water solution, but no leaching was observed in acetonitrile solution. The as-formed hybrid system showed high activity in photocatalytic C-O and C-C hydrogenolysis of

a model biomass substrate (Figure 1.2.8). Importantly, this transformation was performed at room temperature and aerobic conditions, while conventional hydrogenolysis requires high temperature and oxidizing agents.

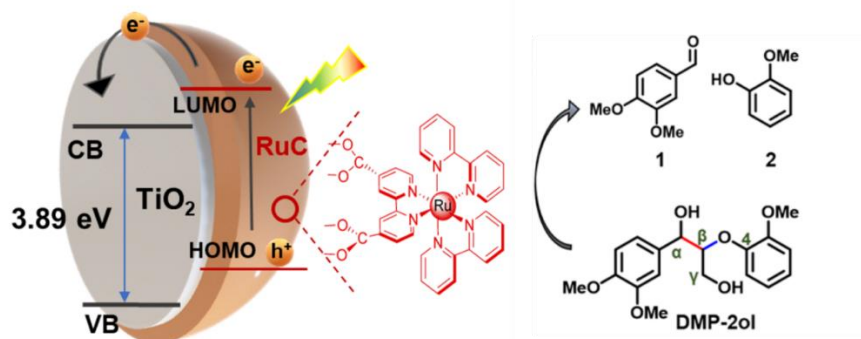


Figure 1.2.8 Structure of TiO₂ NP-RuC hybrid system and the transformation catalyzed by this system. Reprinted from ref¹⁴⁸.

In a study of Romero and coworkers hybrid systems composed of Ru NPs supported on TiO₂, a PS, and triethanolamine (TEOA) as a sacrificial electron donor were synthesized¹⁴⁹. Among three PS, [Ru(bpy)₃]²⁺, RuP or QuPh⁺-NA (see Figure 1.2.9 a), only RuP resulted in a system active in H₂ evolution reaction (HER). Authors presumed that phosphonic acid anchors facilitated electron transfer enabling HER. TiO₂ on another side, acted as both NP support and electron-transfer mediator.

Direct attachment of Ru(II)(bpy)₃ complexes to the NPs can also yield promising catalytic performance. De Tovar and colleagues synthesized Co NPs that were oxidized and consequently functionalized with Ru(II)(bpy)₃ complexes bearing two (PS1) or four (PS2) phosphonic acid pending groups (Figure 1.2.9 b)¹⁵⁰. The covalent grafting of PS1 and PS2 was confirmed by IR analysis. The synthesized hybrid systems were tested in light-driven water oxidation with a sacrificial electron-acceptor and the results were compared with the systems where the PSs were unbound (added directly before the catalytic test). The authors showed that activity in oxygen generation depended on the efficient electron transfer from Co₃O₄ to the PS meaning that the stability of the NP-PS system was crucial. Thus, systems with covalently bonded PS showed higher activity than the ones with unbonded complexes. Also, Co₃O₄-PS2 showed better results than Co₃O₄-PS1. The difference in activity was attributed to higher amount of phosphonate anchoring groups and bigger amount of PS2 complexes on the surface of Co₃O₄ NPs that lead to their higher stability.

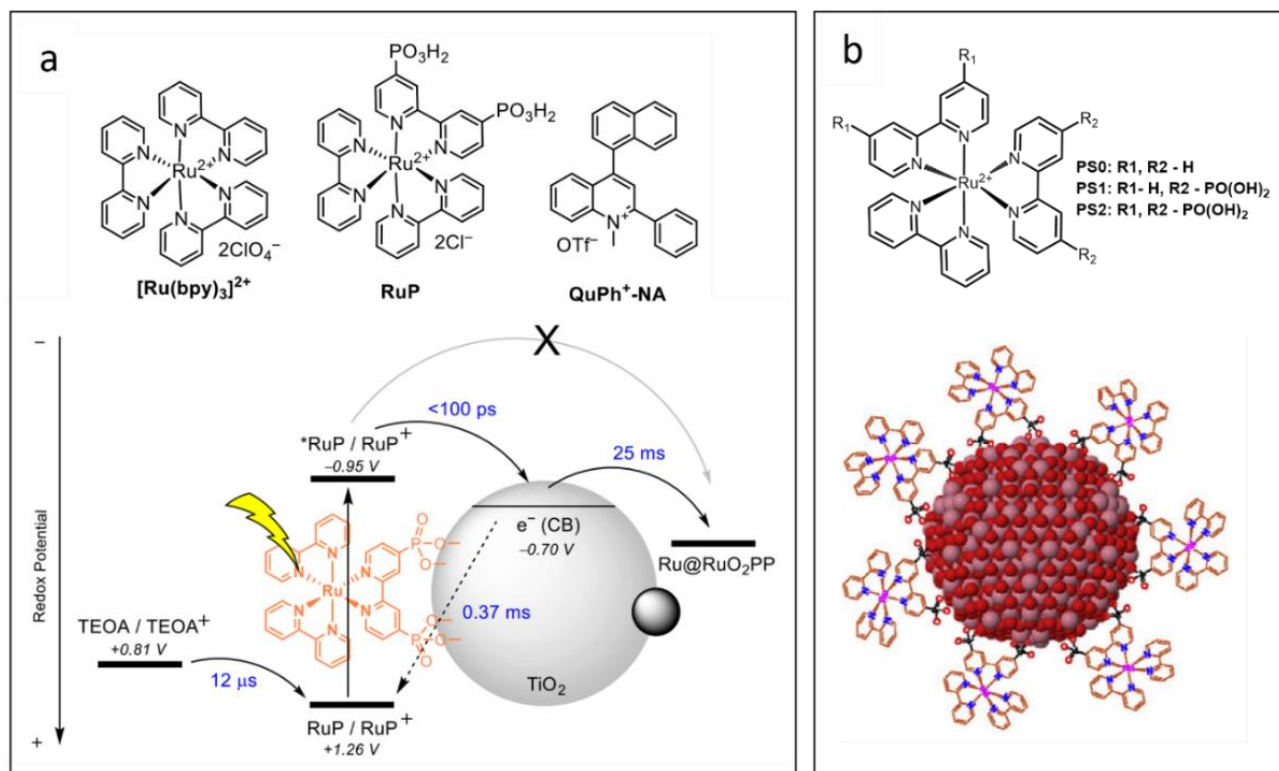


Figure 1.2.9 a) Illustration of PS structures and of the electron transfer mechanism in Ru NP-TiO₂-PS system. Reproduced from ref¹⁴⁹. b) Illustration of PS structures and a structure of resulting Co₃O₄-PS NPs. Adapted from ref¹⁵⁰.

1.2.3.3.2. Case of metal porphyrins

Porphyrins is another class of PSs widely applied in photocatalysis. In particular, many studies are devoted to modification of porphyrins with photoactive fragments to further enhance ligand-to-metal charge transfer (LMCT) and electron injection to the catalyst^{151–153}. An example of efficient photocatalytic HER was recently reported by Nikolaou *et al.*¹⁵⁴. They synthesized (BODIPY)₂-Zn-porphyrin complex and attached it through a carboxylate linker to the surface of TiO₂/Pt (Figure 1.2.10 a). Functionalization of a zinc-porphyrin with two BODIPY fragments resulted in highly efficient LMCT which further enhanced electron transfer to the NP. The resulting material showed excellent performance in HER with 18600 TONs.

In a study of Wang and colleagues Cu(II) tetra(4-carboxylphenyl)porphyrin (TCPP) was anchored to TiO₂ NPs and tested in CO₂ reduction (Figure 1.2.10 b)¹⁵⁵. Remarkably, the 0.5% Cu(II)TCPP/TiO₂ system showed high selectivity towards methane producing approximately 46 times more CH₄ than generated by the semiconductor alone. The authors attributed this high performance to general effects that arise by covalent attachment of a PS, such as increased light absorption and improvement of electron-hole separation. However, they did not comment the selectivity towards methane.

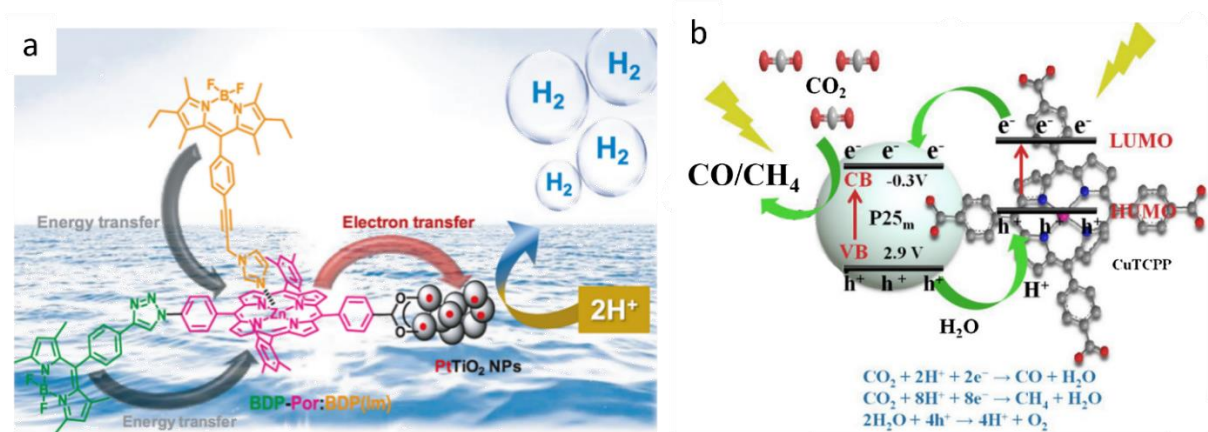


Figure 1.2.10 a) Illustration of $\text{TiO}_2/\text{Pt}-(\text{BODIPY})_2\text{-Zn(II)porphyrin}$ hybrid system used for HER. Reproduced from ref¹⁵⁴. b) Illustration of Cu(II)TCPP/TiO_2 system applied in CO_2 reduction. Reproduced from ref¹⁵⁵.

1.2.3.4. Complex as an active center

Metal-porphyrins play essential role in natural catalytic processes. For example, in living organism iron-porphyrin takes part in oxygen reduction reaction (ORR), whereas in plants magnesium porphyrin is a part of a catalytic system for CO_2 reduction. Inspired by nature, scientists developed plenty of porphyrin-containing systems for the above-mentioned applications. Among them, hybrid systems with an electron donor strongly attached to the active center showed promising activity in electro- and photocatalytic reduction reactions. This concept was further applied to other photoredox active catalysts, so nowadays one can find many studies where MC acts as an active catalyst^{156,157}. Representative examples of such systems are described in this section as well as cases of hybrid systems used in conventional catalysis.

Arcudi and colleagues designed a QD-porphyrin system for CO_2 reduction where a QD acted as a PS and a porphyrin as a catalyst. Namely, a hybrid system was made of negatively charged phenyl-sulfonate-modified Co(III)porphyrin and CuInS_2 QDs stabilized with positively charged amine or ammonium salts (Figure 1.2.11 a)¹³³. Excellent results were obtained for the system – TON was more than 80000 and selectivity to CO exceeded 99%. Authors ascribed this result to few factors. Firstly, electrostatic interactions allowed fast electron injection from the QD to the complex and colocalization of protons near CO_2 and catalyst; secondly, amine/ammonium ligands interaction with CO_2 increased its concentration near the catalyst (see Figure 1.2.11 b); additionally, the authors supposed that the amine/ammonium ligands could activate CO_2 for C-O bond cleavage.

In another study with QD as a PS, a cobaloxime complex was used as an active catalyst. Huang and colleagues covalently attached the complex to the surface of CdSe/ZnS quantum dots with a phosphoryl linker (Figure 1.2.11 b)¹⁵⁸. Using transient absorption spectroscopy, they showed

that by covalent grafting the complex to a quantum dot, electron transfer to the complex is favored (average time constant of 105 ps), whereas charge recombination process proceeds much slower (time constant is bigger than 3 ns). The efficient electron transfer to the cobaloxime catalyst yielded a fast formation of active Co(I) catalyst and efficient hydrogen generation with a TON over 10000.

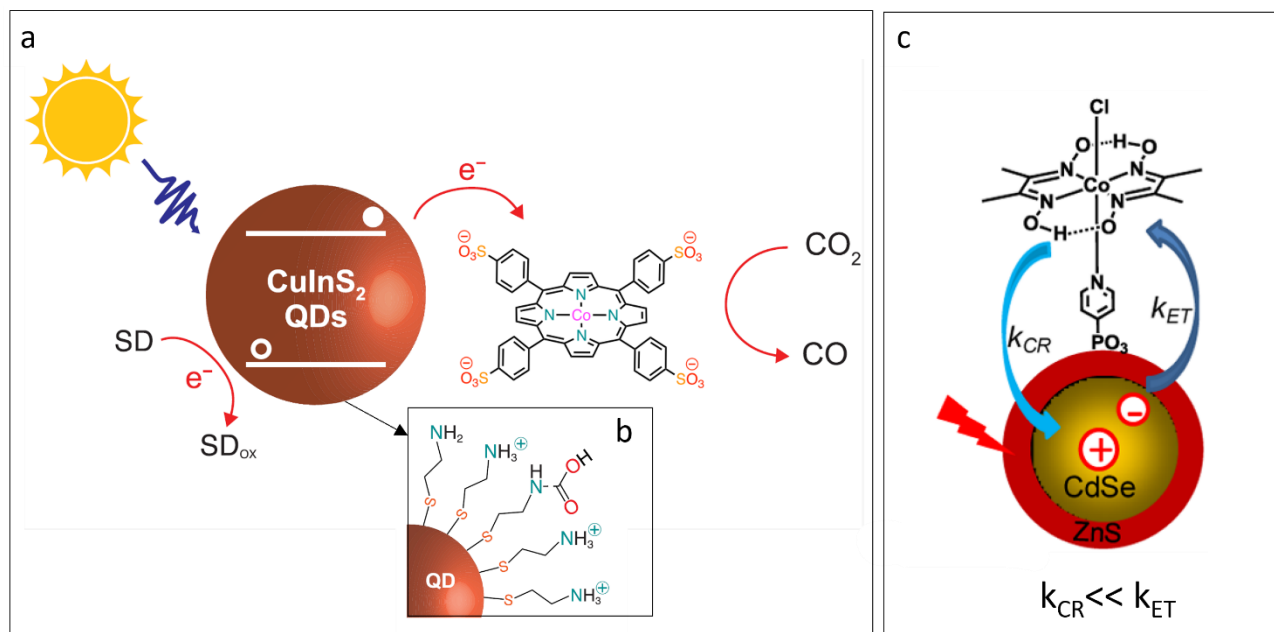


Figure 1.2.11 a) Illustration of electron transfer in a hybrid QD-Co(III)porphyrin system; b) inset of the surface of QD covered with ligands that reversibly interact with CO₂ with formation of a carbamic acid. Adapted from ref¹³³. c) Illustration of QD-Co(III) complex hybrid system. Reprinted from ref¹⁵⁸.

Other hybrid systems containing carbon materials and porphyrin complexes are also active in electrocatalysis. Exceptional activity was observed by Li and colleagues with carbon nanotubes (CNTs) and covalently grafted cobalt corroles in water splitting¹⁵⁹. They synthesized hybrid materials of CNTs functionalized by Co corroles using different methods: covalent attachment with short conjugated linkers (compound **I**, hybrid material **H1**), with long alkyl chains (compound **I**, hybrid material **H2**), grafting using π - π interactions (compound **II**, hybrid material **H3**) or simple adsorption (compound **III**, hybrid material **H4**) (Figure 1.2.12). An activity trend **H1** >> **H3** > **H2** \approx **H4** was obtained in HER and OER. Interestingly, for porphyrins free in solution the HER activity order was **III** > **II** > **I** while on CNTs, the reverse order **H1** > **H3** > **H4** was obtained showing the critical role of the covalent linkage on electron transfer ability and consequently on electrocatalysis. Moreover, authors suppose that strong coordination of **I** to a CNT in **H1** material is responsible for the stability of the system at 0-14 pH. The lower activity of **H2** is explained by much bigger HOMO-LUMO gap due to the alkane chain, leading to stronger suppression of electron transmission.

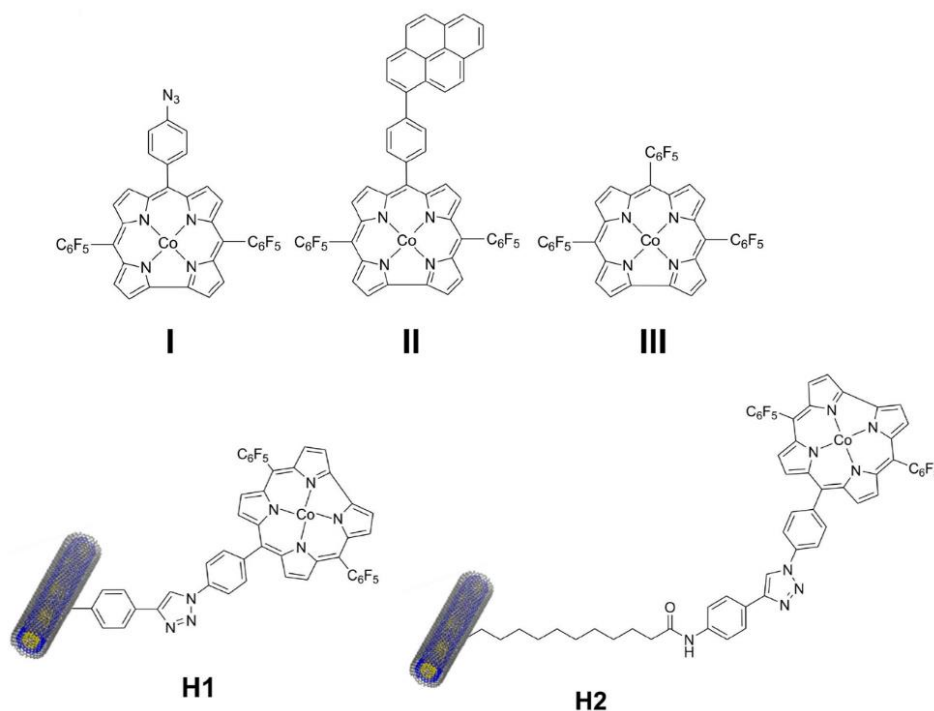


Figure 1.2.12 Structure of cobalt porphyrins and a hybrid materials of CNT and complex I. Adapted from ref¹⁵⁹.

Campidelli and co-workers found an elegant way to immobilize porphyrins on CNTs¹⁶⁰. They used MWCNT as a template for polymerization of cobalt(II)meso-tetraethynylporphyrins. As a resulting configuration, the formation of porphyrin multilayers around the CNT was suggested (Figure 1.2.13). The ORR performance of the hybrid materials in acidic conditions was higher than for the system where the porphyrins were physisorbed to the surface of CNT. The number of transferred electrons was close to 4 indicating a 4-electron-assisted mechanism with complete oxygen reduction was the dominating reduction pathway. The higher efficiency of the system was attributed to the multilayer stacked geometry of the porphyrins around the CNTs.

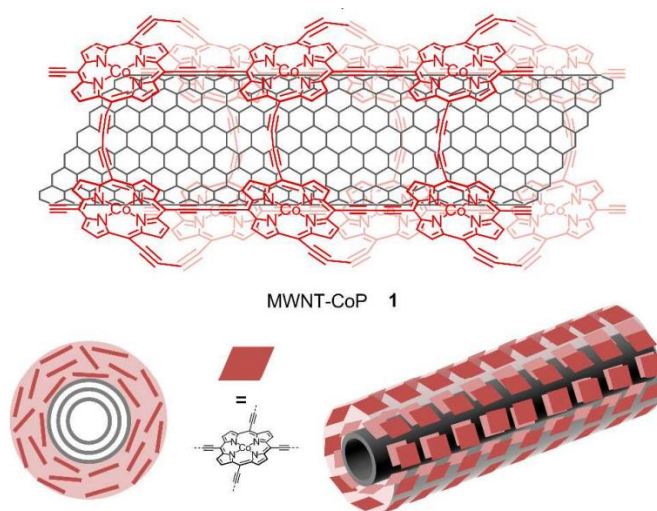


Figure 1.2.13 Illustration of CNT-Co-porphyrin hybrid system. Reprinted from ref¹⁶⁰.

Of course, such hybrid materials were tested in conventional catalysis as well. For example, Sheet and colleagues synthesized Au NPs with covalently grafted iron(II) α -ketoacid complex through a three-step post-functionalization of thiol-capped Au NPs¹³⁰. The as-prepared catalyst was used in Fe(II) complex catalyzed oxidative decarboxylation of benzoylformic acid. The authors observed enhanced performances for the hybrid system comparing to the free complex. The increased reactivity was related to the surface properties providing suitable orientation or to the confinement of the complex, so the role of the Au NPs in this case was more as a support. Similarly, complexes covalently grafted to Au NPs were used as heterogeneous analogs to homogeneous catalysts, for example, in enantioselective transformations^{161–163}.

Recently a prominent example of a hybrid material where both NP and MC were used as catalysts was provided by Kalsi and colleagues¹⁶⁴. In their study a hybrid system containing Ru NPs and Cu(I) N-heterocyclic carbene supported on silica was synthesized (Figure 1.2.14 a). The authors used the catalytic material in one-pot synthesis of a big scope of allylamines and alkylamines starting from amines, formaldehyde, and terminal alkynes (Figure 1.2.14 b). In this system Cu(I) complex was responsible for coupling of amine, formaldehyde, and terminal alkyne. Consequently, by charging the vessel with hydrogen and adjusting reaction conditions Ru NPs could efficiently catalyze the hydrogenation of the coupling product.

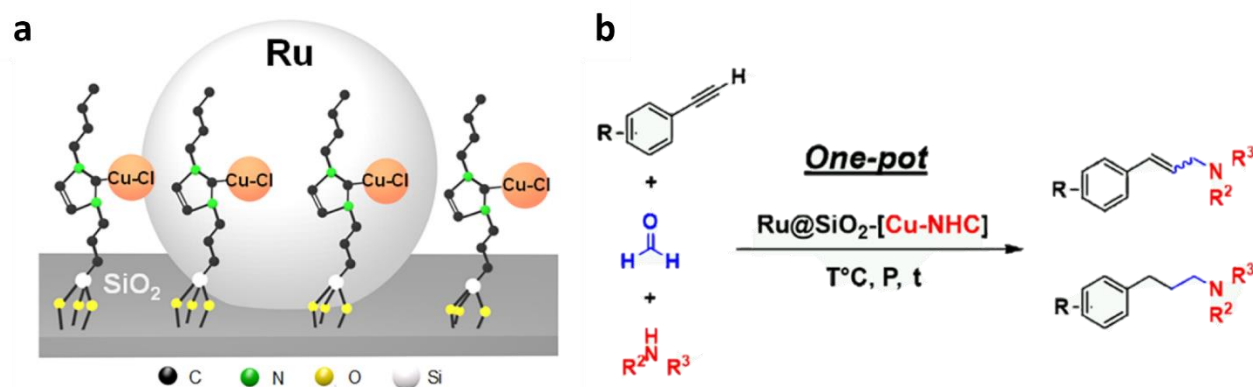


Figure 1.2.14 a) Illustrations of Ru NP-Cu(I) NHC hybrid system; b) scheme of a one-pot reaction. Adopted from ref¹⁶⁴.

1.3. Conclusions

Thanks to modern characterization and nanofabrication techniques, it became possible to distinguish the roles of a metal core and a surface ligand to design nanoobjects with desired functions. This chapter showed that ligands cannot be considered as an innocent spectator species but as active participators in SA of NPs or in catalysis. Basically, the control of SA formation is only possible by tuning the ligand attractive-repulsive forces. Such forces can be controlled by the nature of the functional moieties and by their response to physico-chemical stimuli, such as solvent, pH, light, temperature or extra linkers. Different roles of ligands in catalysis were demonstrated, starting from modification of electron density of active catalytic sites and finishing with NP-ligand cooperative effects. A particular case of hybrid systems of nanoobject-metal complex type was also discussed. Such systems are mostly based on excited state electron or energy transfer from or to the metal complex, so that the complex can be used as a photosensitizer or as an active catalyst. The combination of two parts that are independent catalysts leads to synergetic effects in important transformations like water splitting, ORR, or CO₂ reduction. The principles of the ligand selection demonstrated in the chosen examples can be used to design NPs of tailor-made properties to meet specific needs and applications.

CHAPTER 2. Platinum nanoparticles stabilized by functionalized cyclodextrins for selective hydrogenation

2.1. NPs stabilized with CD-SH: catalytic performances regulated by the ligands.....	62
2.1.1. General synthetic procedure for the Pt-CD systems	64
2.1.2. Pt-b2 catalyst: optimization of the synthetic procedure	66
2.1.2.1. Characterisation	66
2.1.2.2. Catalytic performance	69
2.1.2.3. Comparison with Ru-0.5b2	70
2.1.3. Pt-0.5CD catalysts: biphasic catalysis.....	72
2.1.3.1. Characterisation	72
2.1.3.2. Catalytic performance in THF	74
2.1.3.3. Catalytic performance in water	76
2.1.3.4. Influence of an inhibitor and of an extra amount of b1	78
2.1.4. Pt-b1 catalyst: influence of the ligand ratio on the catalytic activity	79
2.1.4.1. Characterisation	79
2.1.4.2. Catalytic performance with a model substrate	84
2.1.4.3. Catalytic tests with other substrates using Pt-0.1b1	85
2.1.4.4. Catalyst stability test	86
2.2. NPs stabilized with alfa-CD-SPO: introduction of an activation moiety	88
2.2.1. Synthesis and characterization of the systems	89
2.2.2. Identification of active species in selective cinnamyl alcohol formation	92
2.3. Conclusions and perspectives	95
2.4. Experimental part	95
2.4.1. General	95
2.4.2. Analytics	96
2.4.3. Experimental procedures	97

2.1. NPs stabilized with CD-SH: catalytic performances regulated by the ligands

Hydrogenation is a fundamental and inevitable synthetic step in most of the industrial big scale processes, as well as in fine chemistry syntheses. Therefore, many scientists try to understand the mechanisms of hydrogenation to develop catalysts of tailor-made selectivity. It was shown that metal nanoparticles have the advantages of both homo- and heterogeneous systems since they can be recycled, they show higher activity than bulk heterogeneous catalysts, and their selectivity can be greatly modified by various factors. Such factors are grouped in the steric and electronic effect families and summarized in Figure 2.1.1 on the example of selective hydrogenation of a C=O bond of α,β -unsaturated aldehydes.

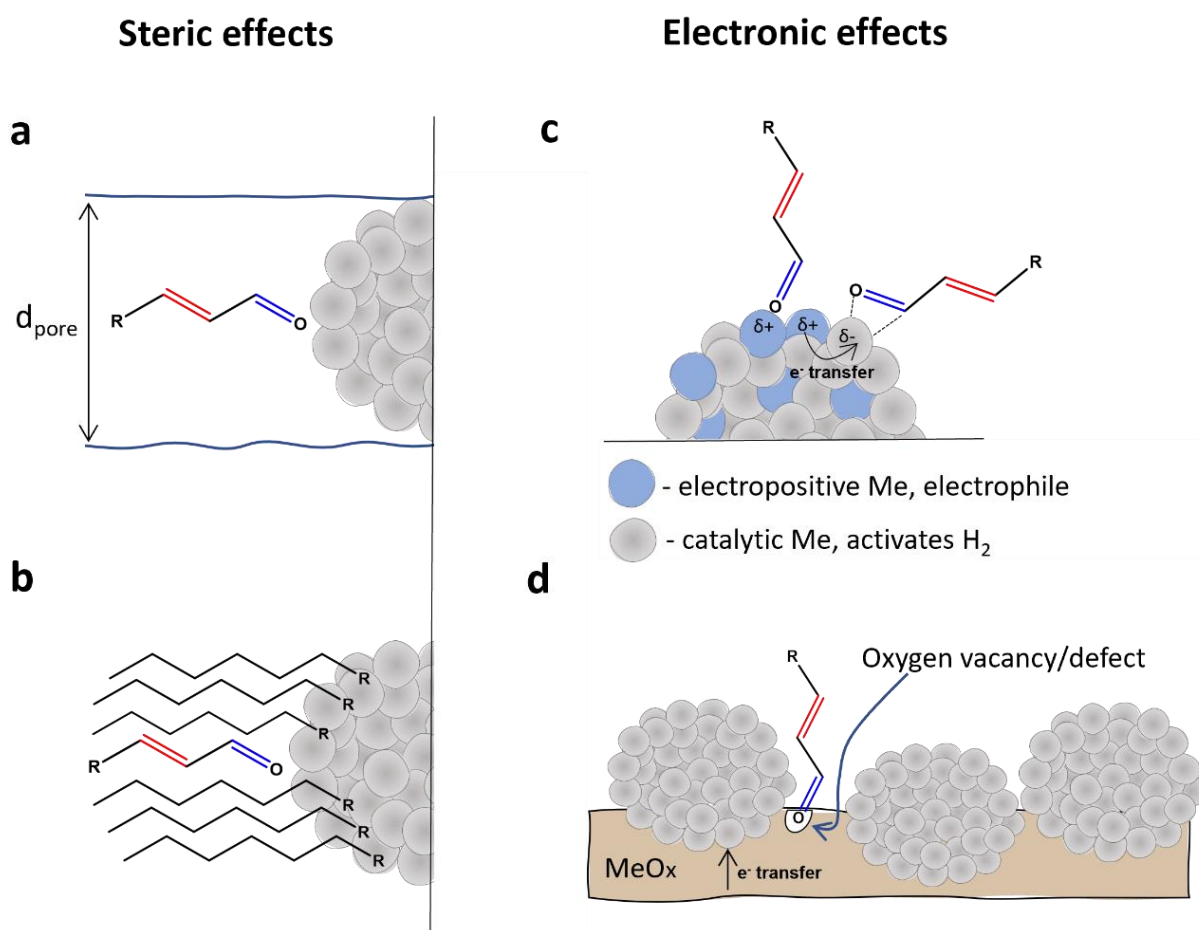


Figure 2.1.1 Strategies for C=O adsorption; a) NPs confinement; b) ligand steric effect; c) bimetallic NPs, two effects: increase of electron density on the active metal, and creation of electrophilic sites; d) reducible metal oxide support, two effects: adsorbs substrate on oxygen vacancies and defects, and donates electron density to the active metal sites.

The most pronounced effect on selectivity comes from electronic modification of the active sites which occurs via electron donation to the catalytic moieties. Few methods to achieve electron-

donation can be applied, such as using an electron-donating support^{165–169}, adding more electropositive metal^{170–172}, or an electron-donating ligand, like it was discussed in Chapter 1.

Creating steric hindrance is another wide-spread strategy of selectivity control. Using NPs confined in porous supports, it is possible to prone hydrogenation of C=O bond of substituted aldehydes^{173–176}. Alternatively, steric hindrance can be created by the ligands which will dictate the adsorption mode of the substrate^{57,177}. In this sense, NPs stabilized with CD molecules are particularly appealing, since catalysis can take place inside the ligand cavity. The formation of inclusion complexes “CD-substrate” induces steric effects as well as ligand-substrate interactions. Also, CD may serve as dispersing or mass transfer agent as it was presented in Chapter 1.

In addition to these general effects that in theory are characteristic for any NP-CD system, CD functionalized with thiol groups (CD-SH) should strongly interact with metal NPs. First reports of NP-CD-SH systems mainly described the complexation behavior of the systems^{178,179}. Further, the NPs stabilized with CD-thiols proved to be active in hydrogenation and C-C coupling reactions^{180–182}. In the work of Mhadgut and colleagues the benefits of phase-transfer and cavity effects of CD were reported for catalytic hydrogenation¹⁸³. They synthesized Pd NPs stabilized with per-6-thio- β -CD and compared their activity with Pd black in ethanol and in water. While in ethanol activity of Pd black in isophorone hydrogenation was higher, in water Pd-CD-SH outperformed the commercial catalyst. Authors explained it by efficient phase-transfer of the substrates to the NP-CD-SH systems.

Our collaborator, Dominique Armspach and colleagues investigated properties of CD-SH in solution and on Au surfaces¹⁸⁴. They found that the binding constant of the substrates and the CD on the Au surface is higher than in the solution. We expect that this increase of binding strength can possibly direct the substrates to the cavity rather than to the CD-free surface of the NPs which consequently influence the selectivity of the reaction. Inspired by the promising results with NP-CD-SH systems, we decided to form NPs applying CD-monothiol and CD-dithiol as stabilizers. All the cyclodextrins used in the study were kindly provided by our collaborators – Dominique Armspach and Sebastian Jung from Strasbourg University. In these systems we expected covalently grafted CD-monothiol molecules to have more motion freedom on the surface of the NP, whereas two thiol functions on CD could induce stronger “face-on” coordination of the CD, which is essential to benefit from the selectivity provided by the hydrophobic cavity. Moreover, in these systems, electron effects might appear due to possible strong interactions between sulfur of the CD and Pt. Thus, our idea was to use CD-thiol as a stabilizing agent in the synthesis of NPs that show high performance

in hydrogen activation (Pt, Ru) in order to achieve a selective catalyst stabilized with a small amount of a CD-SH.

2.1.1. General synthetic procedure for the Pt-CD systems

The synthesis of Pt-CD NPs was performed by decomposition of a platinum precursor with hydrogen gas in the presence of the required amount of ligand. Two Pt precursors, Pt(nbe)₃ (platinum (0) tris(norbornene)) and Pt₂(dba)₃ (diplatinum(0) tris(dibenzylidene acetone)), were tested to prepare the NPs. In these complexes, Pt is already in atomic state and the ligands weakly coordinate to the metal, so the complexes can be decomposed using mild reducing agents like H₂. Regarding the ligand choice, we used five functionalized cyclodextrins with different size of the ring (α or β) and functionalization degree (no SH, mono-SH, di-SH) (Figure 2.1.2). The amount of the CD itself with respect to the total platinum amount was also varied in order to find materials that met our requirements, which were: solubility in water and stability on air, high activity and selectivity in catalysis, recyclability.

A general scheme of the synthesis is illustrated on the Figure 2.1.3. Solutions of Pt(nbe)₃ or Pt₂(dba)₃ and CD solutions were prepared in THF and mixed in a Fisher-Porter bottle inside the glovebox. In the case of Pt(nbe)₃, after adding the ligand, the color of the Pt precursor solution changed from pale brown – almost colorless – to light-orange, indicating the beginning of the decomposition of the platinum precursor. Right after the addition, the solution was taken out of the glovebox and charged with 3 bar of H₂. A color change from orange to black was observed within the first minute. With Pt₂(dba)₃ the color of the solution has changed from dark-violet to black in one minute after H₂ addition. The solution was left stirring at room temperature for 18 h, to complete the reaction. Later, it was washed with pentane to remove ligands and was dried under vacuum at room temperature. Black powders were obtained with all the CDs tested conditions except for **Pt-0.05b2** (appearance as a sticky oily solid) and **Pt-0.5bMe**. In the latter case, after H₂ addition to the solution of Pt(nbe)₃ and **bMe**, a black precipitate of bulk platinum was formed, indicating that 0.5 equivalent (eq) of beta-CD-perMe cannot provide an efficient stabilization for NPs, in agreement with literature results⁹¹. Initially, **b2** was chosen to test the influence of the ligand amount on the size and the catalytic properties of Pt NPs. The choice of **b2** was based on the hypothesis that the bigger size of the ring of beta-CD will allow to host bigger molecules, such as substituted aromatics, and two thiol groups will allow a strong “face-on” coordination to the NP (Figure 2.1.4).

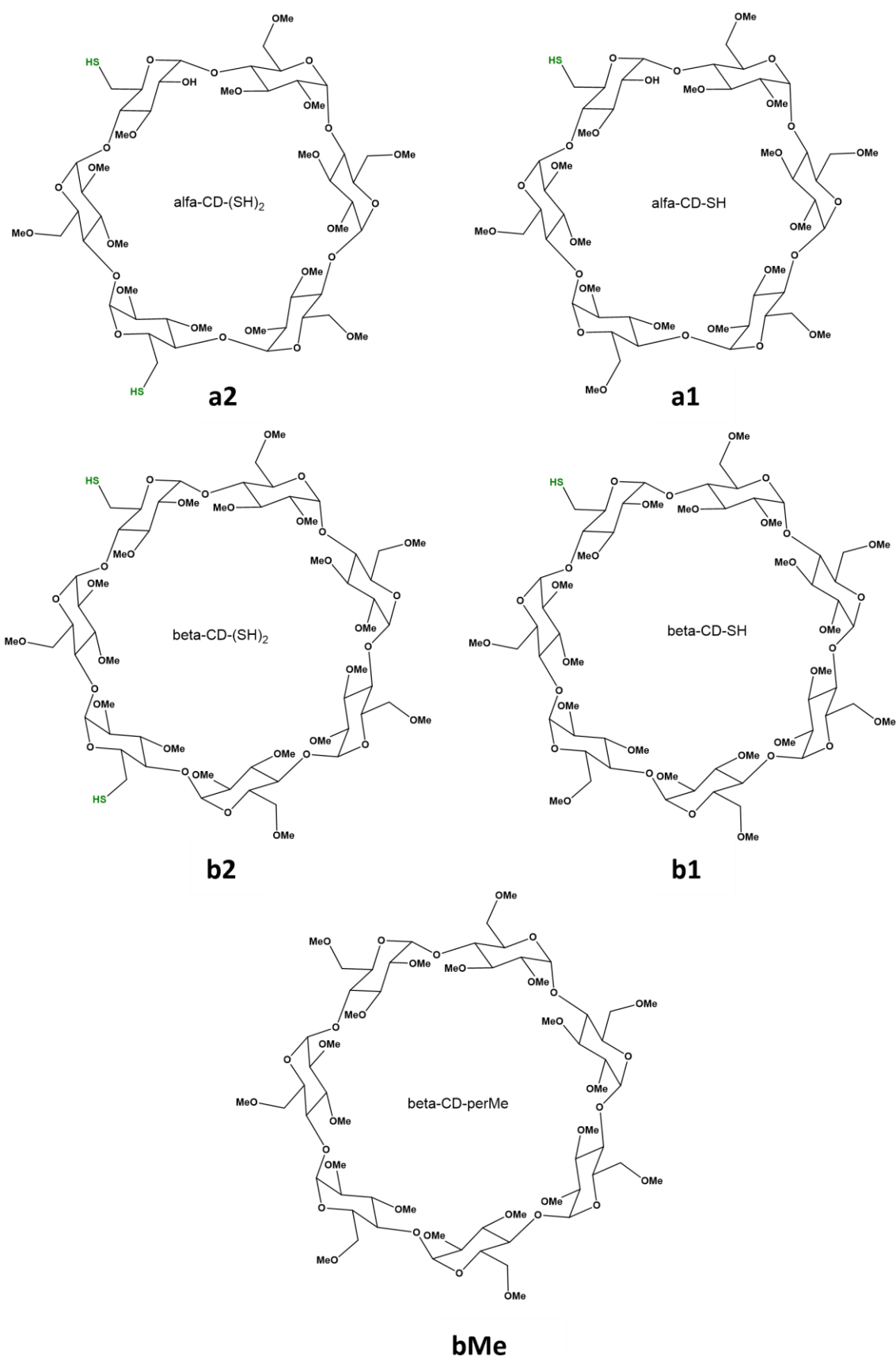


Figure 2.1.2 Structures of the CDs used in the study, with abbreviations.

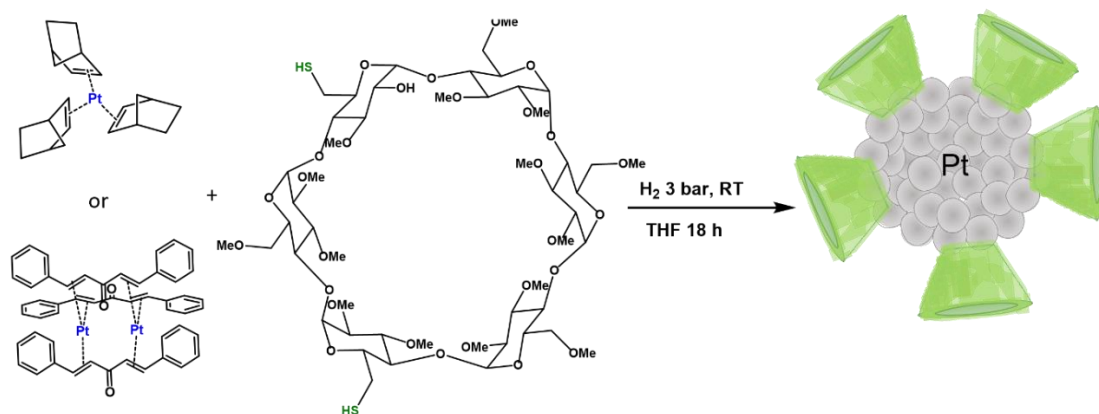


Figure 2.1.3 Scheme of the synthesis of Pt-CD NPs, example with **b2**.

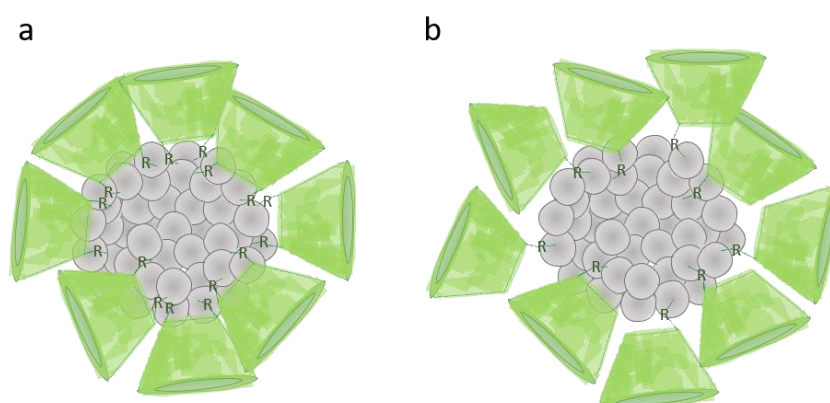


Figure 2.1.4 Illustration of a) more rigid face-on configuration of CD-di-SH on the surface of NP; b) different configuration modes of CD-mono-SH on the surface of NPs.

2.1.2. Pt-**b2** catalyst: optimization of the synthetic procedure

2.1.2.1. Characterization

The average size and dispersion of **Pt-b2** NPs were characterized by TEM (Figure 2.1.5). Well-dispersed small NPs (1-2 nm) were observed in each case confirming a good stabilization of NPs with **b2**. By decreasing the amount of **b2**, we observed a slight increase in NP size, consistent with the literature¹⁸¹. Going from 0.5 eq to 0.1 eq and 0.05 eq of **b2** with respect to the total amount of Pt size of NPs increased from 1.1 nm to 1.6 nm to 2.0 nm. Change of Pt precursor from $\text{Pt}_2(\text{dba})_3$ to $\text{Pt}(\text{nbe})_3$ did not influence the size of the NPs (Figure 2.1.5).

To find out the nature of interaction between Pt and CD, ^1H NMR and diffusion-ordered NMR spectroscopy (DOSY) analyses were performed. On ^1H NMR spectrum of **Pt-0.1b2** (Figure 2.1.6) we could observe a broadening of the CD peaks, which is commonly attributed to lower mobility of the molecules which are close to NPs. The broadening was still present on the spectrum of **Pt-0.5b2**; however, the appearance of sharper peaks in addition to the wide ones indicated that there were unbonded CDs. On the spectrum of **Pt-0.5b2** in the 2.7 ppm, 2.9 ppm, and 7.2 ppm we also observed

protons which correspond to the benzyl acetone ligand from the $\text{Pt}_2(\text{dba})_3$ precursor which was not completely removed by washing with pentane. Other sharp peaks present on the three spectra belong to solvents.

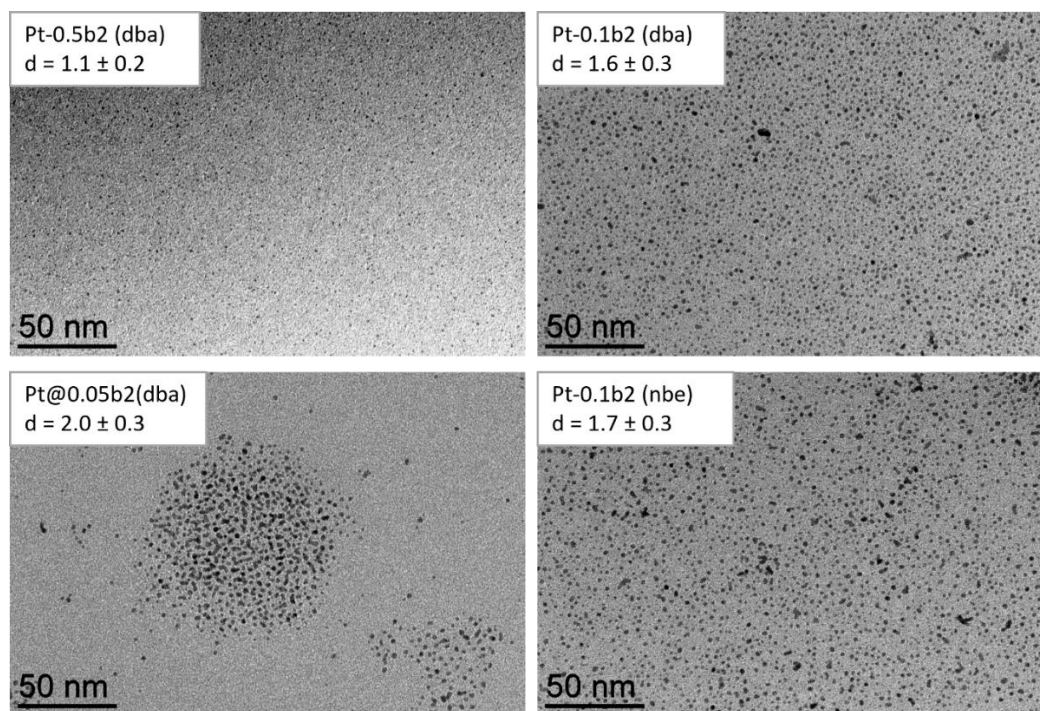


Figure 2.1.5 TEM images of **Pt-b2** NPs, varying the CD relative amount and the nature of the Pt precursor.

A DOSY experiment can be presented as a 2D spectrum with ^1H spectrum on X axis and a logarithm of diffusion coefficient on Y axis. Since a diffusion coefficient depends on the size of the object (Equation 2.1), it is possible to distinguish NMR signals of the free CD and of the one attached to the NP surface.

$$D = \frac{kT}{6\pi\eta r}, \quad (2.1)$$

where k - Boltzman constant, T - absolute temperature, η - viscosity of the medium, r - radius of the molecule.

On the Figure 2.1.7 spectra of **b2**, **Pt-0.1b2**, and **Pt-0.5b2** are present. From this experiment we could extract diffusion coefficients for **b2** ($D=6.9 \times 10^{-10} \text{ m}^2/\text{s}$), and **Pt-0.1b2** ($D=2.9 \times 10^{-10} \text{ m}^2/\text{s}$). The signal of **Pt-0.5b2** had contributions of two populations of **b2**: free and grafted **b2**. Thus, in **Pt-0.5b2** system CD was in excess. On the spectrum of **b2** we could also see a population of bigger size which might correspond to a dimer of the CD with 2 intramolecular disulfide bridges¹⁸⁵.

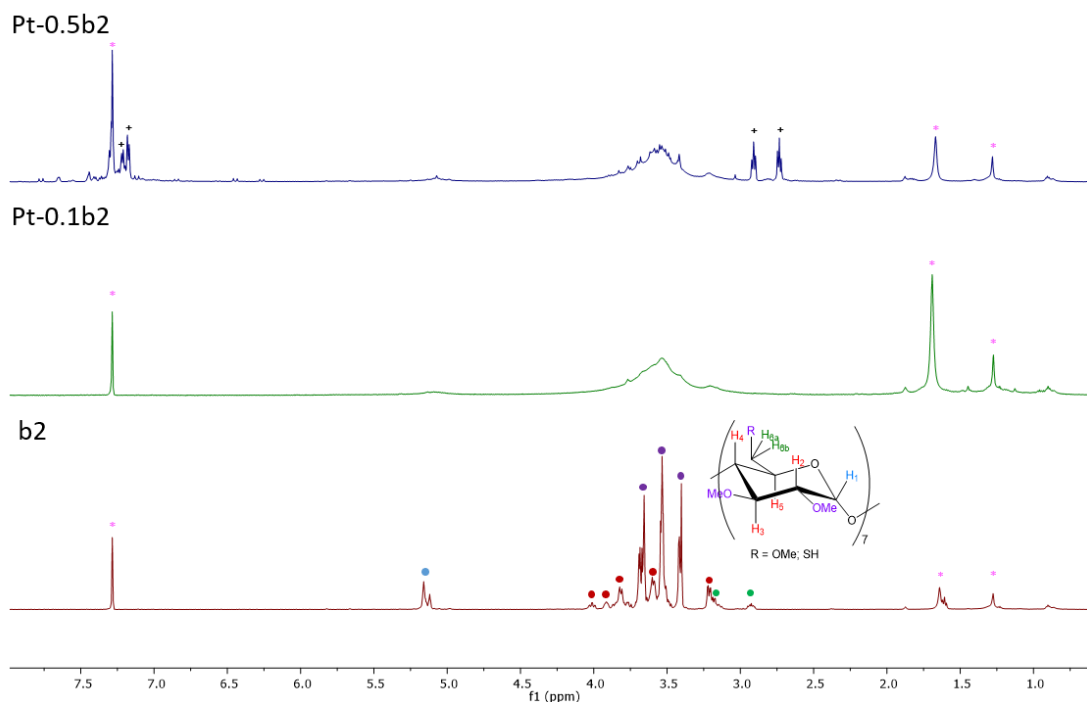


Figure 2.1.6 ^1H NMR spectra of free **b2**, **Pt-0.1b2** NPs, and **Pt-0.5b2** NPs. The balls indicate signals of the CD, the pink asterisks indicate the solvent signals, the black pluses indicate a benzyl acetone contamination.

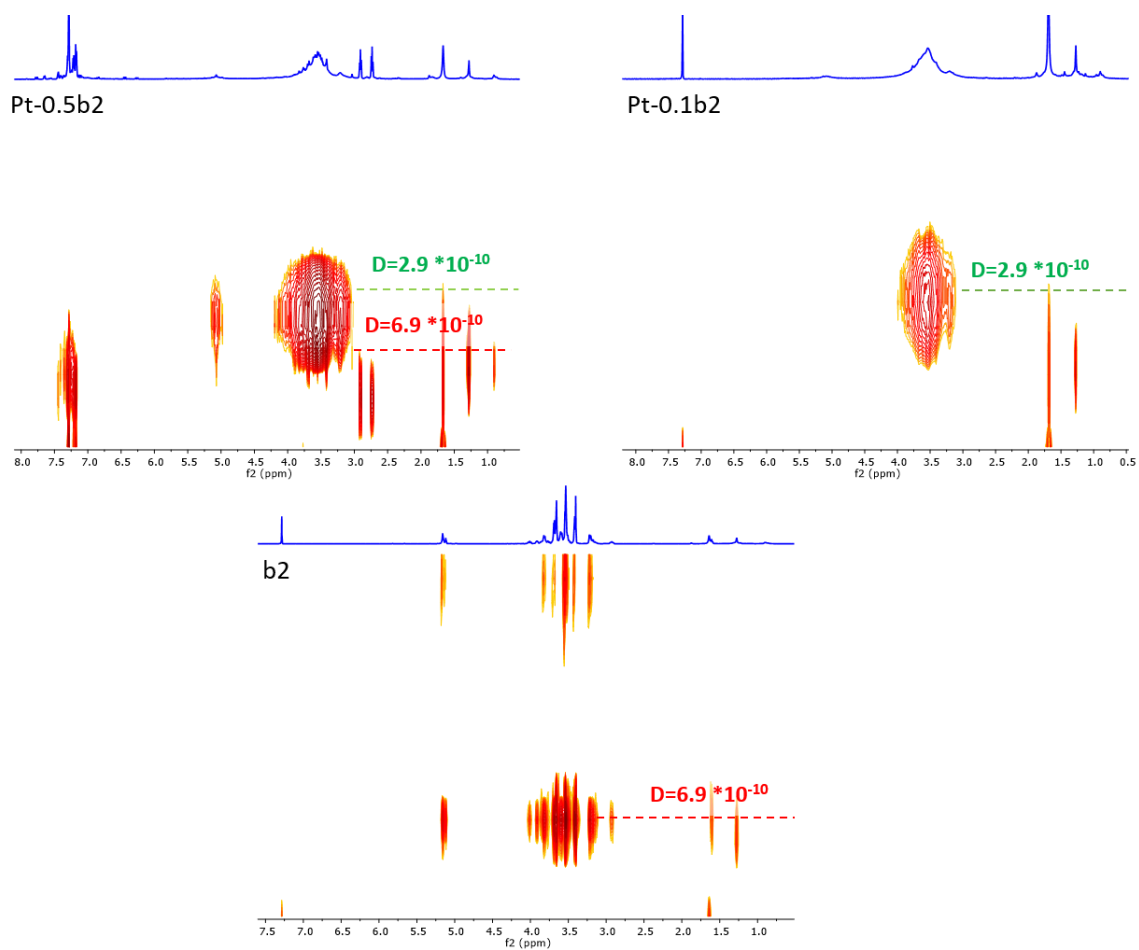


Figure 2.1.7 2D DOSY spectra of **b2**, **Pt-0.1b2** NPs, and **Pt-0.5b2** NPs with diffusion coefficients.

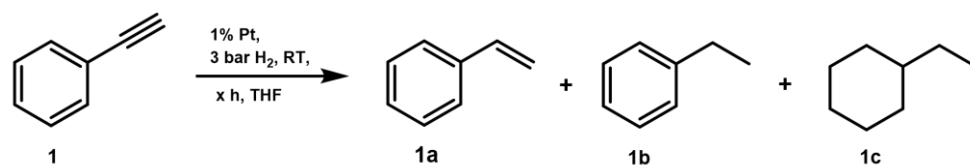
2.1.2.2. Catalytic performance

To probe the catalytic activity of Pt-CD systems, phenylacetylene (**1**) hydrogenation reaction was used. Depending on the selectivity of the catalytic system, the possible products include styrene (**1a**) where triple bond is hydrogenated to double, ethylbenzene (**1b**) where double bond becomes saturated, or completely hydrogenated product – ethylcyclohexane (**1c** - Table 2.1.1). The selectivity of this reaction towards partially saturated products **1a** and **1b** is often explained by steric^{186,41} or electronic properties of the catalyst surface. Interestingly, while in many cases selectivity towards alkene is ascribed to the electron enrichment of the surface^{42,187} in other papers high selectivity was achieved with more electron-withdrawing ligands like thiols¹⁸⁸ or carboxylic acids¹⁸⁹.

In our case steric effects of the CD ring may dictate the selectivity of catalysis. With Pt-CD systems, we expect that hydrogenation happens when the molecule is confined in space inside the cyclodextrin ring. In this way the substrate cannot be adsorbed on the Pt surface via aromatic ring due to the cavity size, so the ring must stay unhydrogenated. However, we found that **Pt-b2** systems were poorly soluble in water, so preliminary catalytic tests with Pt-CD materials were done in THF. In this case, we should consider that catalysis does not necessary take place in the cavity of the cyclodextrin since THF is more lipophilic than water and thus complexation of an organic substrate of CD will be less energetically beneficial in organic medium than in water.

In hydrogenation of the substrate **1** using **Pt-0.05/0.1/0.5b2(dba)** (Table 2.1.1, run 1-11 we found that **1b** was the main product. However, the activity was higher when using NP stabilized with lower amount of the ligand, even though the NP size increased thus leading to less surface for a same mass of NP. Precisely, using **Pt-0.5b2(dba)** after 1h of the reaction, conversion was as low as 10% while full conversion was observed with **Pt-0.1b2(dba)** and **Pt-0.05b2(dba)**. We relate this increase in activity to steric hindrance created with more CD molecules as well as to possible poisoning of active platinum sites with strongly coordinating thiol **b2** ligand¹⁸⁸. In the same table the results of the catalytic test performed with **Pt-0.1b2** synthesized from Pt(nbe)₃ precursor are present (Table 2.1.1 run 12-15). Catalytic activity of **Pt-0.1b2(nbe)** was higher than of **Pt-0.1b2(dba)** so we kept Pt(nbe)₃ precursor for further syntheses.

Table 2.1.1 Hydrogenation of phenylacetylene with Pt-CD catalyst.

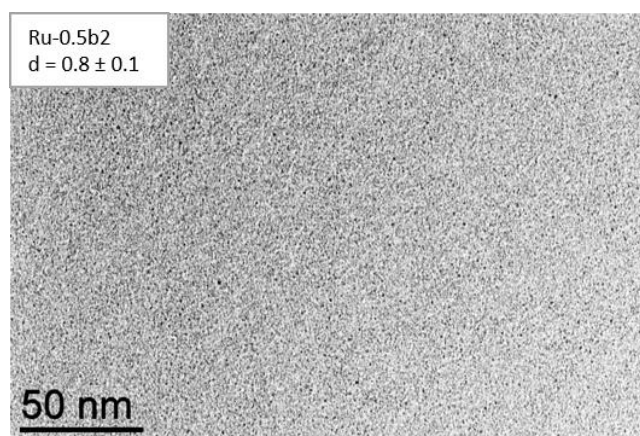


Run	Catalyst	t, h	X (%)	Y 1a (%)	Y 1b (%)	Y 1c (%)
1	Pt-0.05b2(dba)	0.5	100	34	66	0
2		1	100	0	98	2
3		5	100	0	97	3
4		24	100	0	94	6
5	Pt-0.1b2 (dba)	0.5	67	55	12	0
6		1	100	0	99	1
7		5	100	0	99	1
8		24	100	0	98	2
9	Pt-0.5b2(dba)	1	10	7	3	0
10		5	40	32	8	0
11		24	100	0	100	0
12	Pt-0.1b2(nbe)	0.5	100	49	51	0
13		1	100	0	99	1
14		5	100	0	99	1
15		24	100	0	97	3

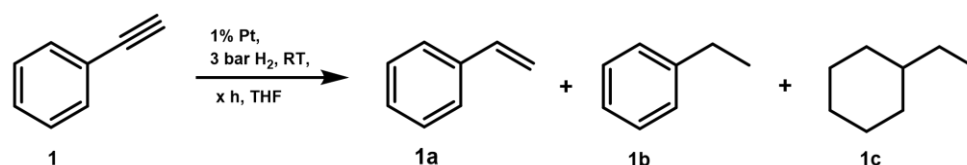
Reaction conditions: Catalyst (0.01 mmol Pt), substrate (1 mmol, 100 eq.), solvent (THF 2 mL), H₂ (3 bar), RT. Yield is determined as an average of two runs by GC-FID using dodecane as an internal standard. X = conversion; Y = yield.

2.1.2.3. Comparison with Ru-0.5b2

For comparison, Ru NPs were synthesized, since ruthenium is another active metal in catalytic hydrogenation which in some cases, is preferential to platinum due to its lower cost. **Ru-0.5b2** NPs were synthesized using the procedure similar to the one used for Pt-CD systems starting from Ru(COD)(COT) ((1,5-cyclooctadiene)(1,3,5-cyclooctatriene) ruthenium(0)) (**Ru-0.5b2**). NPs were extremely small – around 0.8 nm (Figure 2.1.8).

Figure 2.1.8 TEM image of **Ru-0.5b2**.

Catalytic performance of **Ru-0.5b2** NPs was lower than that of **Pt-0.5b2** (Table 2.1.2). In agreement with observations made for **Pt-0.05/0.1/0.5b2** series, since the size of **Ru-0.5b2** is even smaller, poisoning and steric effects could play even bigger role and cause the decrease in the activity. Interestingly, after 24h of reaction we found 70% of the product **1a** at 91% of conversion, meaning that hydrogenation of triple bond proceeded faster than of double bond. The selective hydrogenation towards product **1a** would be worth further investigation. Unfortunately, the catalytic performance of the NPs was not reproducible from batch to batch, so we decided to focus on development of the Pt catalyst.

Table 2.1.2 Comparison of activity of **Pt-0.5b2** and **Ru-0.5b2** in hydrogenation of **1**.

Run	Catalyst	t, h	X (%)	Y 1a (%)	Y 1b (%)	Y 1c (%)
1	Pt-0.5b2(dba)	1	10	7	3	0
2		5	40	32	8	0
3		24	100	0	100	0
4	Ru-0.5b2	1	7	6	1	0
5		5	24	20	4	0
6		24	91	70	21	0

Reaction conditions: Catalyst (0.01 mmol Pt), substrate (1 mmol, 100 eq.), solvent (THF 2 mL), H₂ (3 bar), RT. Yield is determined as an average of two runs by GC-FID using dodecane as an internal standard.

2.1.3. Pt-0.5CD catalysts: biphasic catalysis

2.1.3.1. Characterization

Having the synthetic procedure and preliminary tests with **Pt-b2**, other CD were used to obtain Pt NPs. Pt NPs with **a1**, **a2**, and **b1** CDs starting from $\text{Pt}(\text{nbe})_3$ precursor were synthesized, fully characterized and compared to Pt NPs with **b2**. To ensure that all the surface of the NP is completely covered with ligands the ratio $\text{Pt}/\text{CD}=1/0.5$ was chosen in agreement with NMR DOSY results for **Pt-0.5b2**. One should notice that the present series were made with the $\text{Pt}(\text{nbe})_3$ precursor, whereas it is compared with **Pt-0.5b2(dba)**. **Pt-0.5b2(nbe)** was unfortunately not synthesized because of a lack of the **b2** precursor. An average size and dispersion of the NPs was characterized with TEM (Figure 2.1.9). Neither the size of CD ring nor the functionalization degree of the CD changed the size of NPs.

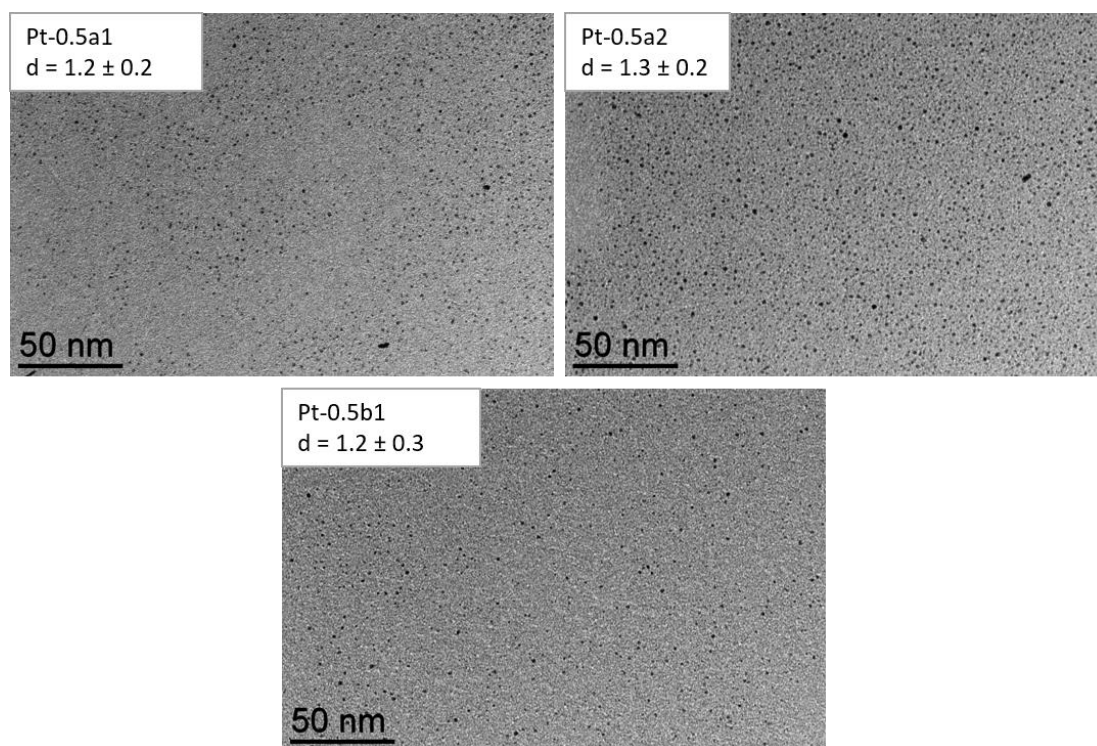


Figure 2.1.9 TEM images of **Pt-0.5CD**.

ATR-FTIR spectroscopy (attenuated total reflection - Fourier-transform infrared spectroscopy) of the samples after CO adsorption was performed. IR study of CO adsorption is a popular tool to investigate electron density correlations on the surface. This analysis is based on the interaction of CO with metal surface atoms. There, CO forms σ -bond with metal atom(s), and metal interacts with CO by π -backdonation from the partially filled d-orbitals. π -backbonding stabilizes Pt-C bond and destabilizes C-O bond due to the increase of electron density on CO antibonding orbitals. These interactions result in decrease in energy (wavenumbers) of CO absorption band.

Consequently, the more electron-rich is the surface, the stronger is π -backdonation and the lower is stretching frequency of CO vibration. In Figure 2.1.10 Pt-CD spectra are demonstrated together with reference spectrum of naked Pt NPs which were synthesized as described in the Chapter 4. On the spectrum of naked Pt NPs, we could see an intense vibration at 2042 cm^{-1} that is commonly attributed to CO adsorbed in linear mode, whereas absorption bands at 1889 and 1809 cm^{-1} were attributed to CO adsorbed in bridged mode^{190,191}. In the case of **Pt-0.5CD** materials the characteristic vibrations of the CD ring together with a CO vibration were observed. Precisely, a broad peak at $2925\text{-}2850\text{ cm}^{-1}$ belongs to C-H stretch of CH_3 and CH_2 groups, a band at 1352 cm^{-1} could be attributed to the bending vibration of CH_3 group of a CD, a broad intense absorption peak at $1030\text{-}1100\text{ cm}^{-1}$ evidences C-C and C-O stretch vibrations. No SH absorption band which is usually located at $2600\text{-}2550\text{ cm}^{-1}$ was found, even for free CD molecules. However, it is a common observation for thiol molecules, since this vibration is very weak. Finally, the vibration of CO adsorbed in linear mode was found in all the samples. It was located at 2042 cm^{-1} for **Pt-0.5a1**, at 2040 cm^{-1} for **Pt-0.5a2**, and at 2040 cm^{-1} for **Pt-0.5b1**. Almost no shift of CO vibration indicated that no strong ligand-induced electronic effects occurred at the surface of Pt NPs. The absorption bands of bridged CO molecules were less pronounced in case of Pt-CD samples than the ones on the spectrum of the naked Pt. Since bridged CO is a common adsorption mode on planes, the decrease of the intensity of a bridged CO band suggests that the terrace sites on **Pt-0.5CD** NPs were less accessible to CO due to the coordination of the CD.

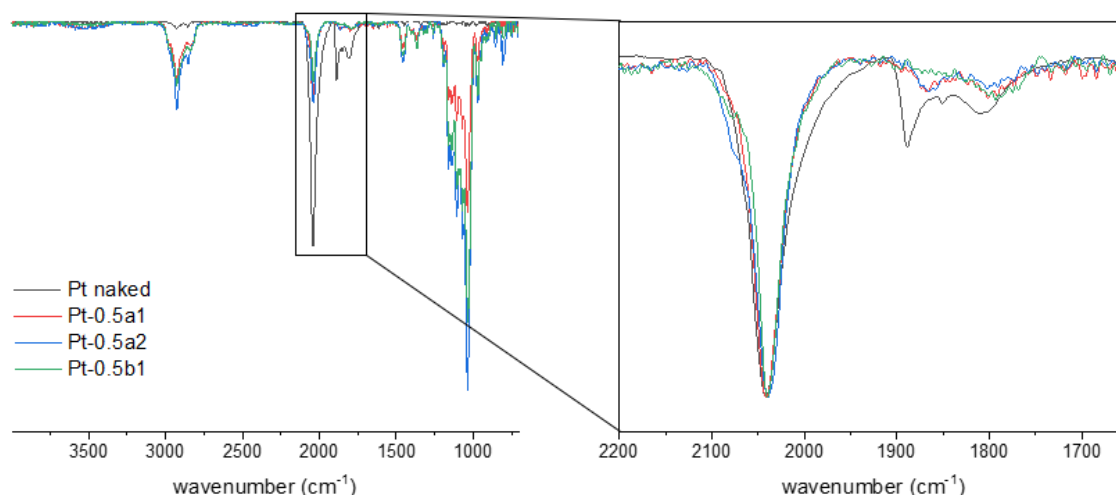


Figure 2.1.10 ATR-FTIR spectra of **Pt-0.5CD** with zoom at absorption bands of CO adsorbed in linear and bridged modes.

XRD analysis was conducted with **Pt-0.5a1**, **Pt-0.5a2**, and **Pt-0.5b1** to have an idea about long-order atom arrangement in the NPs (Figure 2.1.11). The samples were measured in powder state on air. The XRD patterns of three NPs look similar. In each of them we observe broadening of

peaks due to the ultra-small size of the NPs. The few wide peaks which were visible confirmed the formation of a Pt-*fcc* structure. However, the pics were not sharp enough to accurately extract crystallite sizes.

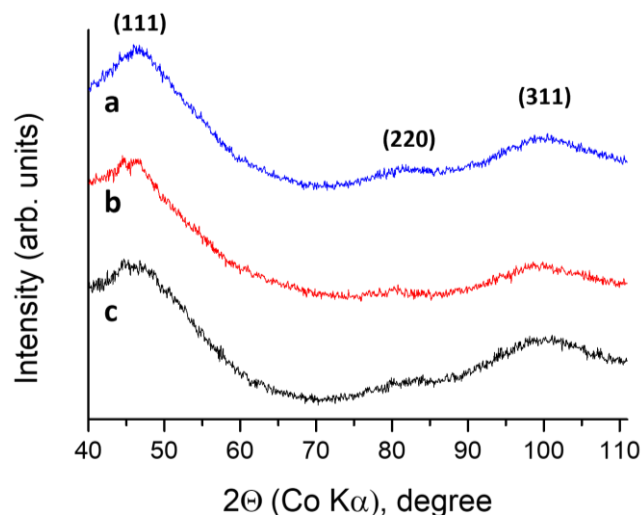
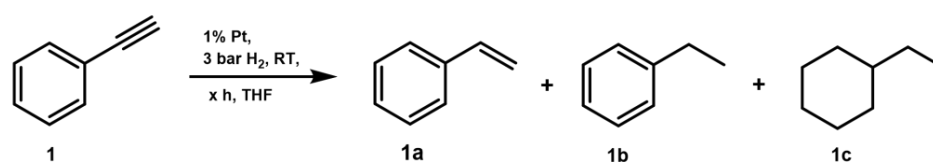


Figure 2.1.11 Diffractograms of a) Pt-0.5a1; b)Pt-0.5a2; c)Pt-0.5b1.

2.1.3.2. Catalytic performance in THF

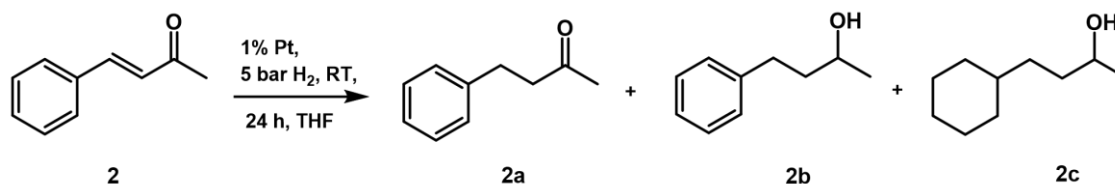
Pt NPs stabilized with CD with different ring size and functionalisation degree were tested in the hydrogenation of **1** (Table 2.1.3). The results of catalysis with **Pt-0.5a1**, and **Pt-0.5b1** (Table 2.1.3 run 1, 2) pointed out that the size of the ring did not influence activity or selectivity of hydrogenation of the substrate **1**. Similarly, the results of catalysis with **Pt-0.5a1**, and **Pt-0.5a2** (Table 2.1.3 run 1, 3) pointed out that the number of thiol moieties did not influence activity or selectivity of hydrogenation in these catalytic conditions. However, we admit that it is difficult to make rational conclusions while obtaining full conversion of the substrate like in this case. At the same time **Pt-0.5b1** showed higher activity than **Pt-0.5b2(dba)** (Table 2.1.3 run 2,4). We assume that lower activity with **b2** ligand may be due to a $\text{Pt}_2(\text{dba})_3$ precursor that was used for the synthesis **Pt-0.5b2(dba)** and due to the dibenzyl acetone that was not removed completely. Considering these results **Pt-b2** NPs were excluded from further investigation.

Table 2.1.3 Hydrogenation of phenylacetylene with **Pt-0.5CD** catalyst.

Run	Catalyst	t, h	X (%)	Y 1a (%)	Y 1b (%)	Y 1c (%)
1	Pt-0.5a1	5	100	0	100	0
2	Pt-0.5b1	5	100	0	99	1
3	Pt-0.5a2	5	100	0	100	0
4	Pt-0.5b2(dba)	5	40	32	8	0

Reaction conditions: Catalyst (0.01 mmol Pt), substrate (1 mmol, 100 eq.), solvent (THF 2 mL), H₂ (3 bar), RT. Yield is determined as an average of two runs by GC-FID using dodecane as an internal standard.

Pt-0.5b1, **Pt-0.5a1**, and **Pt-0.5a2** were tested in hydrogenation of a conjugated ketone – benzylidene acetone (**2**), and its aldehyde analogue – cinnamaldehyde (**3**). In the beginning, tests were performed in THF because of the low solubility of **a2** in water. The results are shown in Table 2.1.4 and Table 2.1.5. Conversion of **2** was complete in 24 h and all the three catalysts showed similar activity and selectivity towards the product **2a** (75 - 79 %). However, a significant amount of **2b** points out that **2a** is not a thermodynamic but rather a kinetic product favored under the chosen reaction conditions.

Table 2.1.4 Hydrogenation of benzylidene acetone with **Pt-0.5CD** catalyst.

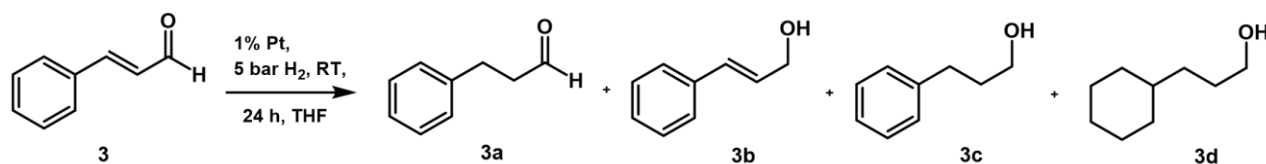
Run	Catalyst	X (%)	Y 2a (%)	Y 2b (%)	Y 2c (%)
1	Pt-0.5a1	100	75	25	0
2	Pt-0.5a2	100	77	23	0
3	Pt-0.5b1	100	79	21	0

Reaction conditions: Catalyst (0.01 mmol Pt), substrate (1 mmol, 100 eq.), solvent (THF 2 mL), H₂ (5 bar), RT, 24h. Yield is determined as an average of two runs by GC-FID using dodecane as an internal standard.

Hydrogenation of **3** went a bit slower and we did not reach a full conversion after 24 h. Both intermediate products **3a** and **3b** were found, together with further hydrogenated product **3c**. Such stepwise hydrogenation with the faster hydrogenation of C=C bond is a typical catalytic behaviour of noble metal NPs¹⁹². Thus, CD did not assist in substrate activation and as a result it was not possible to hydrogenate C=O double bond exclusively. Indeed, since the tests were conducted in

THF we should not expect much of CD-induced selectivity. So, to favor substrate complexation and hydrogenation inside the cavity of CD the water-soluble Pt NPs stabilized by the monofunctionalized CDs a1 and b1 were further used in the catalytic study.

Table 2.1.5 Hydrogenation of cinnamaldehyde with **Pt-0.5CD** catalyst.



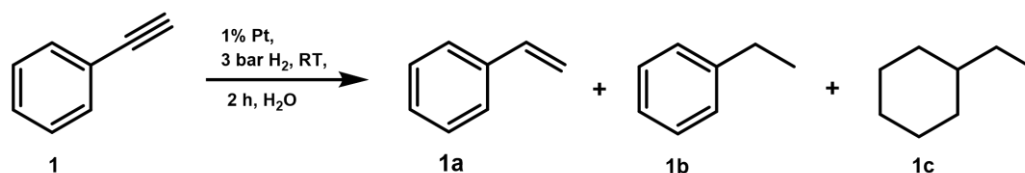
Run	Catalyst	X (%)	Y 3a (%)	Y 3b (%)	Y 3c (%)	Y 3d (%)
1	Pt-0.5a1	71	29	8	34	0
2	Pt-0.5a2	82	29	7	46	0
3	Pt-0.5b1	87	28	10	49	0

Reaction conditions: Catalyst (0.01 mmol Pt), substrate (1 mmol, 100 eq.), solvent (THF 2 mL), H₂ (5 bar), RT, 24h. Yield is determined as an average of two runs by GC-FID using dodecane as an internal standard.

2.1.3.3. Catalytic performance in water

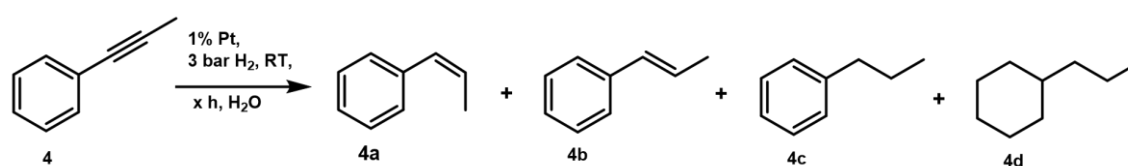
Catalytic performance of Pt NPs stabilized with CD-mono-SH in water was tested in hydrogenation of unsaturated carbon-carbon bonds as well as carbon-oxygen double bonds. Hydrogenation of terminal alkyne **1** and internal alkyne, phenylpropyne (**4**), was complete in 2 h with excellent yields towards phenylalkanes (Table 2.1.6, Table 2.1.7).

Table 2.1.6 Hydrogenation of phenylacetylene with **Pt-0.5CD** catalyst in water.



Run	Catalyst	X (%)	Y 1a (%)	Y 1b (%)	Y 1c (%)
1	Pt-0.5a1	100	0	97	3
2	Pt-0.5b1	100	0	98	2

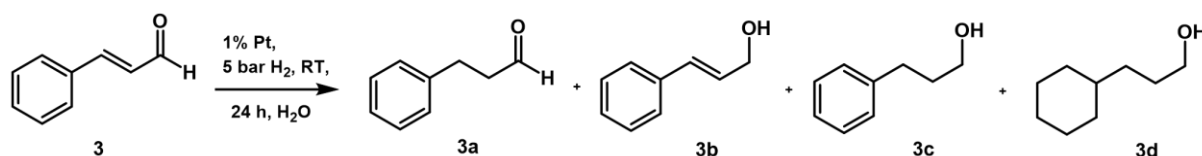
Reaction conditions: Catalyst (0.01 mmol Pt), substrate (1 mmol, 100 eq.), solvent (H₂O 3 mL), H₂ (3 bar), RT. Yield is determined as an average of two runs by GC-FID using dodecane as an internal standard.

Table 2.1.7 Hydrogenation of phenylpropyne with **Pt-0.5CD** catalyst in water.

Run	Catalyst	t, h	X (%)	Y 4a (%)	Y 4b (%)	Y 4c (%)	Y 4d (%)
1	Pt-0.5a1	2	100	0	0	99	1
2	Pt-0.5b1	2	100	0	0	99	1

Reaction conditions: Catalyst (0.01 mmol Pt), substrate (1 mmol, 100 eq.), solvent (H₂O 3 mL), H₂ (3 bar), RT. Yield is determined as an average of two runs by GC-FID using dodecane as an internal standard.

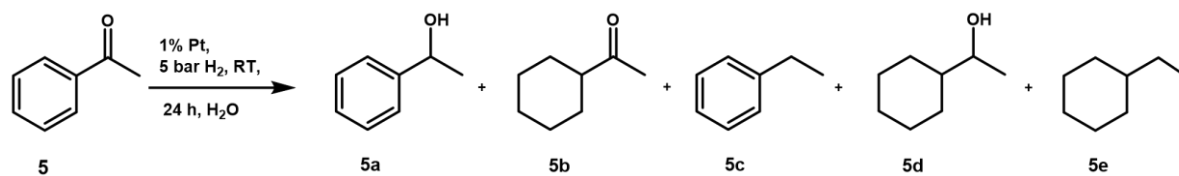
Hydrogenation of cinnamaldehyde proceeded slower in water than in THF (Table 2.1.5, Table 2.1.8). Such behaviour was expected for biphasic system. At those reaction conditions, **3a** was a major intermediate that, together with the minor intermediate **3b**, was slowly transformed in the final product **3c**. No significant catalytic difference was observed between **Pt-0.5a1** and **Pt-0.5b1**. Thus, we can conclude that presence of CD with different size of the cavity on the surface of Pt did not influence the hydrogenation pathway.

Table 2.1.8 Hydrogenation of cinnamaldehyde with **Pt-0.5CD** in water.

Run	Catalyst	X (%)	Y 3a (%)	Y 3b (%)	Y 3c (%)	Y 3d (%)
1	Pt-0.5a1	53	38	7	9	0
2	Pt-0.5b1	47	37	4	7	0

Reaction conditions: Catalyst (0.01 mmol Pt), substrate (1 mmol, 100 eq.), solvent (H₂O 3 mL), H₂ (5 bar), RT. Yield is determined as an average of two runs by GC-FID using dodecane as an internal standard.

Hydrogenation of acetophenone (**5**) was performed as well (Table 2.1.9). At almost full conversion the major product was **5a**, where C=O bond was hydrogenated. However, product **5b** was also detected, which indicates a parallel hydrogenation of benzene ring, although it proceeds slower than the C=O hydrogenation, in accordance with literature⁹¹. After the extraction of products, the catalysts in water phase were reused (Table 2.1.9 run 2, 4). Similar activity and selectivity were observed with the reused catalyst, which points out their stability.

Table 2.1.9 Hydrogenation of acetophenone with **Pt-0.5CD** in water (with recycling).

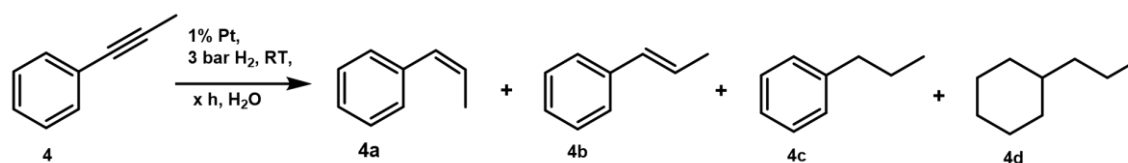
Run	Catalyst	X (%)	Y 5a (%)	Y 5b (%)	Y 5c (%)	Y 5d (%)	Y 5e (%)
1	Pt-0.5a1	93	73	8	1	10	1
2 ^a		97	73	11	3	8	3
3	Pt-0.5b1	92	64	16	1	8	2
4 ^a		99	70	11	5	9	4

a: recycled catalyst. Reaction conditions: Catalyst (0.01 mmol Pt), substrate (1 mmol, 100 eq.), solvent (H₂O 3 mL), H₂ (5 bar), RT. Yield is determined as an average of two runs by GC-FID using dodecane as an internal standard.

2.1.3.4. Influence of an inhibitor and of an extra amount of **b1**

Since catalysis in water did not result in increased selectivity, it raised a question where the reaction takes place: inside or outside the CD cavity. If hydrogenation proceeds exclusively while the product was inside the cavity, then blocking of the cavity with stronger coordinating molecule would result in a complete shutdown of the reaction. To perform this test, an adamantanol was chosen since adamantane derivatives are known to form strong inclusion complexes with CD¹⁹³. **Pt-0.5b1** NPs were stirred during 1 h together with 5 eq. of adamantanol with respect to the calculated CD amount. Then, substrate **4** was added and reaction was conducted under usual conditions (Table 2.1.10 run 2). The same test was done without the inhibitor molecule (Table 2.1.10 run 1). We observed only a small decrease in conversion from 56 % to 43 %, and not a full inhibition, indicating that hydrogenation could take place both inside and outside the cavity.

In some papers a “shuttle” effect of CD was observed when working in an excess of CD⁹⁵. In these conditions, free CD can form an inclusion complex with a substrate and transfer it to the surface of NPs. An improved mass transfer then results in higher conversions. Thus, in the hydrogenation of **4**, **Pt-0.5b1** catalyst and 4.5 eq of **b1** with respect to the Pt amount were added and the reaction was conducted as usually. Results (Table 2.1.10, run 3) revealed that with a higher amount of CD, the conversion appeared to be lower, contrary to the literature results. This difference may be caused by the structure of the CD. In our case, strong coordination through the thiol moiety may poison the catalyst, so the addition of the extra **b1** molecules may result in a decrease of the activity of the nanoparticles. In addition, shuttle effect occurs due to fast exchange of adsorbed CD with CD in solution. However, in our case, thiol moieties may slow down such exchange and it will hamper the shuttle effect.

Table 2.1.10 Influence of addition of the inhibitor and b1 on hydrogenation of phenylpropyne with **Pt-0.5b1** catalyst in water.

Run	Remarks	t, h	X (%)	Y 4a (%)	Y 4b (%)	Y 4c (%)	Y 4d (%)
1	-	1	56	32	6	18	0
2	Adamantanol	1	43	16	4	24	0
3	4.5 eq of b1	1	42	25	5	12	0

Reaction conditions: Catalyst (0.01 mmol Pt), substrate (1 mmol, 100 eq.), solvent (H₂O 3 mL), H₂ (3 bar), RT. Yield is determined as an average of two runs by GC-FID using dodecane as an internal standard.

2.1.4. Pt-b1 catalyst: influence of the ligand ratio on the catalytic activity

2.1.4.1. Characterisation

The results of the previous part pointed out that CD served only as a stabilizing agent for Pt-NP. More precisely, it helps to control the size of the NPs by adjusting the ratio Pt:CD, it enables solubility in water of the catalyst. However, it does not influence on the selectivity in alkynes hydrogenation towards alkenes or in conjugated aldehydes hydrogenation towards unsaturated alcohols. Thus, we decided to optimize our system and develop the catalyst with a ratio of Pt:b1 that will have the highest activity together with a preserved stability in water.

In addition to **Pt-0.5b1**, Pt NPs stabilized with 0.2, 0.1, and 0.05 eq of **b1** were synthesized and characterized. The size of the NPs increased with the decrease of **b1** amount, as it was observed for the **Pt-b2** systems (Figure 2.1.12). Here, going from 0.5 to 0.1 eq of CD, the size of the NPs increased from 1.2 to 1.6 nm. By further decreasing the CD amount to 0.05 eq, coalescence of nanoparticles was observed due to a too low amount of the stabilizer (Figure 2.1.12). These nanoparticles were also less dispersed in water than the ones with more ligand.

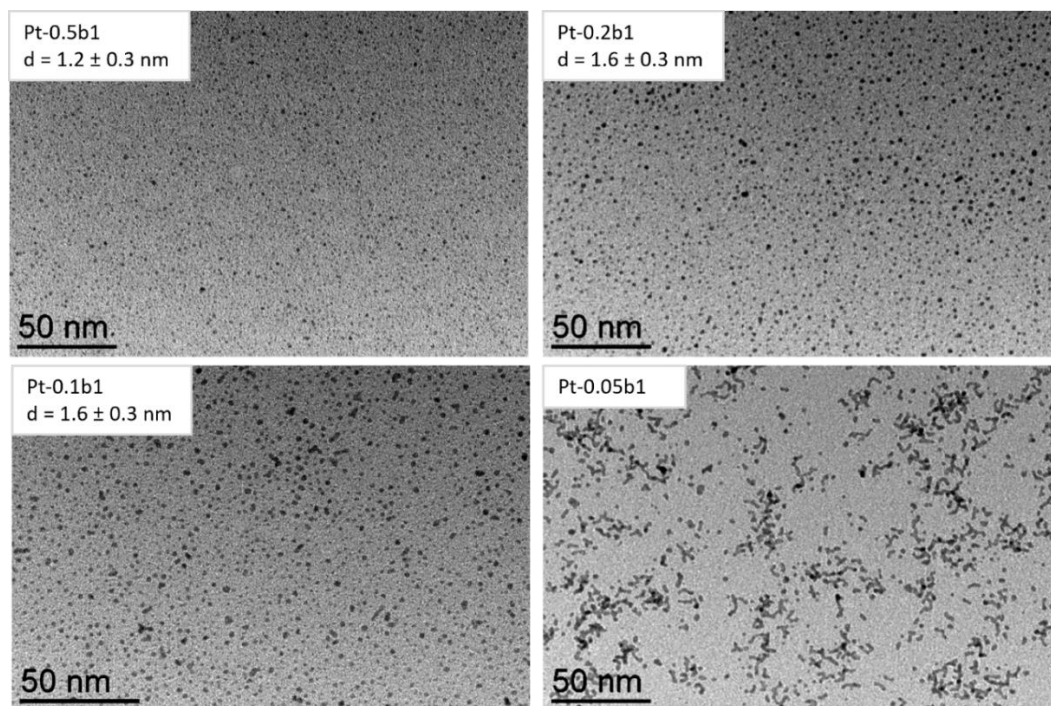


Figure 2.1.12 TEM images of **Pt-b1** NPs.

Powder XRD analysis was performed for **Pt-0.05b1**, **Pt-0.1b1**, and **Pt-0.5b1** NPs (Figure 2.1.13). As expected, the peaks became more pronounced with the size increase, and for **Pt-0.1b1** and **Pt-0.05b1** samples, it was possible to attribute the signals to a Pt-*fcc* structure. The crystallite sizes of **Pt-0.1b1** and **Pt-0.05b1** were determined by the Scherrer formula and were found to be equal to 1.6 nm and 1.4 nm respectively. The accordance with the size measured by TEM confirms the monocrystallinity of the NPs.

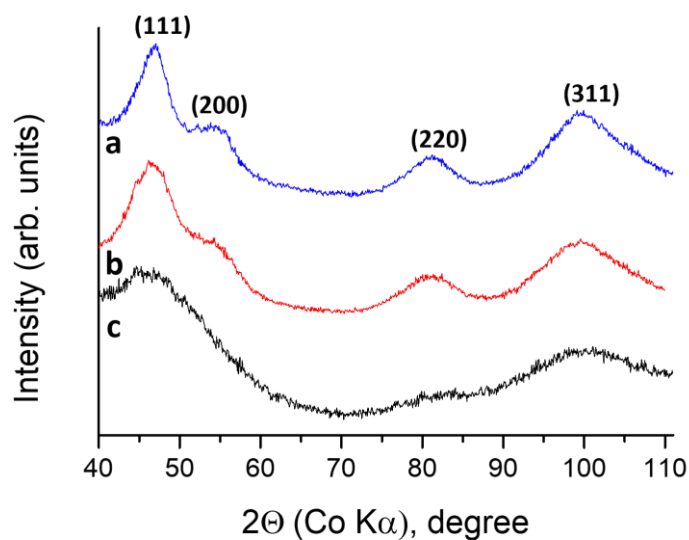


Figure 2.1.13 XRD patterns of a) **Pt-0.05b1**; b) **Pt-0.1b1**, and c) **Pt-0.5b1** NPs.

TGA of the samples was in a good agreement with the expected loading. A little higher experimental Pt loading than calculated may indicate a partial removal of CD ligands during the washing step (Table 2.1.11).

Table 2.1.11 TGA results of platinum loading.

Catalyst	w _{TGA} (Pt), %	w _{theor} (Pt), %
Pt-0.5b1	23	22
Pt-0.2b1	42	41
Pt-0.1b1	62	58
Pt-0.05b1 ^a	ND	74

^a TGA for Pt-0.05b1 failed due to the insufficient amount of the sample.

XPS analysis of the Pt NPs stabilized with 0.05 and 0.5 eq of **b1** was performed to see possible alterations in oxidation states of S and Pt. XPS spectra at the Pt4f edge are presented in Figure 2.1.14 a. Two pairs of doublets were observed. For **Pt-0.5b1** peaks at 71.3 and 74.6 eV were ascribed to the Pt4f core level spectra of Pt⁰, while a doublet with the peaks of 72.4 eV and 75.8 eV corresponded to the Pt4f core level of oxidized Pt attributed to Pt atoms at the NP surface¹⁹⁴. In the case of **Pt-0.05b1** binding energy values were almost the same as for the previous system, 71.3 and 74.7 eV for metallic platinum and 72.4 and 76.4 eV for oxidized platinum. However, the amount of the oxidized part was different in these two systems. Precisely, 40% of oxidized platinum were found in the sample of **Pt-0.5b1** and 23% in the sample of **Pt-0.05b1**. Increase in the amount of oxidized Pt in **Pt-0.5b1** could be ascribed to both the size of the nanoparticles and the amount of CD. **Pt-0.5b1** NPs have smaller size meaning there are more low-coordinated Pt atoms on the surface that can interact with the ligand. From another side, bigger amount of CD leads to more interactions with metal sites. The S2p edge spectra are shown in Figure 2.1.14 b. On the spectrum of **b1** alone two main peaks were found. The signals at 163.1 and 164.3 eV correspond to S2p_{3/2} and S2p_{1/2} in thiol. The small supplementary fraction with signals around 168-169 eV was ascribed to sulfate species, which came from synthesis of the ligand. When moving to the S2p spectrum of **Pt-0.5b1** two signals of lower energy were found, namely peaks at 162.4 and 163.8 eV, which are generally assigned to S2p_{3/2} and S2p_{1/2} of thiols bond to metals¹⁹⁵. By further decrease of the amount of the ligand, the spectrum of **Pt-0.05b1** became noisy; however, S2p peaks at 162.4 and 163.7 eV could be attributed to coordinated thiols, similarly to **Pt-0.5b1**. To sum up, XPS analysis showed that there is an exchange of electron density between platinum and sulfur with possible formation of Pt-S bond.

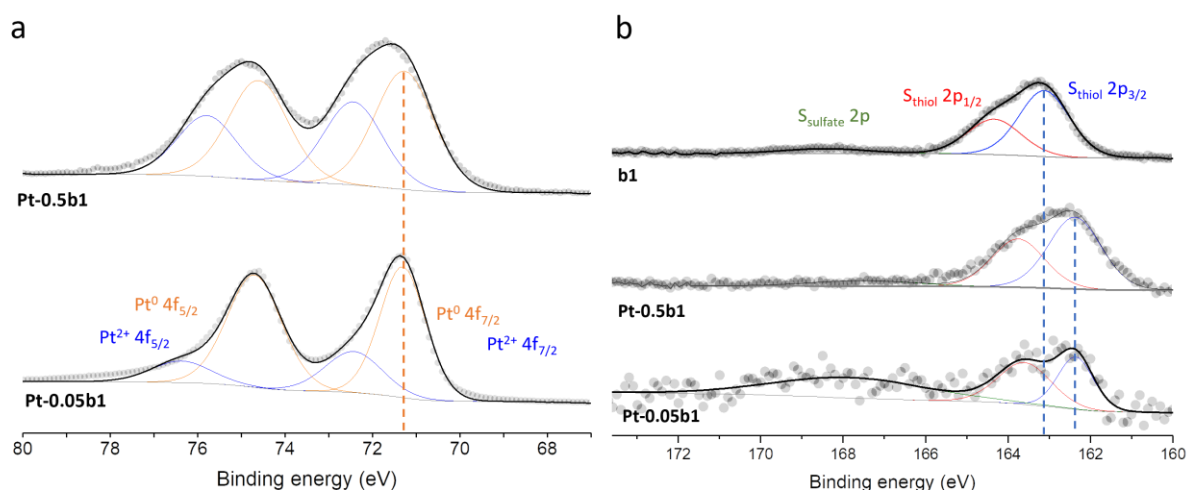


Figure 2.1.14 XPS spectra of **b1**, **Pt-0.05b1**, and **Pt-0.5b1** with zoom at the a) Pt4f edge; b) S2p edge.

^1H NMR and DOSY experiments were conducted with **b1**, **Pt-0.05b1**, and **Pt-0.5b1** samples. On the ^1H spectrum of liquid state NMR, there is a broadening of the CD signals in the region 2.9–4.1 ppm for **Pt-0.05b1**, and **Pt-0.5b1** (Figure 2.1.15). However, sharp peaks were observed together with the broad ones that may indicate the presence of a free **b1** even in the **Pt-0.05b1** sample. By comparison, with the **Pt-0.1b2** system no free CD was detected, showing that the number of coordinating thiols per molecule can influence its interaction with the surface of Pt NPs.

DOSY experiments gave a diffusion coefficient value of $3.7 \pm 0.2 \cdot 10^{-10} \text{ m}^2/\text{s}$ for **b1**. At the same time two populations were observed in the case of **Pt-0.05b1** (Figure 2.1.16), namely the free **b1** ($36 \pm 5\%$ of the population with $D = 3.8 \pm 0.3 \cdot 10^{-10} \text{ m}^2/\text{s}$) and **b1** coordinated to the surface of Pt NPs ($64 \pm 5\%$ of the population with $D = 1.2 \pm 0.3 \cdot 10^{-10} \text{ m}^2/\text{s}$). Processing of **Pt-0.5b1** spectrum resulted in only one population with a diffusion coefficient $D = 2.1 \pm 0.3 \cdot 10^{-10} \text{ m}^2/\text{s}$. Getting only one diffusing species suggests that either there is a fast exchange between grafted and free CD in the case of 0.5 equivalent of **b1** while for **Pt-0.05b1** less of **b1** is available, so the exchange is less pronounced; or the size of **Pt-0.5b1** is so small that it is difficult to distinguish population of grafted and free **b1**.

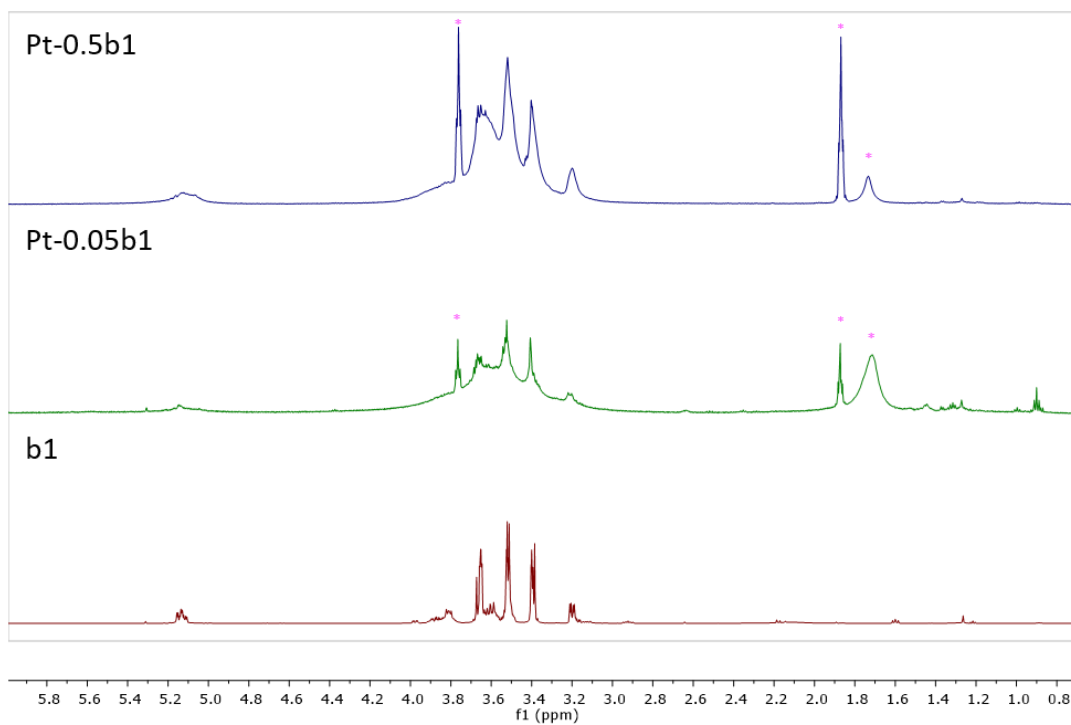


Figure 2.1.15 ^1H NMR of **b1**, **Pt-0.05b1**, and **Pt-0.5b1**. Pink asterisks indicate solvents.

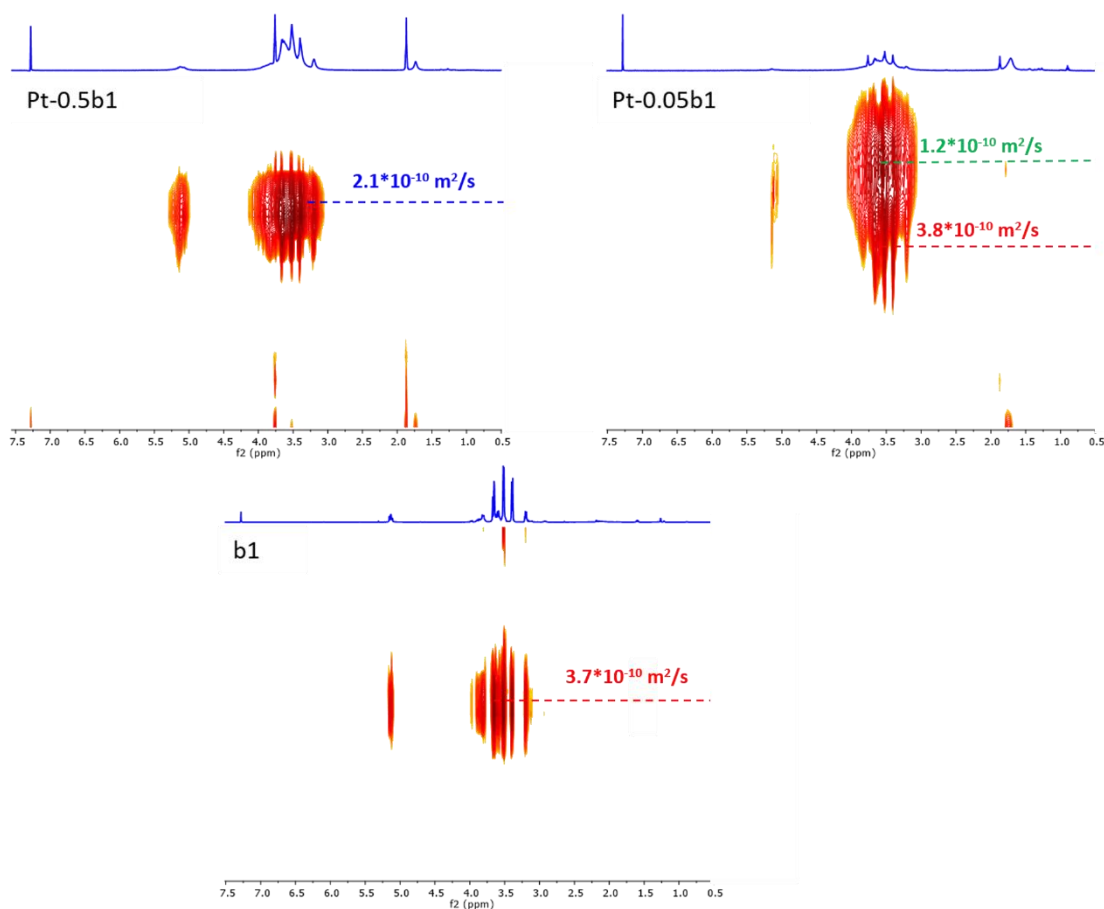


Figure 2.1.16 NMR-DOSY spectra of a) **Pt-0.5b1**; b) **Pt-0.05b1**; c) **b1**.

Even with 0.05 eq of CD, we noticed there are free CD molecules in solution. To justify this observation, the following discussion aims at making a rough estimation of the particle surface and the number of surface sites for **Pt-0.1b1**. The total amount of atoms (N_t) and the amount of surface Pt atoms (N_s) was calculated using formulas (2.3) and (2.4) taken from references ¹⁹⁶ and ¹⁹⁷. Ideal *fcc* Pt NP with the size of 1.6 nm will contain 154 atoms among which 98 atoms are located on the surface (64%). According to TGA analysis mass fraction of Pt is 62 %. If we consider that the rest is **b1** molecules (38%) it gives around 13 CD/NP. It indicates that there would be still plenty of active surface atoms even if we have all the **b1** coordinated which is not the case according to DOSY results. Now if we roughly calculate the surface of **Pt-0.1b1** ($d=1.6$ nm) presuming it spheric it will make 8.0 nm² while the surface of smaller opening of β -CD ($d=1.5$ nm) is 1.77 nm². That indicates that the 1 NP with around 100 Pt surface atoms can accommodate around 4 CD in “face-on” coordination mode. These calculations together with obvious size and activity trends for NPs stabilized with different amounts of **b1** suggest coexistence of few coordination modes of CD on the Pt surface.

Formula for total number of atoms in a NP:

$$N_t = \frac{2\pi}{3} \left(\frac{D}{a}\right)^3 \quad (2.2)$$

where D is the mean diameter of a NP and a is the size of a unit cell.

For *fcc* crystals:

$$N_t = \frac{\pi\sqrt{2}}{6} \left(\frac{D}{2r}\right)^3 \quad (2.3)$$

where r is the radius of a metal atom.

Formula for a number of surface atoms:

$$N_s = 10m^2 - 20m + 12, \quad (2.4)$$

where m is a number of shells in a NP and can be calculated using the following equation:

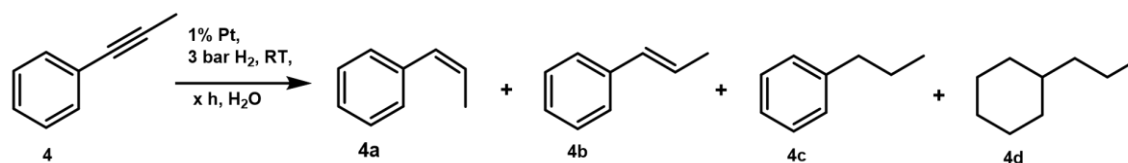
$$N_t = \frac{1}{3}(2m - 1)(5m^2 - 5m + 3) \quad (2.5)$$

2.1.4.2. Catalytic performance with a model substrate

In hydrogenation of the substrate **4**, the activity of the NPs increased while decreasing the amount of **b1** from 0.5 to 0.1 eq (Table 2.1.12). By further decreasing the amount of the ligand to 0.05 eq, the activity did not increase significantly, probably due to the lower dispersity of **Pt-0.05b1** in water

as well as the coalesced state of the NPs, which decreases active surface area. Considering the obtained results **Pt-0.1b1** NPs were used in hydrogenation of other substrates.

Table 2.1.12 Hydrogenation of phenylpropyne with **Pt-b1** catalysts.



Run	Catalyst	t, h	X (%)	Y 4a (%)	Y 4b (%)	Y 4c (%)	Y 4d (%)
1	Pt-0.5b1	1	56	32	6	18	0
2	Pt-0.2b1	1	72	43	6	22	0
3	Pt-0.1b1	1	99	23	7	69	0
4	Pt-0.05b1	1	98	14	5	78	1

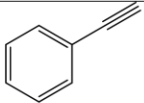
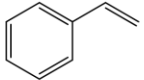
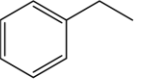
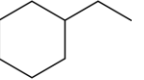
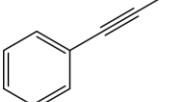
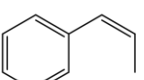
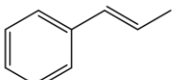
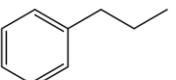
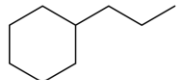
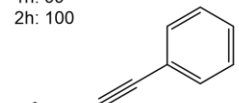
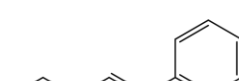

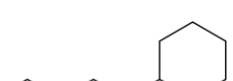
Reaction conditions: Catalyst (0.01 mmol Pt), substrate (1 mmol, 100 eq.), solvent (H₂O 3 mL), H₂ (3 bar), RT. Yield is determined as an average of two runs by GC-FID using dodecane as an internal standard.

2.1.4.3. Catalytic tests with other substrates using **Pt-0.1b1**

Hydrogenation of terminal and internal alkynes was performed with **Pt-0.1b1**. It was accomplished in short reaction times with formation of phenyl alkanes (Table 2.1.13). Precisely, already after 1 hour, almost full conversions were obtained for phenylpropyne and diphenylacetylene, while phenylacetylene required 2 h to reach a full conversion. In all cases, hydrogenation of alkynes was complete, preserving the aromatic ring.

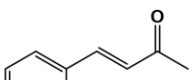
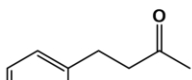
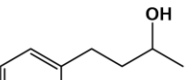
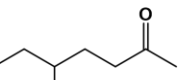
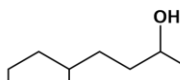
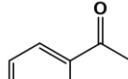
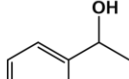
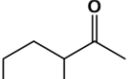
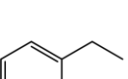
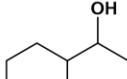
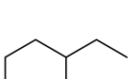
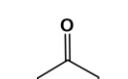
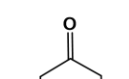
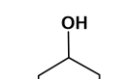
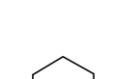
Hydrogenation of ketones was performed at harsher reaction conditions (80°C, 10 bar H₂, 6h) since typical reaction conditions used in the study gave a complex mixture of products, even after 24h. The catalytic transformation of ketones resulted in saturated alcohols formation as a main reaction product (Table 2.1.14). Interestingly, using **Pt-0.1b1** hydrogenation of the ring of the benzylidene acetone was possible, which was not observed with **Pt-0.5b1** in milder reaction conditions (RT, 5 bar H₂, 24h). In reaction with acetophenone, a significant amount of deoxygenated product **5e** was also observed. This is indeed a peculiar performance for a catalyst that contains no acidic sites and works at relatively mild reaction conditions. It would be interesting to further investigate the deoxygenation activity.

Table 2.1.13 Scope of alkyne reduction with **Pt-0.1b1**.

 1 Conversion 1h: 83 2h: 100	 1a 72 5	 1b 11 93	 1c 0 2	
 4 Conversion 1h: 99 2h: 100	 4a 22 0	 4b 7 0	 4c 70 99	 4d 0 1
 6 Conversion 1h: 100	 6a 0	 6b 100	 6c 0	

Reaction conditions: Catalyst (0.01 mmol Pt), substrate (1 mmol, 100 eq.), solvent (H₂O 3 mL), H₂ (3 bar), RT. Yield is determined as an average of two runs by GC-FID using dodecane as an internal standard. Diphenylacetylene was dissolved in a small amount of hexane/diethylether mixture to perform the reaction.

Table 2.1.14 Scope of ketone reduction with **Pt-0.1b1**.

 2 Conversion: 100	 2a 0	 2b 0	 2c 44	 2d 56	
 5 Conversion: 100	 5a 0	 5b 2	 5c 2	 5d 61	 5e 35
 7 Conversion: 100	 7a 28	 7b 71	 7c 1		

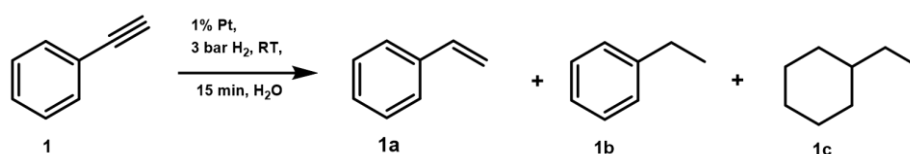
Reaction conditions: Catalyst (0.01 mmol Pt), substrate (1 mmol, 100 eq.), solvent (H₂O 3 mL), H₂ (10 bar), 80°C, 6h. Yield is determined as an average of two runs by GC-FID using dodecane as an internal standard.

2.1.4.4. Catalyst stability test

Phenylacetylene reaction was used to perform stability tests of **Pt-0.1b1** NPs (Table 2.1.15). The time of the run was decreased to 15 minutes to be able to observe changes in activity at the initial

stage of hydrogenation. After each run products were extracted and a new portion of reagent was added. After the first run, we observed 15% of conversion with 13% of product **1a**. Conversion after the second run increased to 24% with 21% of product **1a**. This change may be ascribed to a partial removal of the CD, which could unblock reactive sites of Pt NPs. Presence of S in the first extract was confirmed by elemental analysis. In next runs, the conversion stayed mostly the same 21-23%, however yield of **1b** increased from 2% to 7%. Bigger amount of the product **1b** may be related to incomplete removal of the products on the previous steps. Mass balance of the run 3 and 4 proves that some amount of reagent-product mixture was left from the previous runs. In general, no catalyst deactivation was observed during at least five cycles, which confirms the stability of the catalyst. TEM after the last test revealed that the size of the NPs did not change, although the formation of clusters of NPs in some regions was observed (Figure 2.1.17).

Table 2.1.15 Results of stability test with phenylacetylene as a reagent and **Pt-0.1b1**.



Run	X (%)	Y 1a (%)	Y 1b (%)	Y 1c (%)	Mass balance
1	15	13	2	0	94
2	24	21	2	0	96
3	21	14	7	0	102
4	22	15	6	0	106
5	23	17	7	0	97

Reaction conditions: Catalyst (0.01 mmol Pt), substrate (1 mmol, 100 eq.), solvent (H₂O 3 mL), H₂ (3 bar), RT, 15 min. Yield is determined as an average of two runs by GC-FID using dodecane as an internal standard.

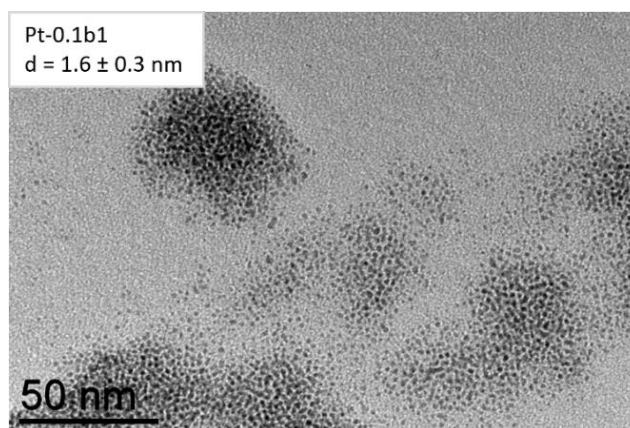


Figure 2.1.17 TEM of **Pt-0.1b1** NPs after the stability test.

2.2. NPs stabilized with alfa-CD-SPO: introduction of an activation moiety

In this section stabilization of Pt NPs with CD functionalized with secondary phosphine oxide (SPO) moiety is discussed (Figure 2.2.1 a). Mostly SPO exists as P(V) isomer; however, it can undergo an isomerisation with formation of a P(III) isomer – a phosphinous acid (PA), formation of which is favoured upon coordination to a metal by a lone pair of a PA (Figure 2.2.1 b). P-coordination mode can also be provided upon SPO deprotonation when it becomes a phosphoryl anion and interacts with low-coordinated Pt atoms on the surfaces with formation of P-bonded complexes (Figure 2.2.1 b). The ligand binding depends on the structure of the SPO⁷⁶. Also, deprotonation of PA can lead to O-bonded complexes which is more the case of a first-row transition metals (not shown)¹⁹⁸. We would like to note that in the text the ligands will be called SPO, although we do not know their coordination mode. SPO ligands are air-stable, water-soluble electron-donating ligands. Furthermore, SPOs can serve as bifunctional ligands which assist in heterolytic cleavage of hydrogen molecule and enable selective hydrogenation of polar bonds like C=O double bonds^{75,76,199}, as it was discussed in Chapter 1. Finally, the CDs anchored to the surface of the Pt NPs are expected to act as hosts for the model substrates - hydrophobic ketones or aldehydes but to have less affinity towards the resulting more hydrophilic alcohols thus releasing them without further hydrogenation (Figure 2.2.2).

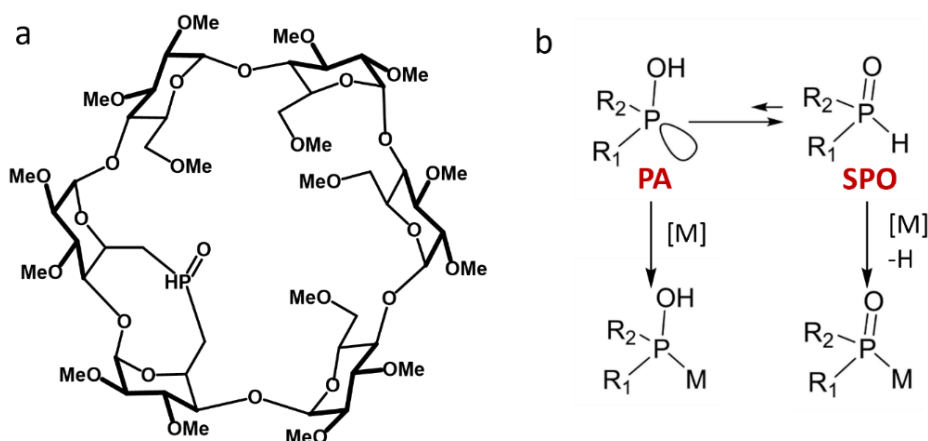


Figure 2.2.1 a) alfa-CD-SPO formula; b) illustration of PA-SPO isomerization and possible complexation modes.

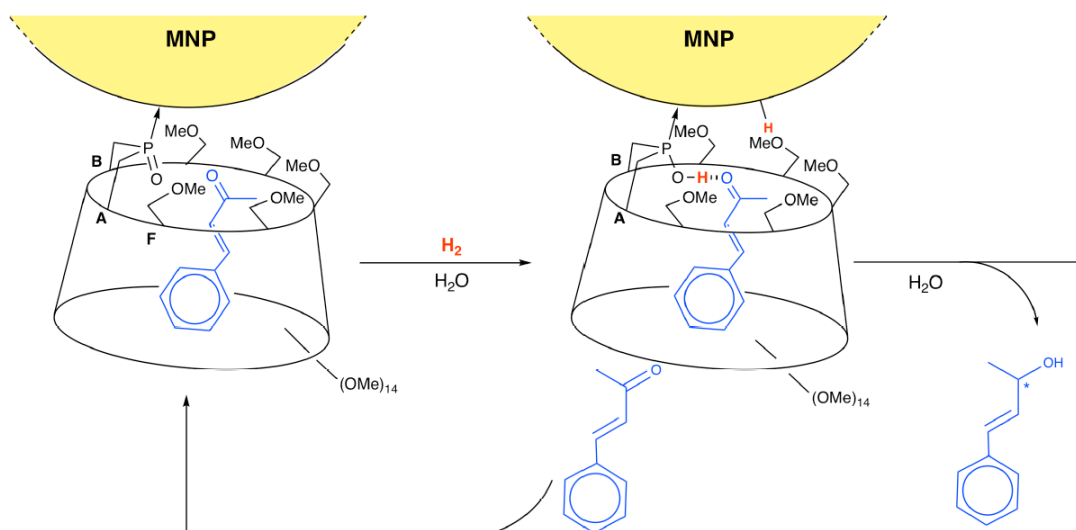


Figure 2.2.2 Illustration of selective hydrogenation of ketones with NP-CD-SPO system.

2.2.1. Synthesis and characterization of the systems

CD-SPO ligand can exist as two stereoisomers: endo-O- and exo-O-isomer (Figure 2.2.3). In complexes with the endo-O isomer, the electron pair of phosphorus required for the formation of coordination bond points *outside* the cavity; the metal thus coordinates outside the cavity. On the contrary, in the case of exo-O isomer, the metal can be placed inside the cavity since the electron pair required for coordination bond formation is facing inside the cavity. According to this information, only endo-O isomer can coordinate to Me NPs surface, as a NP is too big to enter inside the cavity. However, it is extremely difficult to separate the isomers, so to stabilize Pt NPs a mixture of isomers was used. The first synthesis was performed with a combination of endo-O:exo-O = 10:90 using exactly the same procedure as for synthesis of Pt-CD-SH systems which is using $\text{Pt}(\text{nbe})_3$ precursor and 0.5 eq of CD-SPO (0.05 eq of endo-O and 0.45 eq of exo-O isomer), exposing the solution to hydrogen (3 bar) at room temperature for 18 h, washing and drying.

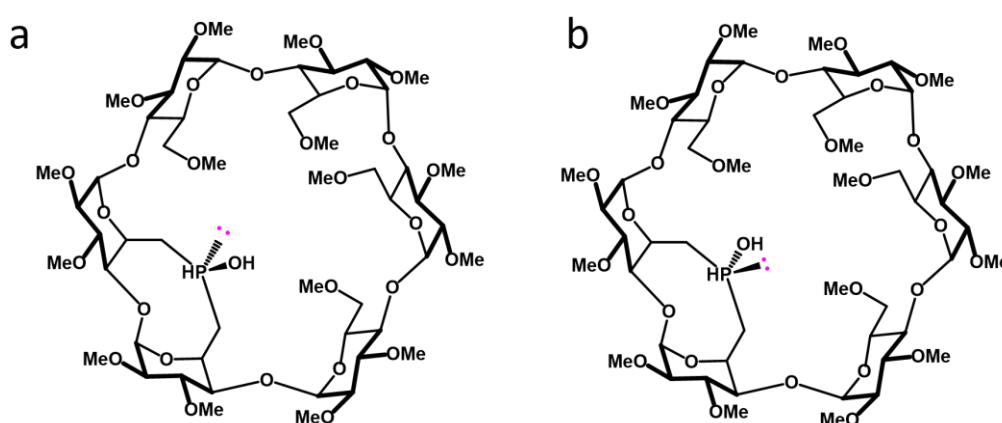


Figure 2.2.3 CD-SPO isomers: a) endo-O; b) exo-O.

^{31}P NMR of the CD and Pt-0.5CD-SPO (further **Pt-0.5P1**) showed that the signal of the endo-O isomer at 25 ppm is not present at the spectrum of **Pt-0.5P1**, which could mean that all endo-O isomer has coordinated to the surface of NPs (Figure 2.2.4). TEM showed coalescence of NPs similar to what we observed with **Pt-0.05CD-SH** systems (Figure 2.2.5). This observation further confirms the hypothesis that only endo-O isomer was able to coordinate to NPs. The appearance of the peak at 47.6 ppm indicated formation of a minor impurity which did not appear on the ^{31}P spectrum when using D_2O as a solvent; neither it was identified by thin-layer chromatography (TLC) (DCM/MeOH 9/1). We suppose that Pt-SPO complexes could be formed before the decomposition of the precursor with hydrogen; however, due to the small amount of the impurity we used NPs without any additional purification.

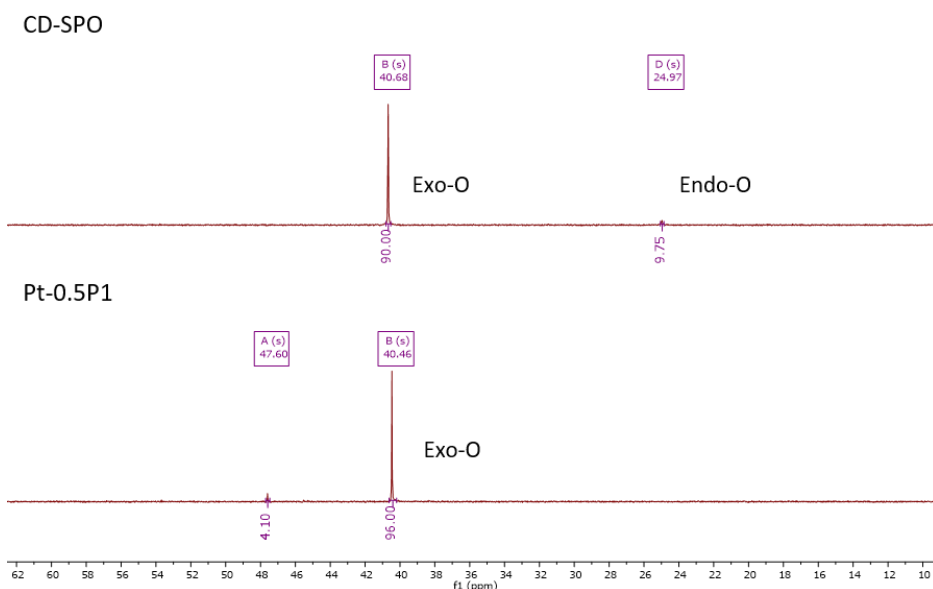


Figure 2.2.4 ^{31}P NMR of **CD-SPO** and **Pt-0.5P1**.

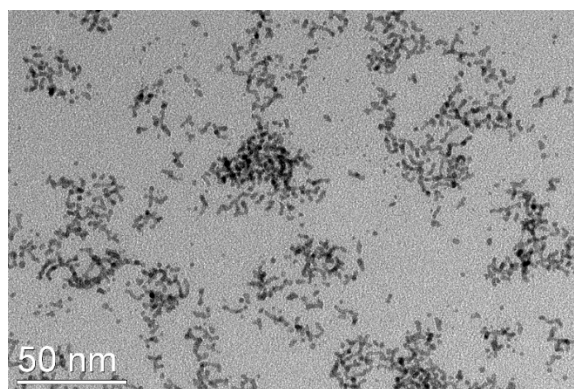


Figure 2.2.5 TEM image of **Pt-0.5P1**.

Later, we discovered that the equilibrium between endo-O and exo-O isomers could be shifted towards endo-O in acidic conditions. ^{31}P NMR of CD-SPO confirmed that the amount of the

endo-O isomer increased from 10 to $\approx 40\%$ after stirring with HCl overnight (Figure 2.2.6). A new synthesis of Pt-0.5CD-SPO (**Pt-0.5P2**) was performed where solution of CD-SPO was stirred with HCl overnight before being added to the Pt(nbe)₃ solution. ³¹P NMR of **Pt-0.5P2** showed peaks of both isomers at 30.4 ppm and 44.8 ppm. In addition, new peaks at 52.3 ppm and 87.5 ppm appeared. According to previous reports peaks at 87.5 ppm and 52.3 ppm might correspond to Pt⁰-SPO or Pt²⁺-SPO complexes, for example trans- or cis-PtL₂(SPO)₂ or PtL₃SPO complex^{200,201}. On TEM images small NPs could be found as well as some agglomerates (Figure 2.2.7).

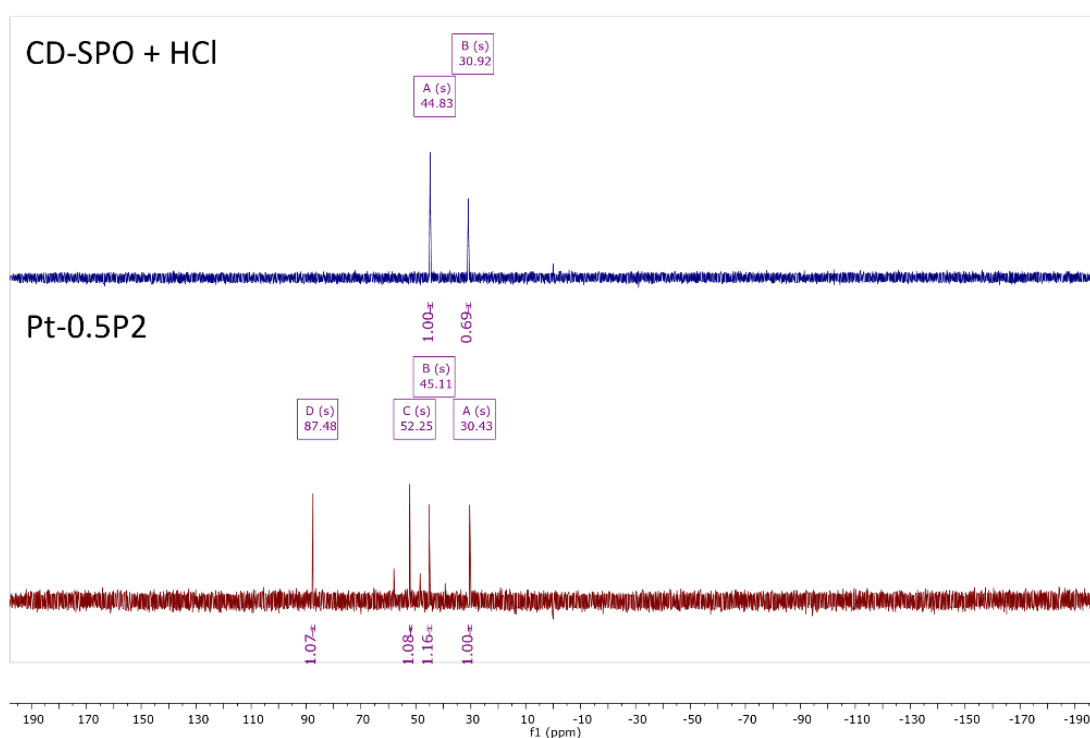


Figure 2.2.6 ³¹P NMR of CD-SPO after acid treatment overnight (in D₂O) and NMR of **Pt-0.5P2** materials (done in H₂O+D₂O).

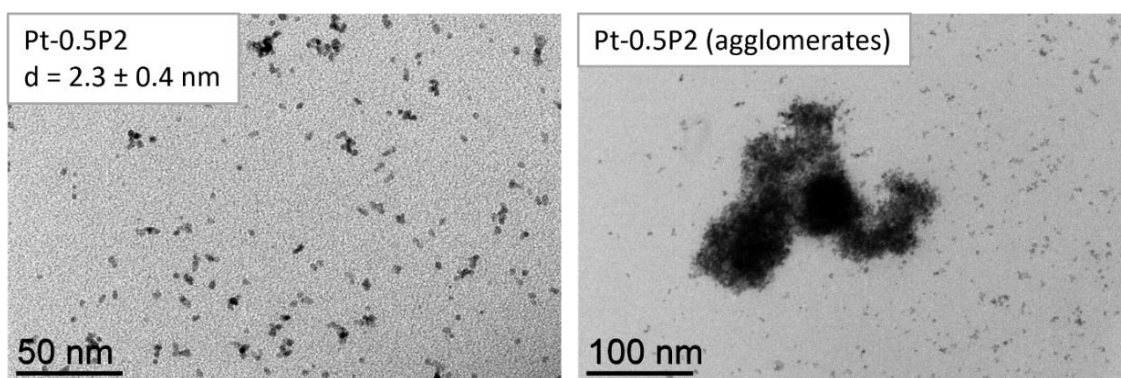


Figure 2.2.7 TEM images of **Pt-0.5P2**.

2.2.2. Identification of active species in selective cinnamyl alcohol formation

Hydrogenation of the substrate **3** was used as a model reaction to test the hypothesis of preferential hydrogenation of polar C=O bond with assistance of SPO ligand. Gladly, we found that **Pt-0.5P2** was selective towards the product **3b** with a yield of 70% at 98% of conversion (Table 3.15). To find out whether the selectivity towards the unsaturated alcohol was provided by the catalytic system or due to the presence of HCl coming from the synthetic procedure a new batch of the Pt-0.5CD-SPO NPs (**Pt0.5-P3**) was synthesized. For this batch, water solution of CD-SPO was stirred with HCl at r.t. overnight. Later, acid was neutralized with NaHCO₃, and CD-SPO was extracted and dried. The resulting compound contained 43% of the active isomer, as determined by NMR (Figure 2.2.8). This batch consisted of small well-dispersed NPs around 1.6 nm in size (Figure 2.2.8). Regarding the catalytic performance, this system did not show the selectivity toward the product **3b**. Increasing additions of acid did not change the activity or the selectivity of the reaction, meaning that HCl was not responsible for the selectivity either (Table 2.2.1 – runs 3-5).

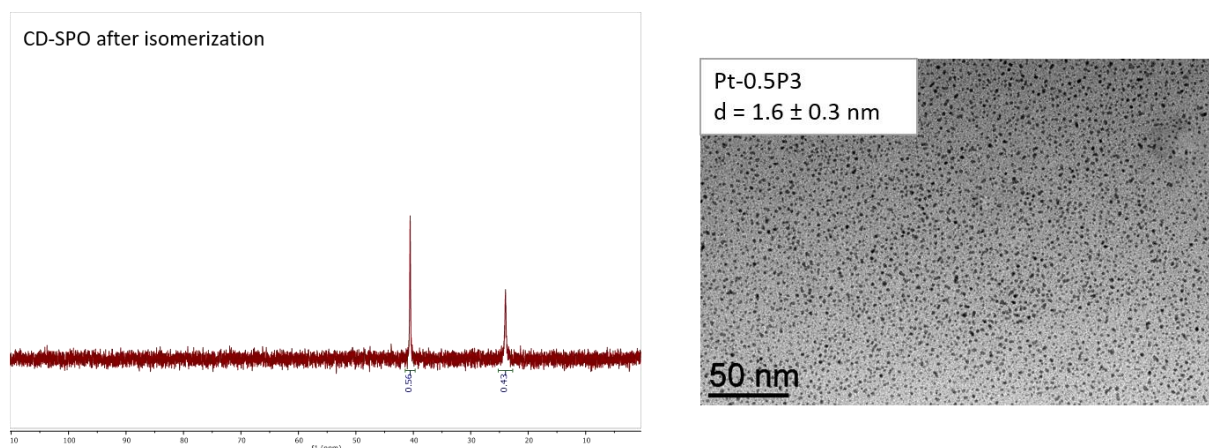


Figure 2.2.8 ³¹P NMR of CD-SPO after isomerization with 1M HCl (in CD₃Cl); TEM image of **Pt-0.5P3**.

To investigate whether the amount of active ligand on the surface influences the selectivity in catalysis Pt NPs were synthesized with 1.25 eq of CD-SPO (**Pt-1.2P4**) where 40% were endo-O isomer meaning 0.5 eq of an active isomer. TEM confirmed the formation of small Pt NPs of 1.1 nm (Figure 2.2.9). On ³¹P NMR we did not observe any peaks except the signal of exo-O-isomer, suggesting that all the active isomer was coordinated (Figure 2.2.9). Catalytic hydrogenation of the substrate **3** resulted in 31% of conversion with 7% of product **3b** (Table 2.2.1 – run 6). Thus, by changing the amount of the ligand it was not possible to change the selectivity of the reaction.

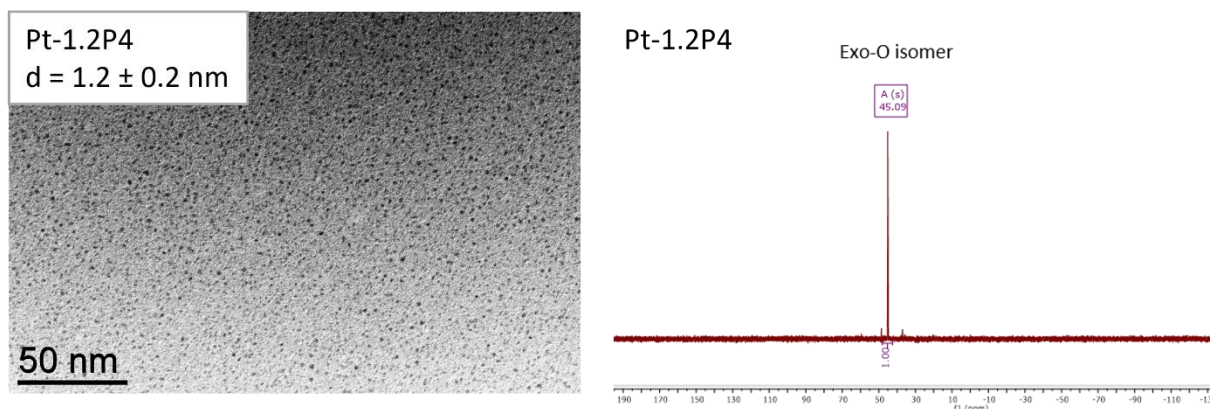
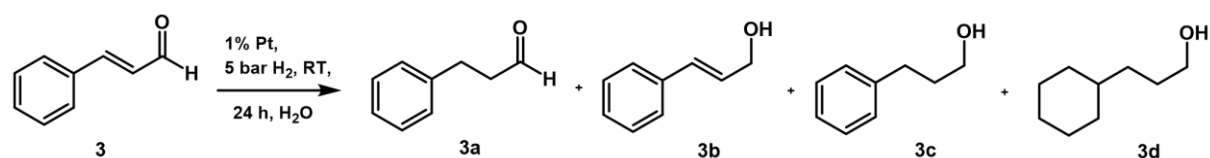


Figure 2.2.9 TEM image and ^{31}P NMR of **Pt-1.2P4** in D_2O .

Table 2.2.1 Hydrogenation of cinnamaldehyde with **Pt-0.5CD-SPO** in water.



Run	Catalyst	c(HCl) (M)	X (%)	Y 3a (%)	Y 3b (%)	Y 3c (%)	Y 3d (%)
1	Pt-0.5P2	0	98	5	70	23	0
2	Pt-0.5P3	0	72	34	19	19	0
3	Pt-0.5P3	$2.5 \cdot 10^{-6}$	71	37	17	17	0
4	Pt-0.5P3	$1 \cdot 10^{-5}$	66	37	14	15	0
5	Pt-0.5P3	$1.7 \cdot 10^{-3}$	78	40	18	20	0
6	Pt-1.2P4 ^a	0	31	18	7	6	0

Reaction conditions: Catalyst (0.01 mmol Pt), substrate (1 mmol, 100 eq.), solvent (H_2O 3 mL), H_2 (5 bar), RT, 24h. Yield is determined as an average of two runs by GC-FID using dodecane as an internal standard. a – one catalytic run.

The coordination of the endo-O isomer was confirmed using ^{31}P CP MAS NMR of the four catalysts (Figure 2.2.10). We observed on the NMR of alfa-CD-SPO two signals at 25 and 45 ppm that correspond to endo-O and exo-O isomer respectively. Then, on the NMR of **Pt-0.5P3** the sharp signal at 25 ppm disappeared while a broad signal at the region of 10-110 ppm appeared, which could be attributed to the endo-O isomer in close proximity to the surface of Pt. The same signals were observed on the spectrum of **Pt-1.2P4**. The shift of the signal to higher chemical shifts could be the consequence of a Knight shift, already observed on ultra-small platinum NPs²⁰². An additional experiment showed that the broad signal had a long relaxation time (T_1). The long T_1 indicated a presence of slow local motions at the phosphorus level. The broadness appeared due to structural heterogeneity, which is an expected behavior of coordination on the surface of NPs. In case of **Pt-0.5P2** an overlap of the signals at 30 ppm and 45 ppm with few other signals was observed in accordance with the liquid state ^{31}P NMR.

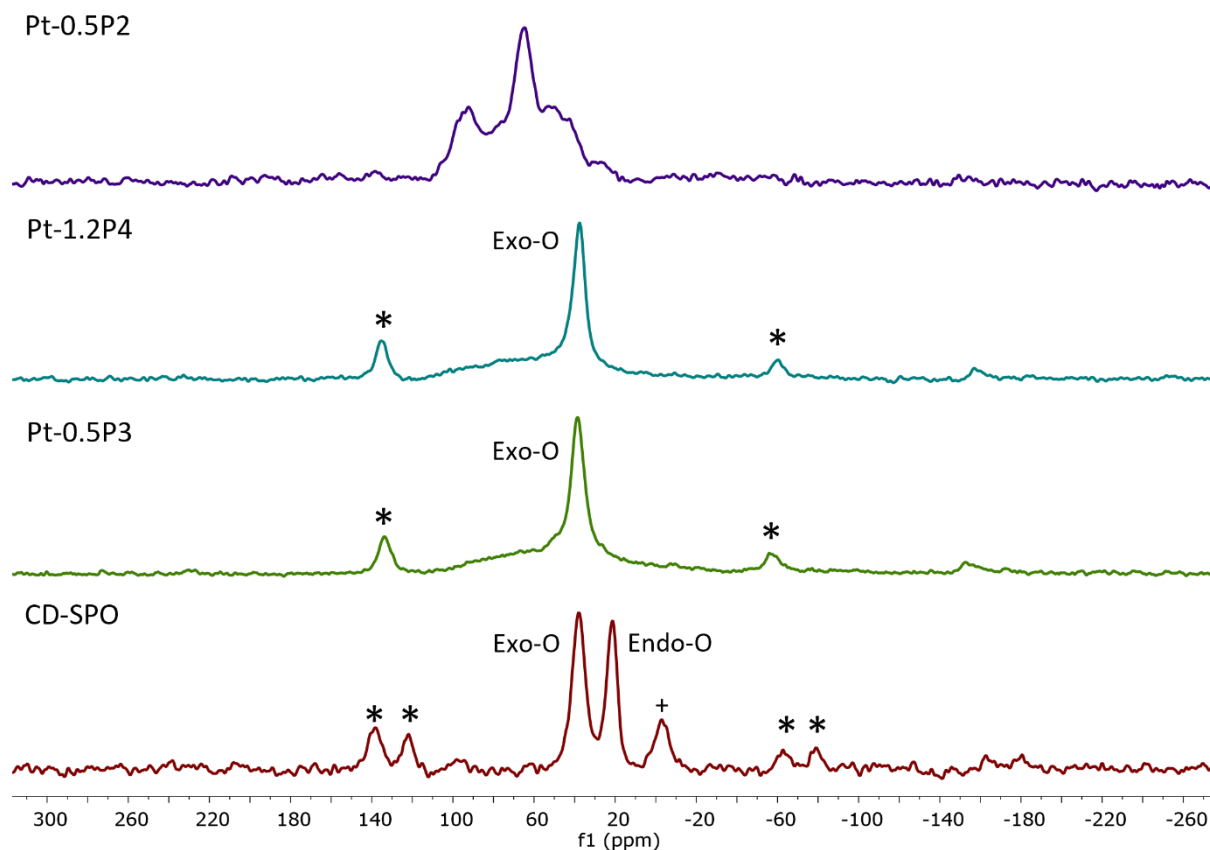


Figure 2.2.10 ^{31}P CP-MAS NMR of **Pt-CD-SPO** systems. The asterisks indicate spinning side bands; the plus indicates unknown contamination.

To sum up, selective hydrogenation of cinnamaldehyde towards cinnamyl alcohol was achieved with **Pt-0.5P2** NPs. On ^{31}P NMR of these NPs, new signals were observed probably due to the side reactions of CD-SPO with $\text{Pt}(\text{nbe})_3$ in acidic conditions. According to the control experiments neither the acid addition nor the bigger amount of endo-O were responsible for the selectivity control. The presence of a non-coordinating exo-O isomer doesn't allow to use IR to identify all the side-products. We tried to remove exo-O SPO by centrifugation of the solution with a membrane centrifugating tubes; however, after 3 washings exo-O isomer was only partially removed. We also failed to separate the NPs from other by-products in **Pt-0.5P2** batch using the same procedure. Thus, another purification method should be applied for this system. We speculate that the new species formed during the synthesis of **Pt-0.5P2**, eventually organometallic complexes, were responsible for the formation of cinnamyl alcohol. Additional experiments are required to prove the hypothesis.

2.3. Conclusions and perspectives

Pt NPs were synthesized following an organometallic approach. They were stabilized with small amounts of functionalized cyclodextrins that assured solubility and stability of NPs in water. Pt-CD-thiol NPs showed high activity although, often strongly coordinating ligands like thiols tend to poison active Pt sites and block the activity. Moreover, the **Pt-0.1b1** catalyst could be reused in biphasic catalytic hydrogenation of phenylacetylene during at least five cycles. Pt-CD-thiol systems hydrogenated both the C=C and C=O double bonds and much less the aromatic ring at mild reaction conditions (5 bar H₂ RT), while at slightly increased pressure and temperature, the main product of aromatic ketone hydrogenation was fully saturated alcohol.

Pt-CD-SPO NPs were synthesized in order to have an activation group which can help heterolytic dissociation of hydrogen to selectively attack C=O bond of unsaturated aldehydes and ketones. This system was tested in hydrogenation of cinnamaldehyde. We found a moderate selectivity towards cinnamyl alcohol (70 % at 98 % of conversion) when using HCl during the synthesis of the NPs. Further investigations are required to identify the species responsible for this selectivity. For example, we could use a MALDI MS to try identify by-products of the **Pt-0.5P2** synthesis. Then, we would need to find a method to separate NPs from other by-products and to conduct hydrogenation tests. In this way, we could find whether a C=O selective catalyst is heterogeneous or homogeneous in nature. Also, it would be interesting to try synthesizing Pt NPs from the preformed Pt-SPO complexes like it was done for Au NPs⁷⁵ to compare the influence of the synthetic procedure on the SPO coordination mode and on the catalytic properties of the NPs.

2.4. Experimental part

2.4.1. General

Synthesis of the Me-CD catalysts was carried out under an inert atmosphere in the glovebox and using standard Schlenk techniques. The synthesized nanoparticles were stored in the glovebox. Pt(*nbe*)₃, Pt₂(*dba*)₃, and Ru(COD)(COT) were purchased from NanoMePS. THF for the synthesis was collected from an MBraun purification system, degassed and stored in the glovebox. Preparation of catalytic solutions was done on air. All the substrates were purchased from commercial sources and used without further purification.

2.4.2. Analytics

TEM images were collected using a JEOL JEM 1400 operated at 120kV and using a tungsten filament. The NP size and distribution was determined from the measurement of over 150 particles.

FT-IR spectra were recorded on a Thermo Scientific Nicolet 6700 FT-IR spectrometer in the range 4000-700 cm^{-1} , using a Smart Orbit ATR platform. To prepare IR samples small amounts of the catalysts were dissolved in THF. The vessels with the solutions were charged with 1 bar of CO in a Fisher-Porter bottle and left for 18h. Then, CO was evacuated, and a drop of a solution was deposited on the ATR_{Ge} stage. The spectra were recorded after the samples were dried on air.

TGA was performed in a TGA/DSC 1 STAR System equipped with an ultra-microbalance UMX5, a gas switch GC200 and DTA and DSC sensors to determine Pt mass fraction.

XRD diffractograms were recorded on an Empyrean PANalytical diffractometer using Co K α radiation equipped with X'Celerator detector. The working voltage is 45 kV for a current of 35 mA.

XPS spectra were recorded using a monochromatised Al K α ($h\nu = 1486.6$ eV) source on a ThermoScientific K-Alpha system. The X-ray Spot size was about 400 μm . The Pass energy was fixed at 30 eV with a step of 0.1 eV for core levels and 160 eV for surveys with a step of 1eV. The spectrometer energy calibration was done using the Au 4f_{7/2} (83.9 ± 0.1 eV) and Cu 2p_{3/2} (932.8 ± 0.1 eV) photoelectron lines. XPS spectra were recorded in direct mode N (Ec) and the background signal was removed using the Shirley method. The flood gun was used to neutralize charge effects on the top surface.

Liquid-state NMR were recorded on a Bruker Avance 600 NEO spectrometer equipped with a 5 mm triple resonance inverse Z-gradient probe (TBI ¹H, ³¹P, BB). All diffusion measurements were made using the stimulated echo pulse sequence with bipolar gradient pulses. The diffusion delay and the gradient pulse duration was set in order to obtain 1-5% residual signal with maximum gradient strength. The diffusion delay varied from 90 to 250 ms and the gradient pulse duration from 1.8 to 3.2 ms. The recycle delay was adjusted to 3 s. Rectangular shapes were used for the gradients and a linear gradient ramp with 16 or 32 increments between 2% and 95% was applied for the diffusion relevant gradients. For 2D diffusion ordered spectroscopy (DOSY), after Fourier transformation and baseline correction, the diffusion dimension was processed with the Bruker Topspin software package DOSY. The diffusion dimension was processed with different algorithms: single-exponential and multi-exponential analysis involving least-squares fitting and the Laplace inversion routine CONTIN (Topspin software).

Solid-state NMR experiments were recorded on a Bruker Avance 400 III HD spectrometer operating at magnetic fields of 9.4 T. Samples were packed into 3.2 mm zirconia rotors under argon inside a glove box. The rotors were spun between 12 and 16 kHz at 295 K. ^{31}P CP MAS spectra were recorded with a recycle delay of 3 s and contact times of 1 ms. ^{31}P Hahn-echo were synchronized with the spinning rate and performed with a recycle delay of 20 s. Chemical shifts were referenced to TMS and 85% H_3PO_4 for ^1H and ^{31}P , respectively.

NMR analysis and data processing were performed by Yannick Coppel at LCC, Toulouse.

Gas chromatography (GC) was performed on a PerkinElmer 580 gas chromatograph equipped with an FID-detector and a CP-WAX-52CB column using H_2 as carrier gas. The GC is coupled to a Clarus SQ8T mass spectrometer (MS). The peaks were assigned by injection of the pure substances or by GC-MS. For quantification, dodecane was added as an internal standard. Conversion and yields were obtained by comparison of the peak areas of reagent, products and internal standard. The correction factors were determined by calibration of the pure reagents and products in relation to the internal standard.

2.4.3. Experimental procedures

Synthesis of Me-CD NPs

Synthesis of the Pt-CD NPs followed the same synthetic protocol as described on the example of Pt-0.1b1 synthesis.

Pt-0.1b1 synthesis

In a glovebox $\text{Pt}(\text{nbe})_3$ (199 mg) and beta-CD-mono-SH (**b1**) (60 mg) were dissolved in 3 mL and 2 mL of THF respectively. The solutions were mixed in a Fisher-Porter (FP) bottle (100 mL) equipped with a manometer and evacuated from the glovebox. Color changed to reddish after solutions mixing. Then the bottle was charged with 3 bar of H_2 while stirring at RT. The color changed from reddish to black in less than a minute after H_2 addition. Solution was left stirring at RT for 18 h. Then, hydrogen was evacuated with a Shlenk line and the solvent was evaporated till ~ 2 mL. Further, the solution was washed with 10 mL of pentane 3 times, redissolved in THF to transfer it in a 4 mL vial and dried under vacuum at RT. Yield: 121 mg.

Ru-0.5b2 synthesis

In a glovebox solutions of $\text{Ru}(\text{COD})(\text{COT})$ (40 mg) and beta-CD-bi-SH (**b2**) (90 mg) in 3 mL and 2 mL of THF respectively were prepared. Then the Ru precursor solution was deepened in a acetone-liquid

nitrogen cold bath and the CD solution was cannulated into the Ru(COD)(COT) solution. The bottle was charged with 3 bar of H₂ while stirring. Then the cold bath was removed and in ~5 min color has changed from yellow to dark-brown. The solution was left stirring at RT for 18h. Then, the NPs were washed and dried as described in the Pt-0.1b1 synthesis. Yield: 90 mg.

Catalytic tests in THF

A catalyst (0.01 mmol metal according to TGA results), a substrate (100 eq (1 mmol)) and a solvent (THF) were weighed in air into the FP bottle (100 mL). The bottle was charged with 3 or 5 bar of hydrogen and left stirring (1000 rpm) for a certain amount of time at RT. Later, the bottle was depressurized. GC samples were prepared by filtering a sample through a small celite column. Dodecane (internal standard, 1 mmol) and THF were added to the filtrate to have 2 mL solution. A GC sample was prepared by taking an aliquot of the catalytic solution (50 µL) and diluting it with 1.5 mL of THF.

Catalytic tests in water

A catalyst (0.01 mmol metal), a substrate (100 eq (1 mmol)) and a solvent (deionized water) were weighed in on air into the FP bottle (100 mL). The bottle was charged with 3 or 5 bar of hydrogen and left stirring (1000 rpm) for a certain amount of time at RT or 50°C. In the end of a reaction the bottle was cooled down and depressurized. Organic compounds were separated by extraction with Et₂O/hexane mixture 0.5mL/2.5mL for 3 times. MgSO₄ was added to remove traces of water. Dodecane (internal standard, 1 mmol) was added to the solution. A GC solution was prepared by taking an aliquot of the catalytic solution (50 µL) and diluting it with 1.5 mL of hexane.

CHAPTER 3. Iron-platinum nanoparticles immobilized on supported ionic liquid phases - a catalytic study

3.1. FePt@SILP in the context of bimetallic NP catalysts for selective hydrogenation.....	100
3.2. Synthesis of Fe _x Pt _{100-x} nanoparticles on imidazolium-based SILP.....	101
3.2.1. Synthetic optimization	101
3.2.2. Optimized synthetic procedure.....	103
3.3. Characterization of the catalytic materials.....	104
3.4. Catalytic performance of Fe _x Pt _{100-x} @SILP	110
3.4.1. Benzylidene acetone hydrogenation	110
3.4.2. Acetophenone hydrogenation and hydrodeoxygenation.....	111
3.4.3. Selective hydrogenation of unsaturated aldehydes	115
3.4.4. Hydrogenation of other substrates.....	117
3.5. Conclusions	117
3.6. Experimental part	119
3.6.1. General	119
3.6.2. Analytics	119
3.6.3. Procedures	119

3.1. FePt@SILP in the context of bimetallic NP catalysts for selective hydrogenation

Bimetallic nanoparticles are of huge research interest due to the synergetic effects that are not possible to reach with monometallic materials^{172,203,204}. In these systems two metals may both participate in different elementary steps of a catalytic reaction or only one metal works as the active catalyst while the other metal is added to modify the structure of the active surface. The interaction between metals can result in geometric or/and electronic effects which will dictate the selectivity of the reaction.

Synthesis of bimetallic NPs is widely applied in our group. For example, core-shell NP with magnetic metal core and active metal shell, such as FeC@Ru²⁰⁵ were used for magnetically induced catalysis, whereas colloidal NP alloys of PdNi⁴⁹ or RuIr⁵⁰ showed high selectivity in a hydrogen isotope exchange reaction.

In the team of Alexis Bordet where I had an internship bimetallic NPs supported on SILP are systematically compared to each other in terms of their physico-chemical properties and catalytic performance. Bimetallic FeRu, CoRu, or CoRh NPs synthesized in the team displayed interesting selectivity in hydrogenation. For instance, Rengshausen *et al.* reported selectivity changes in hydrogenation of bicyclic heteroaromatics using CoRh with different ratios of metals²⁰⁶. Namely, with Co₂₅Rh₇₅@SILP, similar to Rh@SILP, full hydrogenation of both rings was performed whereas by a slight change of metal ratio in Co₃₀Rh₇₀@SILP selective hydrogenation of solely heterocycles was achieved. Here, authors suppose that geometric (dilution with Co) effects influenced the selectivity since X-ray absorption spectroscopy (XAS) did not evidence major electronic differences between Co₂₅Rh₇₅@SILP and Co₃₀Rh₇₀@SILP. In another example, Goclik and colleagues used Fe₂₅Ru₇₅@SILP for selective hydrodeoxygenation of hydroxyacetophenones to ethylphenols, while monometallic Ru@SILP resulted in a mix of hydrogenated and hydrodeoxygenated products with saturated rings²⁰⁷. The hydrodeoxygenation activity was attributed to the strong mesomeric effect of -OH substituent since without it HDO was not observed.

The system we decided to study was FePt NPs immobilized on SILP (Fe_xPt_{100-x}@SILP). Platinum itself is one of the most active hydrogen activators which is often used in a combination with a second metal to reach desired selectivity in hydrogenation and dehydrogenation, reforming or CO oxidation reactions²⁰⁸⁻²¹⁰. Previously, bimetallic FePt materials were used in catalysis, mostly

in hydrogenation of aldehydes^{170,171,211–217} and nitroaromatics^{218,219}, in oxygen reduction reaction²²⁰ or in magnetism studies^{221–223}.

For example, Zhang and colleagues used bimetallic supported FePt NPs in hydrogenation of cinnamaldehyde²¹⁴. High selectivity towards cinnamyl alcohol was achieved (89.2% at 95.7% conversion) with one of the highest TOFs reported - 19440 h⁻¹. The authors confirmed with XRD and XPS that iron species coexisted with platinum, as PtFe fcc alloy or FeO_x species, and that electron transfer proceeded from Fe to Pt, which could be responsible for the remarkable catalytic performance. Indeed, higher electron density on the surface of Pt increases its activity in hydrogen dissociation and decreases the probability of adsorption of C=C double bond due to four electron repulsion interaction. Simultaneously Fe becomes more electrophilic attracting oxygen of C=O bond. At the same time, in a study of Bai *et al.*²²⁴ high selectivity towards cinnamyl alcohol (95.5% of selectivity at 95.7% of conversion) with FePt zigzag nanowires (ZNWs) was attributed to lower electron density on Pt²²⁴, although, the bonding energy change of Pt⁰ in Pt ZNWs (70.2 eV) and PtFe ZNWs (70.5 eV) was not significant.

Considering the interesting outcomes of interaction of Pt with Fe and having in hand the experience of both teams in the synthesis of bimetallic NPs we decided to synthesize Fe_xPt_{100-x}@SILP materials and to use them in hydrogenation of C-O and N-O bonds.

3.2. Synthesis of Fe_xPt_{100-x} nanoparticles on imidazolium-based SILP

3.2.1. Synthetic optimization

Fe_xPt_{100-x}@SILP materials were synthesized following organometallic approach similar to Fe_xRu_{100-x}@SILP synthesis²²⁵ which includes impregnation of precursors solutions with a support and following decomposition of precursors with hydrogen gas. Silica with covalently linked imidazolium ionic liquid, [1-butyl-3-(triethoxysilylpropyl) imidazolium]NTf₂, was used as a support since it proved to assure nanoparticles stabilization and dispersion^{119,122,226}. As Fe precursor, Fe₂[N(Si(CH₃)₃)₂]₂ was chosen because it contains a weakly coordinating ligand and thus can be decomposed with hydrogen at room temperature and has an optimal decomposition rate which allows to use it in the synthesis of alloys²²⁵. Considering Pt metal precursors, Pt(nbe)₃, PtMe₂(cod), and Pt₂(dba)₃ were tested in the synthesis (see Figure 3.2.1).

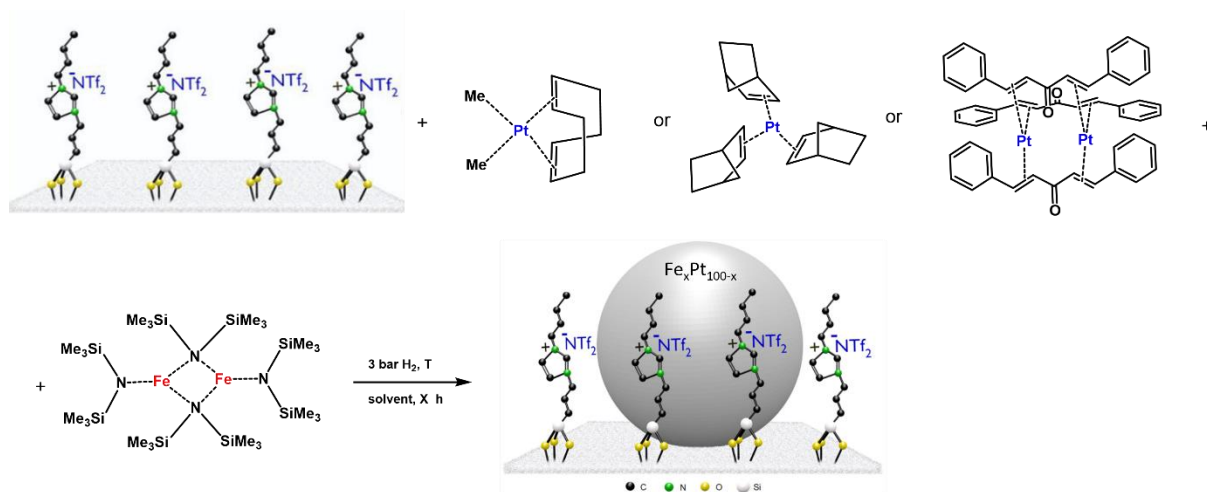


Figure 3.2.1 Scheme of synthesis of Fe_xPt_{100-x}@SILP.

Using Pt(nbe)₃ we observed change in color of the solution from light-brown to dark-brown after the addition of Fe precursor and during the impregnation step that is likely due to the fact that Pt(nbe)₃ is not stable at room temperature and gets decomposed during impregnation. Attempt to cannulate Fe precursor solution into cooled Pt(nbe)₃ solution outside the glovebox failed, because Fe₂[N(Si(CH₃)₃)₂]₂ is highly air sensitive. More precisely, during the cannulation attempts change of color of Fe solution from light green to brown was observed. In all attempts performed with Pt(nbe)₃ precursor, NPs looked aggregated (Figure 3.2.2 a), although they were active in catalysis, as discussed later. With PtMe₂(cod) big agglomerates were formed on the support, so the synthesis was not optimized further (Figure 3.2.2 b).

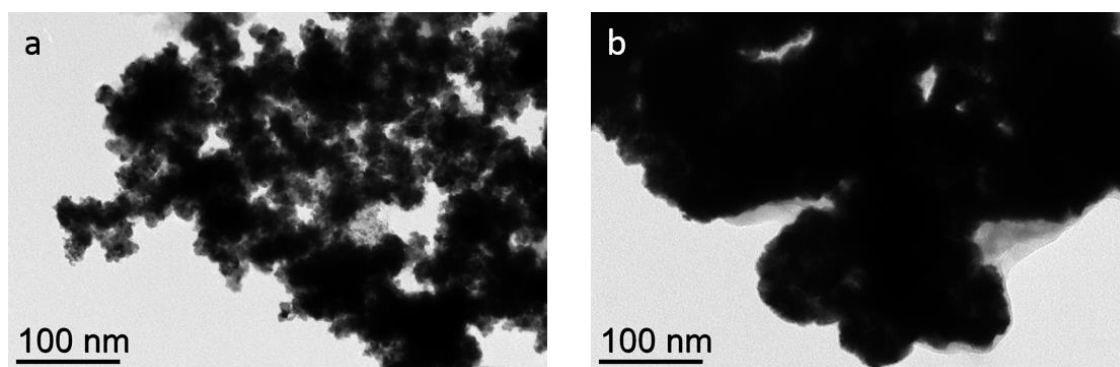


Figure 3.2.2 Fe₂₅Pt₇₅@SILP synthesized from a) Pt(nbe)₃, b) PtMe₂(cod).

Synthesis with Pt₂(dba)₃ led to small nanoparticles, so this precursor was chosen for the next optimization step. Since Pt₂(dba)₃ is more polar than Pt(nbe)₃ and PtMe₂(cod), it is not soluble in low polarity solvents such as mesitylene or toluene. THF, 1,2-dimethoxyethane (DME), dioxane, and anisole were tested during the synthesis optimization. Obtained catalytic samples were analyzed by TEM (Figure 3.2.3). Only in case of anisole/THF mixture, we did not observe the formation of colloidal NPs (*i.e.* not adsorbed on the substrate). To discover whether IL leaching from the support

could be a reason of free NPs formation, SILP was washed with DME and supernatant was analyzed by NMR. The same experiment was performed with anisole/THF mixture. While in the first case, we saw signals that correspond to the imidazolium ionic liquid in the second case we did not see any imidazolium IL signals. This result implies that there is IL leaching in DME but not in Anisole/THF. Since anisole afforded partial solubility of the precursors and chemical stability of the substrate and THF addition resulted in complete solubility of Pt precursor a mixture of abovementioned solvents was used for the $\text{Fe}_x\text{Pt}_{100-x}\text{@SILP}$ ($x = 0, 20, 40, 60, 75, 80, 100$) series.

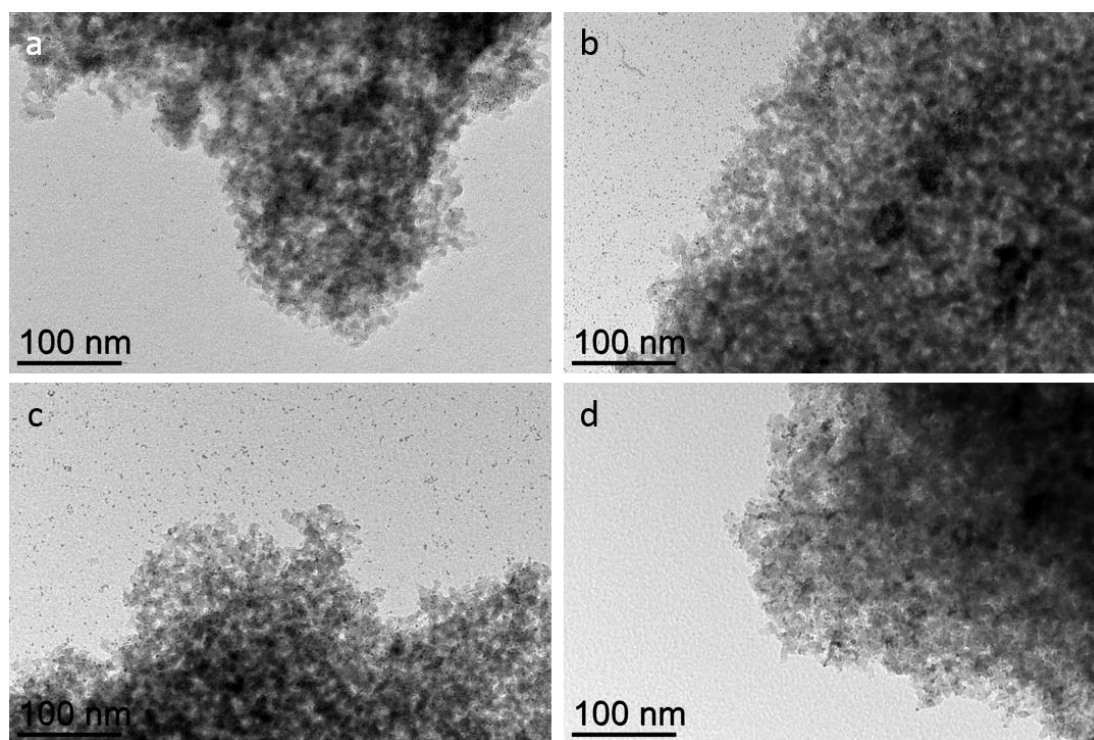


Figure 3.2.3 $\text{Fe}_{40}\text{Pt}_{60}\text{@SILP}$ NPs synthesized in a) THF; b) DME; c) dioxane; d) anisole/THF.

3.2.2. Optimized synthetic procedure

In a glovebox an anisole solution of $\text{Fe}_2[\text{N}(\text{Si}(\text{CH}_3)_3)_2]_2$ precursor was mixed together with an anisole/THF solution of $\text{Pt}_2(\text{dba})_3$ precursor and SILP support. After 2 h of impregnation the solution was filled with 3 bar of H_2 and left stirring for 18 h at room temperature. Upon reductive conditions color of the solution turned from dark-violet to black (after 3 min under H_2) to colorless (after 18 h under H_2). At the same time SILP powder turned from white to black that indicates metal precursors decomposition with NPs formation on the support. Finally, catalytic materials were washed with toluene and pentane to remove reduced ligands and dried at room temperature under vacuum. This synthetic protocol was applied to all the $\text{Fe}_x\text{Pt}_{100-x}\text{@SILP}$ catalysts where Fe:Pt ratio was modified by adjusting precursors amounts. For comparison purposes, $\text{Fe}_{40}\text{Pt}_{60}$ nanoparticles were synthesized using unmodified silica as a support ($\text{Fe}_{40}\text{Pt}_{60}\text{@SiO}_2$) following the same synthetic protocol.

3.3. Characterization of the catalytic materials

To confirm the ratio of metals and metal loading in $\text{Fe}_x\text{Pt}_{100-x}\text{@SILP}$ materials SEM-EDX and ICP analyses were performed. The results are collected in the Table 3.3.1. Theoretical metal loading was kept at $0.35 \text{ mmol}\cdot\text{g}^{-1}$ till the ratio of metals 40:60, while it was decreased to 0.2 for the ratio 20:80 and to $0.1 \text{ mmol}\cdot\text{g}^{-1}$ for monometallic catalysts to avoid agglomeration of NPs on the surface. Analyzing the obtained data, we found that orders of magnitude in metal loading are correct, although some variations are observed both in ICP and SEM-EDX. ICP gave underestimated values for metal loading and particularly for the Pt mass fraction. It can be explained by incomplete digestion of Pt during ICP sample preparation. In turn, SEM-EDX results in general confirmed the metal ratio, with slightly higher amount of Fe in the bimetallic NPs in each case. Some discrepancy between theoretic and experimental loadings may be because of the small loading of metals, reaching the limits of measurements of SEM-EDX technique.

Table 3.3.1 Metal ratio and loading of NPs determined using SEM-EDX and XPS.

Catalyst	Metal loading [mmol·g ⁻¹]			Metal ratio (%)			
	theor	SEM-EDX	ICP	SEM-EDX		ICP	
				Fe	Pt	Fe	Pt
$\text{Fe}_{80}\text{Pt}_{20}\text{@SILP}$	0.36	0.31 ± 0.02	0.26 ± 0.0	84 ± 1	16 ± 1	84 ± 1	16 ± 1
$\text{Fe}_{60}\text{Pt}_{40}\text{@SILP}$	0.35	0.27 ± 0.01	0.24 ± 0.0	64 ± 2	36 ± 2	65 ± 1	35 ± 1
$\text{Fe}_{50}\text{Pt}_{50}\text{@SILP}$	0.36	0.40 ± 0.02	ND	53 ± 2	47 ± 2	ND	ND
$\text{Fe}_{40}\text{Pt}_{60}\text{@SILP}$	0.37	0.49 ± 0.02	0.25 ± 0.0	42 ± 2	58 ± 2	46 ± 1	54 ± 1
$\text{Fe}_{20}\text{Pt}_{80}\text{@SILP}$	0.19	0.26 ± 0.02	0.11 ± 0.0	19 ± 4	81 ± 4	30 ± 1	70 ± 1
Pt@SILP	0.1	0.14 ± 0.01	0.06 ± 0.0	1 ± 1	99 ± 1	0	100
$\text{Fe}_{40}\text{Pt}_{60}\text{@SiO}_2$	0.35	0.24 ± 0.05	ND	46 ± 3	54 ± 3	ND	ND

Metal loading = (amount of Fe + amount of Pt)/m(ct), Metal ratio = [(amount of Me)/(amount of Fe + amount of Pt)]×100.

Characterization of the $\text{Fe}_x\text{Pt}_{100-x}\text{@SILP}$ materials by TEM evidenced the formation of NPs of around 2 nm on the SILP surface (Figure 3.3.1). We found that increase of Pt content in bimetallic NPs resulted in a little increase in the size and higher aggregation degree of NPs. Luska *et al.* analyzed alloy properties of $\text{Fe}_x\text{Ru}_{100-x}\text{@SILP}$ materials and found higher extend of homoatomic Ru-Ru and Fe-Fe interactions than in a perfect bimetallic structure²²⁵. Accordingly, with our materials we can assume that higher aggregation may be due to strong homophylic Pt-Pt interactions with increasing amount of Pt.

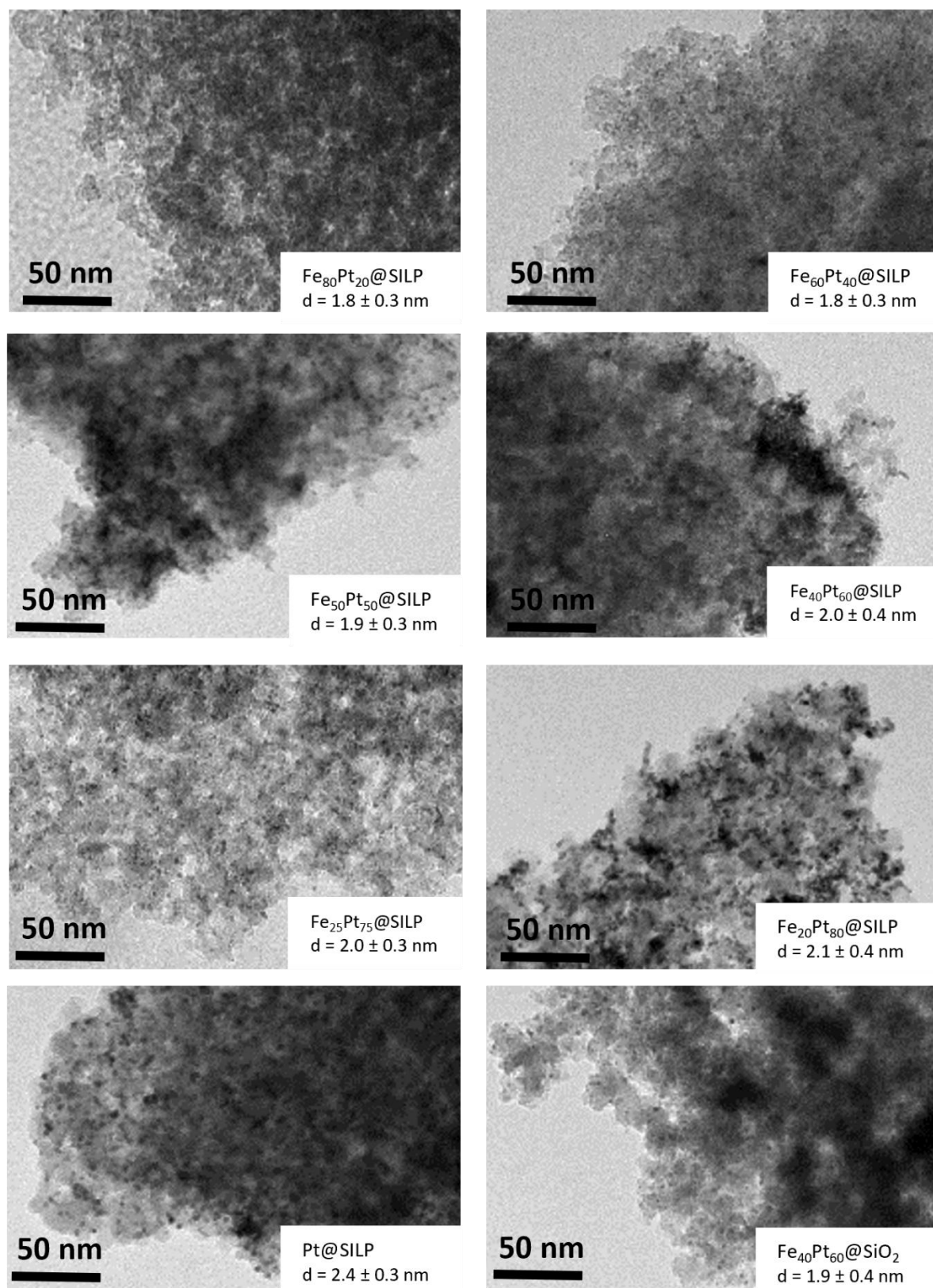


Figure 3.3.1 TEM images of Fe_xPt_{100-x}@SILP and Fe₄₀Pt₆₀@SiO₂ with average sizes of nanoparticles.

Elemental mapping using STEM-HAADF-EDX (STEM – scanning transmission electron microscopy; HAADF - high angle annular dark field; EDX - energy-dispersive X-ray spectroscopy) together with STEM-EDX on single particles confirmed bimetallic nature of Fe₄₀Pt₆₀ NPs (Figure 3.3.2).

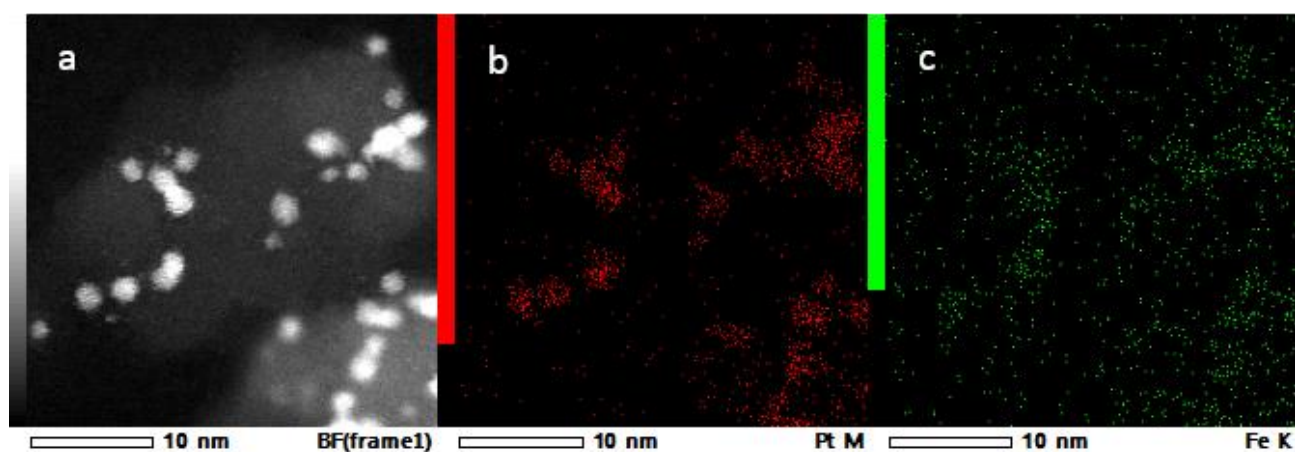


Figure 3.3.2 a) STEM-HAADF image of $\text{Fe}_{40}\text{Pt}_{60}@SILP$, b) STEM-HAADF-EDX elemental mapping of $\text{Fe}_{40}\text{Pt}_{60}@SILP$ looking at Pt, and c) STEM-HAADF-EDX elemental mapping of $\text{Fe}_{40}\text{Pt}_{60}@SILP$ looking at Fe.

$\text{Fe}_x\text{Pt}_{100-x}@SILP$ ($x = 0, 25, 40, 60$) were analyzed by XPS to define the oxidation state of the metals. However, due to the air exposure of the samples the results could not be univocally interpreted. Nevertheless, XPS analysis could be used to confirm the ratio of metals (Table 3.3.2).

Table 3.3.2 XPS results of Me ratio quantification.

Catalyst	Fe	Pt
$\text{Fe}_{60}\text{Pt}_{40}@SILP$	61	39
$\text{Fe}_{40}\text{Pt}_{60}@SILP$	40	60
$\text{Fe}_{25}\text{Pt}_{75}@SILP$	26	74

CO adsorption test was performed with $\text{Fe}_x\text{Pt}_{100-x}@SILP$ ($x = 0, 20, 40, 60, 80$) since it is a sensitive probe for surface electron density alterations²²⁷. The spectra of SILP support and of $\text{Fe}_{40}\text{Pt}_{60}@SILP$ after CO absorption are shown in Figure 3.3.3. The spectrum of SILP shows a broad band around 3500 cm^{-1} , which is typically assigned to hydroxyl groups of silica or water. The signals around 3100 cm^{-1} are characteristic for the C-H stretching of aromatic rings, while absorption bands around 2900 cm^{-1} are assigned to C-H stretching of alkyl moieties. Broad signals at 2000 and 1869 cm^{-1} correspond to the first overtones of Si-O in silica framework²²⁸. Next sharp signals at 1565 cm^{-1} and 1450 cm^{-1} are attributed to aromatic ring symmetric and asymmetric stretching as well as C-H bending vibrations. An absorption band at 1346 cm^{-1} may originate from the counter-anion NTf_2^- and may be attributed to S=O stretch or C-F stretch. A broad band $1000\text{-}1200\text{ cm}^{-1}$ and intense bands at 800 cm^{-1} and 480 cm^{-1} are described in literature as a superposition of different Si-O stretching, Si-O deformation, and Si-O-Si deformation signals. Additionally, this region contains C-H and C-C wagging and bending vibrations that are overlapped with the signals from silica. Spectrum of SILP treated with CO shows no changes, which is expected. However, on the spectrum of $\text{Fe}_{40}\text{Pt}_{60}@SILP$ after CO treatment a new absorption band appears at 2018 cm^{-1} which indicates CO adsorption.

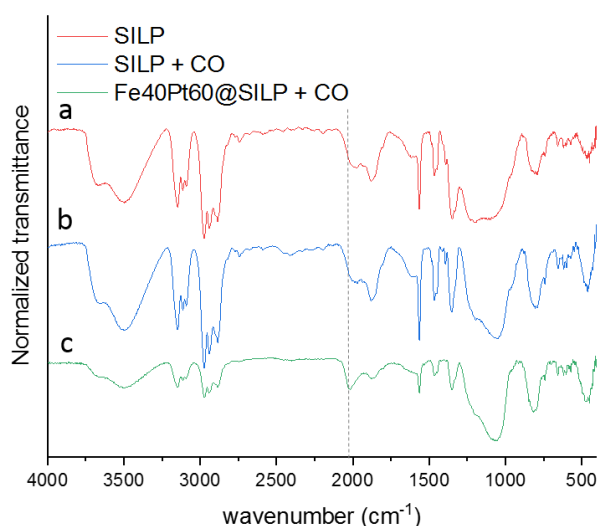


Figure 3.3.3 FTIR spectra of a) SILP, b) SILP+CO, and c) Fe₄₀Pt₆₀@SILP. Gray dash line appears at CO adsorption band (2018 cm⁻¹) of the spectrum c.

The spectra of Fe_xPt_{100-x}@SILP (x = 0, 20, 40, 60, 80) catalysts treated with CO are present in Figure 3.3.4. Pt@SILP spectrum shows a new peak at 2049 cm⁻¹ that is usually attributed to linearly adsorbed CO on small Pt nanoparticles or on low coordination Pt sites¹⁹¹. The wavenumbers of the CO absorption band with bimetallic nanoparticles are lower than for pure Pt in agreement with literature^{229,230}. More precisely, wavenumber of CO vibration on Fe₂₀Pt₈₀ it is equal to 2037 cm⁻¹, on Fe₄₀Pt₆₀ – 2018 cm⁻¹, on Fe₆₀Pt₄₀ – 2034 cm⁻¹, and on Fe₈₀Pt₂₀ – 2043 cm⁻¹. A position of CO absorption band depends on a few factors, namely, the adsorption mode of CO, Pt oxidation state and coordination number, concentration of CO, oxidation state of the support and Fe. In our case the decrease in C-O bond frequency and strength was likely due to the increased π -back donation from Pt that stabilizes Pt-C bond and weakens C-O bond. Consequently, we can assume that Pt could attract electronic density from more electropositive Fe sites. Interestingly, we observe a non-monotonous shift of the CO band with the increase on the Fe content. We suggest that the decrease in a wavenumber from Fe₂₀ to Fe₄₀ may be due to the stronger electron-donation to Pt with increased amount of Fe. Upon further increase of Fe content to Fe₆₀ and Fe₈₀ the wavenumber may increase due to few reasons. On one side, the geometry of the alloy changes with different amount of Fe that may result in different positions and coordination numbers of Pt. On another side, a partial oxidation of Fe during the synthesis is possible since it was already observed for FeRu@SILP that in Fe-rich alloys Fe was partially oxidized even working in inert conditions²²⁵. If in our case there are Fe^{x+} sites being electron-poor they will attract the electron density from Pt. In this case one would expect an absorption band value in the alloy with partially oxidized Fe to be somewhere in between Pt and Fe₄₀Pt₆₀.

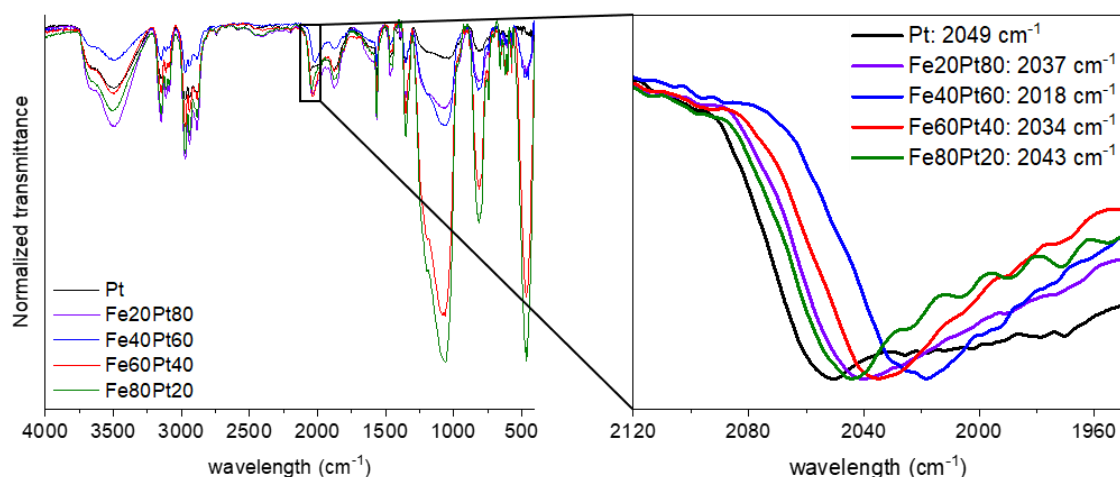


Figure 3.3.4 FTIR spectra of $\text{Fe}_x\text{Pt}_{100-x}@\text{SILP}$ ($x = 0, 20, 40, 60, 80$) with zoom at the region of CO adsorption band.

Magnetometry was performed to find out the oxidation state of Fe sites. While Fe NPs are ferromagnetic, Fe_xO_y NPs show antiferromagnetic behavior. By measuring magnetization vs applied magnetic field one can distinguish contributions of Fe and Fe_xO_y NPs. The measurements were performed with vibrating-sample magnetometer (VSM) in classical mode and by field cooling-zero field cooling (FC/ZFC) experiment. In Figure 3.3.5 magnetization vs applied magnetic fields curves after removal of paramagnetic contribution of $\text{Fe}_x\text{Pt}_{100-x}@\text{SILP}$ with $x = 40, 60,$ and 80 are present. The hysteresis opening and spontaneous magnetization (M_{spont}) of $\text{Fe}_{40}\text{Pt}_{60}$ (see Table 3.3.3) pointed out a ferromagnetic behavior. The same sample after the oxidation in air showed lower values of saturation magnetization and appearance of bis exchange field (H_{ex}). These results suggest the presence of antiferromagnetic iron oxide. For $\text{Fe}_{60}\text{Pt}_{40}@\text{SILP}$, M_{spont} value was observed than in the case of $\text{Fe}_{40}\text{Pt}_{60}@\text{SILP}$, which may be attributed to a partial oxidation of Fe in this sample. $\text{Fe}_{80}\text{Pt}_{20}@\text{SILP}$ had even lower magnetization and appearance of H_{ex} , meaning that even less of metallic iron was present in the sample. In addition, field cooling-zero field cooling experiments (FC/ZFC) showed a field increase at very low temperatures with $x > 60$. Such a behavior at low temperature is a signature of antiferromagnetic states (Figure 3.3.6), attributed to the presence of oxidized species. Also, we noticed a decrease of the blocking temperature T_b from 24 K to 10 K when the proportion of iron increased to from 40 % to 80 %. This trend can be associated to a decrease of the magnetic core size as a function of the partial oxidation of the NPs. For pure $\text{Fe}@\text{SILP}$, an antiferromagnetic or ferrimagnetic state was attributed, meaning that Fe was mostly oxidized during the synthesis. Thus, the results obtained with VSM, in agreement with IR results, support the hypothesis that in the samples where $x > 60$ iron appeared in partially or completely oxidized state.

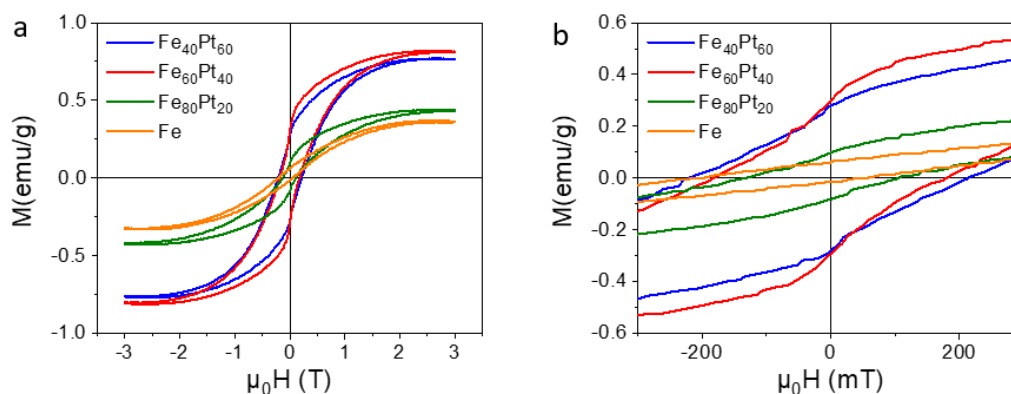


Figure 3.3.5 a) Magnetization vs applied magnetic fields curves of $\text{Fe}_x\text{Pt}_{100-x}\text{@SILP}$ at 5K obtained after paramagnetic contribution removal. b) zoom on the low field magnetization to determine the coercive field ($H_C = \frac{H_C^+ - H_C^-}{2}$) and the exchange bias field ($H_{ex} = \frac{H_C^+ + H_C^-}{2}$).

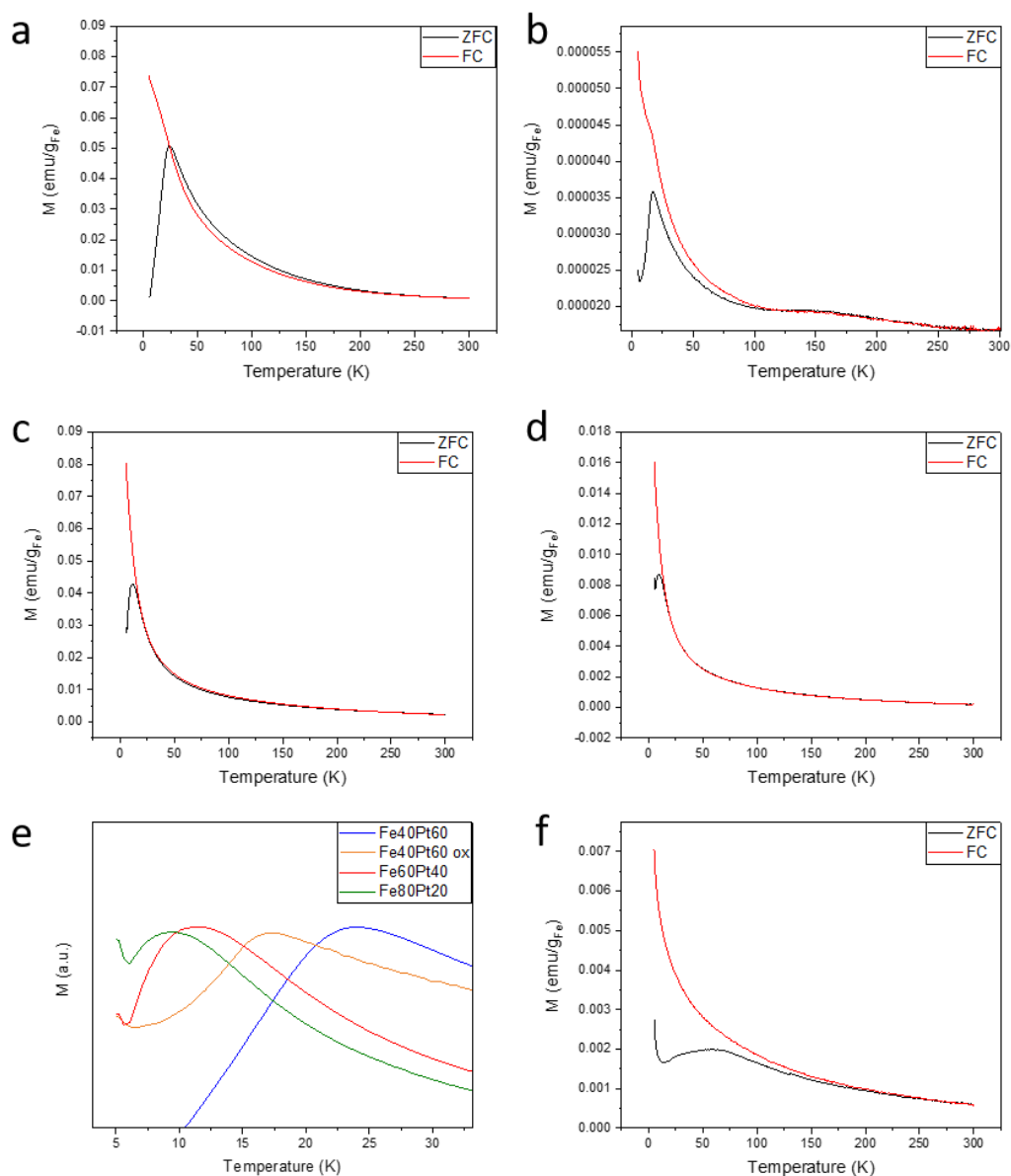


Figure 3.3.6 FC/ZFC curves of a) $\text{Fe}_{40}\text{Pt}_{60}\text{@SILP}$; b) $\text{Fe}_{40}\text{Pt}_{60}\text{@SILP}$ oxidized; c) $\text{Fe}_{60}\text{Pt}_{40}\text{@SILP}$; d) $\text{Fe}_{80}\text{Pt}_{20}\text{@SILP}$; e) normalized curves at low temperature; f) FC/ZFC curve of Fe@SILP .

Table 3.3.3 Coercive field and spontaneous magnetization values for Fe_xPt_{100-x}@SILP samples

Sample	μ_0H_c , mT	μ_0H_{ex} , mT	M_{spont} , emu/g
Fe ₄₀ Pt ₆₀ @SILP	220	-	0.77
Fe ₄₀ Pt ₆₀ @SILP (oxidized)	130	-5	0.20
Fe ₆₀ Pt ₄₀ @SILP	180	-	0.82
Fe ₈₀ Pt ₂₀ @SILP	115	-15	0.44
Fe	125	-75	0.36

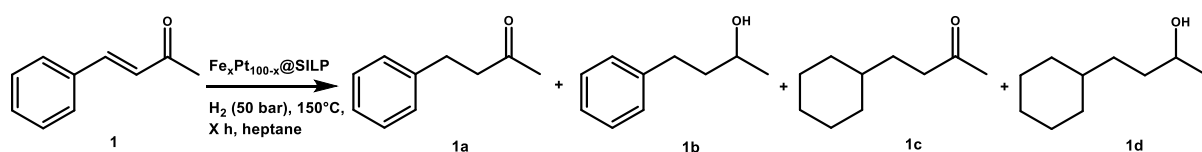
H_c : coercive field, H_{ex} : exchange bias field; M_{spont} corresponds to the spontaneous magnetization, calculated after the removal of the paramagnetic contribution.

3.4. Catalytic performance of Fe_xPt_{100-x}@SILP

3.4.1. Benzylidene acetone hydrogenation

Catalytic activity of the material was examined by hydrogenation of benzylidene acetone (**1**). It possesses an aromatic ring, a conjugated double bond, and a non-benzylic ketone function that allows to systematically study and compare the reactivity of Fe_xPt_{100-x}@SILP catalysts.

Firstly, activity of catalysts synthesized with different Pt precursors was compared, results are summarized in Table 3.4.1. Under standard reaction conditions (1 mol% ct, 50 bar H₂, 150°C) conversion of **1** was complete with Fe₂₅Pt₇₅@SILP(nbe) and Fe₂₅Pt₇₅@SILP(dba) while Fe₂₅Pt₇₅@SILP(cod) showed almost no activity. In the case of Fe₂₅Pt₇₅@SILP(cod) catalyst it was not possible to synthesize NPs using the optimized synthetic procedure so this might be a reason of such low activity. However, we did not investigate this catalyst in details. Among Fe₂₅Pt₇₅@SILP(nbe) and Fe₂₅Pt₇₅@SILP(dba) activity of the latest was higher with formation of 99% of product **1b**, while Fe₂₅Pt₇₅@SILP(nbe) afforded 49% of **1b**. Lower reactivity of Fe₂₅Pt₇₅@SILP(nbe) is expected because of agglomeration of nanoparticles and their bigger size in comparison with Fe₂₅Pt₇₅(dba) NPs. In addition, Pt(nbe)₃ was decomposing during impregnation step, that might affect the surface composition of Fe₂₅Pt₇₅(nbe) NPs. In other words, it is likely, that core of Fe₂₅Pt₇₅(nbe) NPs will be rich in Pt due to the instability of the Pt(nbe)₃ precursor. Consequently, surface of Fe₂₅Pt₇₅(nbe) NPs will have relatively more Fe sites and less Pt sites than Fe₂₅Pt₇₅(dba) surface. An additional hydrogenation test of **1** with Fe₂₅Pt₇₅@SILP(dba) was done increasing time from 5h to 16h. The selectivity towards product **1b** was preserved and no ring hydrogenation was observed, while with monometallic catalyst Pt@SILP(dba) 68% of overhydrogenated product **1d** was formed. Further catalytic performance of only Fe_xPt_{100-x}@SILP(dba) was then investigated.

Table 3.4.1 Hydrogenation of **1** with $\text{Fe}_x\text{Pt}_{100-x}\text{@SILP}$ synthesized from different Pt precursors.

Catalyst	t, h	X (%)	Y 1a (%)	Y 1b (%)	Y 1c (%)	Y 1d (%)
$\text{Fe}_{25}\text{Pt}_{75}\text{@SILP}(\text{nbe})$	5	100	51	49	0	0
$\text{Fe}_{25}\text{Pt}_{75}\text{@SILP}(\text{dba})$	5	100	1	99	0	0
$\text{Fe}_{25}\text{Pt}_{75}\text{@SILP}(\text{cod})$	5	1	1	0	0	0
$\text{Fe}_{25}\text{Pt}_{75}\text{@SILP}(\text{dba})$	16	100	0	100	0	0
$\text{Pt@SILP}(\text{dba})$	16	100	0	32	0	68

Reaction conditions: Catalyst (0.005 mmol [Me]), substrate (0.5 mmol, 100 eq.), heptane (0.5 mL), H_2 (50 bar), 150°C. Yield is determined as an average of two runs by GC-FID using tetradecane as an internal standard. X = conversion, Y = yield.

3.4.2. Acetophenone hydrogenation and hydrodeoxygenation

Acetophenone (**2**) is a benzylic ketone that can be used as prototype molecule for HDO of biomass-derived ketones. As reported in the literature, an HDO catalyst usually consists of two parts: hydrogenation catalyst (transition metal) and Lewis acid or Bronsted acid catalyst (reducible metal oxides, zeolites, adsorbed acids)^{231–235}. Using such a catalyst products **2c** and **2e** can be obtained (Figure 3.4.1a). Using monometallic Pt catalyst hydrogenation activity with formation of products **2a**, **2b**, and **2d** is expected.

Figure 3.4.1 b shows conversions and product yields as a function of Pt content in $\text{Fe}_x\text{Pt}_{100-x}$ NPs where all the reactions were performed under identical conditions ($T = 175^\circ\text{C}$, $p(\text{H}_2) = 50$ bar, $t = 16$ h, solvent = heptane). Starting from pure Fe, there was no product formation. An alloy of $\text{Fe}_{80}\text{Pt}_{20}\text{@SILP}$ gave 34% of conversion with a major product **2a** (30%). With $\text{Fe}_{60}\text{Pt}_{40}\text{@SILP}$ catalyst conversion reached 100% and we already could see a sufficient amount of deoxygenated product **1c** (45%), which further increased using $\text{Fe}_{50}\text{Pt}_{50}\text{@SILP}$ and reached a maximum of 84 % of selectivity using the $\text{Fe}_{40}\text{Pt}_{60}\text{@SILP}$ catalyst. Remarkably, this was the first time when bimetallic nanoparticles on unmodified SILP (*i.e.* without any additional acid functionalities) could catalyze hydrodeoxygenation of unsubstituted acetophenone. However, when going to $\text{Fe}_{20}\text{Pt}_{80}\text{@SILP}$, the products with reduced aromatic ring **2d** (53%) and **2e** (5%) were formed. Based on this result we assume that 80% of Pt in the alloy led to the formation of Pt atom ensembles that are big enough to enable planar adsorption and hydrogenation of the aromatic ring. In case of monometallic Pt@SILP, hydrogenation of **2** led to the overhydrogenated product **2d** in 93% yield as it was expected

for noble metal catalyst. The same catalytic test was also performed with $\text{Fe}_{40}\text{Pt}_{60}@SiO_2$. In this case a large amount of products with saturated ring **2d** (14%) and **2e** (43%) were formed. This result indicates that in the sample there are parts where sufficiently big Pt domains exist, so it is not possible to have a controlled formation of bimetallic $\text{Fe}_{40}\text{Pt}_{60}$ NPs on unmodified silica support, in agreement with previous observations^{225,236}.

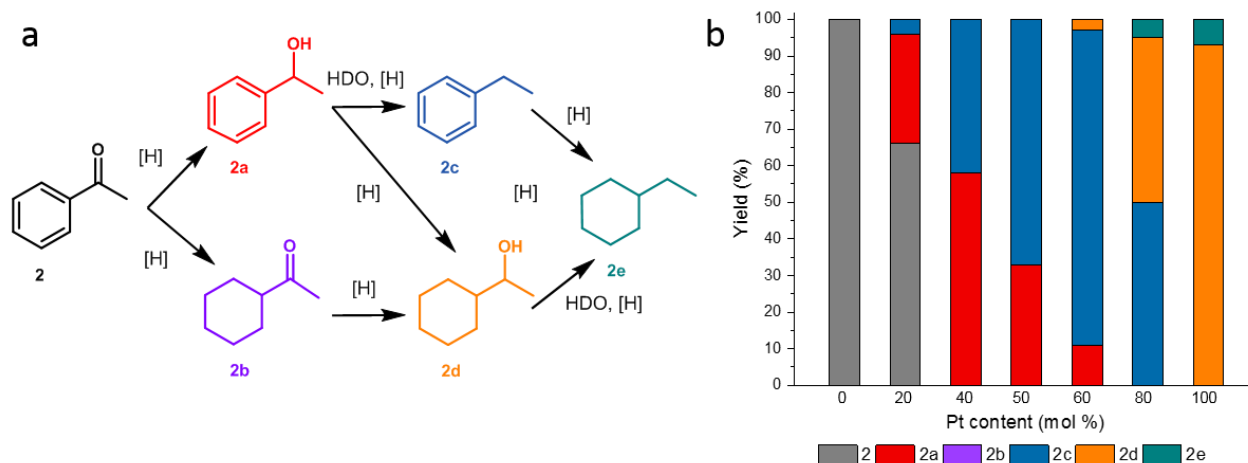


Figure 3.4.1 a) Reaction pathways for the hydrogenation ([H]) and hydrodeoxygenation (HDO) of acetophenone, b) Hydrogenation of acetophenone using a series of $\text{Fe}_x\text{Pt}_{100-x}@SILP$ catalysts with different Fe:Pt ratios. Reaction conditions: catalyst (0.005 mmol [Me]), substrate (0.125 mmol, 25 eq.), heptane (0.5 mL), H_2 (50 bar), 175°C, 16 h. Yield is determined by GC-FID using tetradecane as an internal standard. Data points are average value of minimum two experiments.

To obtain more details about catalyst reactivity, time profiles of product formation were recorded using $\text{Fe}_{40}\text{Pt}_{60}@SILP$ and $\text{Fe}_{20}\text{Pt}_{80}@SILP$ (Figure 3.4.2). In both cases a full conversion of **2** was observed after 1h of reaction, however, there were significant differences in selectivity. In case of $\text{Fe}_{40}\text{Pt}_{60}@SILP$ 55% of aromatic alcohol **2a**, 43% of hydrodeoxygenated product **2c** and 2% of saturated alcohol **2d** were formed. Further, slow deoxygenation of **2a** to **2c** proceeded with the **2c** yield of 95% after 24h of reaction, while **2d** yield reached maximum of 4%. This low yield of the product **2d** indicates that 40% of Fe in the alloy shut down hydrogenation of the aromatic ring. On the contrary, using $\text{Fe}_{20}\text{Pt}_{80}@SILP$ significant amount of saturated alcohol **2d** was produced (50%) from the first hour of the reaction. After 16 h of reaction 42% of product **2c** and 52% of product **2d** were found in the reaction mixture. This observation let us conclude that hydrogenation of the C=O double bond and hydrogenation of the aromatic ring proceeds much faster than the deoxygenation reaction. Interestingly, we observed poor aromatic ring hydrogenation of **2c** to form **2e** (4%). To obtain more details about the ring hydrogenation ability of catalysts, ethylbenzene hydrogenation tests were conducted. $\text{Fe}_{20}\text{Pt}_{80}@SILP$ showed 2% of conversion while complete conversion was achieved with monometallic catalyst Pt@SILP and $\text{Fe}_{40}\text{Pt}_{60}@SiO_2$ (Table 3.4.2). A possible explanation of such selectivity could lay in poor polarity of substrates. We can assume that once a

nonpolar product **2c** is formed it is easily desorbed from the surface that contains an ionic liquid and $\text{Fe}^{\delta+}\text{-Pt}^{\delta-}$ sites. On the contrary, on monometallic Pt surface as well as with $\text{Fe}_{40}\text{Pt}_{60}@SiO_2$, hydrogenation of an aromatic ring can easily proceed with formation of **2e**.

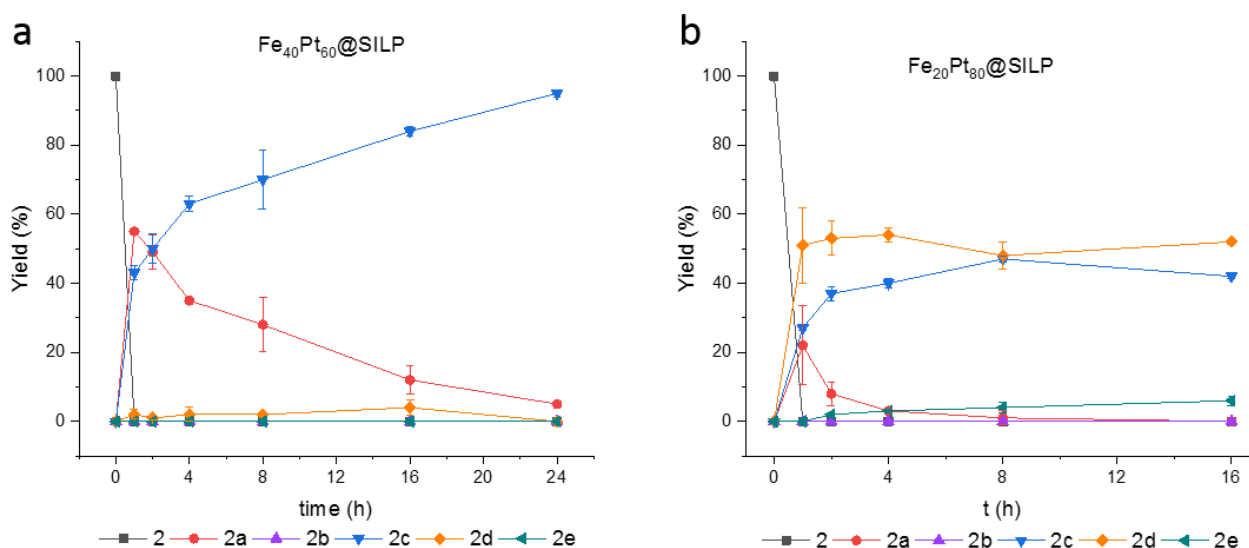
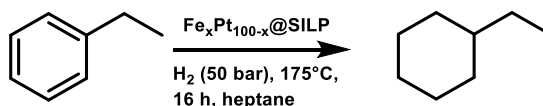


Figure 3.4.2 Time profiles of acetophenone hydrogenations recorded using a) $\text{Fe}_{40}\text{Pt}_{60}@SiO_2$, b) $\text{Fe}_{20}\text{Pt}_{80}@SiO_2$. Reaction conditions: Catalyst (0.005 mmol [Me]), substrate (0.125 mmol, 25 eq.), heptane (0.5 mL), H_2 (50 bar), 175°C . Yield is determined as by GC-FID using tetradecane as an internal standard. Data points are average value of minimum two experiments and error bars represent standard deviations.

Table 3.4.2 Hydrogenation of ethylbenzene (**2c**) with $\text{Fe}_{20}\text{Pt}_{80}@SiO_2$, Pt@SILP, and $\text{Fe}_{40}\text{Pt}_{60}@SiO_2$ catalysts.



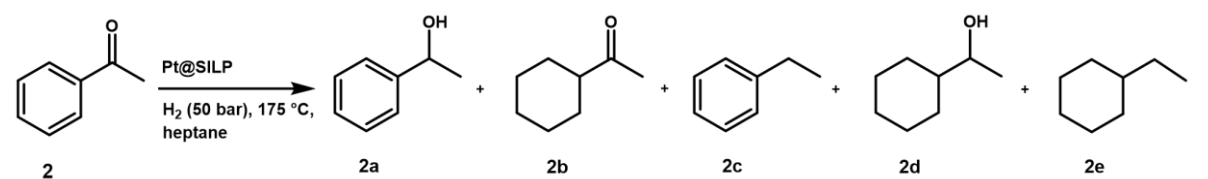
Entry	catalyst	X (%)
1	$\text{Fe}_{20}\text{Pt}_{80}@SiO_2$	2
2	Pt@SILP	100
3	$\text{Fe}_{40}\text{Pt}_{60}@SiO_2$	100

Catalyst (0.005 mmol [Me]), substrate (0.125 mmol, 25 eq.), heptane (0.5 mL). Conversion is determined as average value of minimum two experiments by GC-FID using tetradecane as internal standard. X = conversion.

To find out what were the intermediates in hydrogenation reaction with Pt@SILP, an excess (1500 eq) of **2** was used in the 2h reaction (Table 3.4.3). At 79% of conversion 52% of unsaturated alcohol **2a** together with 13% of saturated ketone **2b** and 14% of the final product **2d** were formed. It suggests that both product **2a** and **2b** are the intermediate states but hydrogenation of C=O double bonds proceeds faster than ring hydrogenation. Interestingly, for bimetallic $\text{Fe}_x\text{Pt}_{100-x}@SiO_2$

catalyst formation of intermediate **2b** was never observed suggesting suppressing of ring hydrogenation with Fe addition.

Table 3.4.3 Hydrogenation of acetophenone (**2**) with Pt@SILP catalyst.

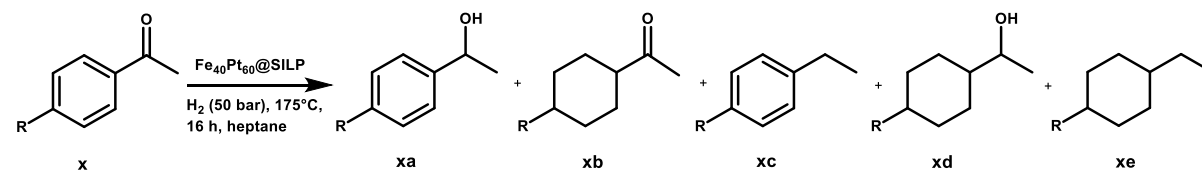


Entry	t, h	Eq 2	X (%)	Y 2a (%)	Y 2b (%)	Y 2c (%)	Y 2d (%)	Y 2e (%)
1	1	25	>99	0	0	0	>99	0
2	1	100	>99	3	0	0	97	0
3	2	1500	79	66	17	0	17	0

Catalyst (0.00125 mmol [Me]), heptane (0.5 mL) H₂ (50 bar), 175°C. Conversion is determined as average value of minimum two experiments by GC-FID using tetradecane as internal standard. X = conversion, Y = yield.

To study the versatility of the catalyst in hydrodeoxygenation reaction para-substituted acetophenone derivatives were chosen for a scope. The results are summarized in Table 3.4.4. A reaction with Fe₄₀Pt₆₀@SILP under standard conditions (H₂ (50 bar), 175°C, 16 h) resulted in full or partial hydrodeoxygenation. Electron-donating substituents increased hydrodeoxygenation rate of acetophenones thus excellent yields of **xc** were achieved (96–>99%). Such increased activity is probably due to a mesomeric and inductive stabilization of the intermediate carbocation. Hydrogenation of acetophenone with electron-withdrawing CF₃ group slowed down the reaction and led to 70% of deoxygenated product, consistent with previous observations^{205,207}.

Table 3.4.4 Selective hydrogenation of acetophenone derivatives using Fe₄₀Pt₆₀@SILP.



Entry	R	X (%)	Y xa (%)	Y xb (%)	Y xc (%)	Y xd (%)	Y xe (%)
1	OCH ₃	>99	0	0	>99	0	0
2	CH ₃	>99	0	0	>99	0	0
3 ^a	Cl	>99	0	0	96	0	0
4 ^a	F	>99	1	0	97	0	0
5	CF ₃	>99	30	0	70	0	0

Reaction conditions: Catalyst (13.6 mg, 0.005 mmol [Me]), substrate (0.125 mmol, 25 eq.), heptane (0.5 mL), H₂ (50 bar), 175°C, 16 h. Conversion and yield are determined by GC-FID using tetradecane as internal standard. Data points are average value of minimum two experiments. X = conversion, Y = yield. ^a side product is **1c**.

For deoxygenation reaction, Bronsted or Lewis acids are required in order to activate a C-O bond. In our case we suppose that oxophilic iron can act as weak Lewis acid sites and interact with aryl C-O bond. Similar explanations were proposed for amides HDO with PtV catalyst²³⁷, furfural HDO with PtFe²¹⁶ catalyst or selective hydrogenation of C=O function of unsaturated aldehydes with PtFe or PtSn catalysts¹⁷⁰.

3.4.3. Selective hydrogenation of unsaturated aldehydes

Selective hydrogenation of allylic aldehydes to unsaturated alcohols is a commercially important industrial process, particularly in fragrance and flavors^{238–240}, agricultural and pharmaceutical sectors²⁴¹. Most groups investigate cinnamaldehyde ((E)-3-phenylprop-2-enal) (**3**) (Figure 3.4.3) hydrogenation since it is a substrate that contains unsaturated polar and unpolar bonds and aromatic ring, so selectivity of the catalyst can be finely tested with this substrate. The most interest present intermediates **3a** and **3b**. Depending on nature of a catalyst a non-polar C=C double bond or a polar C=O double bond can be hydrogenated first. While for noble catalysts hydrogenation of nonpolar unsaturated bonds is typical and product **3b** is expected, diluting a catalyst with oxophilic metal can activate another reaction pathway with hydrogenation of the polar C=O bond and formation of a desired product **3a**. Although FePt nanoparticles are reported in the literature as a selective hydrogenation catalyst for unsaturated aldehydes^{171,211,214,242,243}, we wanted to compare our Fe₄₀Pt₆₀@SILP system in this transformation.

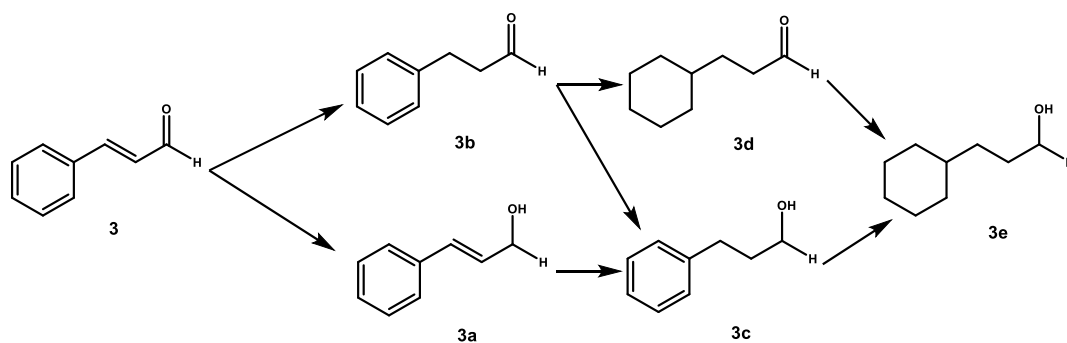
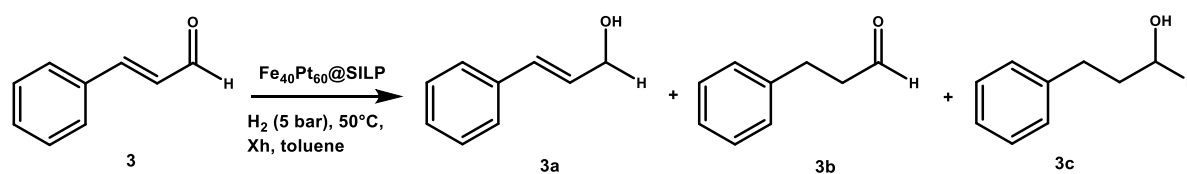


Figure 3.4.3 Scheme with possible products of hydrogenation of a cinnamaldehyde (**3**).

Using Fe₄₀Pt₆₀@SILP and initial reaction conditions (5 bar H₂, 50°C, 2h toluene) we observed formation of **3a** (47% of yield at 48% of conversion) (Table 3.4.5) that is consistent with observations in the literature for the reactivity of FePt NPs^{172,244}. Remarkably, when increasing reaction time to 16h at 100% conversion only 7% of saturated alcohol **3c** were formed. Only in a few papers this excellent selectivity towards unsaturated alcohol **3a** was shown at full conversion with extended reaction times. Usually it is explained by interaction with transition metals^{245,246} or by acidity and

steric effects of supports^{168,247,248}. We can assume that in accordance with the results in the literature²⁴⁹, both steric and electronic effects hampers C=C adsorption and hydrogenation.

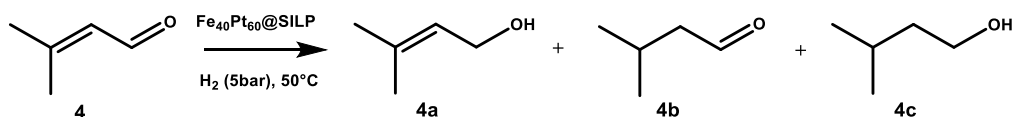
Table 3.4.5 Hydrogenation of cinnamaldehyde with Fe₄₀Pt₆₀@SILP.



Entry	t, h	X (%)	Y 3a (%)	Y 3b (%)	Y 3c (%)
1	2	48	47	0	1
2	6	93	89	0	4
3	16	>99	93	0	7

Reaction conditions: Catalyst (13.6 mg, 0.005 mmol [Me]), substrate (0.5 mmol, 100 eq.), toluene (0.5 mL), H₂ (5 bar), 50°C. Conversion and yield are determined by GC-FID using dodecane as internal standard. Data points are average value of minimum two experiments. X = conversion, Y = yield.

An aliphatic conjugated substrate, prenal (3-methylbut-2-enal) (**4**), was also tested in hydrogenation with Fe₄₀Pt₆₀@SILP (Table 3.4.6). Using mesitylene as reaction medium in 4 h yield of **4a** was 66% at 72% of conversion. Importantly, in 16h high yield of **4a** was preserved (79%). By using isopropanol in 4h reaction conversion increased to 92% keeping excellent selectivity towards unsaturated alcohol **4a** (Y = 86%). Importantly, no acetals formation was observed at chosen reaction conditions. An additional test in i-PrOH was performed in the absence of hydrogen. No conversion was observed that rules out possibility of transfer hydrogenation with autooxidation of isopropanol. However, we cannot discard a possibility of i-PrOH serving as a hydrogen source. Recently, Cardona-Farreny and colleagues performed DFT calculations of furfural hydrogenation with RuNi NPs in isopropanol²⁵⁰. The result suggested that the solvent can adsorb on the support and give a hydride to hydrogenate the substrate. Another explanation of the activity increase with isopropanol is that polar solvent molecules could promote the adsorption and activation processes of hydrophilic C=O bonds. Indeed, reports where influence of solvent polarity is discussed suggest that polar solvents boost the hydrogenation of C=O bonds and raise the selectivity towards the unsaturated alcohol^{251–253}.

Table 3.4.6 Prenal hydrogenation with Fe₄₀Pt₆₀@SILP.

Entry	Solvent	t, h	X (%)	Y 4a (%)	Y 4b (%)	Y 4c (%)
1	Mesitylene	4	72	66	1	6
2	Mesitylene	16	87	79	0	8
3	i-PrOH	4	92	86	0	6
4 ^a	i-PrOH	4	0	0	0	0

a – test without H₂. Reaction conditions: Catalyst (13.6 mg, 0.005 mmol [Me]), substrate (0.5 mmol, 100 eq.), solvent (0.5 mL), H₂ (5 bar), 50°C, 4h. Conversion and yield are determined by GC-FID using dodecane as internal standard. Data points are average value of minimum two experiments. X = conversion, Y = yield.

3.4.4. Hydrogenation of other substrates

FePt catalytic materials were tested in hydrogenation of amides **5**, **6**, an ester **7**, and an acid **8** (Figure 3.4.4). No reaction was observed with these substrates, meaning that activation of N-O bond of amides and C-O bond in acids and esters cannot proceed. However, these tests were performed with one of the first batches - Fe₂₅Pt₇₅@SILP synthesized in non-optimized conditions (THF as a solvent). New attempts of hydrogenation of these substrates with optimized batches of the catalyst were not performed due to the limited time of the internship.

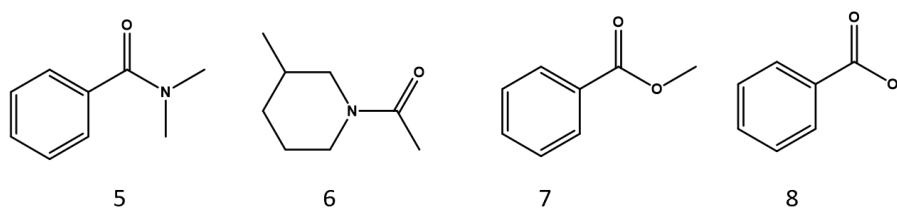


Figure 3.4.4 Other substrates tried in hydrogenation. Conditions for substrates 5,6: Catalyst (0.005 mmol [Me]), substrate (0.125 mmol, 25 eq.), mesitylene (0.5 mL), H₂ (50 bar), 150°C, 48h. Conditions for substrates 7,8: Catalyst (0.005 mmol [Me]), substrate (0.5 mmol, 100 eq.), heptane (0.5 mL), H₂ (50 bar), 150°C, 16h.

3.5. Conclusions

This chapter was dedicated to investigation of new catalytic materials - Fe_xPt_{100-x}@SILP. The work has been performed in collaboration with Alexis Bordet at the Max Planck Institute for Chemical Energy Conversion (MPI CEC) in Mulheim an der Ruhr, Germany. In particular, high-pressure tests and synthetic optimization were conducted at MPI CEC during two stays for four months in total, while syntheses of final catalysts and low-pressure tests were performed at the LPCNO.

FePt NP were synthesized in the presence of imidazolium-based SILP support following an organometallic approach. Limitations in precursor and solvent choice were discussed in the section of synthesis optimization. Following an optimized synthetic procedure small (2 nm) bimetallic nanoparticles were obtained regardless Fe/Pt ratio.

As prepared materials were analyzed with variety of techniques, precisely with TEM and HR-TEM for nanoparticles size and distribution, with SEM-EDX, STEM-EDX, ICP, and XPS for metal loading and metal ratio, with VSM and $\text{IR}_{\text{CO ads}}$ for electronic state of metals and electron density distribution on surface. VSM results pointed out that with the Fe content higher than 60% partial oxidation of iron took place. With IR experiments we observed an increase in electron density on Pt sites of bimetallic nanoparticles comparing to pure Pt, probably due to electron donation from Fe to more electronegative Pt. We suppose that this effect contributes to catalysts selectivity in hydrogenation of C=O bonds.

The catalytic materials were tested in hydrogenation of non-benzylic and benzylic ketones. The products of ketone hydrogenation were dependent on Fe/Pt ratio. Namely, we found that 25% or more of Fe in the alloy is enough to preserve aromaticity of the ring, even working at relatively harsh hydrogenation conditions (50 bar of H_2 , 150 or 175°C). Interestingly, during catalysis of benzylidene acetone, only hydrogenated products were observed, whereas with acetophenone substrate both hydrogenation and deoxygenation activity took place. The best results were obtained with $\text{Fe}_{40}\text{Pt}_{60}@\text{SILP}$ catalyst yielding 95% of ethylbenzene. Deoxygenation of benzylic ketones was shown on example of five other para-substituted acetophenones, with excellent yields for electron-donating substituents and a bit lower activity for electron-withdrawing groups. Interestingly, no overhydrogenation of ethyl benzene ring was observed, probably due to significant difference in polarity of the substrate and the catalytic surface.

Selective hydrogenation of conjugated aldehydes (cinnamaldehyde and prenal) was also successfully performed. High yields of unsaturated alcohols at full or almost full conversions were achieved thanks to the combination of electronic properties that appear with dilution of Pt with Fe and steric properties of the support.

To sum up, a combination of IL modified support and bimetallic nanoparticles resulted in an active hydrogenation catalyst where by simple modification of metal ratio a precise control of selectivity can be achieved.

3.6. Experimental part

3.6.1. General

Synthesis of $\text{Fe}_x\text{Pt}_{100-x}\text{@SILP}$ and $\text{Fe}_{40}\text{Pt}_{60}\text{@SiO}_2$, and preparation of catalytic solutions were carried out under an inert atmosphere in the glovebox and using standard Schlenk techniques. The synthesized nanoparticles were stored in the glovebox. $\text{Fe}_2[\text{N}(\text{Si}(\text{CH}_3)_3)_2]_2$, $\text{Pt}(\text{nbe})_3$, $\text{PtMe}_2(\text{cod})$, and $\text{Pt}_2(\text{dba})_3$ were purchased from NanoMePS. SILP support was synthesized in the team according to previously reported procedure¹²² and was stored under inert conditions. All the substrates were purchased from commercial sources. They were degassed and stored in the glovebox. Solvents were collected from an MBraun purification system and degassed.

3.6.2. Analytics

TEM images were collected using a JEOL JEM 1400 operated at 120kV and using a tungsten filament. The NP size and distribution was determined from the measurement of over 150 particles.

HRTEM analysis was performed using a Probe Corrected JEOL JEM-ARM200F Cold FEG equipped with a High Angle EDX detector working at 200 kV.

SEM-EDS was performed on a JEOL JSM 7800F operated at 10 kV with a thermally assisted Schottky electron gun and equipped with a Bruker XFlash 6|60 detector (silicon drift detector technology).

FTIR spectra were measured inside a glovebox, using a Bruker Alpha spectrometer in transmission mode. The samples were mixed with KBr and pressed in pellets.

GC was performed on a Shimadzu GC-2030 equipped with an FID-detector and a CP-WAX-52CB column from Agilent. Gas chromatography coupled with a mass spectrometer (GC-MS) were performed on a Shimadzu QP2020. The peaks were assigned by injection of the pure substances or by mass spectrometry (GC-MS). For quantification, tetradecane or dodecane were added as internal standards. The correction factors were determined by calibration of the pure substances in relation to the internal standard.

3.6.3. Experimental procedures

Synthesis of $\text{Fe}_x\text{Pt}_{100-x}\text{@SILP}$

Synthesis $\text{Fe}_x\text{Pt}_{100-x}\text{@SILP}$ followed the same synthetic procedure regardless Fe/Pt ratio. Thus, only a synthesis of $\text{Fe}_{40}\text{Pt}_{60}\text{@SILP}$ will be presented as an example.

$\text{Fe}_{40}\text{Pt}_{60}\text{@SILP}$

A solution of $\text{Fe}_2[\text{N}(\text{Si}(\text{CH}_3)_3)_2]_2$ (15 mg, 0.02 mmol Fe) in THF (2 mL) was combined with a solution of $\text{Pt}_2(\text{dba})_3$ (33 mg, 0.03 mmol Pt) in anisole/THF (4/3 mL) in a Fischer-Porter bottle (100 mL). The SILP powder (250 mg) was consequently added to the solution of the metal precursors and the reaction mixture was stirred under argon at room temperature for 2h to allow precursors impregnation. Then, outside the glovebox the vessel was filled with 3 bar of H_2 and left stirring at room temperature for 4h. After this time formation of black powder was observed that indicated formation of NPs. Later, the powder was washed with toluene (10 mL two times) and pentane (10 mL one time), and dried under vacuum at room temperature.

Yield: 253 mg (96%)

CO adsorption test

In a typical CO adsorption experiment a catalyst powder sample (20-30 mg) was placed in a Fischer-Porter bottle (FP) equipped with a manometer head. Then, the bottle was charged with 3 bar of H_2 and left for 18h. Next morning, CO was evacuated during 10 minutes with vacuum line. Then, FP was placed in the glovebox where the powder (10 mg) was mixed with KBr (50 mg) and pressed in pellets. Pellets were analyzed in the glovebox with a Bruker Alpha IR spectrometer in transmission mode.

Catalytic tests in autoclave

A catalyst (0.005 mmol metal), substrate (100 eq (0.5 mmol) or 25 eq (0.125 mmol)) and solvent (heptane, 0.5 mL) were weighed in a glovebox into the autoclave vessel (10 mL). The autoclave was closed, transferred out of the glovebox and pressurized with 50 bar of hydrogen. The autoclave was stirred (500 rpm) at 150 or 175 °C for a certain amount of time. After the reaction the autoclave was cooled down in a water bath and depressurized. GC samples were prepared by filtering a sample through a syringe filter. A tetradecane (internal standard, 20 mg) and hexane (500 mg) were added to the solution that was consequently analyzed with GC-FID.

Catalytic tests in a Fischer-Porter bottle

Catalytic reactions in a Fischer-Porter bottle (100 mL) were performed in the similar manner to autoclave reactions. The reaction solution was prepared in the glovebox, outside charged with 5 bar of hydrogen and left stirring (700 rpm) for a certain amount of time at 50°C. Later, the bottle was cooled down and analyzed with GC-MS using dodecane as an internal standard.

CHAPTER 4. Platinum-porphyrin photoactive nanomaterials

4.1. Introduction to energy transfer in NP-porphyrin hybrid systems	122
4.2. Building blocks	125
4.3. Synthesis of the Pt NP-porphyrin systems	127
4.4. Influence of the porphyrin structure on the SA of NPs	127
4.5. Photophysical response	131
4.5.1. Absorption and emission of the porphyrins	131
4.5.2. PL quenching mechanisms	133
4.5.3. Dynamic quenching	134
4.5.4. Static quenching	137
4.5.5. Electrical properties of the hybrid systems	138
4.6. Conclusions	139
4.7. Experimental part	140
4.7.1. General	140
4.7.2. Analytics	140
4.7.3. Experimental procedures	142

4.1. Introduction to energy transfer in NP-porphyrin hybrid systems

As it was shown in the literature review, porphyrins can be both photosensitizers (PS) and active catalysts. As a PS, a porphyrin in an excited state transfers energy gained from the light to the acceptor. Depending on the distances between the donor and the acceptor, energy transfer processes can be divided into two groups: 1) long-distance interactions, such as Förster resonance energy transfer (FRET) and 2) short-distance interactions, which include Dexter energy transfer and light-induced electron transfer. FRET takes place through nonradiative dipole–dipole coupling between donor and acceptor which appears at distances of 1–10 nm, whereas short-range processes require an overlap of wavefunctions (<1nm).

According to the definition of Lakowicz, FRET presents simultaneous electron transitions in donor and acceptor molecules where the excited electron of a donor comes back to the ground state while the electron of acceptor gets excited (Figure 4.1.1 a)²⁵⁴. Consequently, the donor can release a photon of lower energy or dissipate the energy in the form of heat. FRET is a non-radiative process; however, it requires overlapping of the donor's emission band and acceptors adsorption to have enough resonance energy to excite the acceptor. Fluorophore and acceptor may be free in solution or they may diffuse together as parts of one system, for example in a complex, or attached to a protein.

Dexter energy transfer is defined as an exchange of electrons between the donor and the acceptor. Precisely, the excited electron of the donor LUMO state is transferred to the LUMO state of the acceptor; meanwhile, the acceptor transfers its electron from the HOMO orbital to the HOMO orbital of the donor (Figure 4.1.1 b). In this way, an electron balance is preserved but the energy is transferred in the form of an excited electron. Compared to FRET, Dexter electron exchange is a less common event since it requires closer interactions.

A triplet-triplet annihilation is a special case of Dexter energy exchange. Here, a donor in excited state undergoes intersystem crossing resulting in a change of multiplicity from singlet to triplet excited state: ${}^1D^* \rightarrow {}^3D^*$. In this state a donor can interact with molecules in triplet state like oxygen which will lead to energy exchange and change in multiplicity: ${}^3D^* + {}^3A \rightarrow {}^1D + {}^1A^*$.

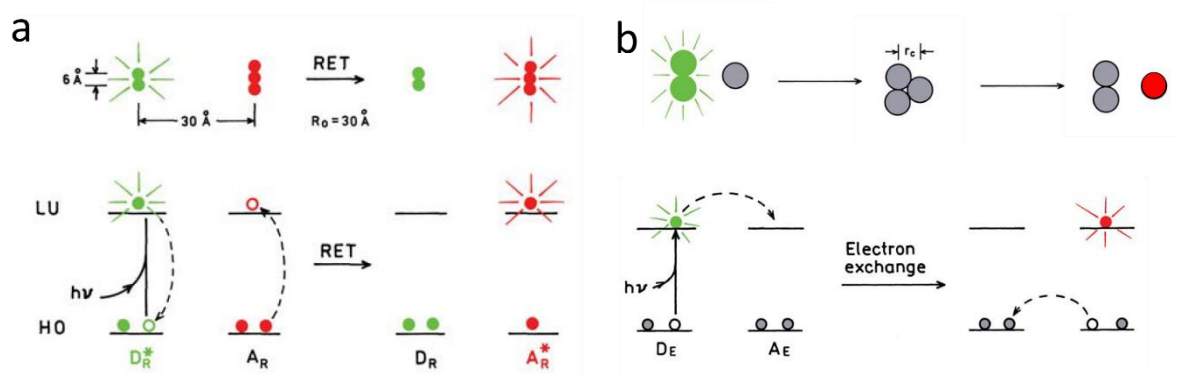


Figure 4.1.1 a) illustration of mechanism of FRET; b) illustration of mechanism of Dexter energy transfer. Adapted from ref²⁵⁴.

Energy transfer from porphyrins found an application in biomedicine, particularly in photodynamic therapy (PDT)^{255–257}. PDT is a type of anticancer therapy which uses a PS to produce reactive oxygen species to cause irreversible damage to the cells. There, a fluorophore gets excited by light and undergoes intersystem crossing. From this state, it transfers energy to surrounding oxygen molecules through triplet-triplet annihilation which transforms triplet oxygen to highly toxic singlet oxygen. Alternatively, a PS can get oxidized or reduced through photoinduced electron transfer generating various reactive radicals which damage cells (Figure 4.1.2).

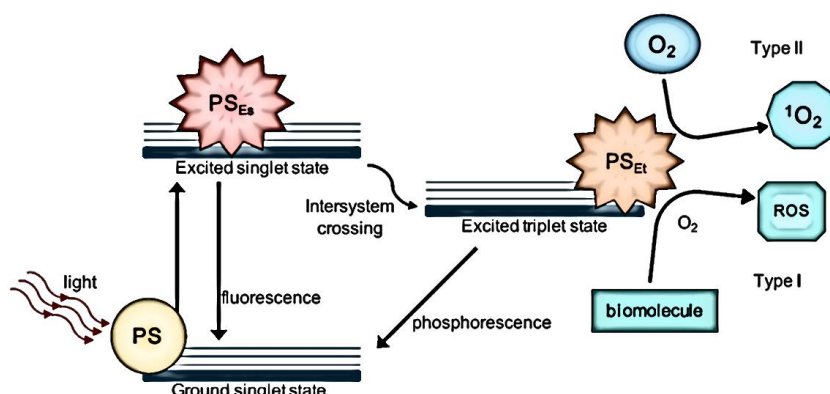


Figure 4.1.2 Jablonski's diagram showing PDT mechanisms. Adapted from ref⁴.

Alea-Reyes and coworkers developed a system that contained Au NPs stabilized with α -thio- ω -carboxy-polyethylene glycol, to make the nanoparticles water-soluble, and pyridinium salt, which acted as a host to incorporate negatively charged zinc porphyrin (Figure 4.3)¹³². This system showed promising results in singlet oxygen generation. Interestingly, the activity of the porphyrin electrostatically attached to Au NPs was higher than of the uncharged porphyrin in solution. Authors ascribed the activity enhancement to highly localized plasmonic field of the Au NP, however no supporting experiments were reported.

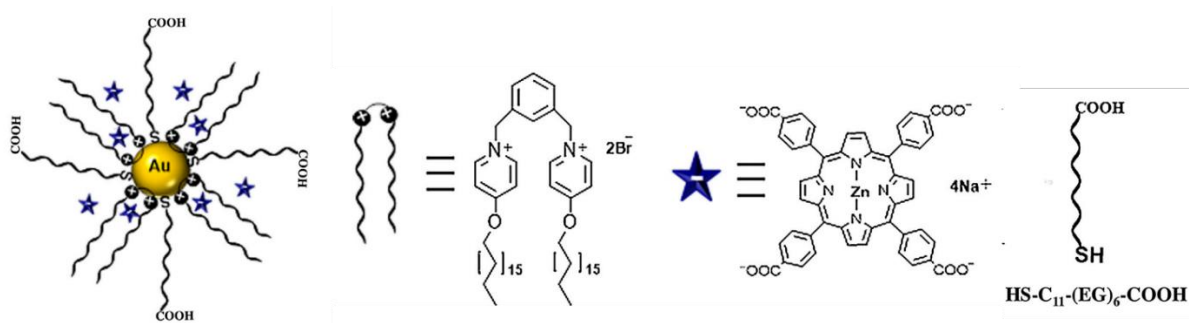


Figure 4.1.3 Illustration of Au NPs-Zn-porphyrin hybrid system. Adapted from ref¹³².

Photoinduced electron transfer is the third important quenching mechanism. In excited state, donor can transfer an electron to an acceptor with a suitable redox potential which leads to the formation of the short-living excited-state donor-acceptor complex. Further, this charge-transfer complex nonradiatively returns to the ground state as an oxidized donor and reduced acceptor. Certainly, an inversed situation where excited fluorophore acts as an electron acceptor also takes place. Applications of photoinduced electron transfer from and to porphyrins were already discussed in the Chapter 1, here I would like to present only one example of Pt-porphyrin hybrid system developed by Zhu and coworkers. In their study Pt NPs were stabilized with anthracene-modified porphyrin²⁵⁸. An intramolecular FRET from anthracene moieties to porphyrin macrocycle and consequent electron transfer to Pt surface was observed (ethanol as a sacrificial electron donor). The proposed mechanism was confirmed by time-resolved photoluminescence (TRPL) analysis where new short-lived excited states were identified. The hybrid system could efficiently catalyze HER under simulated solar irradiation.

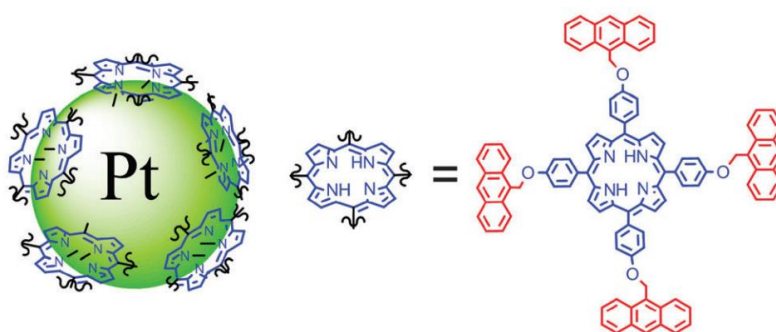


Figure 4.1.4 Illustration of hybrid materials of Pt NP covered with anthracene-porphyrins. Reprinted from ref²⁵⁸.

4.2. Building blocks

Porphyrins are macrocyclic compounds well-known for their photophysical properties. Their planar core with a conjugated pi-system allows high absorption and extinction coefficients while various peripheral functional groups can effectively tune the optical properties of the compound (Figure 4.2.1). Moreover, modification of porphyrin meso-substituents can alter their physical properties (solubility) and the ability to interact with other objects in a hybrid system.

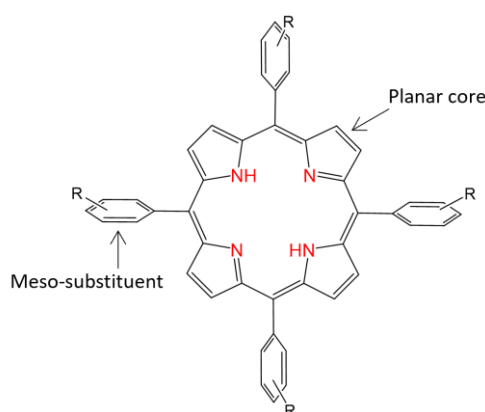


Figure 4.2.1 Illustration of porphyrin containing aryl substituents.

In our study, we decided to combine US Pt NPs and porphyrin complexes with different degrees of substitution to investigate the influence of the substituents in porphyrin on the properties of each component in this hybrid materials. In this system porphyrins can, on one side, serve as antenna molecules that can be activated by light irradiation and subsequently undergo energy transfer events; on another side, they serve as ligands for Pt NPs meaning they can modify the properties of NPs, in particular SA, electronic, or catalytic properties.

Porphyrins used in this investigation are present in Figure 4.2.2. Unmodified porphyrin molecule - 5,10,15,20-tetraphenylporphyrin (**TP**), and its complex with zinc - 5,10,15,20-tetraphenyl-21H,23H-porphine zinc (**ZTP**) were purchased from commercial sources. The modified porphyrins were kindly provided by our collaborators from CEMES Toulouse - Seifallah Abid and Claire Kammerer. Namely, porphyrins with one pyridine meso-substituent: zinc 5-pyridyl-10,15,20-tri-(3,5-(diterbutyl)-phenyl)-21H,23H-porphine (**ZMPy**) and nickel 5-pyridyl-10,15,20-tri-(3,5-(diterbutyl)-phenyl)-21H,23H-porphine (**NMPy**), and with two pyridine fragments: zinc 5,15-dipyridyl-10,20-di-(3,5-(diterbutyl)-phenyl)-21H,23H-porphine (**ZBPY**) and nickel 5,15-dipyridyl-10,20-di-(3,5-(diterbutyl)-phenyl)-21H,23H-porphine (**NBPY**) were used in this study.

Pt NPs serve as a convenient building block since it is possible to synthesize “naked” Pt NPs (without a ligand) and further stabilize them with a ligand of our interest to directly observe its

influence on NPs. Following this approach in our team, hybrid systems with US Pt NPs were developed to modify Coulomb blockade of the NPs by controlling polarizability of a ligand¹⁹⁰ or to tune spin-transition in iron complexes that acted as ligands for NPs²⁵⁹. Finally, the NP size is around 1-1.5 nm that is similar to the size of porphyrins (1.5-2 nm), which allows to consider ligands as equally important part of a hybrid system. Strong interactions between two parts of the system serve as a main tool of precisely controlled organization of a nanomaterial. In our case, these interactions can be provided by pyridine moieties which can coordinate to the surface of Pt NP via nitrogen electron pair.

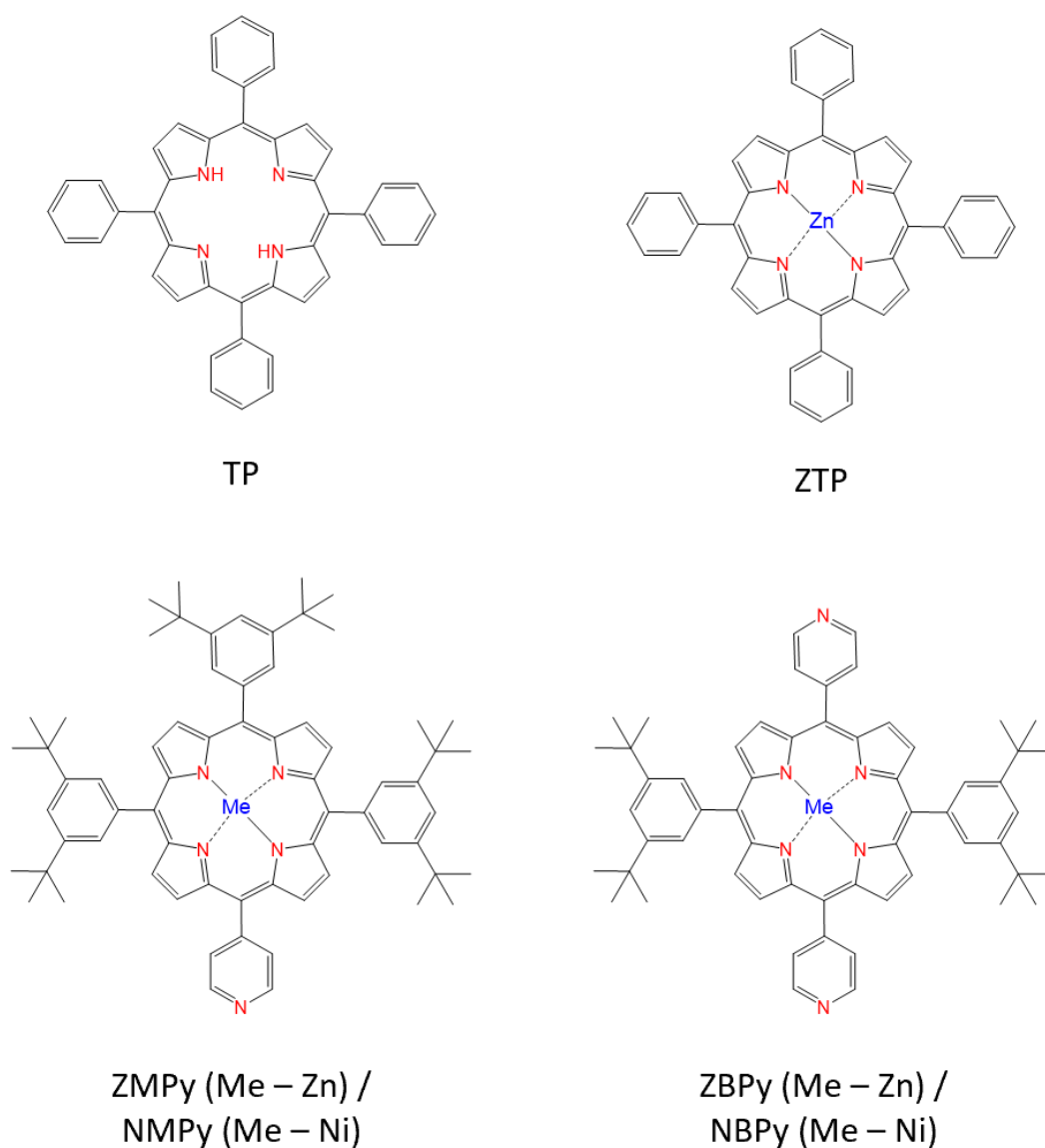


Figure 4.2.2 Structure of the porphyrins used in the study.

4.3. Synthesis of the Pt NP-porphyrin systems

The synthesis of “naked” Pt NPs was conducted following the procedure developed in our team, which includes decomposition of $\text{Pt}_2(\text{dba})_3$ precursor in THF under 1 bar CO and washing with pentane (Figure 4.3.1). As a result, US NPs with a mean size of 1-1.5 nm could be obtained with this procedure (Figure 4.3.1). Importantly, hydrogenated dba ligands could be removed by washing with THF/pentane = 1/10 mixture, which can be followed by IR²⁶⁰. In this way NPs are stabilized only by THF and CO which allows a post-treatment with the ligand of our choice. The possibility of the synthesis of “naked” ultra-small NPs make this method unique and particularly advantageous for the ligand effect studies. Once the NP solution was obtained, a THF solution of porphyrin could be added. The resulting mixtures were stirred during two hours at RT to coordinate the porphyrins to the surface of Pt NPs.

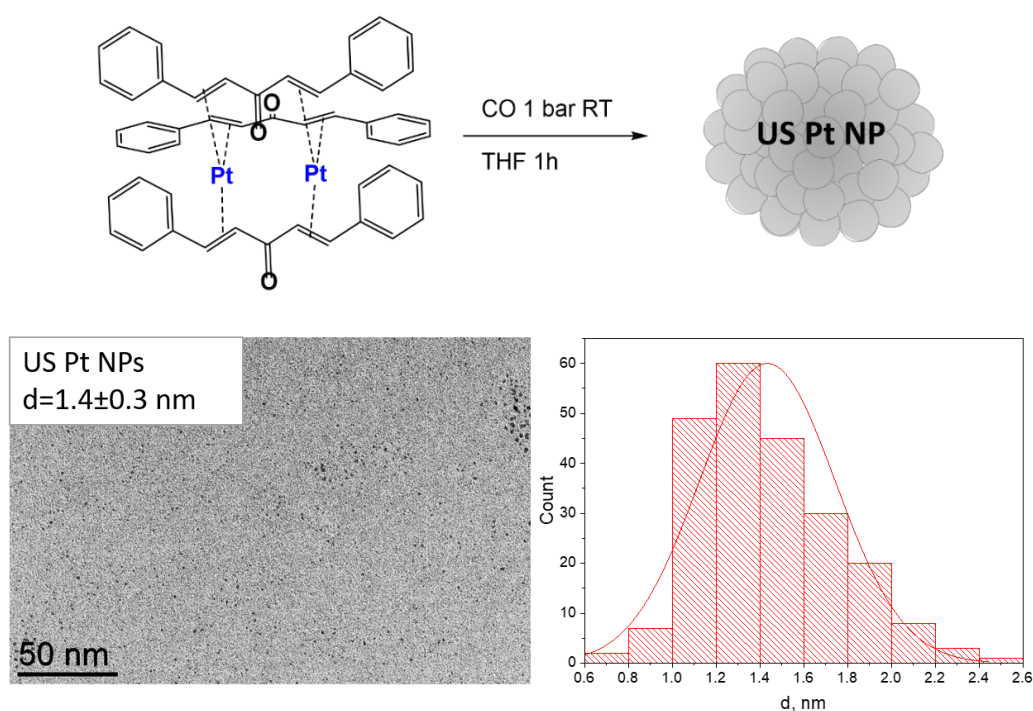


Figure 4.3.1 Scheme of synthesis of the US Pt NPs with a corresponding TEM image and a size distribution diagram.

4.4. Influence of the porphyrin structure on the SA of NPs

The distribution of NPs in Pt-porphyrin materials was analyzed with TEM. We found that NPs stabilized with 0.05 eq of porphyrin with respect to the amount of Pt atoms formed self-assembled structures. The shape of SA depended on the porphyrin structure. In the case of **ZMPy** or **NMPy** which have one coordination site, assemblies appeared as rods (Figure 4.4.1). In the group, we have already observed the formation of rods when synthesizing Pt NPs with thiols²⁶⁰. When **ZBPY** or **NBPY** that have two pyridine binding sites were used to synthesize the materials, sphere-shaped

assemblies were formed. Interestingly, previously with bifunctionalized ligands like dithiols, we observed only shapeless dense agglomerates. Some of us noted spherical shapes formation if water was present in the solvent²⁶¹. To prove that the spherical organization was formed not due to the presence of water, SA was formed again using freshly-dried degassed THF and adding to the solution of NPs molecular sieves. The spherical shape of the assemblies remained, confirming that this type of organization was achieved due to the presence of a porphyrin with two coordination sites. In contrast, with **TP** and **ZTP** which contain no coordination sites dispersed NPs or malformed agglomerates were observed.

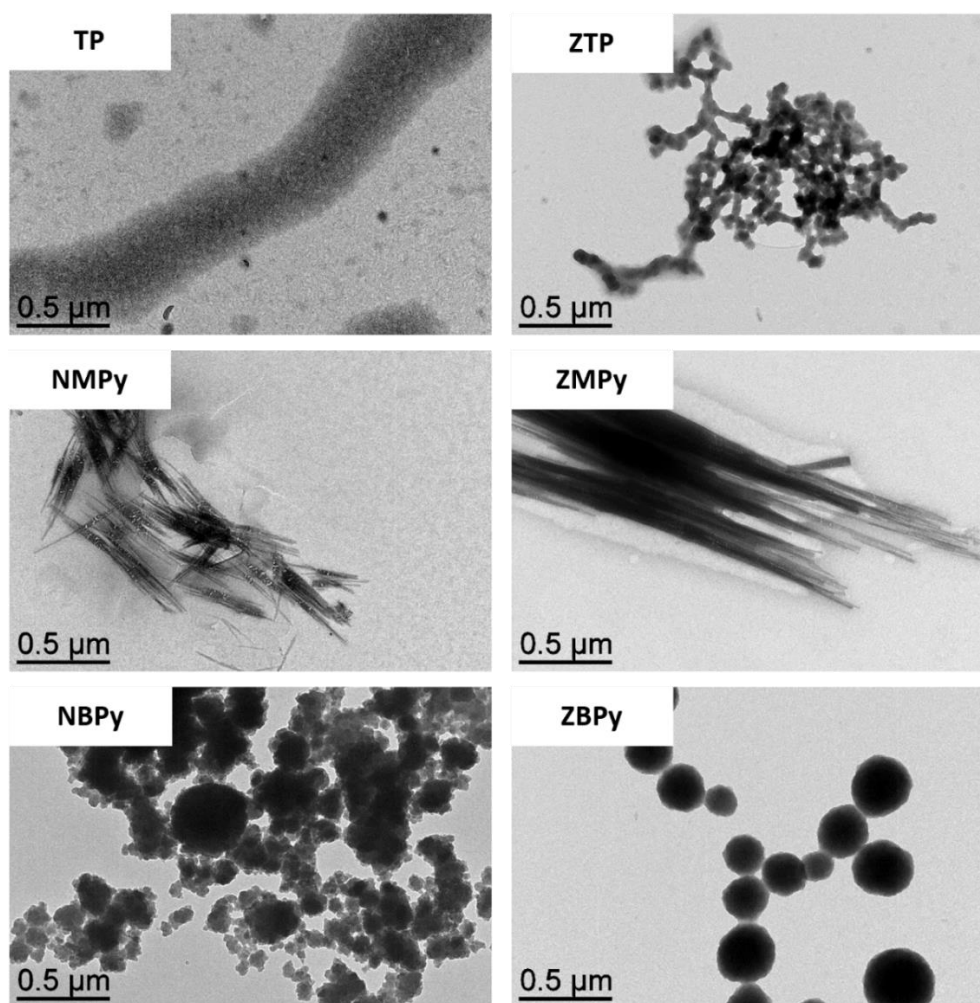


Figure 4.4.1 TEM images of Pt-porphyrin systems.

To confirm 3d-spherical structure of the **MBPy** materials electron tomography was conducted with a **Pt-ZBPY** sample. Results of the analysis clearly showed that NPs formed 3D spheres rather than flat discs. Electron tomography was performed for **Pt-ZMPy** and **Pt-ZTP** systems as well, results are present of Figure 4.4.2.

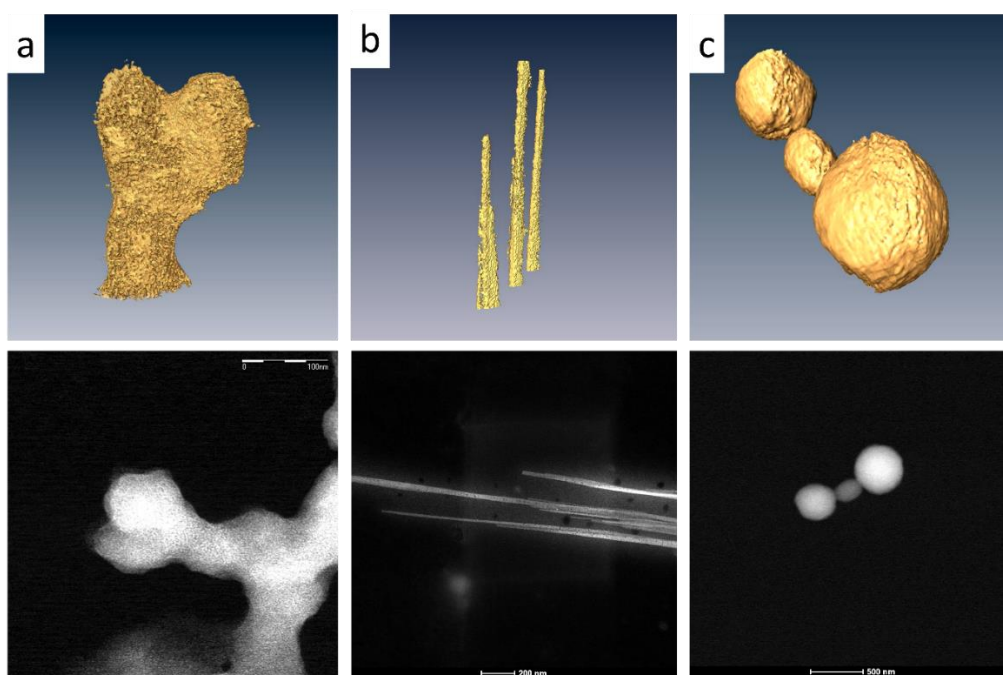


Figure 4.4.2 Electron tomography of a) Pt-ZTP; b) Pt-ZMPy; c) Pt-ZBPy with the corresponding HR-TEM-HAADF images. The Scale bars correspond to a)100 nm; b)200 nm; c) 500 nm.

Small-angle XRD was used for the systems, since it allows to extract a mean distance between NPs in partially ordered systems. The analysis showed pronounced peaks for the systems with mono- and di-substituted pyridine porphyrins, while NPs stabilized with **TP** and **ZTP** showed no peak (Figure 4.4.3). This result once again suggested that pyridine sites on **MMPy** (M stands for metal) and **MBPy** strongly coordinate to the surface of Pt providing NPs organization with typical correlation distances measured between two nanoparticles. According to the measurements, the mean spacing between two NP centers was 2.9 nm for **MMPy** structures and 2.2 nm for **MBPy** structures. The decrease in a mean distance when going from mono- to biofunctionalized porphyrin was expected since two binding groups assure more compact structures and also because less tertbutyl groups create less steric hindrance.

The diameter of **TP** is 1.5 nm²⁶² and we expect **MBPy** to have a similar size. For NPs of 1.4 nm with the mean center-to-center spacing of 2.2 nm, 0.8 nm of space is left for the ligand to occupy. This implies that in addition to coordination to the NP through nitrogen of pyridine, other more compact modes can exist, like a “face-on” bonding mode through metal- π interactions. In addition, Zn can coordinate two more pyridines in axial positions, which was shown in the study of SA of tetrapyrroline-functionalized zinc porphyrin²⁶³. We expect that the Zn-N(pyridine) interactions between porphyrins are much less pronounced in the case of **Pt-ZMPy** due to only one pyridine site. This difference might be responsible for the different shapes of SA. Systematic studies still have to be performed to fully describe the formation of the superstructures.

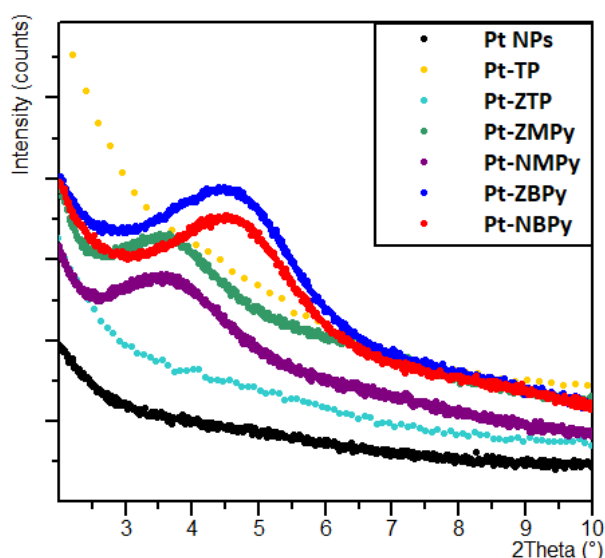


Figure 4.4.3 Low-angle XRD of Pt-porphyrin systems.

Fourier-transform infrared spectroscopy (FTIR) of the Pt NP-porphyrin systems can serve as a proof of strong coordination of the ligand to the surface of Pt NP. Particularly, the shift of the CO absorption band suggests the morphology or electronic density changes on the surface of a NP. Since CO was used to decompose Pt complex, we could follow its signal on the surface of the NPs with IR. A shift of CO band relative to the vibration value of CO attached to “naked” Pt NPs (2041 cm^{-1}) means that electronic density on the surface changed because of porphyrin coordination. On the IR spectrum (Figure 4.4.4) a strong shift of $5\text{--}8\text{ cm}^{-1}$ for NPs stabilized with pyridine functionalized ligands (2046 cm^{-1} for **ZMPy**, 2048 cm^{-1} for **NMPy**, 2046 cm^{-1} for **ZBPy**, and 2049 cm^{-1} for **NBPy**) was observed whereas for **TP** and **ZTP** there was almost no shift (2042 and 2043 cm^{-1}) found. This result suggests strong interaction of pyridine-modified porphyrins and NPs possibly through formation of Pt-N coordination bond.

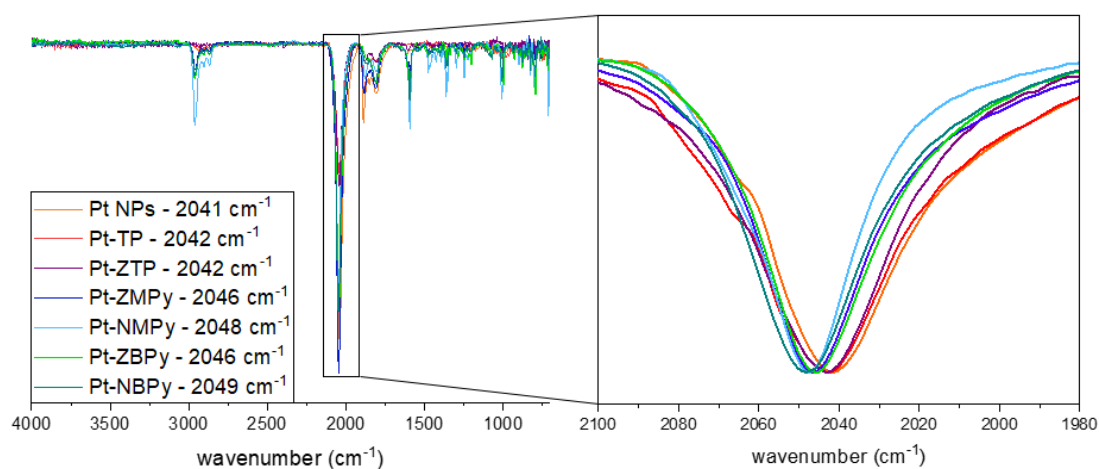


Figure 4.4.4 IR spectra of Pt-Porph systems with zoom on CO absorption band.

Polarizability of each pyridine-functionalized porphyrin was measured by dielectric spectroscopy since it appeared to be an important parameter responsible for electrical properties of Pt NPs SAs¹⁹⁰. Indeed, the higher the dielectric constant, the more polarizable is the molecule, the more facilitated is the electron jump between two NP trough this molecule. The results are summarized in a Table 4.4.1. We found that a dielectric constant was similar for each porphyrin and did not significantly depend on nature of metal center either on porphyrin structure. Since the metal center did not influence properties of the hybrid systems **NMPy** and **NBPpy** were excluded from further investigation.

Table 4.4.1 Polarizability constants of metalated porphyrins used in the study.

Sample	Relative permittivity
ZMPy	2.25
NMPy	2.79
ZBPpy	2.56
NBPpy	2.53

4.5. Photophysical response

4.5.1. Absorption and emission of the porphyrins

The absorption (UV-Vis) spectra of porphyrins usually exhibit an intense Soret band corresponding to $S_2 \leftarrow S_0$ electronic transition in along with four Q-bands ($Q_y(1,0)$, $Q_y(0,0)$, $Q_x(1,0)$, and $Q_x(0,0)$) which represent $S_1 \leftarrow S_0$ transition (Figure 4.5.2). In metalated porphyrins due to increase in symmetry, the Q_x and Q_y bands overlap and form only two peaks – $Q(1,0)$, $Q(0,0)$.

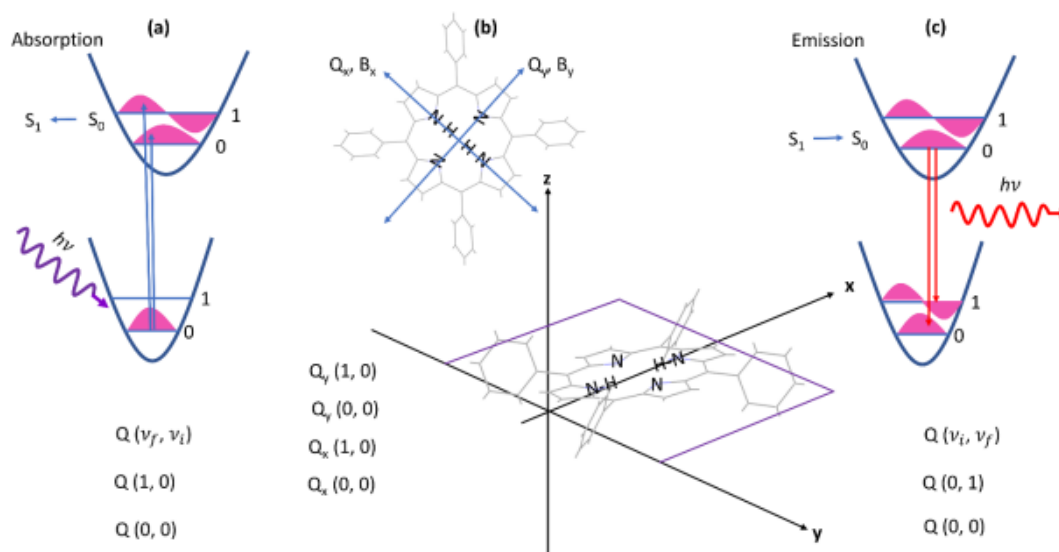


Figure 4.5.1 Illustration of a) electron excitation upon photon absorptions; b) different molecular dipole moments along x and y axis; c) electrons returning to the ground state with an emission of photon. Reprinted from ref²⁶².

The UV-Vis spectra of the four porphyrins are present in Figure 4.5.2 a. An intense Soret band is located at 415 nm for **TP**, and at 425 nm for metallated porphyrins; Q-bands are located over the range of 500–630 nm. To investigate the influence of Pt NPs on photophysical properties of the systems the UV-Vis and PL (photoluminescence) measurements were conducted keeping the concentration of a porphyrin constant at 0.0245 mM but varying Pt NPs concentration from 0.125 to 3.95 mM which corresponds to the relative content of Pt metal atoms from 5 to 160 equivalents (depending on the experiment Pt content was varied). Figure 4.5.2 b demonstrates UV-Vis spectra of **ZMPy** with Pt concentration from 0 to 0.735 mM (0 – 30 eq. of Pt). With increasing Pt content in the systems, we observed an insignificant decrease in the intensity of the Soret band and no Q-band shifts. This result indicates that there were no strong ground-state interactions between two parts of the system which can be identified with UV-Vis. Also, an increase in absorbance all over the spectrum was observed originating from the absorption by Pt NPs. Due to the insufficient changes on the spectrum, we did not focus on UV-Vis measurements for all the series.

The solutions containing a precise amount of Pt NPs were further analyzed with a PL. PL is a more sensitive technique and can give additional information about NP-porphyrin interaction. Samples were irradiated with light of 425 nm, which is a typical value for the Soret band of porphyrins. Two intense emission bands were found at 629 nm and 696 nm for the porphyrin molecule and at 603 nm and 653 nm for metallated porphyrins which correspond to Q (0,0) and Q (0,1) transitions (Figure 4.5.3). A quenching of porphyrins fluorescence was observed as a function of an increase of Pt NP amount in the solution.

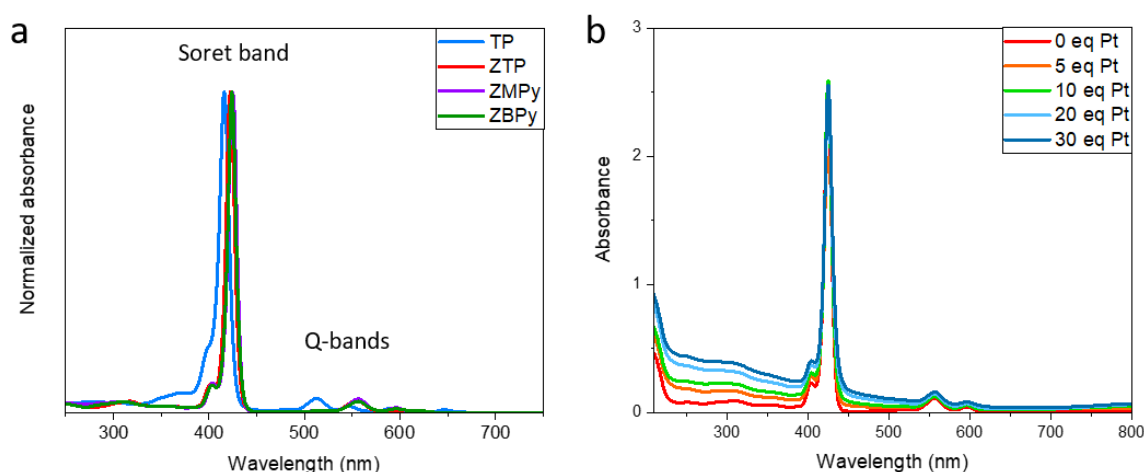


Figure 4.5.2 a) UV-Vis spectra four porphyrins used in the study; b) absorption spectra of ZMPy in the presence of Pt NPs.

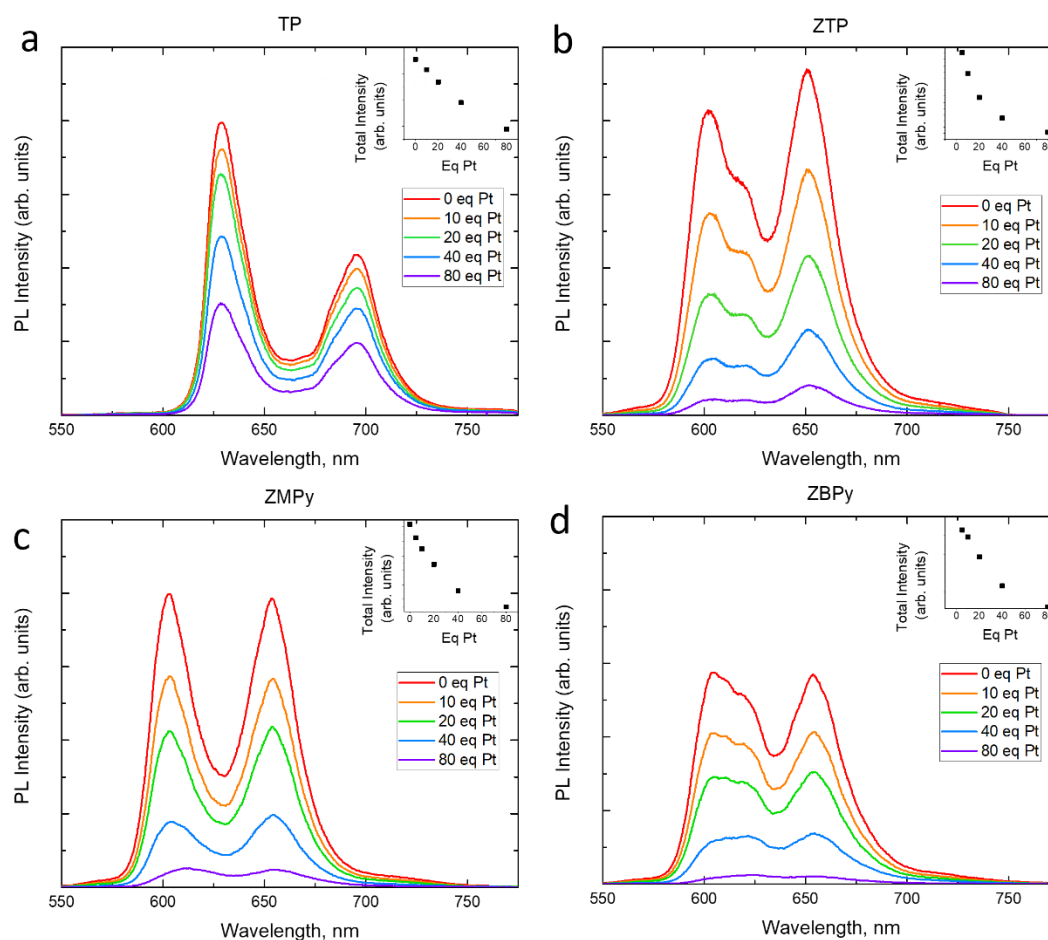


Figure 4.5.3 PL spectra of a) **TP**; b) **ZTP**; c) **ZMPy**; d) **ZBPY** in the presence of different amounts of Pt NPs.

4.5.2. PL quenching mechanisms

There are three main mechanisms of luminescence quenching: static quenching, dynamic quenching and inner filter effect. The last one is observed when the solution is concentrated and emitted photons become reabsorbed. In our study, we ignored it since we worked at moderate concentrations and used a cuvette with a short path length to minimize reabsorption events. Dynamic quenching appears when a fluorophore in an excited state transfers energy to an acceptor. Static quenching occurs when in a ground state a quencher forms a non-fluorescent complex with a fluorophore (Figure 4.5.4). A Stern-Volmer equation (4.1) is generally used to find out whether only one type of quenching occurs in a system. There, a relation of intensities without and with quencher depends linearly on the concentration of a quencher.

$$\frac{I_0}{I} = 1 + K_q[Q], \quad (4.1)$$

where I_0 is a light intensity without a quencher; I is a light intensity with a quencher; K_q is a quenching constant; $[Q]$ is a concentration of quencher.

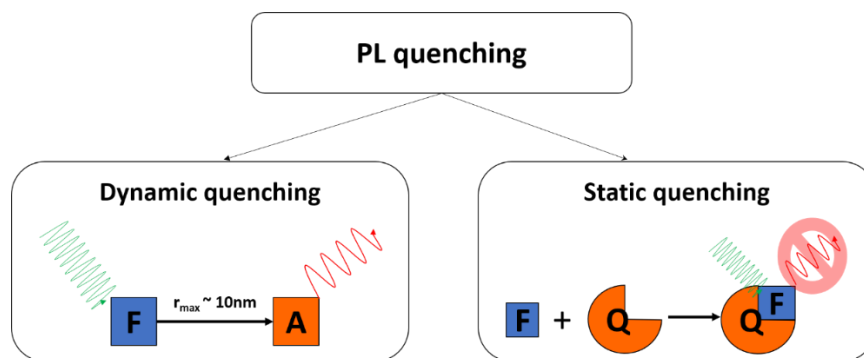


Figure 4.5.4 Illustration of PL quenching mechanisms.

Generally, if only one type of quenching exists in the system, a Stern-Volmer plot must be linear with a slope value of the quenching constant. If both dynamic and static quenching events take place in the system the equation transforms to a quadratic one:

$$\frac{I_0}{I} = 1 + (K_D + K_S)[Q] + K_D K_S [Q]^2, \quad (4.2)$$

where K_D is a dynamic quenching constant and K_S is a static quenching constant

In this case an upward-curving graph will appear. Figure 4.5.5 shows Stern-Volmer plots which correspond to the PL experiments presented in Figure 4.5.3. While mostly linear plots appeared for **Pt-TP** and **Pt-ZTP** the upward curvature of **Pt-ZMPy** and of **Pt-ZBPY** graphs indicated a coexistence of both quenching mechanisms.

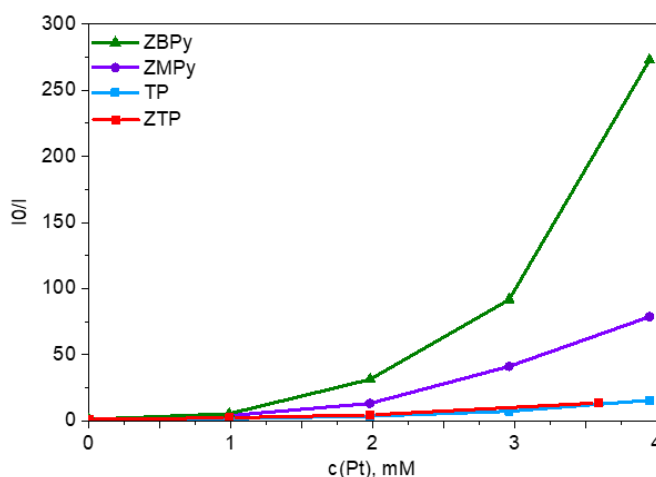


Figure 4.5.5 Stern-Volmer plot of porphyrins with a gradual increase of Pt concentration in the solutions.

4.5.3. Dynamic quenching

Excited state energy transfer processes shorten an excited lifetime of a luminophore because it is an additional rate process that depopulates the excited state, which describes Equation 4.3.

$$\tau = \frac{1}{k_f + k_{ic} + k_{isc} + k_q[Q]} \quad (4.3)$$

where k_f is a fluorescence rate constant; k_{ic} is an internal conversion rate constant; k_{isc} is an intersystem crossing rate constant, k_q is a quenching rate constant, and $[Q]$ is a concentration of a quencher.

This effect can be measured with a time-resolved photoluminescent spectroscopy (TRPL). Figure 4.5.6 presents TRPL spectra of each porphyrin with different amount of Pt NPs. In the case of non-modified porphyrins **TP** and **ZTP**, PL lifetimes did not change with increase of Pt NPs amount and was kept equal to the one of the free molecules - 11 ns for **TP** and 2 ns for **ZTP**. Thus, the nature of quenching in this case is not dynamic. On the contrary, for **ZMPy** and **ZBPY** starting from 40 eq of Pt a new shorter time decay of 1 ns for **ZMPy** and 0.7 ns for **ZBPY** became pronounced, in addition to the decay time of 2.2 ns of the free complexes. By bi-exponential decay fitting (Equation 4.4) the fractions of each population were calculated, the results are presented in

Table 4.5.1. The fitting results suggest an increase of short-lived fraction with bigger content of Pt in the solution. Precisely, at 40 eq of Pt the fraction of a short-lived population was equal to 0.2 and 0.3 for **ZMPy** and **ZBPY** respectively. At 160 eq of Pt the short-lived population was dominant with the fraction value of 0.85 in each case. So, both dynamic and static quenching mechanisms are present in **ZMPy** and **ZBPY** solutions with high Pt content.

Alternatively, the decrease of a lifetime is a common feature for porphyrins in aggregated state²⁶⁴. SA of porphyrins in ordered 3D systems is a well-studied phenomenon which is used to improve properties of porphyrins in catalysis^{263,265}. SA formation is favored due to π - π stacking of flat macrocycles of porphyrins; however, to achieve stable 3D structures, charged substituents in the porphyrin or addition of surfactants are required²⁶⁶. Also, SA is pH- and solvent-sensitive. SA formation results in shifted and wide absorption pics that we did not observe in our case. Besides, Pt is in a big excess so we presume that porphyrins must firstly interact with it rather than with each other. Thus, we suppose that spontaneous aggregation could not take place in our conditions and a new shorter life-time is a signature of energy transfer to the Pt surface. Considering the components of our system, quenching through electron transfer can be discarded, so energy transfer can proceed either through Förster or Dexter energy transfers or through a combination of both.

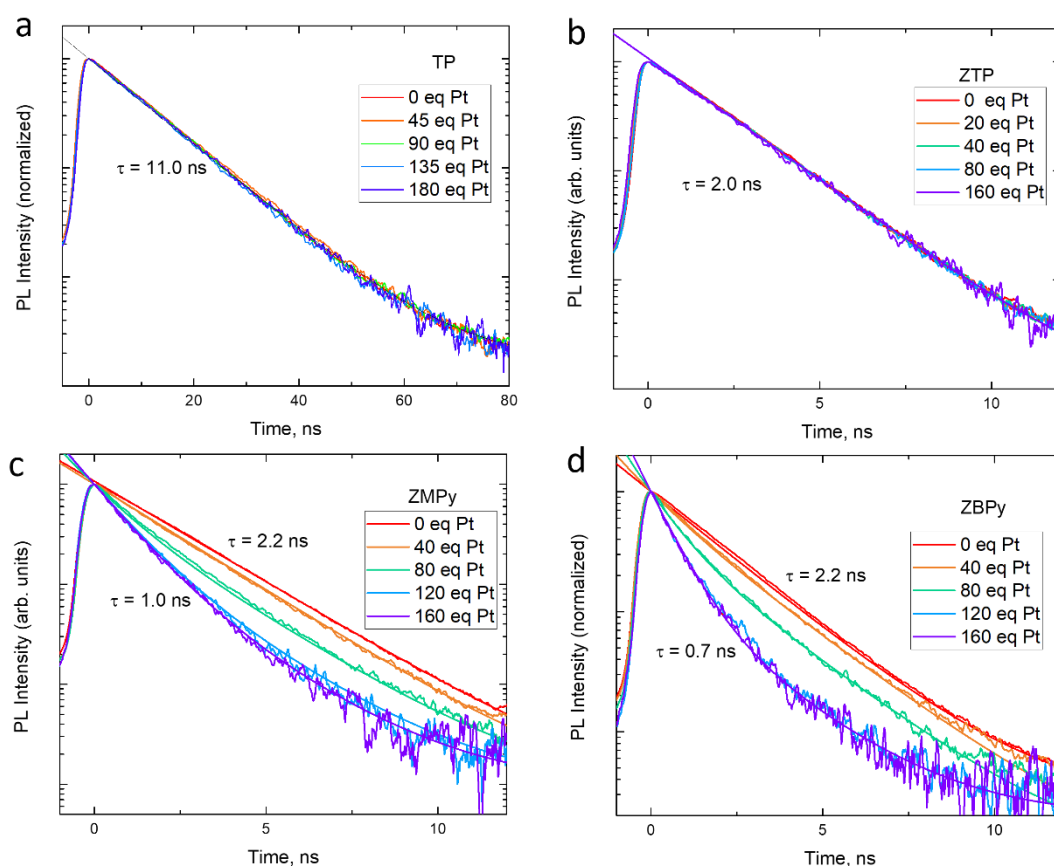


Figure 4.5.6 TRPL spectra of a)Pt-TP; b)Pt-ZTP; c) Pt-ZMPy; d)Pt-ZBPy.

Formula for bi-exponential fitting:

$$I(t) = A_1 * \exp\left(-\frac{t}{\tau_1}\right) + A_2 * \exp\left(-\frac{t}{\tau_2}\right) + y_0 \quad (4.4)$$

Table 4.5.1 Ratio of short- and long-living populations of ZMPy and ZBPy with different additions of Pt.

eq Pt	ZMPy				ZBPy			
	A ₁	τ ₁ (ns)	A ₂	τ ₂ (ns)	A ₁	τ ₁ (ns)	A ₂	τ ₂ (ns)
0	0	-	1	2.2	0	-	1	2.2
5	0	-	1	2.2	0	-	1	2.2
10	0	-	1	2.2	0	-	1	2.2
20	0	-	1	2.2	0	-	1	2.2
40	0.20	1	0.80	2.2	0.30	1	0.70	2.2
80	0.55	1	0.45	2.2	0.53	0.7	0.47	2.2
120	0.82	1	0.18	2.2	0.83	0.7	0.17	2.2
160	0.85	1	0.14	2.2	0.85	0.7	0.15	2.2

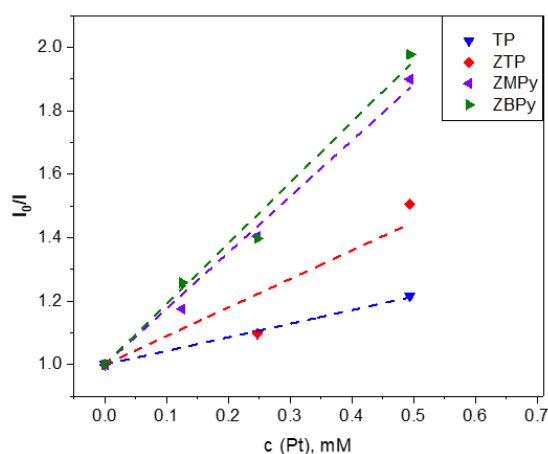
Thus, at higher concentrations of quencher (Pt NPs) we observe an increase of short-living population in agreement with our hypothesis about energy transfer. We suggest that increase of NPs in solution leads to more interactions with a fluorophore which increases energy-transfer efficiency comparing to emission efficiency. This experiment postulates that dynamic quenching happens in the system, however it doesn't discard other quenching mechanisms.

4.5.4. Static quenching

At low concentrations of Pt (till 40 eq) fluorescence lifetime with the quencher (τ) was equal to fluorescence lifetime without it (τ_0). Meanwhile, an emission intensity of the systems decreased ($I < I_0$). This behavior points out static quenching mechanism. Static quenching is a ground-state process of formations of a non-emitting complex with a quencher (Equation 4.5):



In this situation we can again apply a Stern-Volmer equation to find values of the association constant which is equal to the static quenching constant. Stern-Volmer plots at 0 - 20 eq. of Pt are shown in Figure 4.5.7. Small amount of data points did not let us make an adequate fitting, nevertheless, it may be used to describe a general trend in static quenching constants. The fitting was done keeping the value of the intercept equal to 1 in accordance with the Equation 4.1. The slope values that correspond to a static quenching constant increased from unmodified phenyl porphyrins to pyridine-functionalized porphyrins indicating that with covalently-bonded assemblies static quenching is more pronounced.



Compound	K _s , mM ⁻¹
Pt-TP	0.43 ± 0.01
Pt-ZTP	0.9 ± 0.2
Pt-ZMPy	1.8 ± 0.1
Pt-ZBPy	1.9 ± 0.1

Figure 4.5.7 Stern-Volmer plots with linear fitting for Pt-porphyrin hybrid systems at platinum concentration from 0 to 0.5 mM which corresponds to 0 – 20 eq. of Pt; the corresponding values of static quenching constants.

To sum up, all the studied Pt-porphyrin hybrid systems underwent luminescent quenching. **TP** and **ZTP** followed a static quenching mechanism. For pyridine-functionalized porphyrins, the formation of shorter-lifetime species was observed at the content of Pt equal to or more than 40 eq, which pointed out a dynamic quenching mechanism. Meanwhile, in the regime of low concentration of the quencher, only static quenching occurred. These results indicated that the formation of a covalent bond between Pt NP and **ZMPy** or **ZBPy** resulted in enhanced quenching and energy transfer.

4.5.5. Electrical properties of the hybrid systems

NP SAs present a convenient approach to introduce the functional molecules in ordered SA materials where metal NPs can be considered as nanoelectrodes between each molecule. Our team recently discovered that for US Pt NPs (<2 nm) a Coulomb blockade (CB) occurred at room temperature and could be tuned by the ligand^{190,260}. Coulomb blockade is a low-bias resistance observed as a non-linear I(V) dependence. In a NP system, Coulomb blockade is related to the charging energy (E_c) of a NP, which can be described by an equation (4.6). It depends on three parameters: the size of the NPs, the distance between two nanoobjects, and the relative permittivity of the molecular components:

$$E_c \sim \frac{e^2}{\left(2\pi\epsilon_r\epsilon_0 d \ln\left(\frac{s}{s-d}\right)\right)}, \quad (4.6)$$

where e is an electron charge, ϵ_0 is a permittivity of vacuum, ϵ_r is a relative permittivity of the surrounding molecules, d is a particle diameter, and s is a center-to-center distance between two NPs.

To compare current characteristics in NPs SAs the researchers commonly refer to the equation (4.7).

$$I \propto V^\xi, \quad (4.7)$$

where ξ is a scaling parameter related to the current paths in the system.

To measure the electronic characteristics of the hybrid systems, the solutions of **Pt-TP**, **Pt-ZTP**, **Pt-ZMPy**, and **Pt-ZBPY** containing 0.05 eq of porphyrin were drop-casted on a gold substrate and analyzed performing measurements by conductive atomic force microscopy (CAFM) in different parts of a sample. The results are presented as I-V curves where the current was averaged and normalized at $V = 2$ V. A Coulomb blockade regime was observed in each case at room temperature, originating from the small sizes of the NPs (Figure 4.5.8 a). The inset of Figure 4.5.8 a shows the difference in charging energy between the hybrid systems. Namely three regimes are identified:

- 1) naked NPs with the highest conductivity through the paths where the NPs are close to each other;
- 2) **Pt-TP** and **Pt-ZTP** show higher CB which corresponds to the homogeneous integration of the ligands into the materials;
- 3) **Pt-ZMPy** and **Pt-ZBPY** show the highest CB and ξ values up to 4, comparable with the NP SAs reported in the literature^{190,267,268}.

We were particularly interested in studying a light effect on the electric properties of SAs since in the excited state, electronic density redistribution can affect electron transport through the porphyrins. CAFM light on-off measurements were done with a green laser of 10 mW at 532 nm –

the wavelength close to the Q-bands absorption wavelength. The laser was focalized at the contact of the conductive AFM tip with the sample. At the present moment, the measurements for all the platinum-zinc porphyrin systems were performed, and the measurements of **Pt-TP** are programmed. Figure 4.5.8 b presents the values of I_{on}/I_{off} as an average of 42 measurements. With naked NPs, we observed some light activation effect ($I_{on}/I_{off} \approx 2$), which could be attributed either to a local heating effect or to a polarization of the NP which facilitated electron transport. **Pt-ZTP** showed a minor difference in photoconduction, the results were in the same magnitude as for the naked NPs. Meanwhile, an enhancement of the relative photocurrent was observed in the **Pt-ZMPy** ($I_{on}/I_{off} \approx 9$) and **Pt-ZBPy** ($I_{on}/I_{off} \approx 11$) systems. We could ascribe it to a possible increase of the molecular polarizability in an excited state, which would facilitate the jump of the electrons from one NP to another. The difference between **Pt-ZTP** and systems with pyridine-functionalized NPs may lie in the relative stability of the SAs, where the covalent bond between Pt and porphyrin allows to have stable assemblies with controllable interparticle distances.

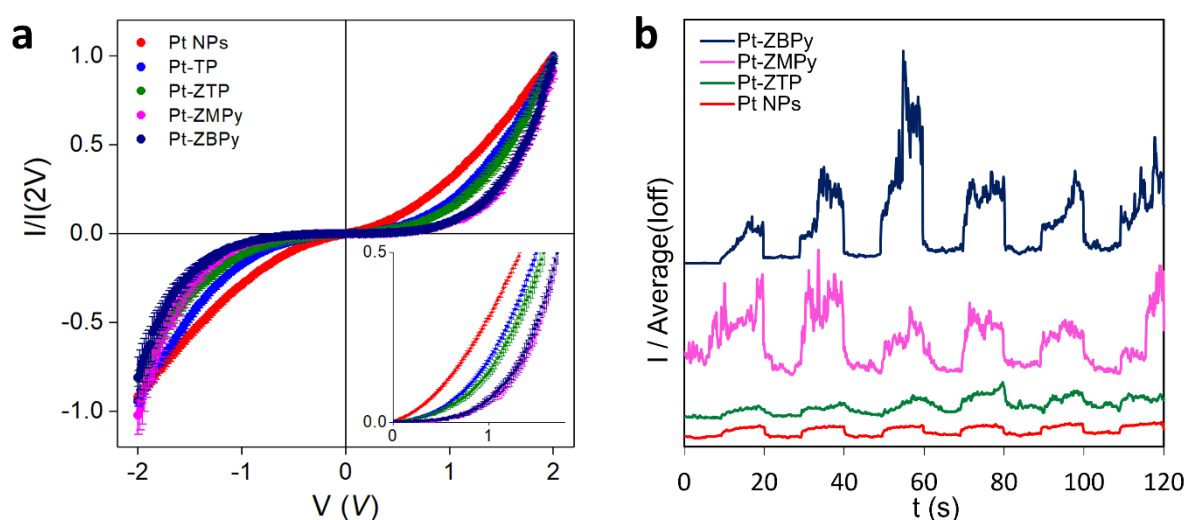


Figure 4.5.8 a) I-V plots of the Pt-porphyrin hybrid systems; b) light effect on conductivity of the hybrid systems.

Thus, in the Pt-porphyrin hybrid systems, electric measurements were found to be dependent on the structure of the porphyrin too. Namely, SAs with covalently bonded porphyrins showed higher CB and higher photo-response comparing to the weakly-bonded hybrid systems.

4.6. Conclusions

The present chapter describes the synthesis and properties of the hybrid materials consisting of two functional blocks – US Pt NPs and porphyrins. While some porphyrins were attached to the surface due to the weak non-covalent interactions, others most likely formed coordination bonds between Pt and N of a pyridine moiety of a porphyrin. The strong interaction in the hybrid systems yielded

SAs of defined shapes and short-range ordering, as well as peculiar photophysical and electric properties. Particularly, energy transfer occurred in **Pt-ZMPy** and **Pt-ZBPy** systems and not in **Pt-TP** or **Pt-ZTP** systems. CB was more pronounced in strongly interacting hybrid systems than in the systems having non-covalent interactions. Also, conductivity enhancement appeared in **Pt-ZMPy** and **Pt-ZBPy** systems under light irradiation, whereas minor changes were observed with **Pt-ZTP** system. In general, this study highlights the influence of strong interactions between the functional blocks in hybrid systems to achieve SAs of defined shapes or to tune the physical properties of the systems.

4.7. Experimental part

4.7.1. General

Synthesis of the Pt NPs and hybrid systems was carried out under an inert atmosphere in the glovebox and using standard Schlenk techniques. Analytical samples were prepared on air. $\text{Pt}_2(\text{dba})_3$ was purchased from NanoMePS. THF for the synthesis was collected from an MBraun purification system, degassed and stored in the glovebox. 5,10,15,20-tetraphenylporphine (purity >99%) and 5,10,15,20-tetraphenyl-21H,23H-porphine zinc (purity 90%) were purchased from Sigma Aldrich and used without further purification. The functionalized porphyrins were synthesized by the team of Claire Kammerer at CEMES, Toulouse.

4.7.2. Analytics

TEM images were collected using a JEOL JEM 1400 operated at 120kV and using a tungsten filament. The NP size and distribution was determined from the measurement of over 150 particles.

High resolution STEM HAADF tomography was performed at the Advanced Microscopy Laboratory (LMA), Instituto Universitario de Nanociencia de Aragon (INA), Zaragoza, Spain, by a FEI Tecnai field emission gun operated at 300 kV. 3D reconstruction was carried out with FEI tomography acquisition software, Inspect 3D and Amira 3D reconstruction software after the acquisition of 140 images. The analysis was performed by Alfonso Ibarra.

FT-IR spectra were recorded on a Thermo Scientific Nicolet 6700 FT-IR spectrometer in the range 4000-700 cm^{-1} , using a Smart Orbit ATR platform. The spectra were recorded after the THF solutions of samples were dried on air.

XRD diffractograms were recorded on an Empyrean PANalytical diffractometer using $\text{Co K}\alpha$ radiation equipped with X'Celerator detector. Small-angle measurements were performed on a microscopy

glass, on which the crude solution was deposited by “drop-casting”. The working voltage is 45 kV for a current of 35 mA.

UV-Vis spectroscopy was performed with spectrometer Cary Series UV-Vis-NIR Agilent. Cuvettes with 2 mm optical path length were used for the measurements.

PL spectra were recorded with fluorimeter of PTI brand equipped with Xenon lamp as irradiation source and a UV-Vis detector.

Time-resolved PL measurements were performed at LPCNO by Delphine Lagarde with a home-made set-up. Namely, the experiments were performed using 1.5 ps laser pulses generated by a tunable mode-locked Ti:Sa laser. A pulse picker was used to reduce the repetition rate from 80 MHz to 4 MHz and a second harmonic generation unit converted the excitation wavelength down to 400 nm. The laser beam was focused onto the cuvette on a $1/e$ diameter spot of ~ 100 μm and an average power of 50 μW . The PL signal was dispersed by a f#-6.5 spectrometer and detected as a function of time by a synchro-scan Hamamatsu streak camera with an overall temporal resolution of 450 ps.

Conductive AFM measurements were conducted with an AIST-NT SmartSPM 1000 microscope, equipped with a conductive AFM unit. The samples were prepared by drop casting of one drop of the crude solution on silicon wafers covered by a ~ 50 nm layer of gold (with a ~ 5 nm chromium anchoring layer). We always used conductive silicon tips covered by platinum (Mikromash HQ-NSC15/Pt), but we double-checked that similar behaviors were observed with doped-diamond coated tips (NT-MDT DCP10), to confirm that the trends did not come from contact effects. Typical measurements consisted in first performing a topography image of the sample and then going in contact on zones with individual assemblies to measure their I-V characteristics. Measurements were performed on several objects per zone and several zones of the substrates. For light on/off measurements a laser of 10 mW and wavelength of 532 nm was applied by 10s intervals.

Dielectric spectroscopy measurements were performed on powder samples compacted between two stainless steel electrodes (diameter 10 mm) in a Teflon sample holder at 23°C. The thickness of the powder was as small as possible (250-400 μm) to increase the sensitivity of the measurement. Dielectric measurements were carried out at frequency 1 and 10^6 Hz using a Novocontrol broadband dielectric spectrometer at an applied AC of 1 mV_{rms}.

4.7.3. Experimental procedures

Synthesis of US Pt NPs

In a glovebox $\text{Pt}_2(\text{dba})_3$ (90 mg) was dissolved in 20 mL of THF. Then, a Fisher-Porter (FP) bottle (100 mL) containing the solution was evacuated from the glovebox. Argon was evacuated from the vessel and it was charged CO to have the pressure of 1 bar. The color of the solution changed from dark violet to dark-brown approximately in 1 minute after CO filling. The solution left stirring at RT 500 rpm during 1 h. Later, CO was evacuated with a Schlenk line and the solvent was evaporated till ~1mL. Further, the solution was washed with 10 mL of pentane and 1 mL of THF 3 times. The solvents were degassed prior to use. After the washings NPs were redispersed in 10 mL of THF and were used in fictionalizations with porphyrins.

Yield: 95%

Functionalization with porphyrins

Solutions of porphyrins were prepared in THF and added to Pt solutions of required concentration. Solutions were stirred for 2h in the glovebox and consequently analyzed. For SA of Pt NPs with **MBPy** analyses were performed next day since we noticed that sphere-shaped assemblies required more time to form. For TRPL measurements Pt NPs solution concentrations were adjusted with THF to have 1 mL solution of desired concentrations. Then, 1 mL of a porphyrin solution with concentration 0.049 mM were added in each solution of Pt NPs so the final concentration of each porphyrin was 0.025 mM. After stirring for minimum 2 h TRPL measurements were performed.

CHAPTER 5. Platinum-ruthenium antenna hybrid systems

5.1 Model compound - ruthenium(II) trisbipyridyl complex	144
5.2 Synthesis of ruthenium bipyridyl imidazolium complexes	146
5.3 Characterization of the complexes	147
5.4 Deprotonation of the L1 complexes	149
5.5 Synthesis of Pt NPs stabilized with L1Cl.....	151
5.6 Conclusions	153
5.7 Experimental part	154
5.8.1 General	154
5.8.2 Analytics	155
5.8.3 Synthetic procedures	155
5.8. Appendix to Chapter 5	161
5.8.1 NMR spectra.....	161
5.8.2 Mass spectra.....	165
Conclusions and perspectives.....	169

5.1 Model compound - ruthenium(II) trisbipyridyl complex

Ruthenium bipyridyl complexes have unique photoproperties which make them a popular choice in photocatalytic and photosensitizing applications. These properties are shortly reviewed on the example of the most-studied system – ruthenium(II) trisbipyridyl (bpy) complex.

$[\text{Ru}(\text{bpy})_3]^{2+}$ complex adsorbs UV and visible light (Figure 5.1.1 a). Adsorption of light around 450 nm by $[\text{Ru}(\text{bpy})_3]^{2+}$ results in the formation of singlet excited metal-to-ligand charge transfer state ($^1\text{MLCT}$). For metal complexes, intersystem crossing is common, thus the most populated excited state for the system is a triplet (T_1 or $^3\text{MLCT}$). From this state the complex can return to the ground state non-radiatively or by means of phosphorescence emitting a photon of 620 nm (Figure 5.1.1 a, b). High quantum yield as for this type of luminophores (2.8% in air-saturated water) allows to use ruthenium polypyridyl complexes as emitting agents, for instance, in cell imaging²⁶⁹. Alternatively, from the triplet excited state T_1 it can undergo energy or electron transfer events with surrounding compounds (Figure 5.1.1 b). T_1 of $[\text{Ru}(\text{bpy})_3]^{2+}$ has a long lifetime (up to 1 ms in degassed AcN), which increases the chances of these events. Moreover, in this state, more electron density is located on a pyridine ring while Ru becomes electron poorer (Figure 5.1.1 c)²⁷⁰. This charge distribution makes the complex both better oxidizer and reducer in excited state than in ground state (for redox potentials see Figure 5.1.1 d). Consequently, it allows to use $[\text{Ru}(\text{bpy})_3]^{2+}$ as a photoredox catalyst as well as an efficient photosensitizer, which was shown in the literature review (Chapter 1). In particular, hybrid systems containing NPs and Ru(bpy) complexes were tested in decomposition of biomass, CO₂ reduction or water splitting reaction^{148,157,271}.

In addition, $[\text{Ru}(\text{bpy})_3]^{2+}$ complex is an efficient two-photon absorbing (TPA) agent and an excellent energy transfer agent which allows to use it for biomedical applications²⁷². For example, in a hybrid system with Au NPs and ruthenium-polypyridyl complexes, efficient energy transfer to the Au NPs was shown to drastically increase heat generation by Au NPs ($\Delta T=38.5$ °C)². Similar to porphyrins, the ruthenium polypyridyl complexes in a triplet excited state are efficient photodynamic therapy (PDT) agents. Moreau and colleagues synthesized Au NPs with a grafted functionalized $[\text{Ru}(\text{tpy})_3]^{2+}$ complex. This hybrid system showed two-photon absorption and singlet oxygen generation performance, which makes it a potential candidate for TPA-TPD applications²⁷³.

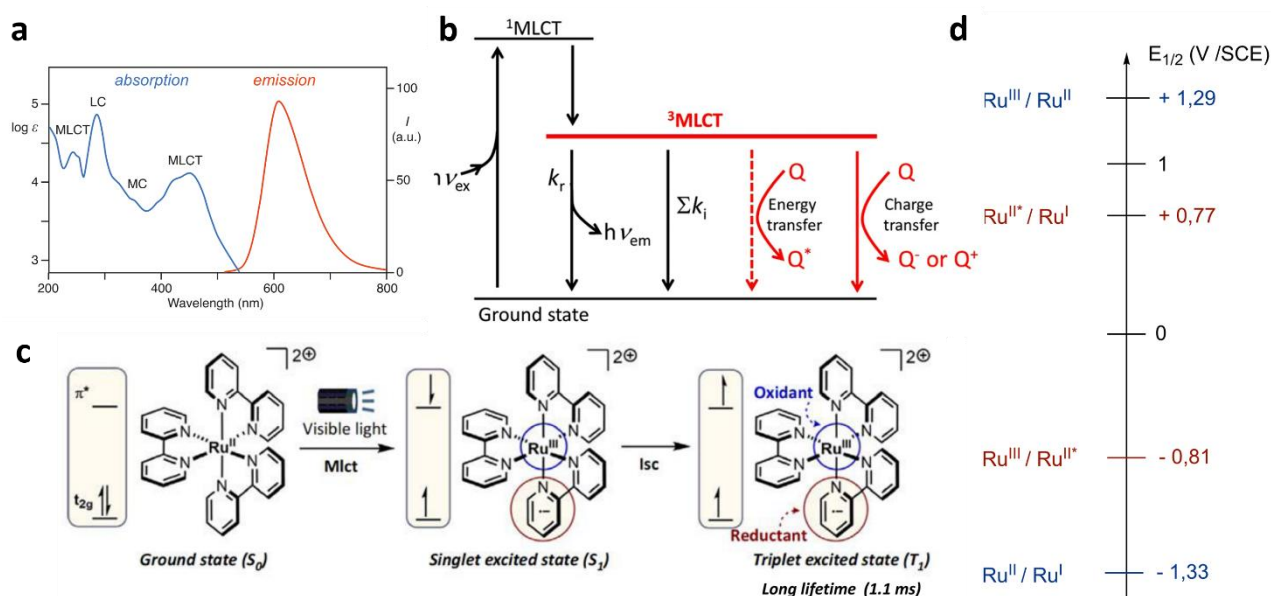


Figure 5.1.1 a) absorption and emission spectra of $[\text{Ru}(\text{bpy})_3](\text{PF}_6)_2$; b) scheme illustrating deactivation processes of the photo-excited triplet state of $[\text{Ru}(\text{bpy})_3]^{2+}$, namely phosphorescence (k_r), energy and electron transfer and other processes (Σk_i); c) illustration of a charge distribution within the complex upon the excitation; d) scheme showing the oxidation and reduction potentials of $[\text{Ru}(\text{bpy})_3]^{2+}$ in the ground and excited state. Note that absolute values of potentials are lower for the complex in the excited state. Reprinted from refs^{270,274}.

In our study we decided to synthesize $[\text{Ru}(\text{bpy})_3]^{2+}$ -based complex and use it as an energy transfer antenna for Pt NPs. To ensure strong coordination of the complex to the surface of Pt NPs we functionalized one of bipyridyl fragments with a chain bearing an imidazolium moiety that can be deprotonated to form an N-heterocyclic carbene (NHC – Figure 5.1.2). NHC is known to form a strong sigma bond with noble metals⁴³, so we expected a formation of a strong coordination bond between the parts of the system. In addition to the methylimidazolium moiety, we synthesized complexes with a mesitylimidazolium fragment, which can better stabilize the NHC. Also, we modified the carbon chain length between the Ru center and the imidazolium fragment to tune the photoproperties of the hybrid systems.

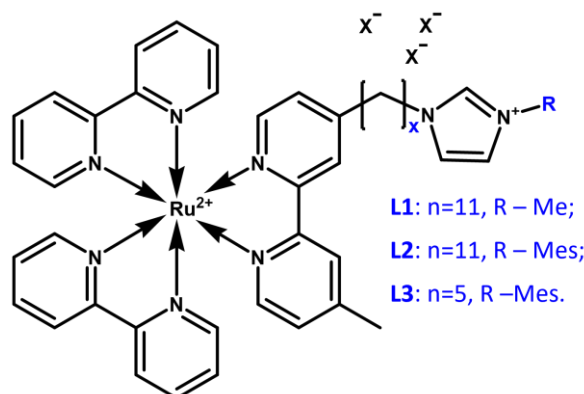


Figure 5.1.2 General structure of Ru(II) bpy complexes.

To form hybrid systems, we used two strategies. The first one was to apply the as-prepared NHC complex as a stabilizer in the synthesis of the NPs. The resulting system can be conveniently analyzed with common characterization techniques such as NMR, XPS, IR, TEM, EDX and others. The following of this chapter will present preliminary results on the preparation of NPs in colloidal solution. Alternatively, the NHC complex can be impregnated on supported NPs. Supported systems have limited possibilities of characterization; however, they tend to show higher stability and better performance in catalysis. The next steps would be to use the characterized systems in model hydrogenation-dehydration reactions and based on the results, to apply the most promising system in relevant Pt-catalyzed chemical transformation, like water splitting or hydrogenolysis of biomass. We believe that thoughtful design and thorough characterization of the formed hybrid materials can provide us with important details of structure-property relations that will help to choose the suitable application for the catalytic systems.

5.2 Synthesis of ruthenium bipyridyl imidazolium complexes

The synthesis of the complexes included several steps with purifications. The general scheme of the syntheses is present in Figure 5.2.1.

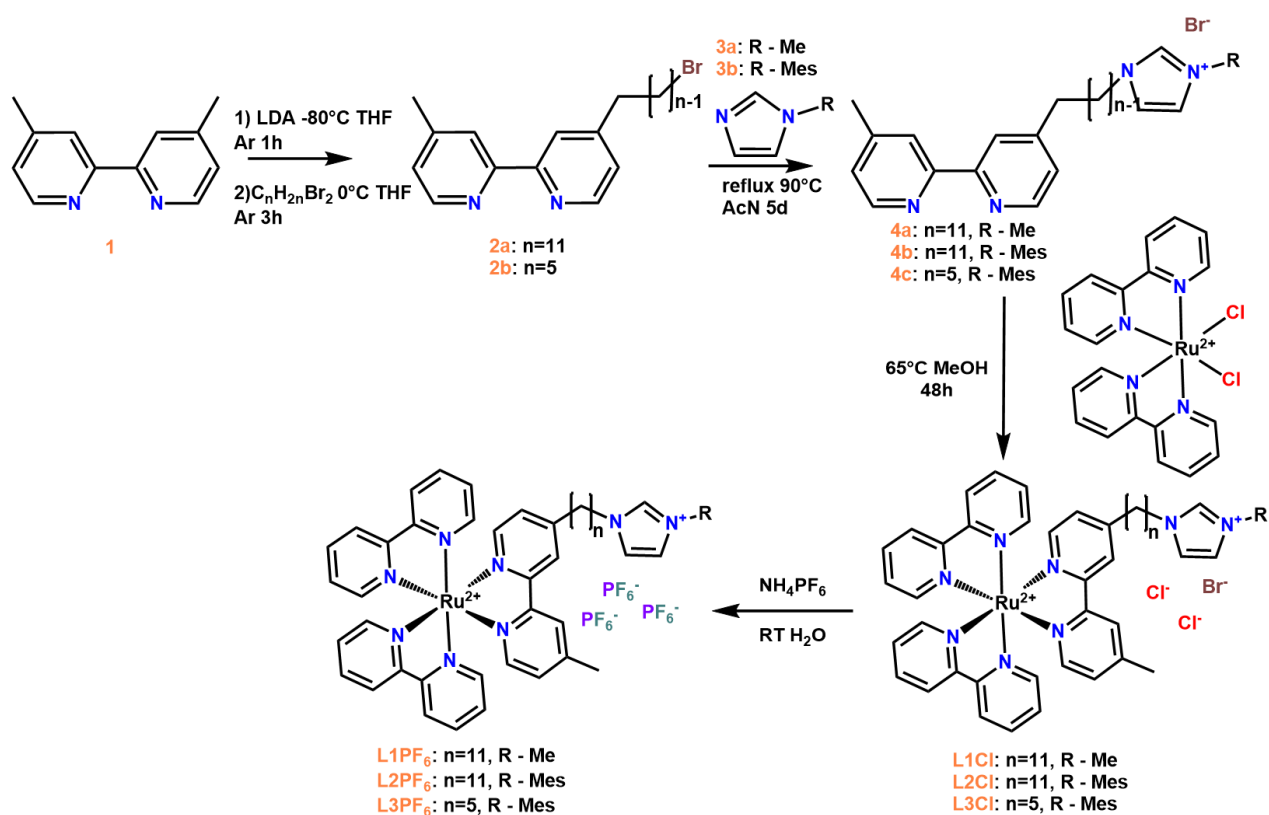


Figure 5.2.1 General scheme of the synthesis of the ruthenium complexes used in the study.

The first step included two one-pot reactions which was reported earlier for the synthesis of functionalized ruthenium complexes²⁷⁵. The first one was the deprotonation of 4,4'-dimethyl-2,2'-dipyridyl (**1**). To deprotonate a methyl group, a strong base such as lithium diisopropylamide (LDA) was required. Consequently, the addition of an excess of alkane functionalized with two bromo moieties on the ends (1,10-dibromodecane or 1,4-dibromobutane) resulted in the formation of (4-methyl-4'-bromoalkane)-2,2'-dipyridyls **2a** and **2b**. The next step was another nucleophilic substitution of bromine by imidazole **3a** (commercial) or **3b** (for the synthesis of **3b** see the experimental part). The complexation step was performed with ruthenium(II) cis-dichlorobis(2,2'-bipyridine) dihydrate and the chelating ligands **4a**, **4b**, **4c**. NMR analysis showed that the formed complexes were not pure. While for **L1** simple recrystallization from water was sufficient, complexes **L2** and **L3** remained contaminated. After a metathesis reaction with ammonium hexafluorophosphate, the resulting complexes with PF₆⁻ counter-anion showed minor impurities (see the experimental section).

5.3 Characterization of the complexes

Figure 5.1.2 presents a proton NMR spectrum of **L1PF₆** in DMSO. 2D COSY, HMBC, and HSQC were conducted for this sample to assign the peaks (see Appendix to Chapter 5). The most deshielded signal belongs to an imidazolium proton which simplifies its following during the deprotonation experiment. Aromatic signals of bpy moieties and two protons of imidazolium are mostly overlapped as well as the signals of the aliphatic chain at C41 – C47. Protons at C39, C40, C48, and C49 show distinct signals due to the different electronic environment, where the protons closer to the imidazolium ring are more deshielded comparing to the ones next to the bpy. Integration of signals did not give accurate values which can originate from different relaxation times of aliphatic protons and aromatic protons close to the metal center. The spectra of **L2** and **L3** are present in the Appendix to Chapter 5.

ESI MS analysis was performed for the complexes **L1Cl**, **L2PF₆**, and **L3PF₆** (for the spectra see Appendix to Chapter 5). The signals of the three-charged complexes were found in each case as well as other peaks depending on the compound. In case of **L3PF₆** an intense peak of a contamination was also detected, it requires further purification.

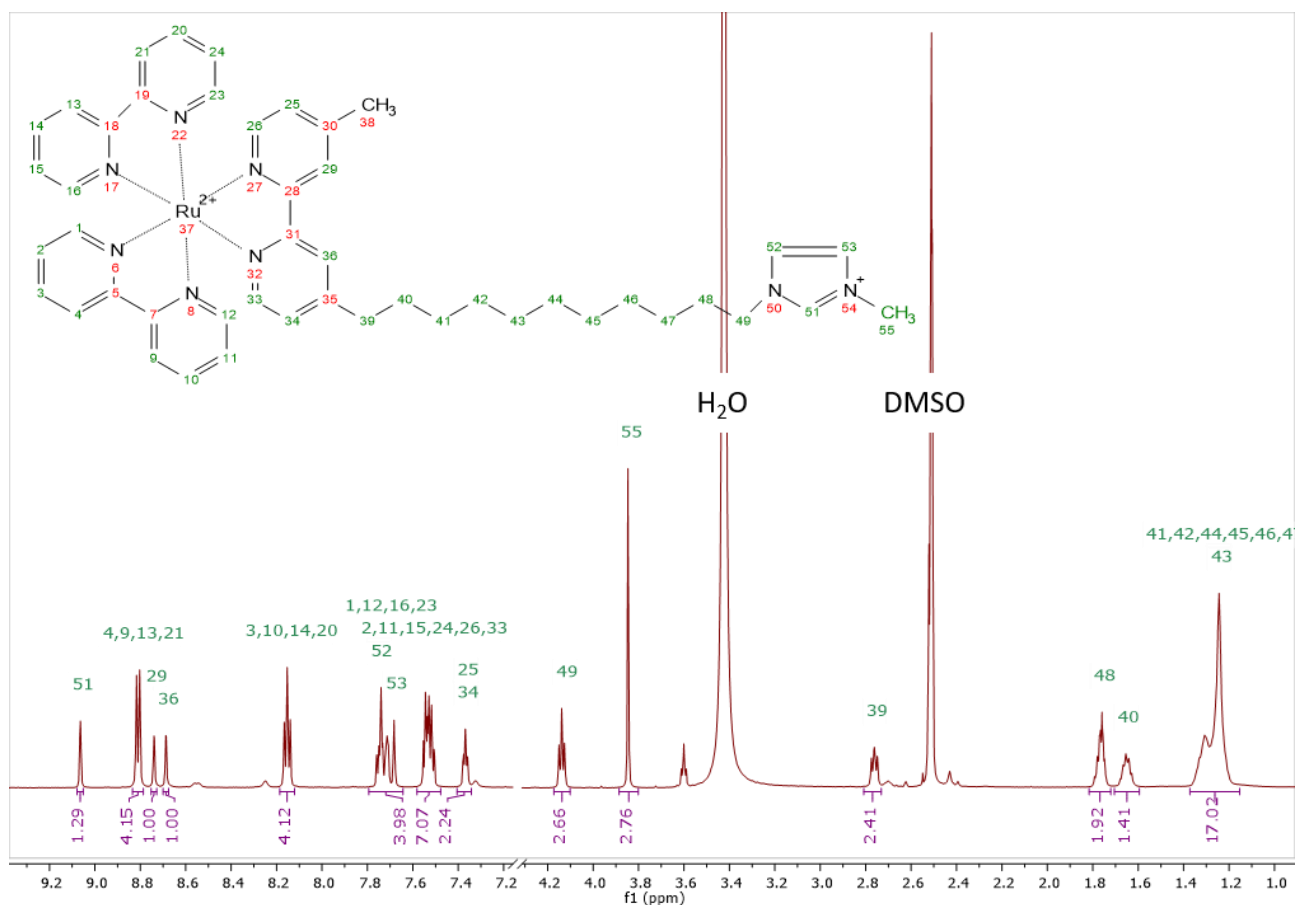


Figure 5.3.1 ¹H NMR spectrum of **L1PF₆** in DMSO-*D*₆. Peak of protons at C38 is hindered by the signal of water.

Absorption and emission spectra of **L1PF₆** -**L3PF₆** were recorded together with a model spectrum tris(4,4'-dimethyl-2,2'-bipyridine)ruthenium(II) hexafluorophosphate (**Ru(dmbpy)₃**) (Figure 5.3.2, Table 5.3.1); the compounds with the same counter-anion were analyzed for comparative reasons. The results showed similar absorption wavelengths for **L1**, **L2**, and **Ru(dmbpy)₃**, while absorption of **L3** was blue-shifted. Also, the emission of **L3** was much less intense than for other samples. TRPL study showed a little higher excited-state lifetime for the **L1** and **L2** (148, 147 ns) than for the model compound (107 ns). In case of **L3** together with a long-lived population (148 ns) a short-lived population with a decay time of 0.9 ns was found. Overall, the results indicated that 1) functionalization with the imidazolium fragments increased PL lifetime; 2) **L3** contains an impurity that quenches its luminescence.

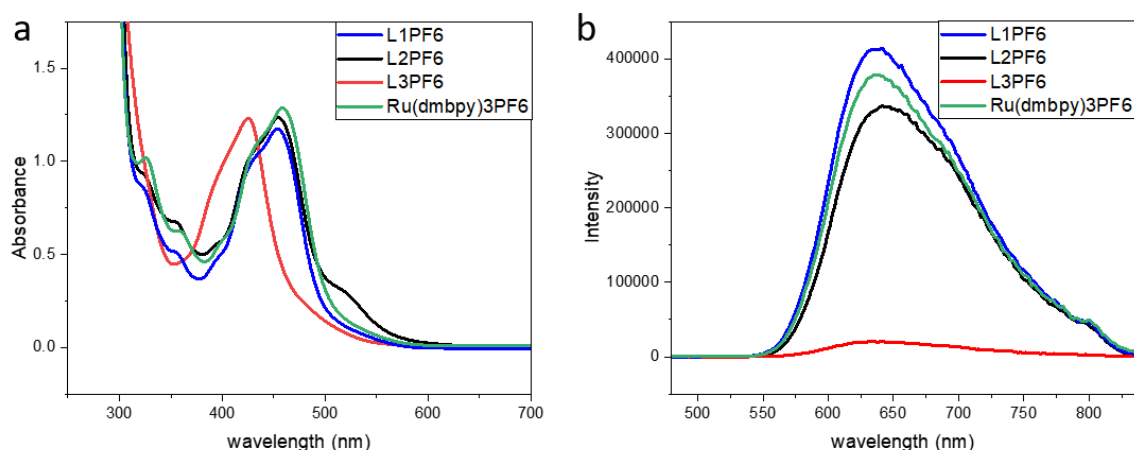


Figure 5.3.2 a) Absorption and b) emission spectra of the acetonitrile solutions of **L1PF6-L3PF6** and **Ru(dmbpy)3PF6**.

Table 5.3.1 Photophysical properties of **L1PF6-L3PF6** and **Ru(dmbpy)3PF6**.

Compound	λ_{abs} , nm	λ_{em} , nm	τ^* , ns
L1PF6	454	634	148
L2PF6	454	641	147
L3PF6	425	635	0.9; 148
Ru(dmbpy) ₃ PF6	458	638	107

*- lifetime measurements were done in aerated acetonitrile.

5.4 Deprotonation of the L1 complexes

Potassium tert-butoxide is a mild base that is commonly used for NHC deprotonation. It was used to deprotonate **L1PF₆** by adding a THF solution of the base into an acetonitrile-d₃ solution of **L1PF₆** and by further stirring of the solution overnight in the glovebox. Once the base was added, the solution changed the color from red to dark-cherry. Next day, a dark-red viscous solution was obtained (Figure 5.4.1). After THF evaporation a proton NMR of the compound was performed. On the NMR, all the aromatic signals were broad and undistinguishable. In the aliphatic part, the signals of tert-butanol were found as well as shifts and appearance of new signals (Figure 5.4.2). Deprotonation was also performed in THF and DMSO solutions; each time only wide peaks were observed in the aromatic part (see

Appendix to Chapter 5). This result did not correspond to our previous observations of NHC deprotonation when a peak of imidazolium proton disappeared and all others stayed sharp. We proposed few reasons why we could observe a broadening of the signals: 1) the KPF₆ salt increases viscosity of the system causing broadening of the signals; 2) the complex is decomposed by a base; 3) methyl moiety of imidazolium is not enough protective for the formed NHC so it is getting protonated during the tube transportation time and NMR analysis.



Figure 5.4.1 Photo of a tube with $L1PF_6$ in $AcN-d_3$ (red) and of $L1PF_6+t-butOK$ in $AcN-d_3$ (dark-red).

To find out the influence of the counter-anion, deprotonation of **L1Cl** was performed in similar manner and consequently 1H NMR was conducted. On the spectrum of **L1Cl** in AcN , a signal of an imidazolium proton occurs at 9.15 ppm (Figure 5.4.3 a). On the spectrum of a possibly deprotonated **L1Cl** we do not see an imidazolium proton at 9.15 ppm; meanwhile, the other aromatic signals looked similar to the ones of a protonated compound (Figure 5.4.3 b). Also, we noticed that signals at 2.80 ppm and 2.53 ppm from the spectrum before the deprotonation (Figure 5.4.3 a) disappeared on the spectra b-d. According to the attribution of **L1PF₆** in DMSO a signal at 2.53 ppm should be a methyl of a modified bipyridyl while a signal at 2.80 ppm should correspond to the first $-CH_2-$ in the chain (the closest to bpy). Normally they should not be affected by deprotonation, so this behaviour will be investigated in future.

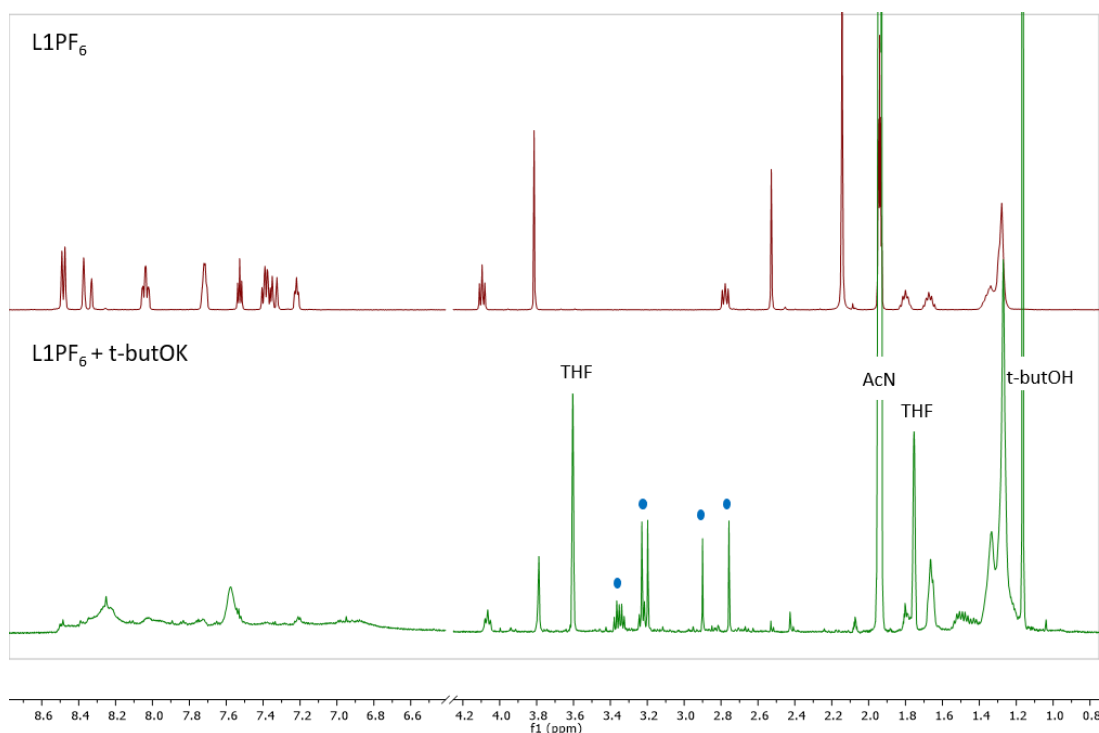


Figure 5.4.2 Deprotonation of **L1PF₆**. 1H NMR spectra of a) **L1PF₆**; b) **L1PF₆** after stirring with *t-butOK* for 24h; blue circles indicate new or shifted signals. NMR solutions were prepared in $AcN-d_3$.

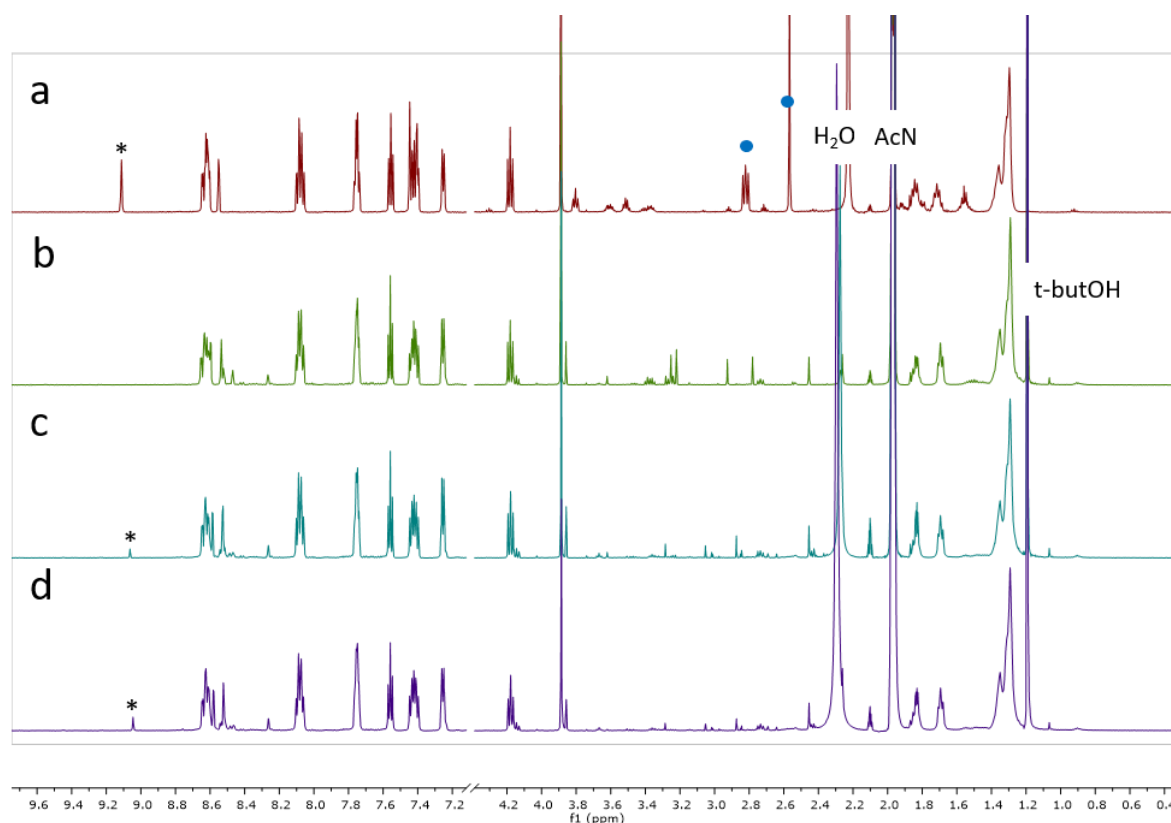


Figure 5.4.3 Deprotonation of **L1Cl**. ^1H NMR spectra in AcN-d_3 of a) **L1Cl**; b) **L1Cl** + *t*-butOK; c) the same tube on air for 24h and d) for 48h. On spectra c) and d) reappearance of imidazolium proton is indicated with a *; disappearance of a triplet at 2.80 ppm and a singlet at 2.53 ppm indicated with a blue circle.

5.5 Synthesis of Pt NPs stabilized with L1Cl

The disappearance of an imidazolium proton signal let us use this complex in the synthesis of Pt NPs. The synthesis was performed by the organometallic approach with decomposition of Pt_2dba_3 precursor under 3 bar of H_2 in the presence of deprotonated **L1Cl** (0.1 eq relative to the Pt amount). After stirring the mixture at RT for 24 h it was washed firstly with pentane three times and then with $\text{AcN/THF}=1/30$ until no colored solution was observed. Consequently, the product was dried with vacuum line overnight. TEM results showed US NPs of 1.4 nm with small size distribution in agreement with the previous reports on the synthesis of NPs stabilized with NHCs (Figure 5.5.1)^{45,46}. NPs were found both in dispersed state and as a part of dense clusters.

On the NMR spectrum of Pt NPs stabilized with **L1Cl** (**Pt-L1Cl**) small broad signals in aromatic and aliphatic regions were found (Figure 5.5.2). Probably, it originates from a combination of several effects: 1) the amount of **L1Cl** on the surface after multiple washings is very low; 2) coordination to the surface of Pt NPs reduces its NMR signal because of a slow tumbling of the resulting objects.

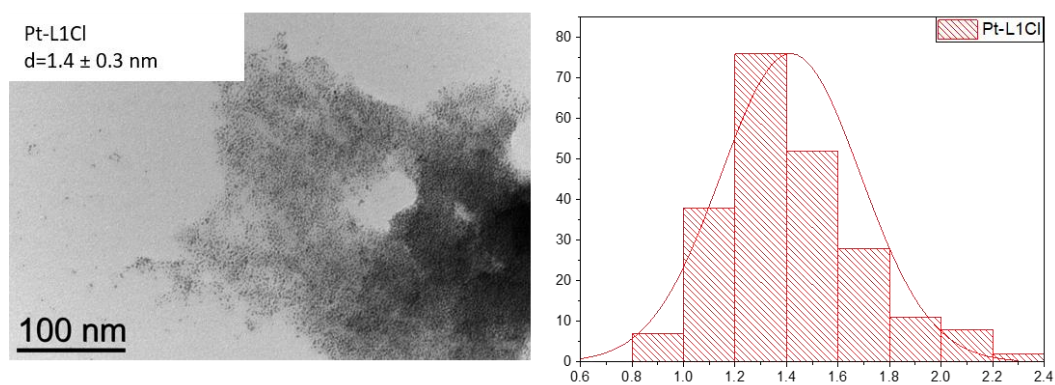


Figure 5.5.1 TEM image and a size distribution diagram of **Pt-L1Cl** NPs.

On ESI-MS (electrospray ionization-mass spectrometry) spectrum of **Pt-L1Cl** intense signals of **L1Cl** were found, which suggests the coordination of **L1Cl** without its decomposition (for the spectrum see Mass spectra in the Appendix). Absorption and emission spectra of **L1Cl** and of **Pt-L1Cl** are shown on the Figure 5.5.3. The **Pt-L1Cl** spectra are similar the **L1Cl** ones with slight bathochromic shifts in absorption (455 nm to 460 nm) and in emission maximums (635 to 639 nm). Emission of the complex attached to the NPs was significantly quenched, which we expect to originate from the energy transfer to Pt in accordance with the literature reports²⁷⁶.

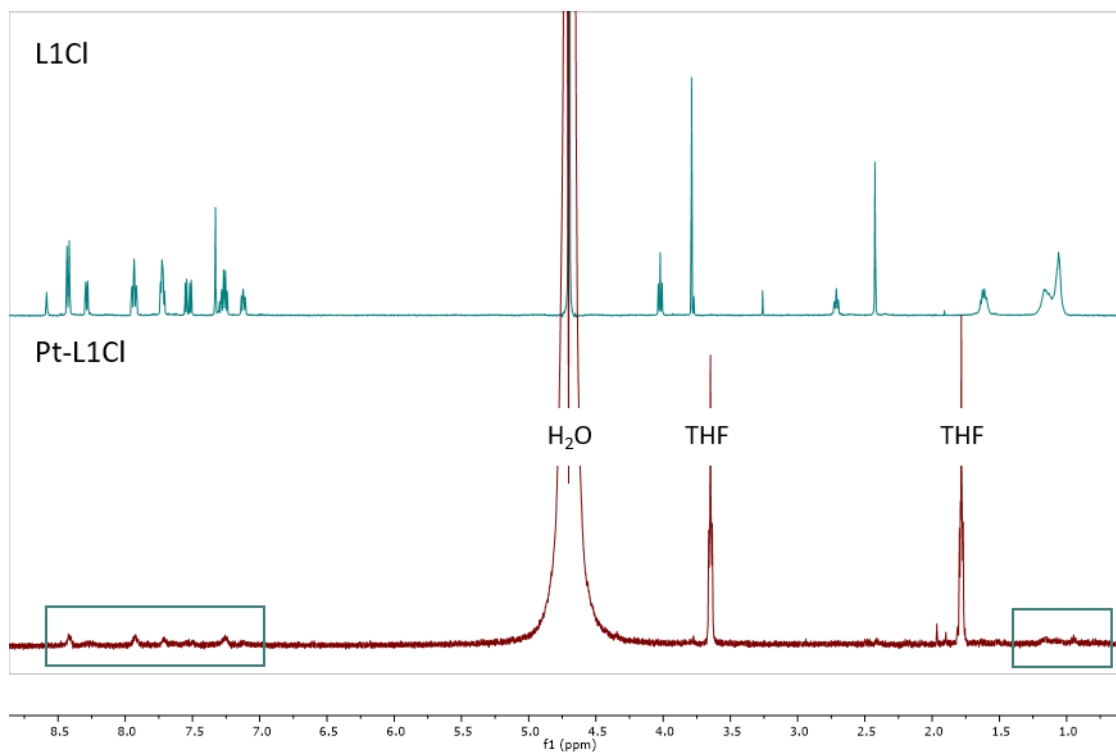


Figure 5.5.2 ¹H NMR spectra of **L1Cl** and **Pt-L1Cl** in D₂O. Frames indicate broad signals of **L1Cl** coordinated to the NPs.

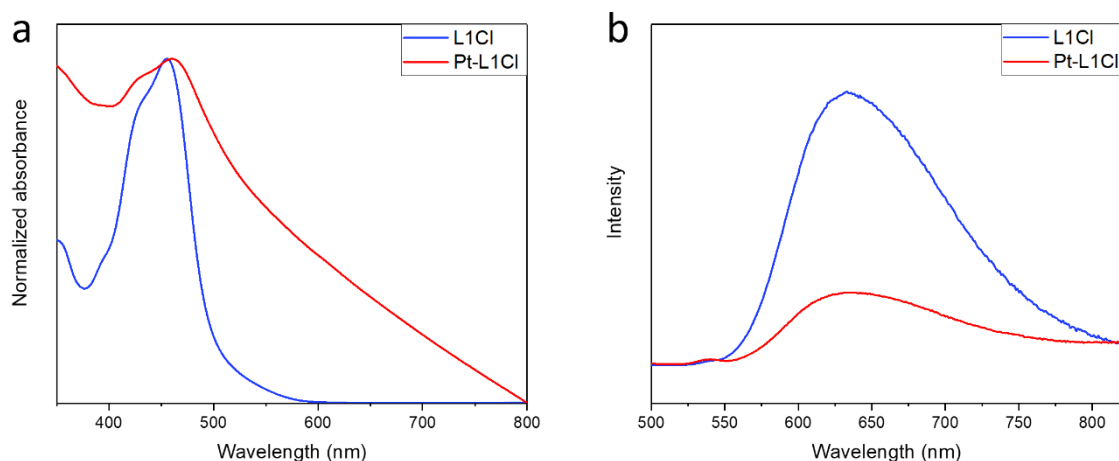


Figure 5.5.3 a) Absorption and b) emission spectra of **L1Cl** (blue) and of **Pt-L1Cl** NPs (red).

5.6 Conclusions

This chapter describes the first results of a project which aims to create hybrid “Pt NP-Ru antenna complex” nanomaterials for photocatalytic applications. Firstly, the functionalization of the ruthenium complexes with an imidazolium fragment was performed. The imidazolium is an important part of the system because by deprotonation it transforms into NHC, which strongly binds to the Pt surface. We have synthesized three complexes varying the substituent of the imidazolium ring and the length of the alkyl chain between the complex and the imidazolium moiety. The complexes showed similar photophysical properties with increased excited state lifetimes compared to the model complex. However, **L2** and especially **L3** complexes contained impurities. Thus, an additional purification step must be performed for these complexes. We plan to use size-exclusion chromatography for these purposes.

For further investigations, we used **L1** complexes. We have shown by NMR that the deprotonation of the **L1Cl** complex can be successfully performed. Moreover, the synthesis of the US Pt NPs was achieved in the presence of deprotonated **L1Cl** being the only stabilizer in the system. MS analysis confirmed the presence of the complex in the NPs, suggesting the stability of **L1Cl** under the synthetic conditions. The PL spectra showed a decreased emission intensity in **Pt-L1Cl**. The PL quenching may occur due to the energy transfer from **L1Cl** to Pt which is an effect we anticipate. TRPL measurements are in progress.

The promising results of the synthesis and characterization of **Pt-L1Cl** NPs encourage us to continue the project. The least what we plan to do includes:

- 1) purification of the **L2** and **L3** complexes and synthesis of Pt NPs stabilized with them.

- 2) synthesis of the complex with a shorter alkyl chain and a methylimidazolium moiety – **L4** (Figure 5.6.1) and the formation of the NPs stabilized with it. The aim is to compare the energy transfer in the systems with different chain lengths and to relate the results to the photocatalytic properties of the hybrid catalysts;

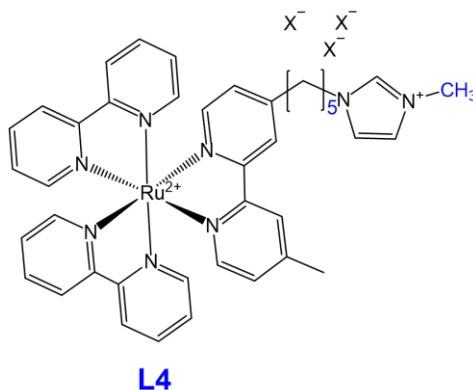


Figure 5.6.1 Structure of an **L4** complex

- 3) synthesis of supported Pt NPs and their post-functionalization with the complex of interest to compare the catalytic performance and stability of the supported and colloidal NPs;
- 4) finally, we aim to test the optimized catalyst in the relevant Pt-catalyzed photocatalytic reaction.

In addition, we have to note that the synthetic procedure was not optimized since we wanted firstly to test the complexes. However, if the catalyst shows high performances, it will be necessary to optimize synthetic and purification steps.

5.7 Experimental part

5.8.1 General

Synthesis of the ruthenium complexes was carried out on air or under an inert atmosphere using standard Schlenk techniques. The synthesized nanoparticles were stored in the glovebox. The chemicals were bought from commercial sources and used without purification (Table 5.7.1). Dry and degassed solvents were used in air- and water-sensitive steps, otherwise, commercial solvents were used without purification. The deprotonation of the ligand and the synthesis of Pt NPs was done in inert conditions.

Table 5.7.1 List of chemicals

Chemical	Producer	Purity,%
Glyoxal	Sigma Aldrich	40% in H ₂ O
Formaldehyde	Alfa Aesar	37
Acetic acid	VRW	≥99
2,4,6-Trimethylaniline	Sigma Aldrich	98
Ammonium acetate	Sigma Aldrich	≥98
4,4'-Dimethyl-2,2'-dipyridyl	Sigma Aldrich	99
Lithium diisopropylamide	Sigma Aldrich	2.0 M in THF
1,10-Dibromodecane	Sigma Aldrich	97
1,4-Dibromobutane	Sigma Aldrich	99
1-Methylimidazol	Sigma Aldrich	99
Cis-dichlorobis(bipyridine) ruthenium(II) dihydrate	Strem	99
Ammonium hexafluorophosphate	Sigma Aldrich	≥99
Potassium tert-butoxide	Sigma Aldrich	98
Tris(dibenzylideneacetone)diplatinum(0)	NanoMePS	≥99

5.8.2 Analytics

Liquid-state NMR ¹H and ¹³C NMR experiments were recorded on a 500 MHz Bruker Avance spectrometer using deuterated solvents with internal or external TMS reference.

Absorption spectroscopy was performed with a spectrometer Cary Series UV-Vis-NIR Agilent. Cuves with 2 mm optical path length were used for the measurements.

PL spectra were recorded with a fluorimeter of PTI brand equipped with Xenon lamp as irradiation source and UV-Vis detector.

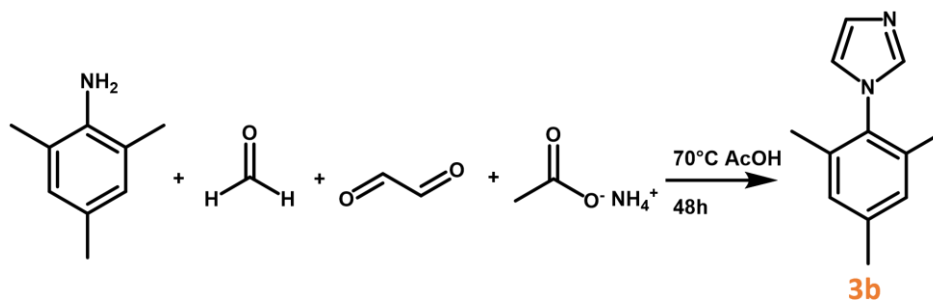
Time-resolved PL measurements were performed at ICT by Charles-Louis Serpentine.

TEM images were collected using a JEOL JEM 1400 operated at 120kV and using a tungsten filament. The NP size and distribution was determined from the measurement of over 200 particles.

Mass spectrometry was performed at ICT by Valerie Bourdon.

5.8.3 Synthetic procedures

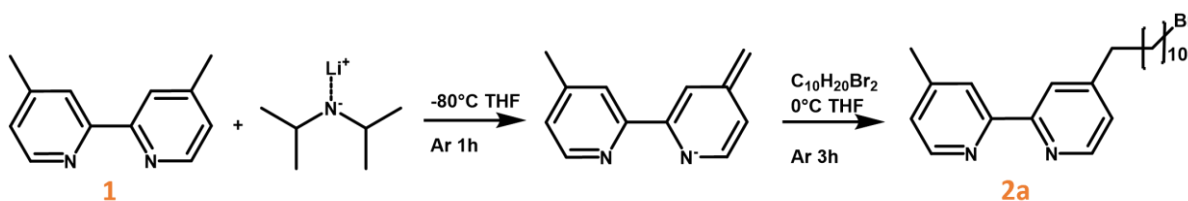
The synthetic scheme for the synthesis of **L1** was developed with the postdoctoral student from our team, Juan Manuel Asensio.

1) Synthesis of 1-mesitylimidazol (3b)

Glyoxal (7.8 mL, 0.068 mol) and formaldehyde (5 mL, 0.067 mol) were mixed together in glacial acetic acid (17.5 mL) in the flask. Then ammonium acetate (5.35 g, 0.068 mol) was dissolved in glacial acetic acid (17.5 mL) and then 2,4,6-trimethylaniline (10 mL, 0.07 mol) was added to the funnel. Solution of ammonium acetate and aniline was slowly added to the flask with other compounds. After, solution left stirring at 70°C for 48 h.

Work-up and purification: reaction was neutralized with sodium bicarbonate and filtered through a Buchner funnel. Resulting black sticky solid was dissolved in acetone and evaporated with rotavap to remove excess of water. Later, the compound was purified by sublimation at 95°C and dynamic vacuum overnight. Resulting white-lemon crystals were analyzed with NMR which showed pure compound. Yield: 6.031 g (48%).

¹H NMR (400 MHz, Chloroform-*d*) δ 7.42 (t, *J* = 1.1 Hz, 1H), 7.21 (t, *J* = 1.1 Hz, 1H), 6.97 – 6.93 (m, 2H), 6.87 (t, *J* = 1.3 Hz, 1H), 2.32 (s, 3H), 1.97 (s, 6H).

2) Synthesis of 4-(11-bromoundecyl)-4'-methyl-2,2'-bipyridine (2a)

4,4'-Dimethyl-2,2'-dipyridyl (**1**) (1.18 g, 6.4 mmol) was dissolved in 45 mL of deaerated dry THF in a Schlenk tube. The tube was placed in an acetone / liquid nitrogen bath (-80°C) and LDA (7.2 mL, 7.2 mmol) was added with a glass syringe drop by drop. The solution was stirred for 1 h at -80°C. In another flask 1,10-dibromodecane (14 mL, 62 mmol) was dissolved in 14.5 mL of THF and cannulated into the bipyridine solution. Meanwhile, the bath was changed to the ice bath (0°C). After the cannulation the solution immediately changed the color to pale yellow. It was stirred for 3h at 0°C.

Work-up and purification: 25 mL of water were added to the tube and pH was adjusted to 7 with 1M HCl. Then, the compounds were extracted with diethyl ether and the solvent was evaporated with a rotavap. NMR analysis showed that the product was contaminated with the starting reagents and side-products. Column chromatography with silica as a steady phase and hexane/ethyl acetate (20/80 with gradual increase of ethyl acetate content) as a mobile phase with pretreatment with triethylamine was used to separate the compounds. Among 34 fractions only in fractions 9-13 the pure compound was found. Other fractions contained dibromodecane, dimethylbipyridine, possibly 4-undecyl-4'-methyl-2,2'-bipyridine and other contaminations. After evaporation of solvents compound appeared as a pale pink sticky powder. Yield: 610 mg (24%).

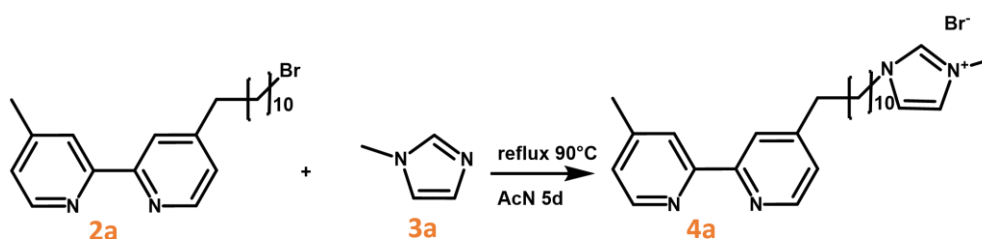
^1H NMR (500 MHz, Chloroform-*d*) δ 8.60 (t, $J = 5.6$ Hz, 2H), 8.33 (s, 2H), 7.23 (s, 2H), 3.43 (t, $J = 6.9$ Hz, 2H), 2.74 (t, $J = 7.7$ Hz, 2H), 2.50 (s, 3H), 1.89 – 1.79 (m, 2H), 1.72 (p, $J = 7.7$ Hz, 2H), 1.46 – 1.17 (m, 14H).

3) Synthesis of 4-(5-bromopentyl)-4'-methyl-2,2'-bipyridine (2b)

The synthesis was performed in the same manner with the same purification as for compound **2a**. $m(\mathbf{1})=1.105$ g (6.0 mmol), $V(\text{LDA})=6.8$ mL (6.8 mmol), $V(\text{C}_4\text{H}_8\text{Br}_2)=5.8$ mL (48 mmol), $V(\text{THF})=55$ mL. Appearance as white sticky powder. Yield: 527 mg (27%).

^1H NMR (400 MHz, Chloroform-*d*) δ 8.58 – 8.47 (m, 4H), 8.22 (ddt, $J = 4.2, 1.7, 0.8$ Hz, 3H), 7.12 (ddt, $J = 5.0, 1.7, 0.8$ Hz, 3H), 3.39 (t, $J = 6.8$ Hz, 2H), 2.79 – 2.63 (m, 2H), 2.43 (d, $J = 0.8$ Hz, 7H), 1.89 (dq, $J = 7.9, 6.8$ Hz, 2H), 1.72 (dddd, $J = 9.4, 7.7, 6.8, 5.3$ Hz, 2H), 1.58 – 1.43 (m, 2H).

4) Synthesis of 3-methyl-1-(11-(4'-methyl-[2,2'-bipyridin]-4-yl)undecyl)-imidazol-3-ium bromide (4a)



To the solution of **2a** (339 mg, 0.84 mmol) in acetonitrile (20 mL) the **3a** (117 μL , 1.47 mmol) was added and the mixture was left stirring at 90°C under reflux for 5 days. Then, solvent was evaporated and compound was used in the next step. Yield: 430 mg (105% due to the excess of methylimidazole).

^1H NMR (500 MHz, Chloroform- d) δ 10.73 (d, J = 1.6 Hz, 1H), 8.60 – 8.52 (m, 2H), 8.27 – 8.22 (m, 2H), 7.33 (t, J = 1.8 Hz, 1H), 7.26 (t, J = 1.8 Hz, 1H), 7.16 (dd, J = 5.1, 1.7 Hz, 2H), 4.37 – 4.28 (m, 2H), 4.15 (s, 3H), 2.74 – 2.67 (m, 2H), 2.46 (s, 3H), 1.93 (p, J = 7.5 Hz, 2H), 1.70 (h, J = 6.9, 6.2 Hz, 2H), 1.31 (d, J = 39.4 Hz, 14H).

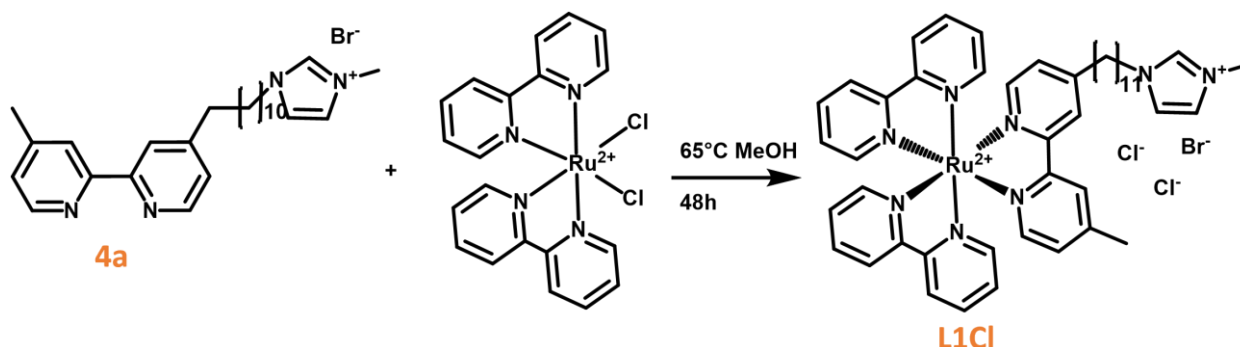
5) Synthesis of 3-mesityl-1-(11-(4'-methyl-[2,2'-bipyridin]-4-yl)undecyl)-imidazol-3-ium bromide (4b)

The synthesis was performed in the same manner as for the compound **4a**. $m(\mathbf{2a})=105$ mg (0.26 mmol); $m(\mathbf{3b})=61$ mg (0.33 mmol); $V(\text{AcN})=14$ mL. Compound was directly used in the next step without characterization. Yield: 133 mg (80%).

6) Synthesis of 3-mesityl-1-(5-(4'-methyl-[2,2'-bipyridin]-4-yl)pentyl)-imidazol-3-ium bromide (4c)

The synthesis was performed in the same manner as for the compound **4a**. $m(\mathbf{2b})=190$ mg (0.60 mmol), $m(\mathbf{3b})=108$ mg (0.58 mmol), $V(\text{AcN})=15$ mL. Compound was directly used in the next step without characterization. Yield: 256 mg (88%).

7) Synthesis of ruthenium(II) bis(bipyridine)(3-methyl-1-(11-(4'-methyl-[2,2'-bipyridin]-4-yl)undecyl)-imidazol-3-ium) dichloride bromide (L1Cl)



4a (284 mg, 0.58 mmol) and cis-dichlorobis(bipyridine) ruthenium(II) dihydrate (276 mg, 0.55 mmol) were dissolved in 50 mL of methanol and left stirring under reflux at 65°C for 48 h. After the solvent was evaporated with a rotavap and a final compound was analyzed with proton NMR. To purify the compound simple recrystallisation from water solution was performed where a dark precipitate was separated from the red solution of the final complex. Yield: 386 mg (72%).

^1H NMR (400 MHz, Deuterium Oxide) δ 8.60 (s, 1H), 8.43 (d, J = 8.2 Hz, 4H), 8.29 (d, J = 6.9 Hz, 2H), 7.95 (d, J = 9.3 Hz, 3H), 7.77 – 7.65 (m, 4H), 7.57 – 7.47 (m, 2H), 7.38 – 7.32 (m, 3H), 7.32 – 7.20 (m,

4H), 7.17 – 7.08 (m, 2H), 4.03 (t, $J = 7.1$ Hz, 2H), 3.83 – 3.79 (m, 3H), 2.70 (t, $J = 7.3$ Hz, 2H), 2.43 (s, 3H), 1.61 (dd, $J = 18.0, 11.0$ Hz, 4H), 1.24 – 0.85 (m, 14H).

8) Synthesis of ruthenium(II) bis(bipyridine)(3-mesityl-1-(11-(4'-methyl-[2,2'-bipyridin]-4-yl)undecyl)-imidazol-3-ium) dichloride bromide (L2Cl)

$m(\mathbf{4b}) = 90$ mg (0.15 mmol), $m(\text{Ru}(\text{bpy})_2(\text{Cl})_2) = 92$ mg (0.18 mmol), $V(\text{MeOH}) = 20$ mL. Yield: 141 mg (88%, not pure).

9) Synthesis of ruthenium (II) bis(bipyridine)(3-mesityl-1-(5-(4'-methyl-[2,2'-bipyridin]-4-yl)pentyl)-imidazol-3-ium) dichloride bromide (L3Cl)

$m(\mathbf{4c}) = 106$ mg (0.25 mmol), $m(\text{Ru}(\text{bpy})_2(\text{Cl})_2) = 120$ mg (0.23 mmol), $V(\text{MeOH}) = 20$ mL. Yield: 203 mg (89%, not pure).

10) Metathesis of L1Cl with NH_4PF_6 salt

L1Cl was dissolved in water and an excess of water solution of NH_4PF_6 was added to the solution of the complex. An immediate formation of orange precipitate was observed. The precipitate was filtered with a Buchner funnel and rinsed with water and diethyl ether. The resulting powder was redissolved in AcN and dried with a rotavap with formation of dark-red dense powder.

^1H NMR (600 MHz, $\text{DMSO}-d_6$) δ 9.06 (s, 1H), 8.81 (d, $J = 8.2$ Hz, 4H), 8.74 (s, 1H), 8.69 (s, 1H), 8.15 (t, $J = 7.9$ Hz, 4H), 7.79 – 7.64 (m, 4H), 7.53 (dq, $J = 13.3, 6.0$ Hz, 7H), 7.37 (t, $J = 4.9$ Hz, 2H), 4.14 (t, $J = 7.3$ Hz, 3H), 3.85 (s, 3H), 2.81 – 2.73 (m, 2H), 1.76 (d, $J = 3.7$ Hz, 2H), 1.65 (s, 1H), 1.28 (d, $J = 38.3$ Hz, 17H).

11) Metathesis of L2Cl with NH_4PF_6 salt

The metathesis was performed in the same manner as for compound **L1Cl**. NMR showed that the compound is mostly pure, however, signals of minor contaminations were also present on the spectrum.

^1H NMR (400 MHz, Acetonitrile- d_3) δ 8.56 (s, 1H), 8.51 – 8.43 (m, 5H), 8.37 (s, 1H), 8.33 (s, 1H), 8.04 (tt, $J = 7.1, 1.6$ Hz, 6H), 7.75 – 7.67 (m, 6H), 7.62 (t, $J = 1.8$ Hz, 1H), 7.52 (dd, $J = 5.8, 3.6$ Hz, 3H), 7.44 (t, $J = 1.9$ Hz, 1H), 7.42 – 7.33 (m, 6H), 7.21 (t, $J = 4.6$ Hz, 3H), 7.14 – 7.08 (m, 2H), 4.23 (t, $J = 7.3$ Hz, 2H), 3.69 – 3.61 (m, 2H), 2.84 – 2.72 (m, 3H), 2.52 (s, 4H), 2.35 (s, 3H), 2.02 (s, 6H), 1.83 – 1.60 (m, 11H), 1.44 – 1.22 (m, 26H).

12) Metathesis of L3Cl with NH₄PF₆ salt

The metathesis was performed in the same manner as for compound *L1Cl*. NMR showed that the compound is mostly pure however integration of the signals did not correspond to what we expected. Mass spectrum showed a presence of a bipyridyl fragment which contained two imidazolium chains. So the contamination that affected NMR integration was the Ru complex bearing the bifunctionalized bipyridyl.

¹H NMR (400 MHz, DMSO-d₆) δ 9.37 (d, J = 5.5 Hz, 1H), 9.33 (d, J = 2.2 Hz, 1H), 8.78 (d, J = 8.2 Hz, 1H), 8.65 (d, J = 8.1 Hz, 1H), 8.51 (dt, J = 10.4, 5.0 Hz, 2H), 8.39 – 8.31 (m, 1H), 8.19 (d, J = 4.1 Hz, 2H), 8.07 – 7.99 (m, 2H), 7.93 (dd, J = 7.7, 5.6 Hz, 1H), 7.84 (d, J = 2.1 Hz, 1H), 7.58 (d, J = 5.6 Hz, 1H), 7.41 – 7.33 (m, 1H), 7.28 (d, J = 5.1 Hz, 2H), 7.10 (d, J = 2.6 Hz, 2H), 4.28 (t, J = 7.0 Hz, 2H), 2.70 (t, J = 7.7 Hz, 3H), 2.44 (s, 3H), 2.31 (s, 3H), 1.99 – 1.90 (m, 10H), 1.81 – 1.59 (m, 3H), 1.27 (q, J = 7.7 Hz, 2H).

13) Synthesis of Pt-L1 NPs

In a glovebox to 19.4 mg of **L1Cl** 5ml THF and 0.5mL of AcN were added. To this partially soluble precursor a THF solution containing t-butOK (2.2 mg) was added under stirring. Next day the solution looked much more soluble, with dark-red color. Note, that the starting compound is poorly soluble in THF but it dissolved gradually during the reaction. A solution of Pt₂dba₃ (109.3 mg) was prepared in THF (20 mL) and deprotonated **L1Cl** solution was added. The Fischer-Porter bottle containing the reagents was charged with 3 bar of H₂ and left stirring at RT for 18h. Later, the solution was washed firstly with THF/pentane and then with AcN/THF mixture until supernatant became colorless.

5.8. Appendix to Chapter 5

5.8.1 NMR spectra

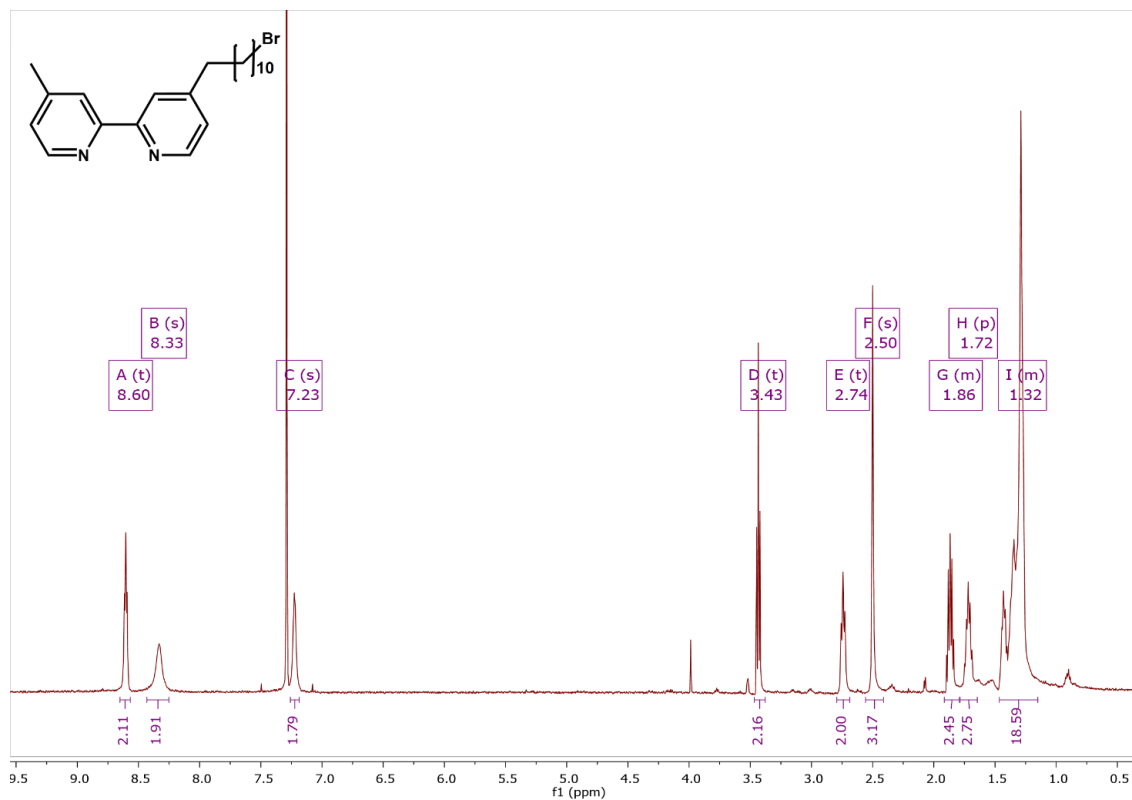


Figure 5.8.1 ^1H NMR spectrum of **2a**.

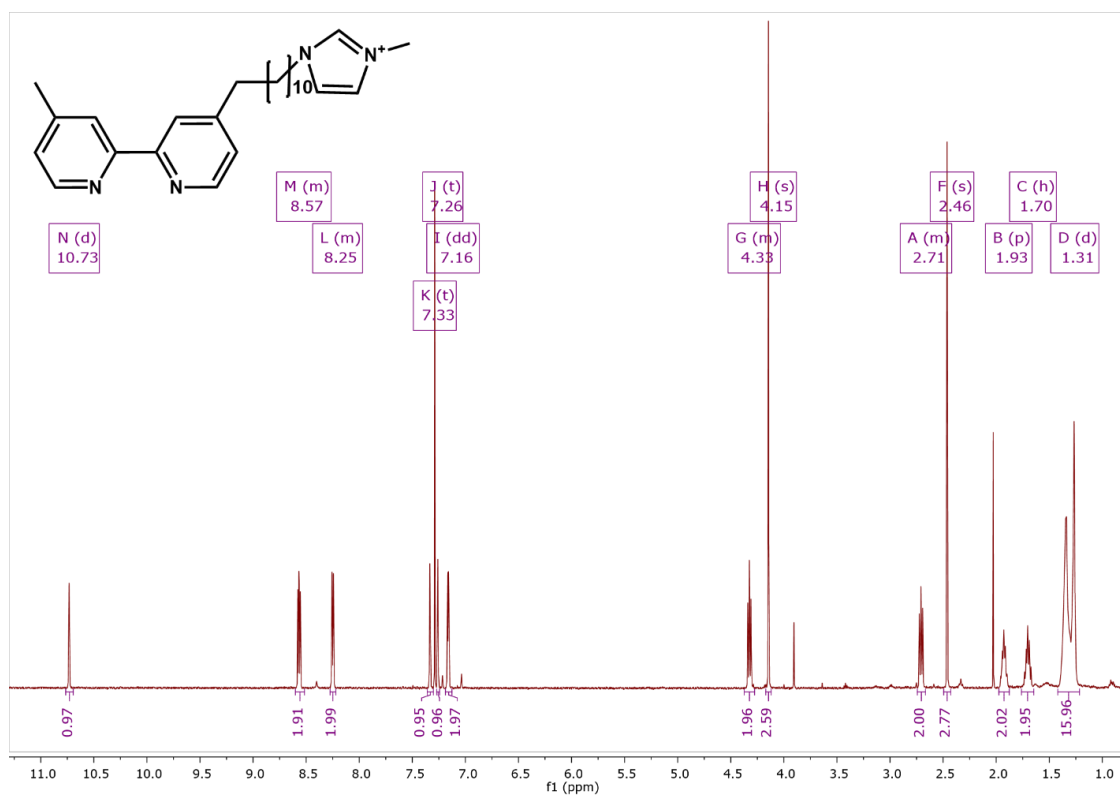
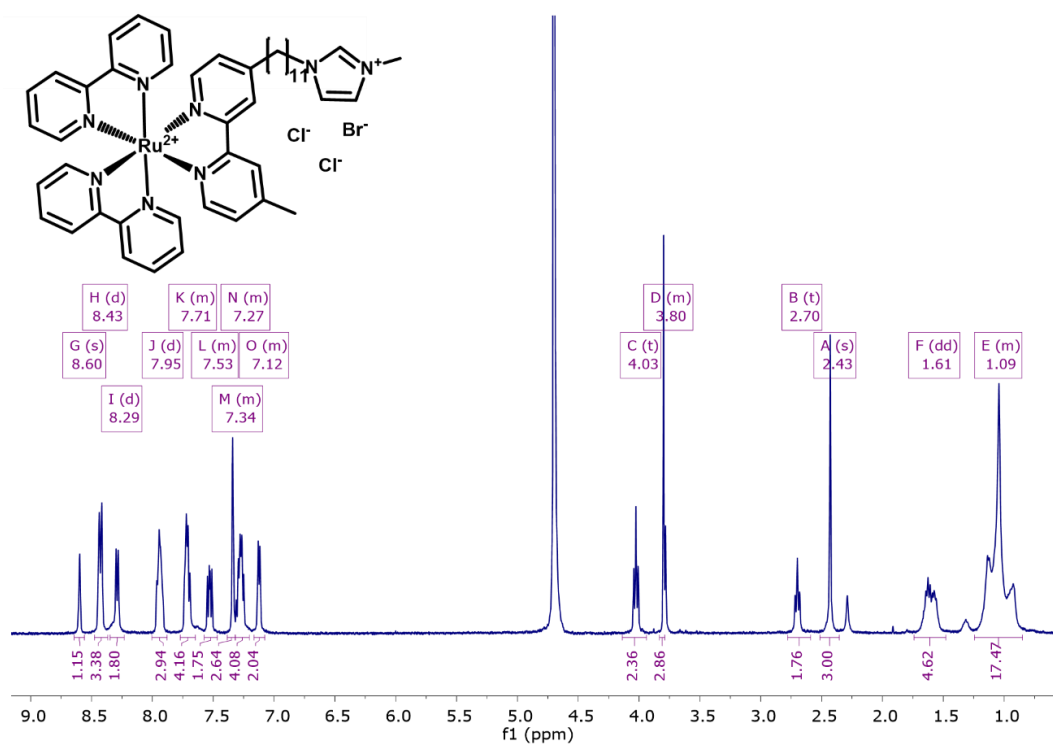
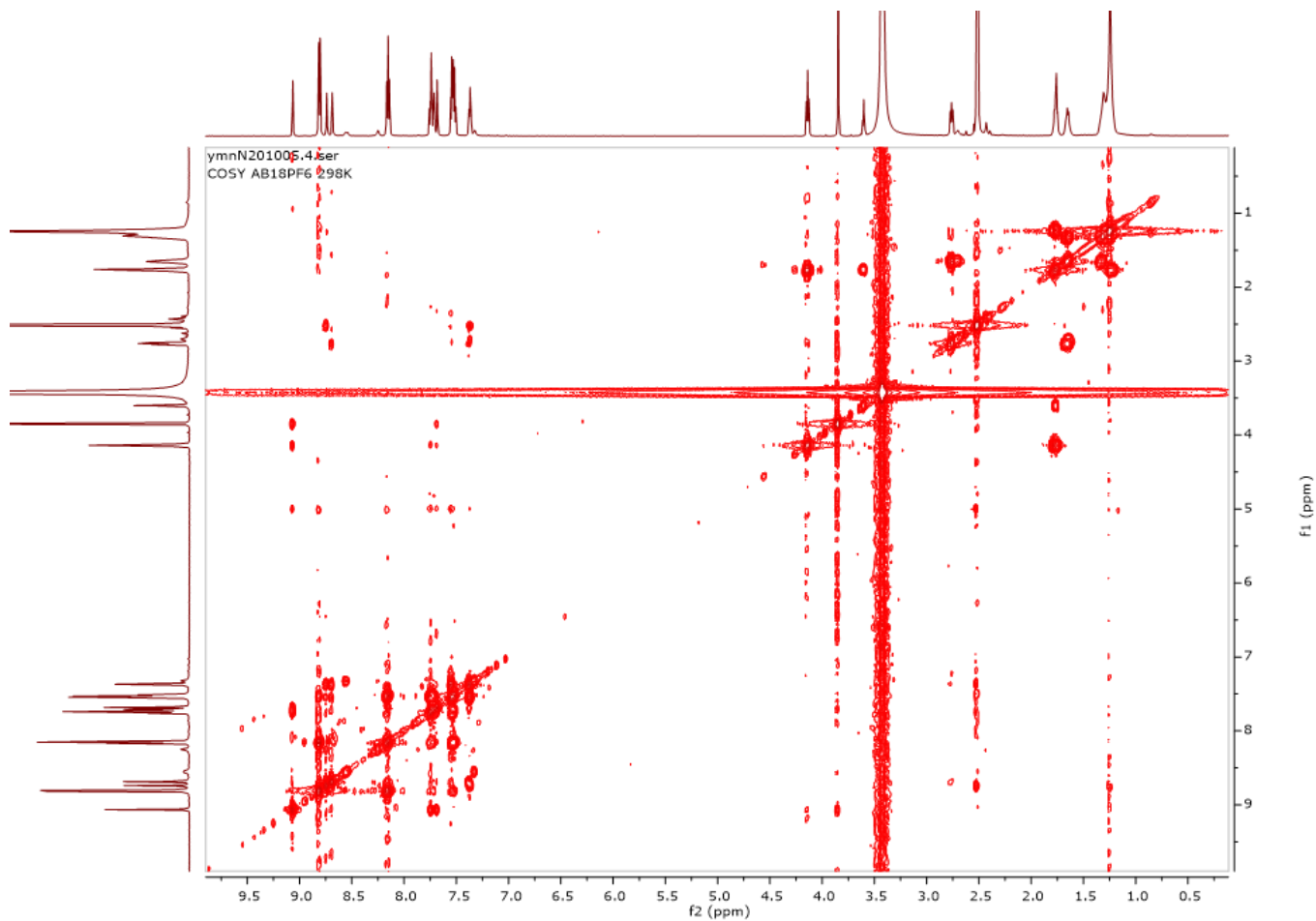
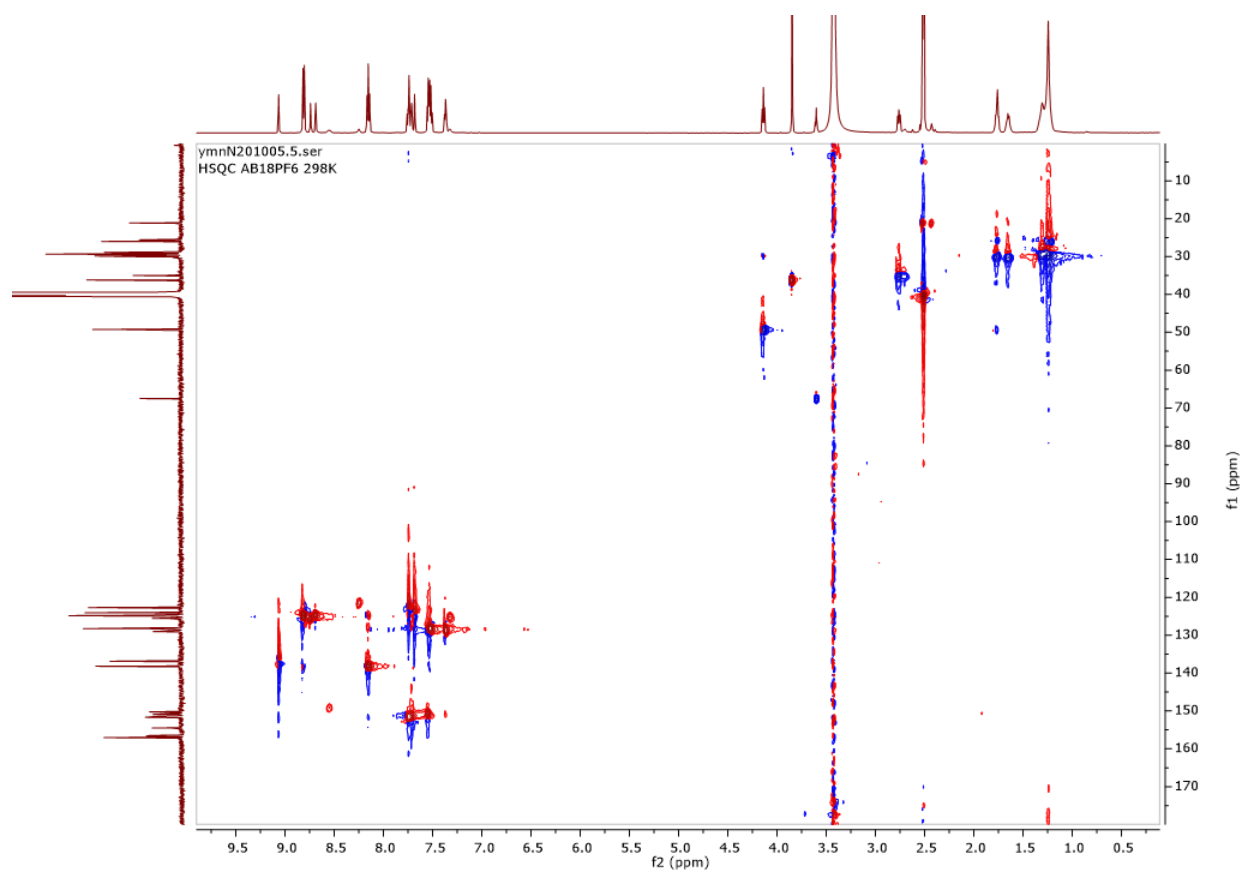
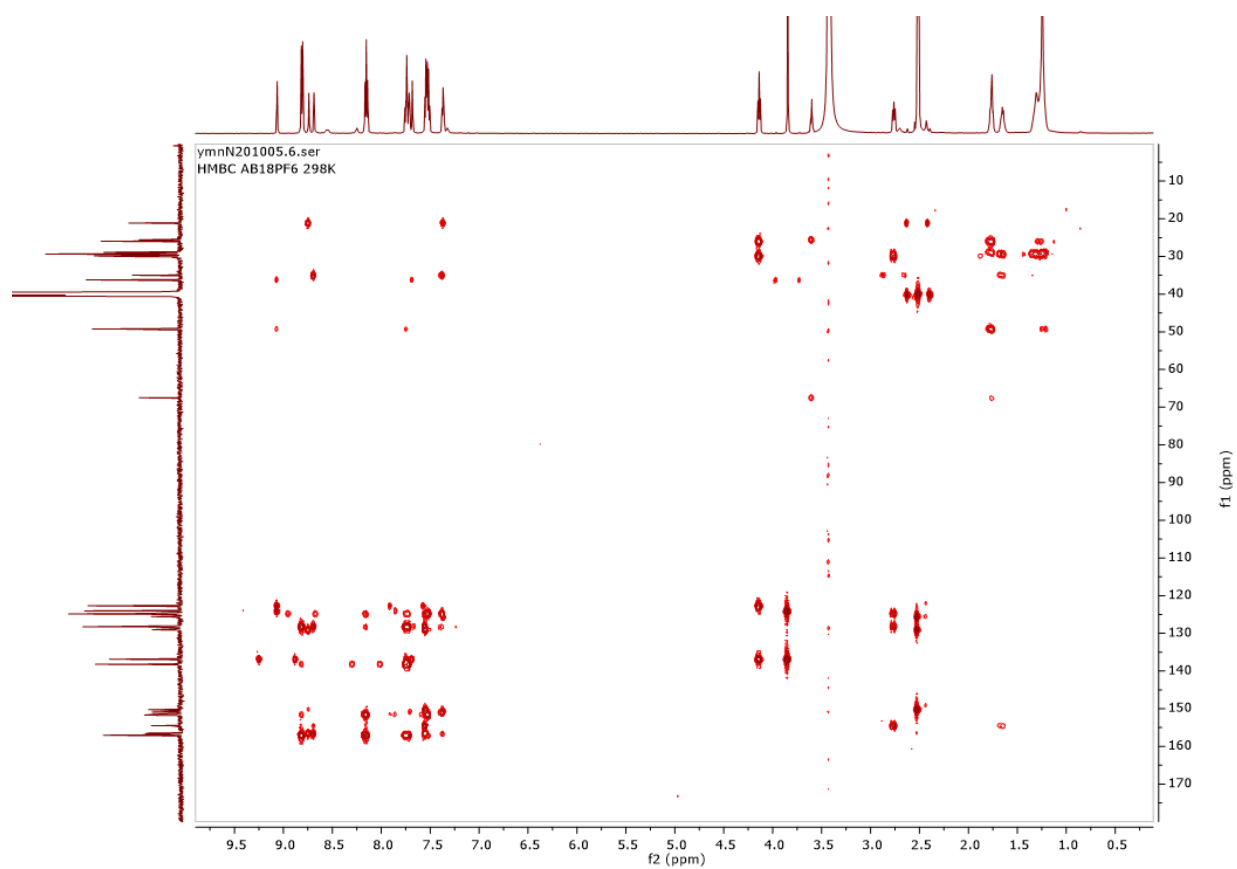
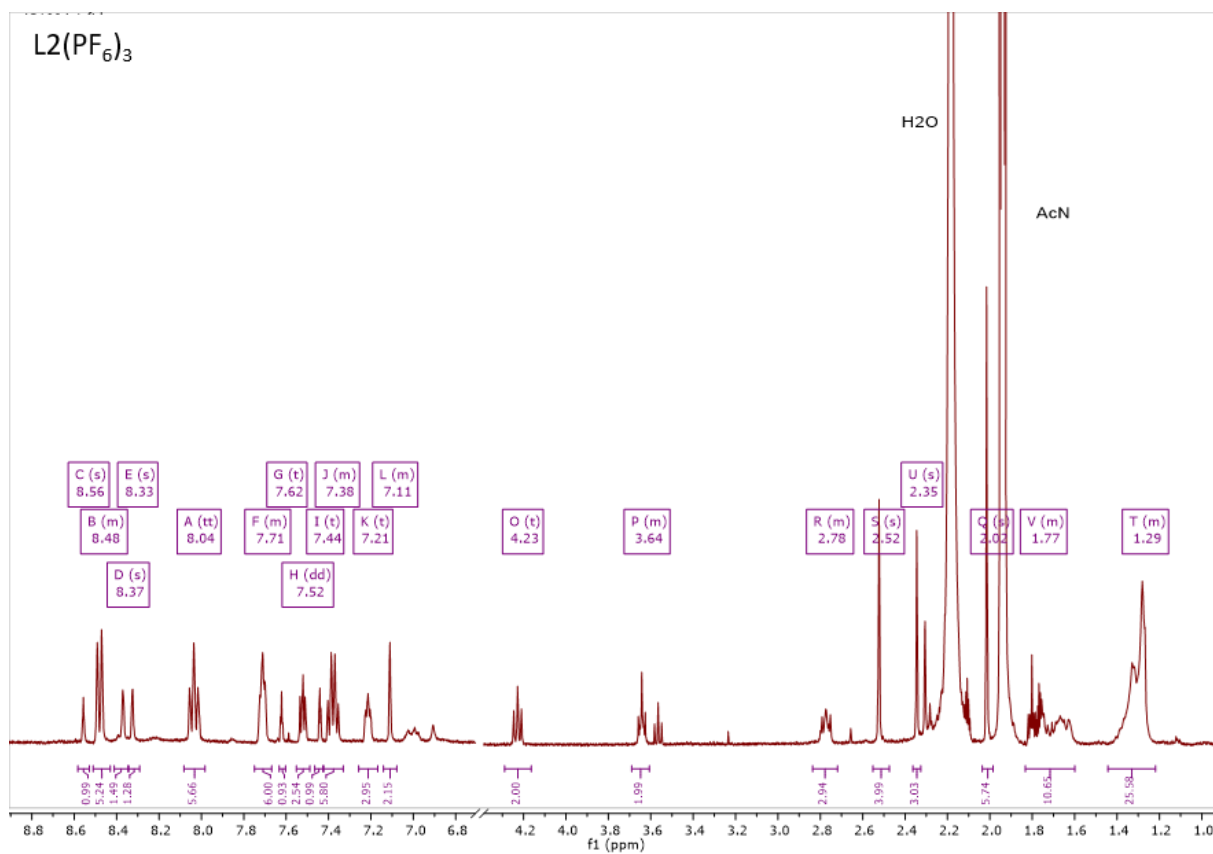
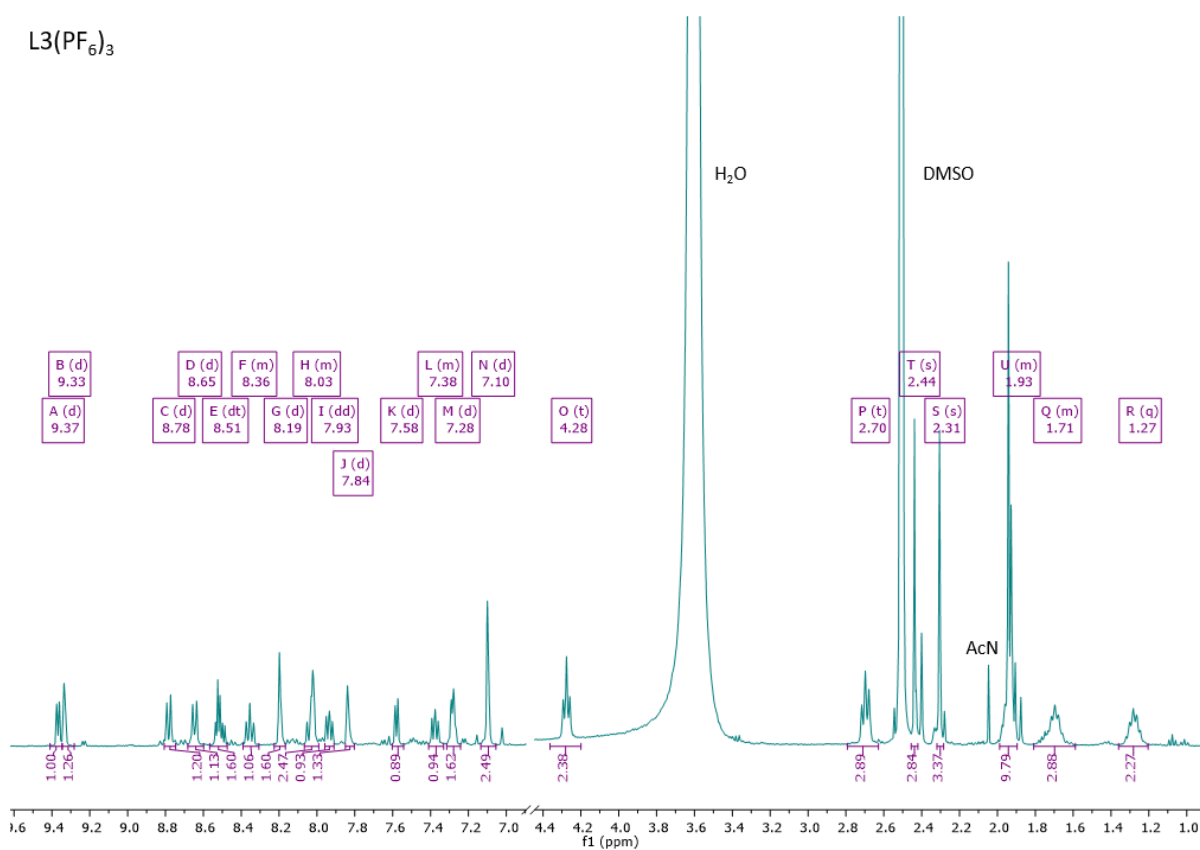


Figure 5.8.2 ^1H NMR spectrum of **4a**.

Figure 5.8.3 ^1H NMR spectrum of L1Cl.Figure 5.8.4 ^1H - ^1H COSY spectrum of L1PF $_6$.

Figure 5.8.5 ^{13}C - ^1H HSQC spectrum of **L1PF₆**.Figure 5.8.6 ^{13}C - ^1H HMBC spectrum of **L1PF₆**.

Figure 5.8.7 ¹H NMR spectrum of L2PF₆Figure 5.8.8 ¹H NMR spectrum of L3PF₆

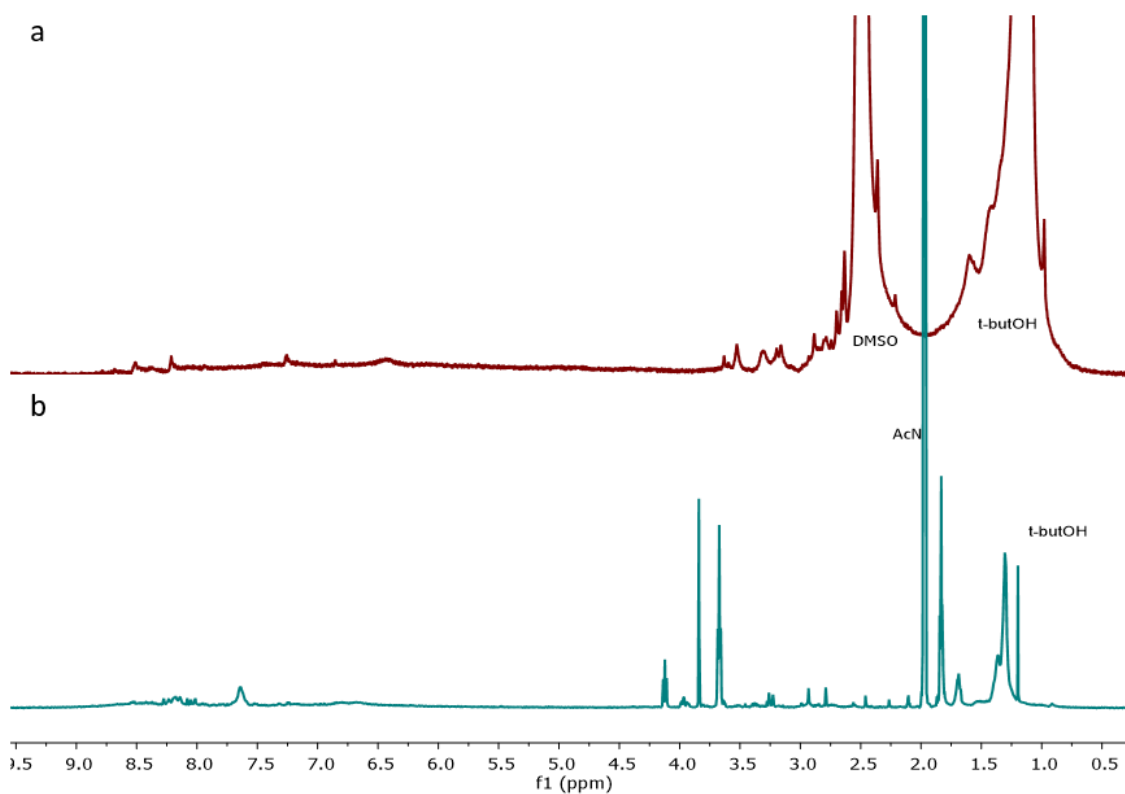
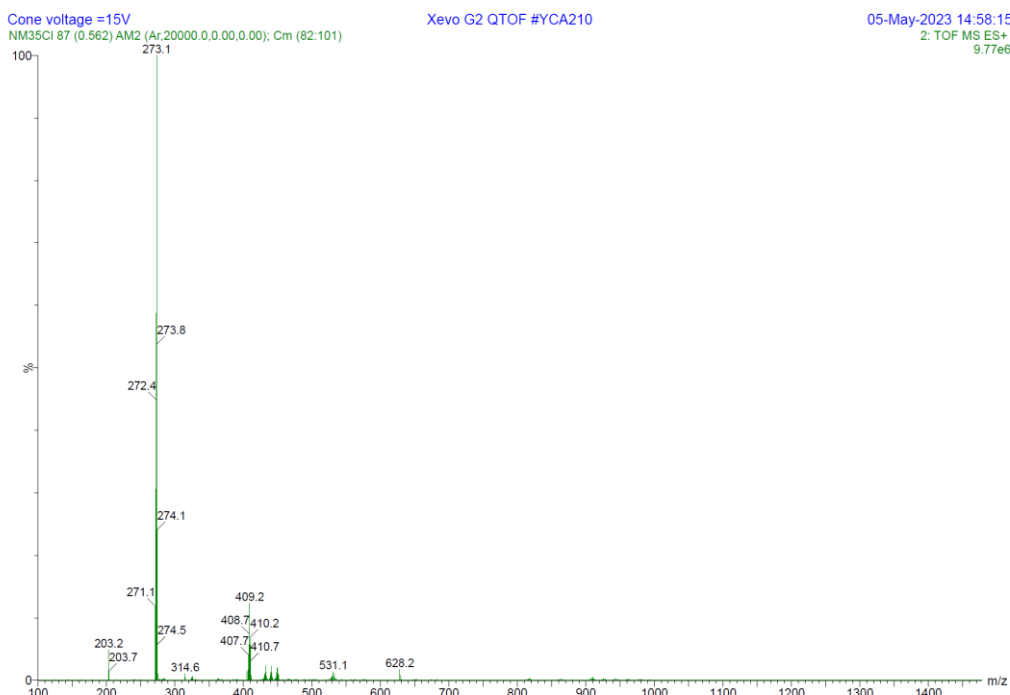


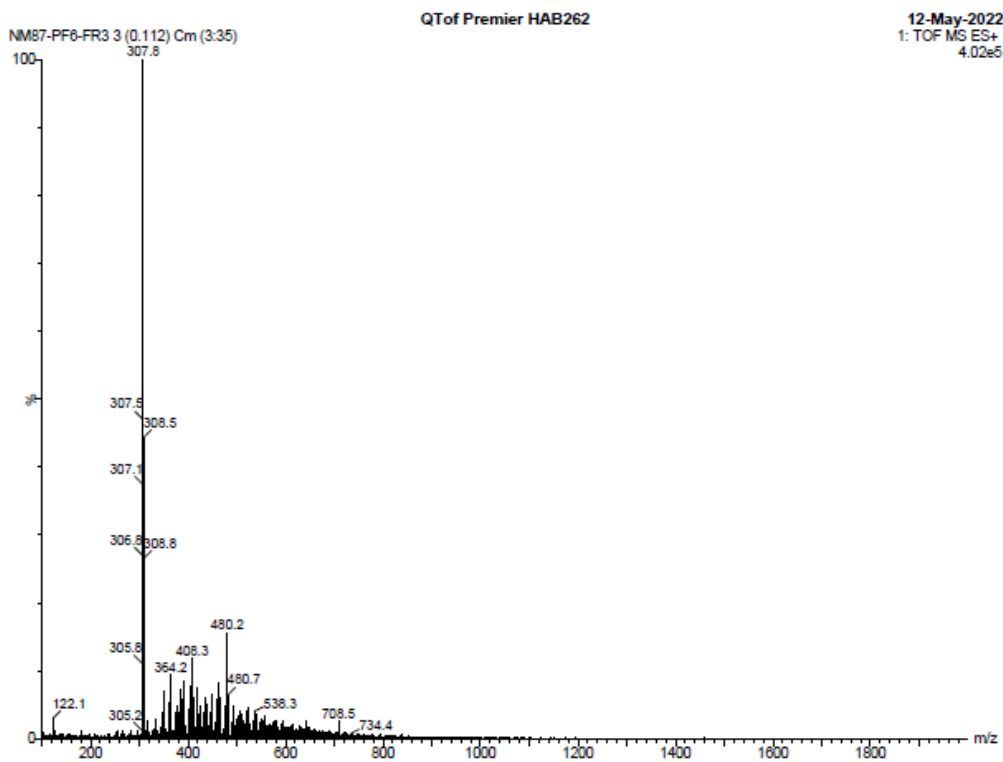
Figure 5.8.9 ^1H NMR of deprotonation of **L1PF₆** in a) DMSO- d_6 and b) THF with its further evaporation and redissolving in AcN- d_3 .

5.8.2 Mass spectra

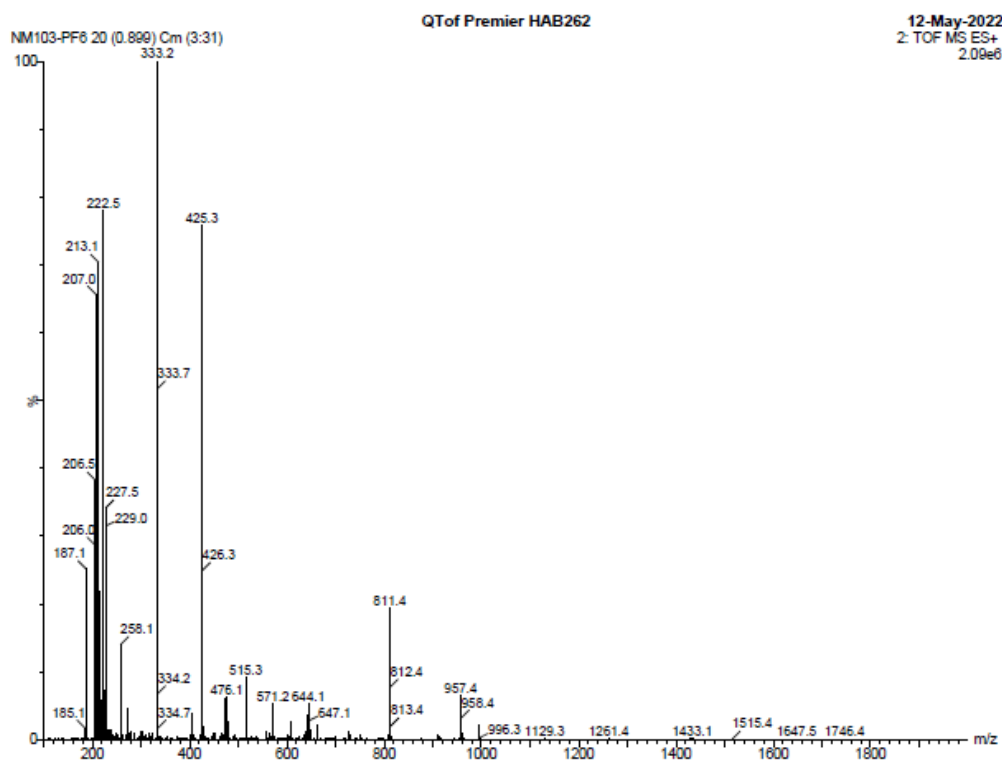
L1Cl



Fragment	M	m/z	Peak
(L1) ³⁺	819.3	273.1	273.1
(L1-H) ²⁺	818.3	409.2	409.2
(L1Br) ²⁺	900.2	450.1	450.1

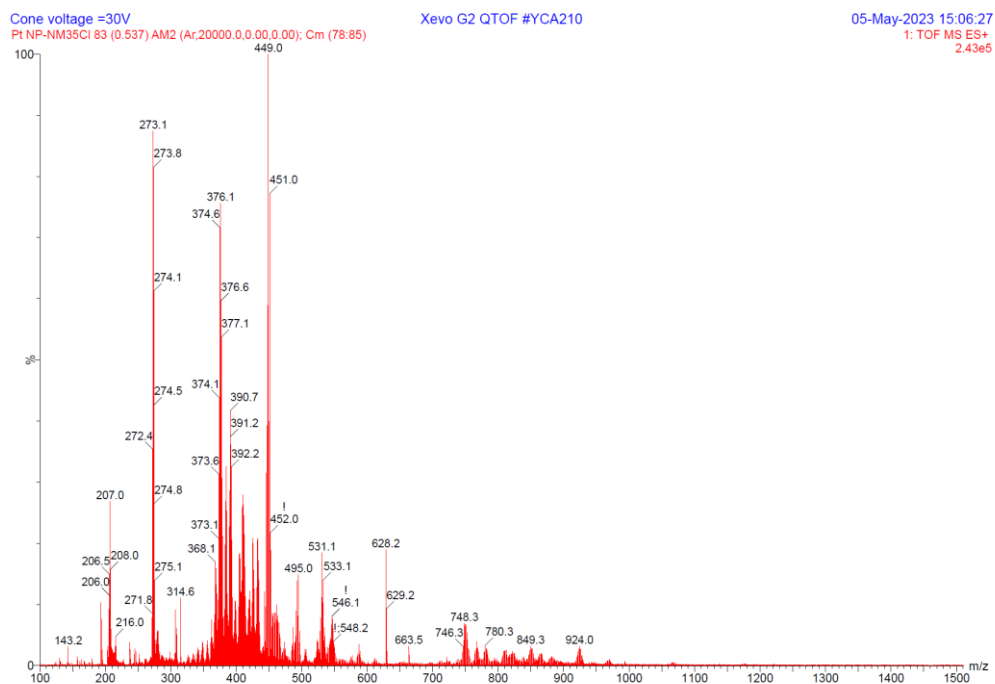
L2PF₆

Fragment	M	m/z	Peak
(L2) ³⁺	923	307	307.8
(L2Cl) ²⁺	958	479	480.2

L3PF₆

Fragment	M	m/z	Peak
Ru(bpy) ₂ ²⁺	414	207	207.0
Bpy(C5ImMes) ₂ ²⁺ H ⁺ (impurity)	667	222.5	222.5
(L3) ³⁺	839	280	279.8 (small)
Bpy(C5ImMes) ₂ ²⁺ (impurity)	666	333	333.2
Bpy(C5ImMes) ⁺ (4c)	425	425	425.3
Bpy(C5ImMes) ⁺ + H ⁺ + PF ₆ ⁻	571	571	571.2
(Bpy(C5ImMes) ₂ PF ₆) ⁺ (impurity)	811	811	811.4

Mass spectrum of PtL1Cl NPs



Fragment	M	m/z	Peak
$\text{Ru}(\text{bpy})_2^{2+}$	414.04	207.02	207.0
$(\text{L1})^{3+}$	819.3	273.1	273.1
$(\text{C}_{23}\text{H}_{36}\text{N}_2)^{2+}\text{Cl}^-$	375.24	375.2	375.2
$(\text{L1})^{2+}\text{Br}^-$	898.3	449.1	449.0

Conclusions and perspectives

The ligand-NP interaction is of significant importance in various fields of science. Starting from the stability of the NPs and ending with optimization of catalytic performance of NPs ligand proved to successfully modulate properties, behaviors, and applications of NPs. This thesis work presents investigations where an organometallic approach was used to synthesize US Pt-based NPs stabilized with various ligands. The obtained systems were systematically characterized with a similar list of techniques and used in various applications, depending on the nature of the ligand and its effect on the NPs.

The results of the first project are gathered in CHAPTER 2. There, modified cyclodextrins were used as stabilizing agents for Pt NPs. Since CD ligands showed to increase the selectivity of organometallic complexes in catalytic transformations, we were eager to know how these macrocycles will behave on the surface of Pt NPs. By tuning the relative amount of the CD, a size control of the NPs was achieved. The CDs induced water-solubility of the NPs allowing to use them in catalysis in biphasic (water-organic substrate) conditions. An obvious trend in the activity of the catalyst was observed with the thiol-modified CDs, where smaller amount of the thiol ligand led to higher catalytic activity. US Pt NPs synthesized with CD-SPO showed similar activity and selectivity in hydrogenation reactions. However, the NPs synthesized in the presence of an acid showed an increased selectivity towards C=O double bonds. The investigation on the nature of the active species responsible for this selectivity are worth to be further pursued.

CHAPTER 3 describes the results on another catalytic project where bimetallic iron-platinum NPs were stabilized with supported ionic liquid phases. This chapter presents many exciting discoveries and trends. For example, we have found that iron in the system plays two roles: 1) it dilutes platinum domains thus shutting down the hydrogenation of the aromatic ring, typically catalyzed by Pt NPs; 2) it activates double C=O bond leading to its hydrogenation and deoxygenation. Moreover, the control experiments showed that an efficient alloying was not possible using an unmodified silica as a support. Thus, each element of the system proved to be responsible for its peculiar properties.

CHAPTER 4 is dedicated to various effects of Pt NPs and porphyrins on each other. In particular, interaction of Pt NPs with pyridine-modified porphyrins resulted in the formation of self-assembled 2D and 3D structures (nanorods and nanospheres). The self-assembled hybrid systems showed higher Coulomb blockade than the Pt-porphyrin materials organized in malformed aggregates. On another side, the interaction of photoactive porphyrins with Pt NPs lead to changes

in the photophysical properties of the complexes. Depending on the type of the interaction between the Pt and the porphyrin a static quenching or a mix of a static quenching and an energy transfer were suggested for these systems.

CHAPTER 5 presents a preliminary results of an ongoing study about another hybrid system where Pt NPs are stabilized with functionalized ruthenium(II) trisbipyridyl complexes. The design of the system presumes that the complex is strongly attached to the Pt surface by a covalent platinum-carbenic carbon bond, which may allow fast energy or electron transfer. The first characterization results provided in the chapter confirmed the possibility of in situ stabilization of Pt NPs by the synthesized ruthenium complex. The project is highly interesting and important since Pt is one of the most active metals in hydrogen activation, so the direct strong attachment of a light-harvesting part can further improve the overall performance of the catalyst in photocatalytic transformations, like hydrogen evolution reaction.

In summary, this thesis presents the results of the four projects focused on the investigation of a ligand effect on the properties of NPs. The uniqueness of this thesis work lies in the fact that by using the same nanoobjects and similar characterization techniques, the direct influence of the ligands on SA, electronic, and catalytic properties of the NPs could be studied. The current work indicates that the stabilizing agent can serve as an additional instrument in the toolbox of nanoscientists to design high-performing nanosystems for specific applications. The results and the trends described in this thesis can be used by other researchers, who work with similar ligands or by those who is interested in tuning the properties of small metal NPs by ligands.

Résumé de la thèse

Les nanosciences sont en plein essor depuis plus de trois décennies et ont trouvé des applications dans les domaines de l'électronique, de l'optique, de la catalyse et de la médecine. Les chercheurs du monde entier continuent à travailler sur le contrôle de la structure et de l'ordonnement des nanoparticules (NP) afin d'obtenir des performances élevées dans les domaines scientifiques susmentionnés. L'un des moyens possibles de contrôler les propriétés des nanoparticules est d'introduire des ligands ayant une fonction spécifique. Par exemple, les chercheurs dans le domaine de la catalyse utilisent des petites molécules organiques pour influencer la densité électronique et l'encombrement de surface des NP afin d'induire une sélectivité des nanocatalyseurs vers les produits souhaités; le transfert d'énergie des ligands aux NP est utilisé dans la thérapie photothermique pour traiter le cancer² ou en nanoélectronique. En ajustant la structure des stabilisateurs, les propriétés de transport d'électrons des nanoparticules peuvent être réglées avec précision³. Parfois, les ligands peuvent même agir comme des espèces réactives indépendantes tandis que les NP agissent comme un vecteur dirigeant les performances du système. Pour n'en citer que quelques exemples, en biomédecine, les NP servent de navettes pour les ligands utilisés dans l'imagerie cellulaire et la thérapie anticancéreuse⁴, en photocatalyse, les NP semi-conductrices transfèrent des électrons aux ligands attachés qui agissent comme des catalyseurs moléculaires⁵. Dans cette thèse, nous avons décidé d'étudier l'influence de différents ligands (cyclodextrines, liquides ioniques supportés, porphyrines, complexes de ruthénium) sur la synthèse et les propriétés de NP ultra-petites à base de platine (<3 nm).

I Étude Pt-CD

La première étude a été consacrée aux NP de Pt stabilisées avec des cyclodextrines (CD) portant des fonctions thiol et oxyde de phosphine secondaire (SPO) (Figure I.1). Les CD sont des oligosaccharides cycliques macromoléculaires. Les CD typiques contiennent six (alfa-CD), sept (bêta-CD) ou huit unités de glucose (gamma-CD) dans un cycle. Les deux ouvertures de l'anneau contiennent des groupes hydroxyles qui confèrent un caractère hydrophile à la molécule. La cavité, quant à elle, présente un caractère plus hydrophobe puisqu'elle est tapissée d'atomes de carbone et d'hydrogène ainsi que de ponts d'oxygène glycosidiques. La présence de régions hydrophobes et hydrophiles permet une grande solubilité dans l'eau ainsi que la possibilité de former des complexes d'inclusion avec des molécules hydrophobes hébergées à l'intérieur de la cavité. Les nanoparticules stabilisées par des molécules CD sont particulièrement intéressantes, car la catalyse peut avoir lieu

à l'intérieur de la cavité du ligand, ce qui induit des effets stériques ainsi que des interactions ligand-substrat. De plus, la CD peut servir d'agent de dispersion ou de transfert de masse. De plus, la fonctionnalisation du CD avec des thiols peut induire des effets électroniques du ligand sur la surface active et assurer une forte coordination avec la surface de Pt. La fonction SPO peut activer l'hydrogène par l'interaction avec les liaisons polaires et donc induire une sélectivité vers l'hydrogénation des liaisons C=O. Enfin, les CD ancrées à la surface des NP de Pt devraient servir d'hôtes pour les substrats modèles - cétones ou aldéhydes hydrophobes - mais avoir moins d'affinité pour les alcools plus hydrophiles qui en résultent, ce qui les libère sans hydrogénation supplémentaire (Figure I.2).

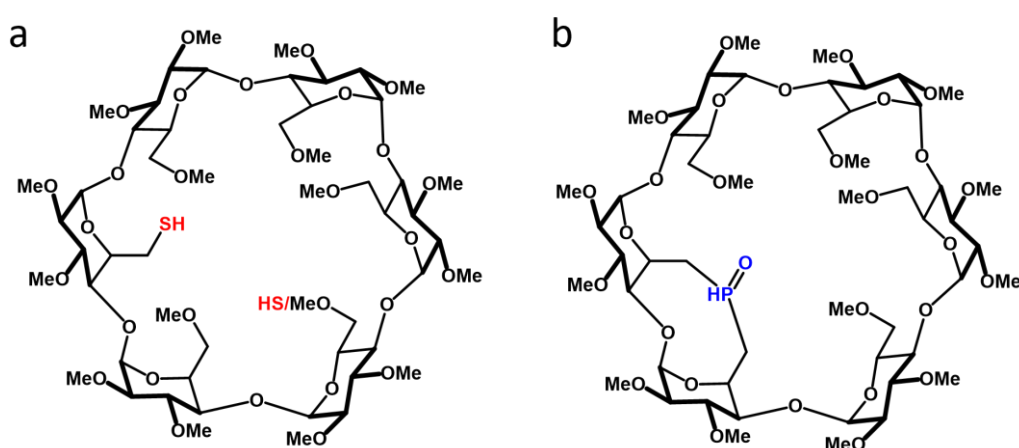


Figure I.1 Structure de a) alpha-CD-monothiol; b) alpha-CD-SPO.

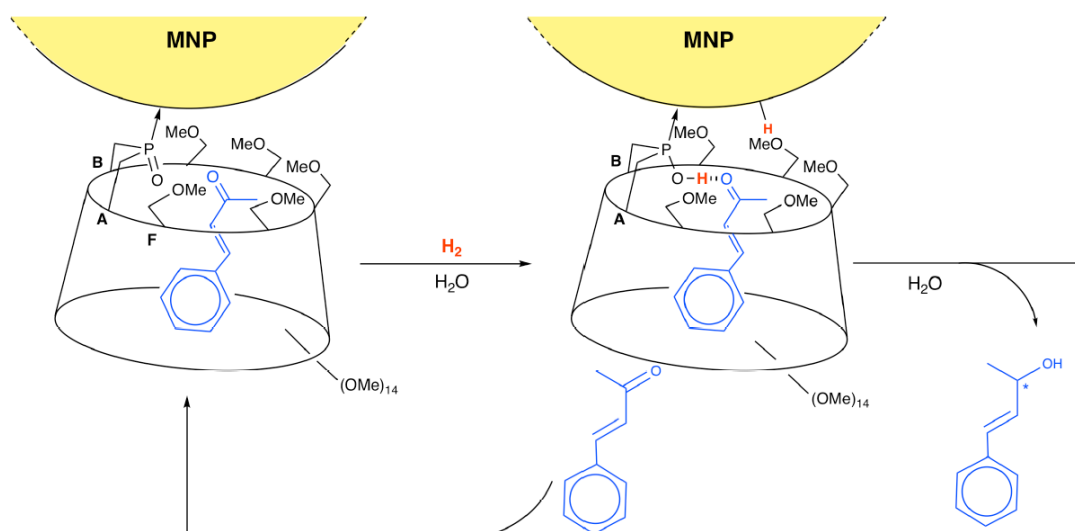


Figure I.2 Illustration de l'hydrogénation sélective des cétones avec le système NP-CD-SPO.

I-A NP de Pt stabilisées avec CD-SH

La synthèse des NP Pt-CD a été réalisée par décomposition d'un précurseur de platine ($\text{Pt}(\text{nbe})_3$ (tris(norbornene) platinum(0)) et $\text{Pt}_2(\text{dba})_3$ (tris(dibenzylideneacetone) diplatine(0))) avec de

l'hydrogène gazeux en présence de la quantité requise de ligand (Figure I.3). En ce qui concerne le choix du ligand, nous avons utilisé cinq cyclodextrines fonctionnalisées dont la taille du cycle (α ou β) et le degré de fonctionnalisation (pas de SH, mono-SH, di-SH) sont différents. Les NP correspondantes ont été appelées **Pt-x a/b 1/2**, où **x** est l'équivalent de CD par rapport à la quantité de Pt ; **a** est alfa-CD et **b** est beta-CD ; **1** est mono-thiol et **2** est bi-thiol.

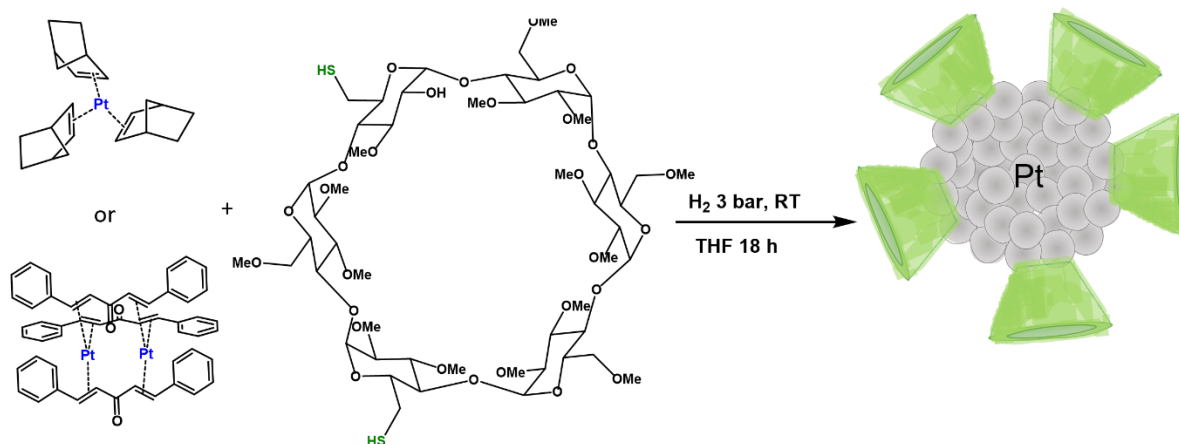
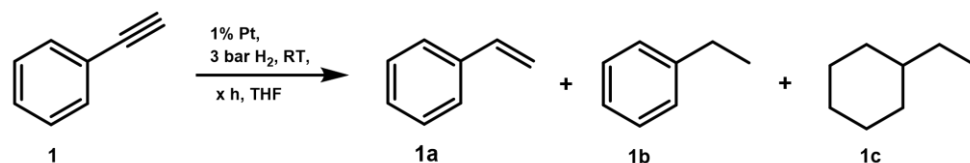


Figure I.3 Schéma de la synthèse des NP Pt-CD, exemple avec **b2**.

Une première caractérisation et des tests catalytiques ont été réalisés avec **b2**. En diminuant la quantité de **b2** par rapport au Pt, nous avons observé une légère augmentation de la taille des NP, en accord avec la littérature¹⁸¹. En passant de 0,5 eq à 0,1 eq et 0,05 eq de **b2** par rapport à la quantité totale de Pt, la taille des NP a augmenté de 1,1 nm à 1,6 nm et 2,0 nm. Le changement de précurseur de Pt de $Pt_2(dba)_3$ à $Pt(nbe)_3$ n'a pas influencé la taille des NP. L'expérience RMN DOSY a donné les coefficients de diffusion pour **b2** ($D = 6,9 \times 10^{-10} \text{ m}^2/\text{s}$) et **Pt-0,1b2** ($D = 2,9 \times 10^{-10} \text{ m}^2/\text{s}$). Le signal du **Pt-0,5b2** avait des contributions de deux populations de **b2** libre et **b2** greffé, ce qui signifie que dans le système **Pt-0,5b2**, la CD était en excès.

Lors de l'hydrogénation du substrat **1** à l'aide de **Pt-0.05/0.1/0.5b2(dba)** (Tableau I.1), nous avons constaté que **1b** était le produit principal. Cependant, l'activité était plus élevée lors de l'utilisation de NP stabilisées avec une quantité plus faible de ligand, même si la taille de la NP augmentait, ce qui conduisait à une surface plus faible pour une même masse de NP. Nous attribuons cette augmentation de l'activité à l'encombrement stérique créé par un plus grand nombre de molécules CD ainsi qu'à l'empoisonnement possible des sites de platine actifs par le ligand thiol **b2** fortement coordinant. L'activité catalytique de **Pt-0.1b2(nbe)** était plus élevée que celle de **Pt-0.1b2(dba)**, de sorte que nous avons conservé le précurseur $Pt(nbe)_3$ pour d'autres synthèses. Nous pouvons supposer que l'activité plus faible du **Pt-0.1b2(dba)** peut être due à l'élimination incomplète des ligands dba qui peuvent empoisonner la surface du catalyseur.

Tableau I.1 Hydrogénation du phénylacétylène avec le catalyseur Pt-CD.



Exécuter	² Catalyseur	t, h	X (%)	Y 1a (%)	Y 1b (%)	Y 1c (%)
1	Pt-0.05b2(dba)	0.5	100	34	66	0
2		1	100	0	98	2
3	Pt-0.1b2 (dba)	0.5	67	55	12	0
4		1	100	0	99	1
5	Pt-0.5b2(dba)	1	10	7	3	0
6	Pt-0.1b2(nbe)	0.5	100	49	51	0
7		1	100	0	99	1

Conditions de réaction : Catalyseur (0,01 mmol Pt), substrat (1 mmol, 100 eq.), solvant (THF 2 mL), H₂ (3 bar), RT. Le rendement est déterminé comme une moyenne de deux passages par GC-FID en utilisant le dodécane comme étalon interne. X = conversion ; Y = rendement.

Des NP de Pt avec des CD **a1**, **a2** et **b1** à partir du précurseur Pt(nbe)₃ ont été synthétisées, entièrement caractérisées et comparées à des NP de Pt avec **b2**. Pour s'assurer que toute la surface de la NP est entièrement recouverte de ligands, le rapport Pt/CD=1/0,5 a été choisi en accord avec les résultats de la RMN DOSY pour **Pt-0,5b2**. La taille moyenne et la dispersion des NP se situent autour de 1,3 nm. Ni la taille de l'anneau CD ni le degré de fonctionnalisation du CD n'ont modifié la taille des NP. Les diffractogrammes XRD de **Pt-0.5a1**, **Pt-0.5a2** et **Pt-0.5b1** ont montré un élargissement des pics dû à la très petite taille des NP (Figure I.4 a). Les quelques pics larges visibles ont confirmé la formation d'une structure Pt-fcc. La spectroscopie FTIR des échantillons après l'adsorption de CO a été réalisée pour étudier les déviations de la densité électronique sur la surface après sa fonctionnalisation avec des CD. Dans chaque échantillon, des vibrations du CO adsorbé en mode linéaire et ponté ont été trouvées (Figure I.4 b). La vibration du CO adsorbé en mode linéaire était située à 2042 cm⁻¹ pour les NP de Pt non fonctionnalisées, à 2042 cm⁻¹ pour **Pt-0.5a1**, à 2040 cm⁻¹ pour **Pt-0.5a2**, et à 2040 cm⁻¹ pour **Pt-0.5b1**. L'absence quasi-totale de déplacement de la vibration du CO indique qu'il n'y a pas d'effets électroniques importants induits par les ligands dans les systèmes. Les bandes d'absorption des molécules de CO pontées étaient moins prononcées dans le cas des échantillons Pt-CD que celles du spectre des NP de Pt non fonctionnalisées, ce qui suggère que les sites de terrasse sur les NP **Pt-0.5CD** étaient moins accessibles au CO en raison de la coordination des CD.

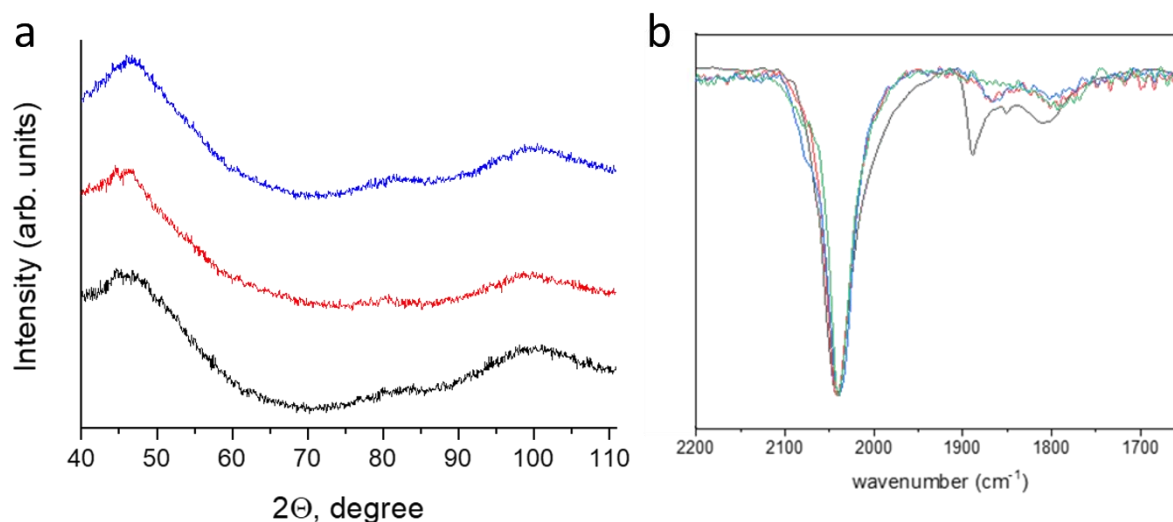


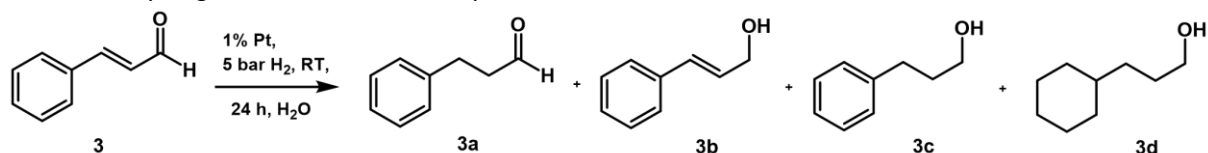
Figure 1.4 a) Diffractogrammes de a) **Pt-0.5a1** ; b) **Pt-0.5a2** ; c) **Pt-0.5b1**; b) Spectres ATR-FTIR de **Pt-0.5CD** avec zoom sur la bande d'absorption CO.

Pt-0.5b1, **Pt-0.5a1**, et **Pt-0.5a2** ont été testés dans l'hydrogénation d'un aldéhyde conjugué - le cinnamaldéhyde (**3**). Au début, les tests ont été effectués dans le THF en raison de la faible solubilité de **a2** dans l'eau. Lors de l'hydrogénation de **3**, les deux produits intermédiaires **3a** et **3b** ont été trouvés, ainsi que le produit hydrogéné **3c** (Tableau I.2). Cette hydrogénation par étapes avec l'hydrogénation plus rapide de la liaison C=C est un comportement catalytique typique des NP de métaux nobles.¹⁹² L'hydrogénation du cinnamaldéhyde s'est déroulée plus lentement dans l'eau que dans le THF. Dans ces conditions de réaction, **3a** était un intermédiaire majeur qui, avec l'intermédiaire mineur **3b**, se transformait lentement en produit final **3c**. Aucune différence catalytique significative n'a été observée entre **Pt-0.5a1** et **Pt-0.5b1**. Nous pouvons donc conclure que la présence de CD avec une cavité de taille différente à la surface de Pt n'a pas influencé la voie d'hydrogénation.

Les résultats de la partie précédente ont mis en évidence que les CD ne servaient que d'agents stabilisants pour les Pt-NP, ce qui signifie qu'elle n'influencent pas la sélectivité dans l'hydrogénation des alcanes vers les alcènes ou dans l'hydrogénation des aldéhydes conjugués vers les alcools insaturés. Nous avons donc décidé d'optimiser notre système et de développer le catalyseur avec un rapport Pt:b1 qui aura l'activité la plus élevée tout en conservant sa stabilité dans l'eau. Des NP de Pt stabilisées avec 0,5, 0,2, 0,1, et 0,05 eq de **b1** ont été synthétisées et caractérisées. La taille des NP augmente avec la diminution de la quantité de **b1**, comme cela a été observé pour les systèmes **Pt-b2**. Ici, en passant de 0,5 à 0,1 eq de CD, la taille des NP a augmenté de 1,2 à 1,6 nm. En diminuant encore la quantité de CD à 0,05 eq, une coalescence des nanoparticules a été observée en raison d'une quantité trop faible du stabilisateur. Ces

nanoparticules étaient également moins dispersées dans l'eau que celles contenant plus de ligands. L'expérience RMN DOSY a montré que même dans le **Pt-0.05b1**, certaines molécules CD étaient libres dans la solution, contrairement aux résultats obtenus avec le **Pt-0.1b2**. Ce résultat indique que la quantité de groupes SH dans le CD influence beaucoup la force de l'interaction entre la NP et le CD.

Tableau I.2 Hydrogénation du cinnamaldéhyde avec **Pt-0.5CD** dans le THF et l'eau.

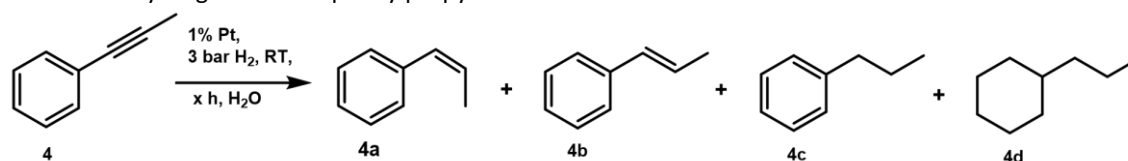


Exécuter	Catalyseur	X (%)	Y 3a (%)	Y 3b (%)	Y 3c (%)	Y 3d (%)
1	Pt-0,5a1	71	29	8	34	0
2	Pt-0,5a2	82	29	7	46	0
3	Pt-0.5b1	87	28	10	49	0
4*	Pt-0,5a1	53	38	7	9	0
5*	Pt-0.5b1	47	37	4	7	0

Conditions de réaction : Catalyseur (0,01 mmol Pt), substrat (1 mmol, 100 eq.), solvant (THF 2 mL ou H₂O 3 mL), H₂ (5 bar), RT. Le rendement est déterminé comme une moyenne de deux passages par GC-FID en utilisant le dodécane comme étalon interne. * Les tests ont été effectués dans l'eau.

Lors de l'hydrogénation du substrat **4**, l'activité des NP a augmenté en diminuant la quantité de **b1** de 0,5 à 0,1 eq (Tableau I.3). En diminuant encore la quantité de ligand à 0,05 eq, l'activité n'a pas augmenté de manière significative, probablement en raison de la plus faible dispersion de **Pt-0.05b1** dans l'eau ainsi que de l'état de coalescence des NP, qui diminue la surface active.

Tableau I.3 Hydrogénation du phénylpropyne avec **Pt-b1**.



Exécuter	Catalyseur	t, h	X (%)	Y 4a (%)	Y 4b (%)	Y 4c (%)	Y 4d (%)
1	Pt-0.5b1	1	56	32	6	18	0
2	Pt-0.2b1	1	72	43	6	22	0
3	Pt-0.1b1	1	99	23	7	69	0
4	Pt-0.05b1	1	98	14	5	78	1

Conditions de réaction : Catalyseur (0,01 mmol Pt), substrat (1 mmol, 100 eq.), solvant (H₂O 3 mL), H₂ (5 bar), RT. Le rendement est déterminé comme une moyenne de deux passages par GC-FID en utilisant le dodécane comme étalon interne.

Au vu des résultats obtenus, les NP de **Pt-0.1b1** ont été utilisées pour l'hydrogénation d'autres substrats. L'hydrogénation d'alcynes terminaux et internes (phénylacétylène,

phénylpropyne et diphénylacétylène) a été réalisée en 2 heures avec formation de phénylalcane. L'hydrogénation des cétones (acétone benzylidène, acétophénone, isophorone) a été réalisée dans des conditions de réaction plus sévères (80°C, 10 bar H₂, 6h) et a abouti à la formation d'alcools saturés comme principal produit de réaction. Un test de stabilité a également été réalisé avec le phénylacétylène comme substrat. En général, aucune désactivation du catalyseur n'a été observée pendant au moins cinq cycles, ce qui confirme la stabilité du catalyseur. Le TEM après le dernier test a révélé que la taille des NP n'avait pas changé, bien que la formation d'amas de NP ait été observée dans certaines régions.

I-B NP de Pt stabilisées avec le ligand CD-SPO

Le ligand CD-SPO peut exister sous deux stéréo-isomères : l'endo-O- et l'exo-O-isomère. Dans les complexes avec l'isomère endo-O, la paire d'électrons du phosphore nécessaire à la formation de la liaison de coordination pointe vers l'*extérieure de la cavité* ; au contraire, dans le cas de l'isomère exo-O, la paire d'électrons nécessaire à la formation de la liaison de coordination pointe vers l'intérieur de la cavité. D'après ces informations, seul l'isomère endo-O peut se coordonner à la surface des NP, car une NP est trop grande pour entrer dans la cavité. Cependant, il est extrêmement difficile de séparer les isomères, c'est pourquoi un mélange d'isomères a été utilisé pour stabiliser les NP de Pt. La teneur relative en endo-O/exo-O peut être régulée par isomérisation en présence d'acide, la teneur maximale en isomère endo-O étant égale à 0,5. Nous avons effectué l'isomérisation et le jour suivant nous avons ajouté la solution d'isomères à la solution de Pt(nbe)₃ pour avoir CD/Pt = 0.5/1 et nous avons effectué la catalyse comme pour les NP Pt-CD-SH. En RMN ³¹P des NP nous avons vu une disparition du signal correspondant à l'isomère endo/O ce qui indique la formation de NP Pt-CD-SPO (**Pt-0.5P1**). De plus, nous avons observé un pic exo-O et de nouveaux signaux qui correspondent probablement à des complexes moléculaires Pt-SPO. Nous avons également réalisé la même synthèse mais en isomérisant Endo-O/exo-O et en le séparant de l'acide au préalable (**Pt-0.5P2**). En RMN ³¹P, nous n'avons vu que le pic qui correspond à l'exo-O confirmant que HCl a participé à la formation des impuretés de la première synthèse. Les NP synthétisées à partir de la première synthèse étaient plus grandes et coexistaient à l'état dispersé et à l'état d'amas. Par contre, les NP issues de la seconde synthèse avaient des tailles plus petites et étaient bien dispersées (Figure I.5).

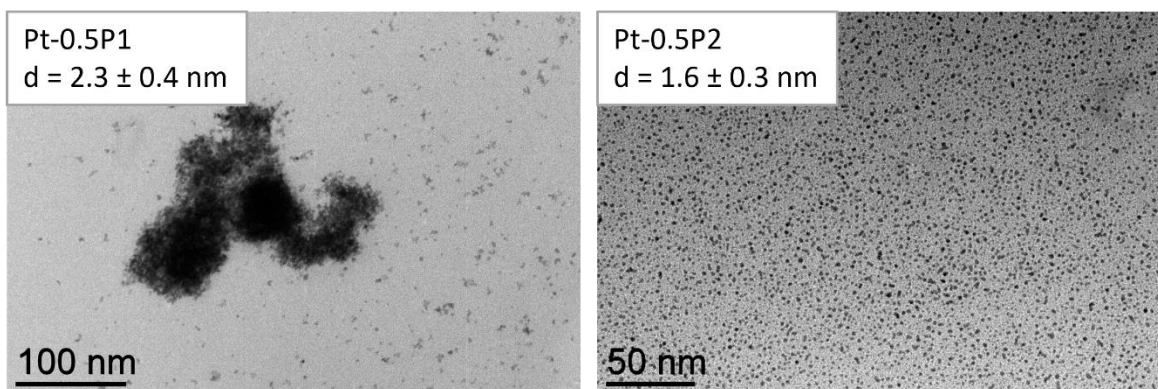


Figure I.5 Images TEM de Pt-0.5P1 et Pt-0.5P2.

La coordination de l'isomère endo-O a été confirmée en utilisant les RMN ^{31}P CP-MAS des quatre catalyseurs (Figure I.6). Nous avons observé sur la RMN de l'alfa-CD-SPO deux signaux à 25 et 45 ppm qui correspondent respectivement à l'isomère endo-O et à l'isomère exo-O. Ensuite, sur la RMN du **Pt-0.5P2**, le signal net à 25 ppm a disparu tandis qu'un signal large dans la région de 10-110 ppm est apparu, ce qui pourrait être attribué à l'isomère endo-O à proximité de la surface du Pt. Dans le cas du **Pt-0.5P1**, un chevauchement du signal à 45 ppm avec quelques autres signaux a été observé, conformément à la RMN ^{31}P à l'état liquide.

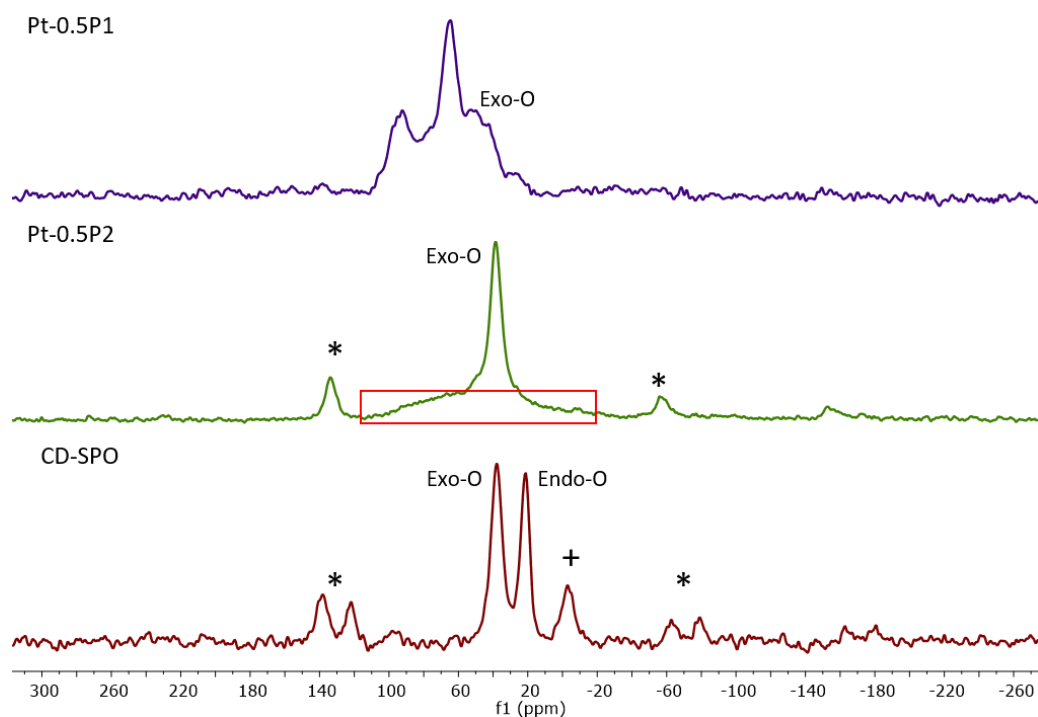
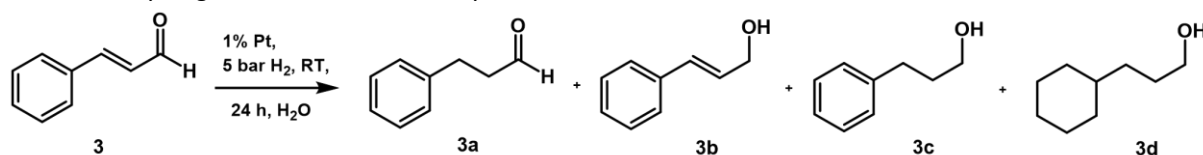


Figure I.6 RMN ^{31}P CP-MAS des systèmes **Pt-CD-SPO**. Les astérisques indiquent les bandes de rotation ; le plus indique une contamination inconnue ; le cadre rouge indique un signal large de l'isomère endo-O coordonné.

L'activité catalytique des catalyseurs a été évaluée dans l'hydrogénation du cinnamaldéhyde (Tableau I.4). **Pt-0.5P1** a montré une sélectivité envers l'alcool insaturé **3b** (70%) à 98% de conversion. Dans le même temps, **Pt-0.5P2** a montré une activité un peu plus faible et une faible

sélectivité vis-à-vis de l'alcool **3b**. L'ajout de HCl au mélange réactionnel n'a pas permis d'obtenir une plus grande sélectivité, ce qui indique la nature différente des espèces actives dans les deux catalyseurs. Nous supposons que des complexes de Pt pourraient être formés dans nos conditions de réaction et qu'ils sont responsables de la sélectivité vis-à-vis de **3b**.

Tableau I.4 Hydrogénation du cinnamaldéhyde avec **Pt-0.5CD-SPO** dans l'eau.



Exécuter	Catalyseur	c(HCl) (M)	X (%)	Y 3a (%)	Y 3b (%)	Y 3c (%)	Y 3d (%)
1	Pt-0.5P1	0	98	5	70	23	0
2	Pt-0.5P2	0	72	34	19	19	0
3	Pt-0.5P2	$2.5 \cdot 10^{-6}$	71	37	17	17	0
4	Pt-0.5P2	$1 \cdot 10^{-5}$	66	37	14	15	0
5	Pt-0.5P2	$1.7 \cdot 10^{-3}$	78	40	18	20	0

Conditions de réaction : Catalyseur (0,01 mmol Pt), substrat (1 mmol, 100 eq.), solvant (H_2O 3 mL), H_2 (5 bar), RT, 24h. Le rendement est déterminé comme une moyenne de deux passages par GC-FID en utilisant le dodécane comme étalon interne. a - un passage catalytique.

II Etude de l'activité catalytique des NP de FePt immobilisées sur des phases liquides ioniques supportées (SILP)

Les nanoparticules bimétalliques suscitent un grand intérêt dans le domaine de la recherche en raison des effets synergiques qui ne peuvent être obtenus avec des matériaux monométalliques^{172,203,204}. L'interaction entre les métaux peut entraîner des effets géométriques et/ou électroniques qui détermineront la sélectivité de la réaction.

Le système que nous avons décidé d'étudier est celui des nanoparticules de FePt immobilisées sur un SILP à base d'imidazolium ($\text{Fe}_x\text{Pt}_{100-x}@\text{SILP}$). Les matériaux $\text{Fe}_x\text{Pt}_{100-x}@\text{SILP}$ ont été synthétisés selon une approche organométallique qui comprend l'imprégnation des solutions de précurseurs avec un support et la décomposition des précurseurs avec de l'hydrogène. Les précurseurs $\text{Fe}_2[\text{N}(\text{Si}(\text{CH}_3)_3)_2]$ et $\text{Pt}_2(\text{dba})_3$ ont été utilisés. Le rapport Fe:Pt a été modifié en ajustant les quantités de précurseurs. À des fins de comparaison, des nanoparticules de $\text{Fe}_{40}\text{Pt}_{60}$ ont été synthétisées en utilisant de la silice non modifiée comme support ($\text{Fe}_{40}\text{Pt}_{60}@\text{SiO}_2$) en suivant le même protocole de synthèse.

Pour confirmer le rapport des métaux et la charge métallique dans les matériaux $\text{Fe Pt}_{x100-x}@\text{SILP}$, une analyse SEM-EDX a été réalisée. Les résultats ont généralement confirmé le rapport des

métaux, avec une quantité légèrement supérieure de Fe dans les NP bimétalliques dans chaque cas. Certains écarts entre les rapports théoriques et expérimentaux peuvent être dus à la faible charge en métaux, qui atteint les limites des mesures de la technique SEM-EDX.

La caractérisation des matériaux $\text{Fe}_x\text{Pt}_{100-x}@\text{SILP}$ par MET a mis en évidence la formation de NP d'environ 2 nm à la surface du SILP. Nous avons constaté que l'augmentation de la teneur en Pt dans les NP bimétalliques entraînait une légère augmentation de la taille et un degré d'agrégation plus élevé des NP. La cartographie élémentaire par STEM-HAADF-EDX (STEM - microscopie électronique à transmission à balayage ; HAADF - champ sombre annulaire à angle élevé ; EDX - spectroscopie de rayons X à dispersion d'énergie) et STEM-EDX sur des particules individuelles ont confirmé la nature bimétallique des NP de $\text{Fe}_{40}\text{Pt}_{60}$ (Figure II.1).

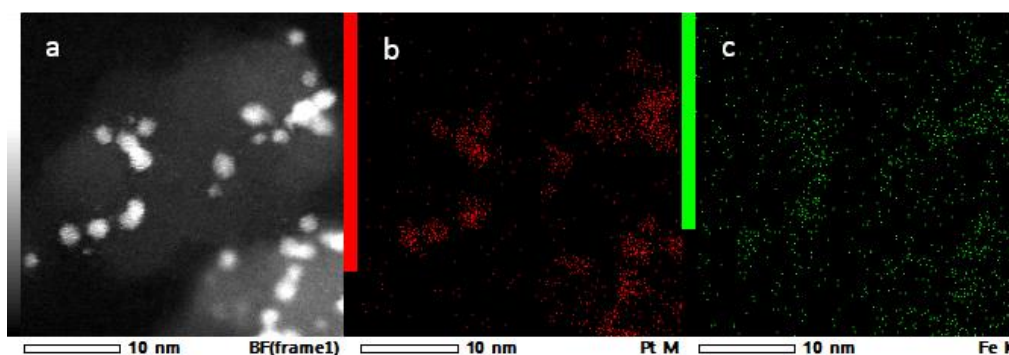


Figure II.1 a) Image STEM-HAADF du $\text{Fe}_{40}\text{Pt}_{60}@\text{SILP}$, b) Cartographie élémentaire STEM-HAADF-EDX du $\text{Fe}_{40}\text{Pt}_{60}@\text{SILP}$ en regardant le Pt, et c) Cartographie élémentaire STEM-HAADF-EDX du $\text{Fe}_{40}\text{Pt}_{60}@\text{SILP}$ en regardant le Fe.

Le test d'adsorption du CO a été réalisé avec $\text{Fe}_x\text{Pt}_{100-x}@\text{SILP}$ ($x = 0, 20, 40, 60, 80$) (Figure II.2 a). Le spectre de $\text{Pt}@\text{SILP}$ montre un nouveau pic à 2049 cm^{-1} qui est généralement attribué au CO adsorbé linéairement sur de petites nanoparticules de Pt ou sur des sites de Pt à faible coordination.¹⁹¹ Les nombres d'ondes de la bande d'absorption du CO avec les nanoparticules bimétalliques sont plus faibles que pour le Pt pur, en accord avec la littérature. Plus précisément, le nombre d'ondes de la vibration du CO sur $\text{Fe}_{20}\text{Pt}_{80}$ est égal à 2037 cm^{-1} , sur $\text{Fe}_{40}\text{Pt}_{60}$ - 2018 cm^{-1} , sur $\text{Fe}_{60}\text{Pt}_{40}$ - 2034 cm^{-1} , et sur $\text{Fe}_{80}\text{Pt}_{20}$ - 2043 cm^{-1} . Nous suggérons que la diminution du nombre d'ondes du Fe_{20} au Fe_{40} peut être due à la plus forte donation d'électrons au Pt avec l'augmentation de la quantité de Fe. En augmentant encore la teneur en Fe jusqu'à Fe_{60} et Fe_{80} , le nombre d'ondes peut augmenter en raison d'une éventuelle oxydation partielle du Fe pendant la synthèse, puisqu'il a déjà été observé pour $\text{FeRu}@\text{SILP}$ que dans les alliages riches en Fe, le Fe était partiellement oxydé, même en travaillant dans des conditions inertes²²⁵. Si, dans notre cas, il existe des sites Fe^{x+} , le fait qu'ils soient pauvres en électrons attirera la densité d'électrons du Pt. Dans ce

cas, on s'attendrait à ce que la valeur de la bande d'absorption dans l'alliage avec du Fe partiellement oxydé se situe quelque part entre le Pt et le Fe₄₀Pt₆₀.

La tendance à l'oxydation a été confirmée par une expérience en VSM (vibrating-sample magnetometry). Sur la Figure II.2 b, sont présentées les courbes d'aimantation en fonction des champs magnétiques appliqués après élimination de la contribution paramagnétique du Fe Pt_{x100-x} @SILP avec x = 40, 60 et 80. L'ouverture de l'hystérésis et l'aimantation à saturation du Fe Pt₄₀₆₀ indiquent un comportement ferromagnétique. Le même échantillon après oxydation dans l'air a montré des valeurs plus faibles d'aimantation de saturation M_s et du champ coercitif H_c . Ce résultat suggère la présence d'un oxyde de fer antiferromagnétique. Pour Fe₆₀Pt₄₀ @SILP, on a obtenu des valeurs H_c et M_s plus faibles que dans le cas de Fe₄₀Pt₆₀ @SILP, ce qui peut être attribué à une oxydation partielle du Fe dans cet échantillon. Fe₈₀Pt₂₀ @SILP présentait une magnétisation encore plus faible, ce qui signifie que l'échantillon contenait encore moins de fer métallique. Ainsi, les résultats obtenus par VSM, en accord avec les résultats IR, soutiennent l'hypothèse que dans les échantillons où la fraction molaire de fer était égale ou supérieure à 60%, le fer apparaissait dans un état partiellement ou complètement oxydé.

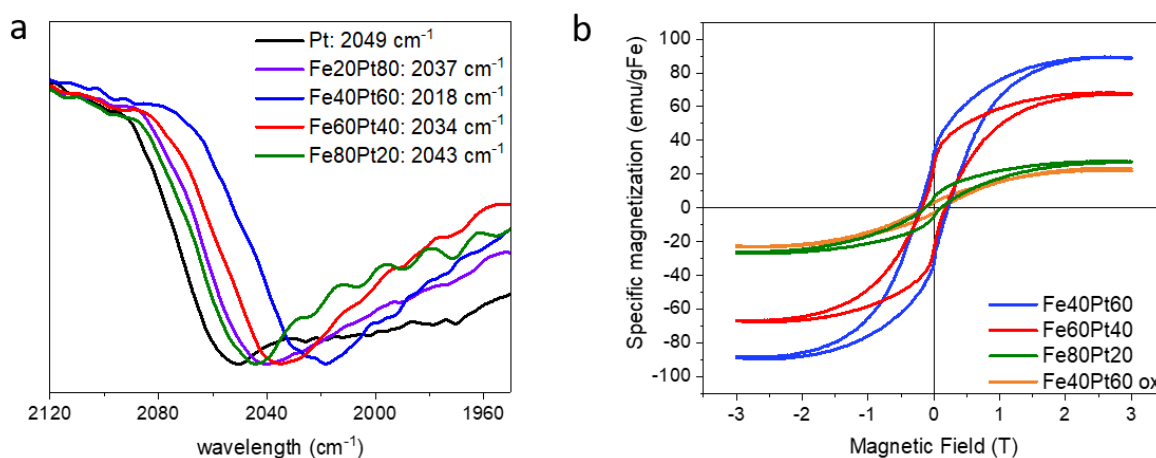


Figure II.2 a) spectres IR du Fe_xPt_{100-x} @SILP avec CO adsorbé (zoom sur la bande d'absorption du CO) ; b) courbes d'aimantation en fonction des champs magnétiques appliqués du Fe Pt_{x100-x} @SILP à 5K.

Des tests catalytiques ont été réalisés avec l'acétophénone qui peut être utilisée comme molécule prototype pour l'HDO (hydrodeoxygenation) des cétones dérivées de la biomasse (Figure 3.4.1 a). La Figure 3.4.1b montre les conversions et les rendements en produits en fonction de la teneur en Pt dans les NP de Fe_xPt_{100-x} où toutes les réactions ont été effectuées dans des conditions identiques ($T = 175\text{ }^{\circ}\text{C}$, $p(\text{H}_2) = 50\text{ bar}$, $t = 16\text{ h}$, solvant = heptane). A partir du Fe pur, il n'y a pas eu de formation de produit. Un alliage de Fe₈₀Pt₂₀ @SILP a donné 34% de conversion avec un produit majoritaire **2a** (30%). Avec le catalyseur Fe₆₀Pt₄₀ @SILP, la conversion a atteint 100 % et nous avons déjà pu observer une quantité suffisante de produit désoxygéné **1c** (45 %), qui a encore augmenté

en utilisant Fe Pt₅₀₅₀ et a atteint un maximum de 84 % de sélectivité en utilisant le catalyseur Fe₄₀Pt₆₀@SILP. Fait remarquable, c'est la première fois que des nanoparticules bimétalliques sur SILP non modifié (c'est-à-dire sans fonction acide supplémentaire) peuvent catalyser l'hydrodésoxygénation de l'acétophénone non substituée. Cependant, en passant au Fe₂₀Pt₈₀@SILP, les produits avec des cycles aromatiques réduits **2d** (53%) et **2e** (5%) ont été formés. Sur la base de ce résultat, nous supposons que 80 % de Pt dans l'alliage ont conduit à la formation d'ensembles d'atomes de Pt suffisamment grands pour permettre l'adsorption planaire et l'hydrogénation du cycle aromatique. Dans le cas du Pt@SILP monométallique, l'hydrogénation de **2** a conduit au produit surhydrogéné **2d** avec un rendement de 93 %, comme prévu pour un catalyseur à base de métal noble. Le même test catalytique a également été réalisé avec Fe₄₀Pt₆₀@SiO₂. Dans ce cas, une grande quantité de produits avec un cycle saturé **2d** (14%) et **2e** (43%) ont été formés. Ce résultat indique qu'il existe dans l'échantillon des parties où les domaines de Pt sont suffisamment grands, de sorte qu'il n'est pas possible d'obtenir une formation contrôlée des NP bimétalliques Fe₄₀Pt₆₀ sur le support de silice non modifié .

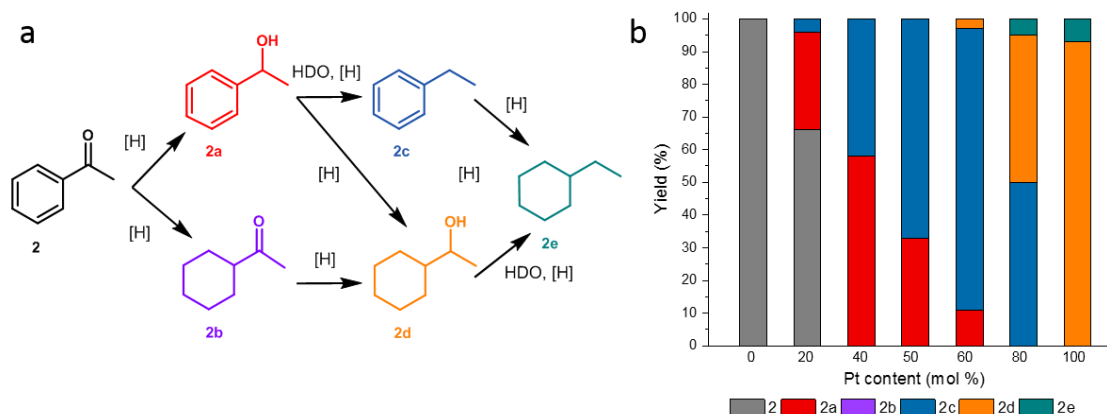
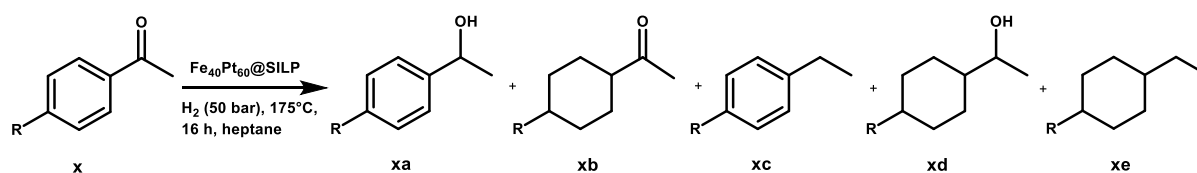


Figure II.3 a) Voies de réaction pour l'hydrogénation ([H]) et l'hydrodésoxygénation (HDO) de l'acétophénone, b) Hydrogénation de l'acétophénone à l'aide d'une série de catalyseurs Fe_xPt_{100-x} @SILP avec différents rapports Fe:Pt. Conditions de réaction : catalyseur (0,005 mmol [Me]), substrat (0,125 mmol, 25 eq.), heptane (0,5 mL), H₂ (50 bar), 175°C, 16 h. Le rendement est déterminé par GC-FID en utilisant le tétradécane comme étalon interne. Les points de données représentent la valeur moyenne de deux expériences au minimum.

Pour étudier la polyvalence du catalyseur dans la réaction d'hydrodésoxygénation, des dérivés d'acétophénone para-substitués ont été choisis comme champ d'application. Les résultats sont résumés dans le Table 3.4.4. Une réaction avec Fe₄₀Pt₆₀@SILP dans des conditions standard (H₂ (50 bar), 175°C, 16 h) a abouti à une hydrodésoxygénation totale ou partielle. Les substituants donateurs d'électrons ont augmenté le taux d'hydrodésoxygénation des acétophénone, ce qui a permis d'obtenir d'excellents rendements de **xc** (96-≥99%). Cette activité accrue est probablement due à une stabilisation mésomérique et inductive du carbocation intermédiaire. L'hydrogénation de

l'acétophénone avec le groupe CF_3 qui attire les électrons a ralenti la réaction et a conduit à 70 % de produit désoxygéné, ce qui est cohérent avec les observations précédentes.^{205,207}.

Tableau I.1 Hydrogénation sélective des dérivés de l'acétophénone à l'aide de $\text{Fe}_{40}\text{Pt}_{60}@\text{SILP}$.

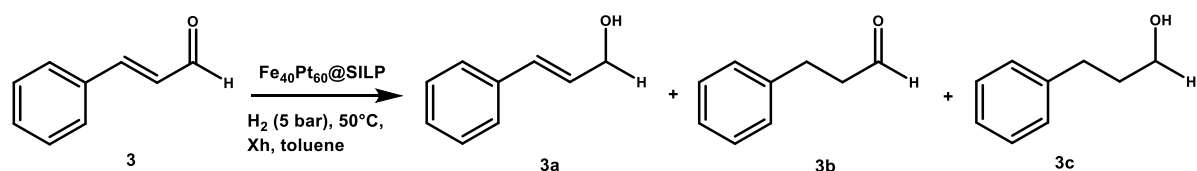


Entrée	R	X (%)	Y xa (%)	Y xb (%)	Y xc (%)	Y xd (%)	Y xe (%)
1	OCH_3	>99	0	0	>99	0	0
2	CH_3	>99	0	0	>99	0	0
3 ^a	Cl	>99	0	0	96	0	0
4 ^a	F	>99	1	0	97	0	0
5	CF_3	>99	30	0	70	0	0

Conditions de réaction : Catalyseur (13,6 mg, 0,005 mmol [Me]), substrat (0,125 mmol, 25 eq.), heptane (0,5 mL), H_2 (50 bar), 175°C, 16 h. La conversion et le rendement sont déterminés par GC-FID en utilisant le tétradécane comme standard interne. Les points de données représentent la valeur moyenne de deux expériences au minimum. X = conversion, Y = rendement. ^a Le produit secondaire est le **1c**.

Le fer ayant montré qu'il activait efficacement la partie $\text{C}=\text{O}$ dans les cétones, l'hydrogénation des aldéhydes insaturés **3** et **4** a été réalisée. En utilisant $\text{Fe}_{40}\text{Pt}_{60}@\text{SILP}$ et les conditions initiales de réaction (5 bar H_2 , 50°C, 2h toluène) nous avons observé la formation de **3a** (47% de rendement à 48% de conversion) (Table 3.4.5). Remarquablement, en augmentant le temps de réaction à 16h à 100% de conversion, seulement 7% de l'alcool saturé **3c** ont été formés. Nous pouvons supposer que les effets stériques et électroniques entravent l'adsorption de $\text{C}=\text{C}$ et son hydrogénation.

Tableau I.2 Hydrogénation du cinnamaldéhyde avec $\text{Fe}_{40}\text{Pt}_{60}@\text{SILP}$.

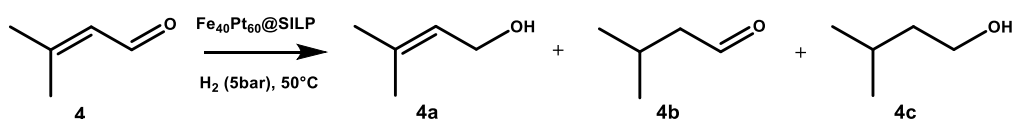


Entrée	t, h	X (%)	Y 3a (%)	Y 3b (%)	Y 3c (%)
1	2	48	47	0	1
2	6	93	89	0	4
3	16	>99	93	0	7

Conditions de réaction : Catalyseur (13,6 mg, 0,005 mmol [Me]), substrat (0,5 mmol, 100 eq.), toluène (0,5 mL), H_2 (5 bar), 50°C. La conversion et le rendement sont déterminés par GC-FID en utilisant le dodécane comme étalon interne. Les points de données représentent la valeur moyenne de deux expériences au minimum. X = conversion, Y = rendement.

L'hydrogénation du substrat **4** en 4 h a donné un rendement de **4a** de 66% à 72% de conversion (Tableau 1.3). Il est important de noter qu'en 16h, le rendement élevé de **4a** a été préservé (79%). En utilisant de l'isopropanol dans la réaction de 4h, la conversion est passée à 92%, tout en conservant une excellente sélectivité vis-à-vis de l'alcool insaturé **4a** (Y = 86%). Il est important de noter qu'aucune formation d'acétals n'a été observée dans les conditions de réaction choisies. Un test supplémentaire dans i-PrOH a été effectué en l'absence d'hydrogène. Aucune conversion n'a été observée, ce qui exclut la possibilité d'une hydrogénation par transfert avec auto-oxydation de l'isopropanol. Nous proposons que l'augmentation de la polarité des solvants puis être responsables de l'augmentation de l'activité.

Tableau 1.3 Hydrogénation du préral avec Fe₄₀Pt₆₀@SILP.



Entrée	Solvant	t, h	X (%)	Y 4a (%)	Y 4b (%)	Y 4c (%)
1	Mesytilène	4	72	66	1	6
2	Mesytilène	16	87	79	0	8
3	i-PrOH	4	92	86	0	6
4 ^a	i-PrOH	4	0	0	0	0

a - test sans H₂ Conditions de réaction : Catalyseur (13,6 mg, 0,005 mmol [Me]), substrat (0,5 mmol, 100 eq.), solvant (0,5 mL), H₂ (5 bar), 50°C, 4h. La conversion et le rendement sont déterminés par GC-FID en utilisant le dodécane comme étalon interne. Les points de données représentent la valeur moyenne de deux expériences au minimum. X = conversion, Y = rendement.

III Étude de matériaux hybrides Pt-porphyrine

Les porphyrines sont des composés macrocycliques bien connus pour leurs propriétés photophysiques. Leur noyau planaire avec un système pi conjugué permet des coefficients d'absorption et d'extinction élevés, tandis que divers groupes fonctionnels périphériques peuvent modifier efficacement les propriétés physiques (solubilité) des porphyrines et la capacité d'interagir avec d'autres objets dans un système hybride. Dans notre étude, nous avons décidé de combiner des NP de Pt ultra-petites (US) et des complexes de porphyrine avec différents degrés de substitution afin d'étudier l'influence des substituants dans la porphyrine sur les propriétés de chaque composant de ces matériaux hybrides. Nous avons utilisé une molécule de porphyrine non modifiée - 5,10,15,20-tétraphénylporphyrine (**TP**), et son complexe avec le zinc - 5,10,15,20-tétraphényl-21H,23H-porphyrine zinc (**ZTP**) ; des porphyrines modifiées avec un méso-substituant pyridine : 5-pyridyl-10,15,20-tri-(3,5-(diterbutyl)-phényl)-21H,23H-porphyrine zinc (**ZMPy**) et 5-

pyridyl-10,15,20-tri-(3,5-(diterbutyl)-phényl)-21H,23H-porphine nickel (**NMPy**), et avec deux fragments de pyridine : 5,15-dipyridyl-10,20-di-(3,5-(diterbutyl)-phényl)-21H,23H-porphine zinc (**ZBPY**) et 5,15-dipyridyl-10,20-di-(3,5-(diterbutyl)-phényl)-21H,23H-porphine nickel (**NBPY**).

La synthèse des Pt NP "nues" a été réalisée selon la procédure développée dans notre équipe, qui comprend la décomposition du précurseur Pt₂(dba)₃ (dba = dibenzylideneacetone) dans le THF sous 1 bar CO et le lavage avec du pentane. Cette procédure a permis d'obtenir des US NP d'une taille moyenne de 1 à 1,5 nm. De cette manière, les NP sont stabilisées uniquement par le THF et le CO, ce qui permet un post-traitement avec le ligand de notre choix. Une fois la solution de NP obtenue, la solution THF de porphyrine a pu être ajoutée. Les mélanges obtenus ont été agités pendant deux heures à température ambiante afin de coordonner les porphyrines à la surface des NP de Pt.

La distribution des NP dans les matériaux Pt-porphyrine a été analysée par TEM et tomographie électronique (Figure III.1). Nous avons constaté que les NP stabilisées avec 0,05 eq de porphyrine par rapport à la quantité d'atomes de Pt formaient des structures auto-assemblées. La forme de l'auto-assemblage dépendait de la structure de la porphyrine. Dans le cas de **ZMPy** ou **NMPy**, qui possèdent un site de coordination, les assemblages se présentent sous la forme de bâtonnets. Lorsque **ZBPY** ou **NBPY**, qui possèdent deux sites de liaison pyridinique, ont été utilisés pour synthétiser les matériaux, des assemblages en forme de sphère ont été formés. En revanche, avec le **TP** et le **ZTP**, qui ne contiennent aucun site de coordination, on a observé des NP dispersées ou des agglomérats mal formés.

La DRX aux petits angles a été utilisée pour les systèmes, car elle permet d'extraire une distance moyenne entre les NP dans des systèmes partiellement ordonnés. L'analyse a montré des pics prononcés pour les systèmes avec des porphyrines pyridiniques mono- et di-substituées, tandis que les NP stabilisées avec **TP** et **ZTP** n'ont montré aucun pic (Figure III.2 a). Ce résultat suggère une fois de plus que les sites pyridiniques sur **MMPy** (M pour métal) et **MBPy** se coordonnent fortement à la surface de Pt, ce qui permet d'organiser les NP avec des distances de corrélation typiques mesurées entre deux nanoparticules. D'après les mesures, l'espacement moyen entre deux centres de NP était de 2,9 nm pour les structures **MMPy** et de 2,2 nm pour les structures **MBPy**.

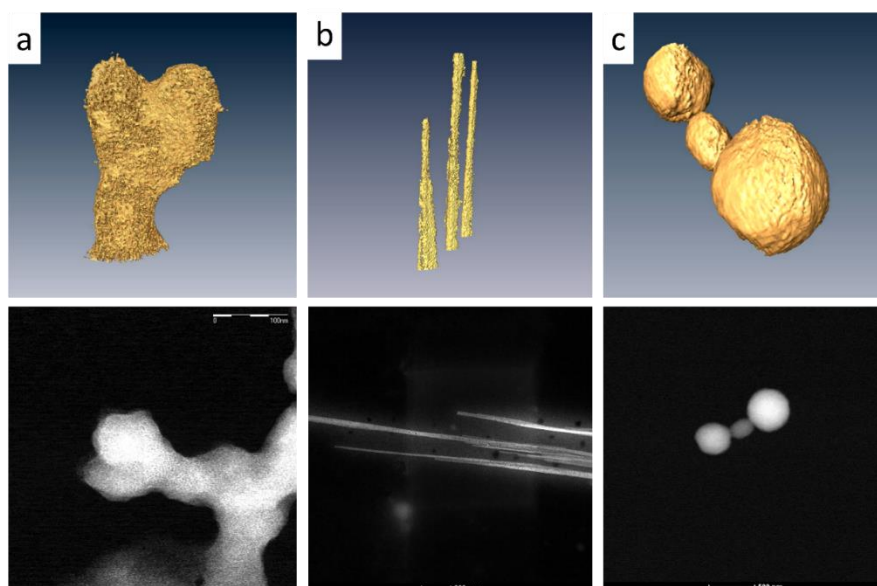


Figure III.1 Tomographie électronique de a) Pt-ZTP ; b) Pt-ZMPy ; c) Pt-ZBPy avec les images HR-TEM-HAADF correspondantes. Les barres d'échelle correspondent à a) 100 nm ; b) 200 nm ; c) 500 nm.

Comme le CO a été utilisé pour décomposer le complexe de Pt, nous avons pu suivre son signal à la surface des NP à l'aide de l'IR. Un déplacement de la bande de CO par rapport à la valeur de la bande de CO attachée aux NP de Pt "nues" (2041 cm^{-1}) signifie que la densité électronique à la surface a changé en raison de la coordination de la porphyrine. Sur le spectre IR ((Figure III.2 b), un fort décalage de $5\text{-}8\text{ cm}^{-1}$ a été observé pour les NP stabilisées avec des ligands fonctionnalisés par la pyridine (2046 cm^{-1} pour **ZMPy**, 2048 cm^{-1} pour **NMPy**, 2046 cm^{-1} pour **ZBPy**, et 2049 cm^{-1} pour **NBPy**) alors que pour **TP** et **ZTP**, il n'y avait presque pas de décalage (2042 et 2043 cm^{-1}). Ce résultat suggère une forte interaction entre les porphyrines modifiées par la pyridine et les NP, peut-être par la formation d'une liaison de coordination Pt-N.

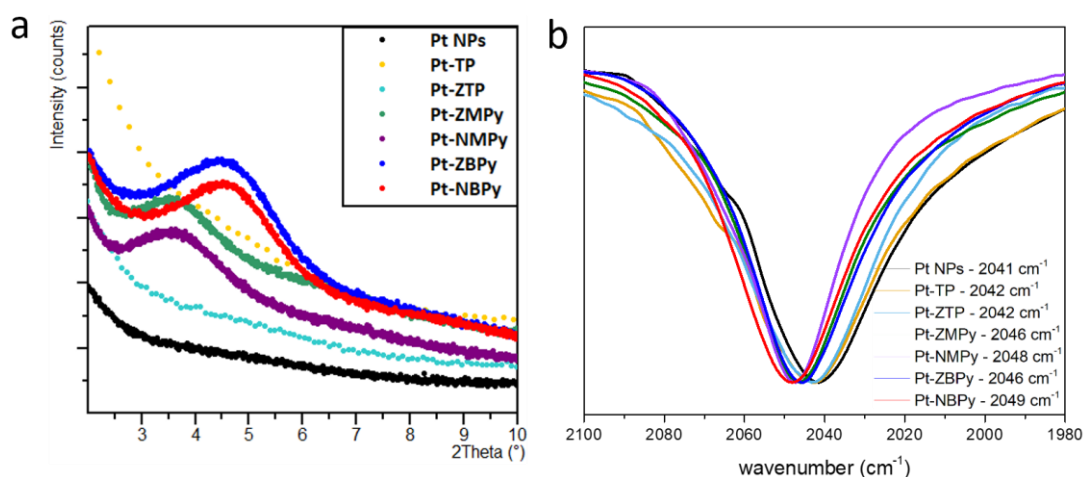


Figure III.2 a) XRD à faible angle des systèmes Pt-porphyrine ; b) spectres IR des systèmes Pt-Porph avec zoom sur la bande d'absorption CO.

Pour étudier l'influence des NP de Pt sur les propriétés photophysiques des systèmes, les mesures PL ont été effectuées en maintenant la concentration d'une porphyrine constante à 0,0245 mM mais en faisant varier la concentration des NP de Pt de 0,125 à 3,95 mM, ce qui correspond à la teneur relative en atomes de métal Pt de 5 à 160 équivalents (Figure III.3). Les échantillons ont été irradiés avec une lumière de 425 nm, qui est une valeur typique pour la bande de Soret des porphyrines. Deux bandes d'émission intenses ont été trouvées à 629 nm et 696 nm pour la molécule de porphyrine et à 603 nm et 653 nm pour les porphyrines métallisées qui correspondent aux transitions Q (0,0) et Q (0,1). Une extinction de la fluorescence des porphyrines a été observée en fonction de l'augmentation de la quantité de NP de Pt dans la solution. Les spectres TRPL de chaque porphyrine avec différentes quantités de NP de Pt ont été enregistrés (Figure III.3). Dans le cas des porphyrines non modifiées **TP** et **ZTP**, les durées de vie PL n'ont pas changé avec l'augmentation de la quantité de NP de Pt et sont restées égales à celles des molécules libres - 11 ns pour **TP** et 2 ns pour **ZTP**. Ainsi, la nature de l'extinction dans ce cas est uniquement statique. Au contraire, pour **ZMPy** et **ZBPY**, à partir de 40 eq de Pt, un nouveau temps de décroissance plus court de 1 ns pour **ZMPy** et de 0,7 ns pour **ZBPY** est devenu prononcé, en plus du temps de décroissance de 2,2 ns des molécules libres. Ainsi, des mécanismes d'extinction à la fois dynamiques et statiques sont présents dans les solutions de **ZMPy** et de **ZBPY** à forte teneur en Pt, alors que seul un mécanisme d'extinction statique a été suggéré pour **TP** et le **ZTP**.

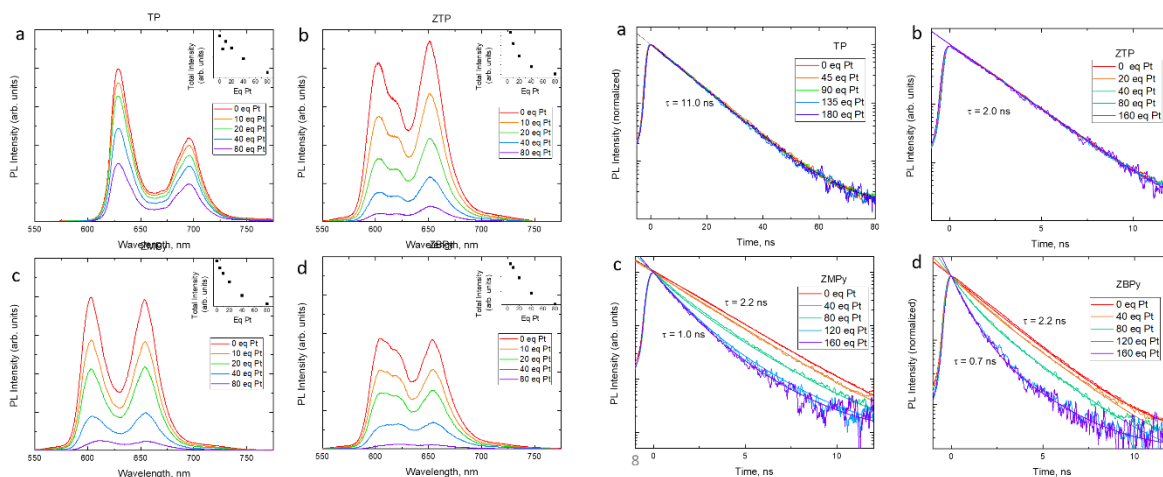


Figure III.3 Spectres PL et TRPL de a)TP ; b)ZTP ; c)ZMPy ; d)ZBPY.

Pour mesurer les caractéristiques électroniques des systèmes hybrides, les solutions de **Pt-TP**, **Pt-ZTP**, **Pt-ZMPy** et **Pt-ZBPY** contenant 0,05 eq de porphyrine ont été déposées sur un substrat d'or et analysées en effectuant des mesures par microscopie à force atomique conductrice (CAFM) dans différentes parties d'un échantillon. Les résultats sont présentés sous forme de courbes I-V où le courant a été moyenné et normalisé à $V = 2$ V. Un régime de blocage de Coulomb (CB) a été

observé dans chaque cas à température ambiante, en raison de la petite taille des NP (Figure III.4 a). L'encadré de la Figure 4.5.8 a montre la différence d'énergie de charge entre les systèmes hybrides, c'est-à-dire en passant des Pt NP au **Pt-TP**, au **Pt-ZTP**, au **Pt-ZMPy**, et au **Pt-ZBPy**, le CB a augmenté. Sous irradiation lumineuse (10s de lumière allumée, 10s de lumière éteinte) avec des NP nues, le courant a légèrement augmenté, ce qui pourrait être attribué soit à un effet de chauffage local, soit à une polarisation de la NP qui a facilité le transport des électrons (Figure III.4 b). Le **Pt-ZTP** a montré une différence mineure dans la photoconduction, les résultats étaient du même ordre de grandeur que pour les NP nues. Cependant, une augmentation du photocourant relatif a été observée dans les systèmes **Pt-ZMPy** et **Pt-ZBPy**. Nous pourrions l'attribuer à une possible augmentation de la polarisabilité moléculaire dans un état excité, ce qui faciliterait le saut des électrons d'une NP à l'autre. La différence entre les systèmes **Pt-ZTP** et les systèmes avec des NP fonctionnalisées à la pyridine pourrait résider dans la stabilité relative des SA, où la liaison covalente entre le Pt et la porphyrine permet d'obtenir des assemblages stables avec des distances interparticulaires contrôlables.

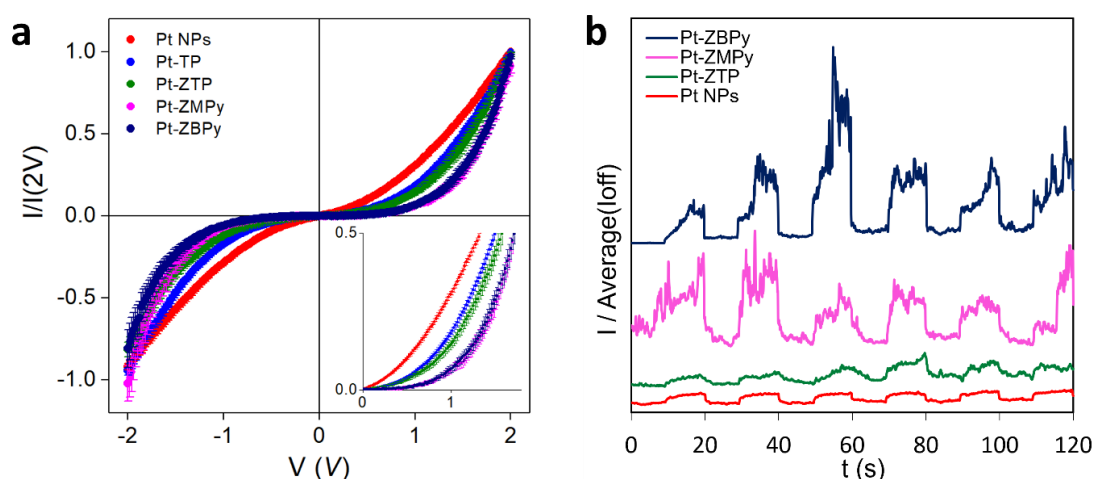


Figure III.4 a) tracés I-V des systèmes hybrides Pt-porphyrine ; b) effet de la lumière sur la conductivité des systèmes hybrides.

IV Étude sur le système hybride Pt NP-Ru(II) trisbipyridyle

Les complexes de ruthénium bipyridyle ont des propriétés photométriques uniques qui en font un choix populaire dans les applications photocatalytiques et photosensibilisantes. Dans notre étude, nous avons décidé de synthétiser le complexe $[\text{Ru}(\text{bpy})_3]^{2+}$ et de l'utiliser comme antenne de transfert d'énergie pour les nanoparticules de platine. Pour assurer une forte coordination du complexe à la surface des NP de Pt, nous avons fonctionnalisé l'un des fragments de bipyridyle avec

une chaîne portant une partie imidazolium qui peut être déprotonée avec la formation de NHC pour se lier fortement aux NP de Pt.

La synthèse des complexes a comporté plusieurs étapes avec des purifications. Le schéma général des synthèses est présenté sur la Figure IV.1. La première étape comprenait deux réactions en une seule étape, comme cela a été rapporté précédemment pour la synthèse de complexes de ruthénium fonctionnalisés.²⁷⁵ La première était la déprotonation du 4,4'-diméthyl-2,2'-dipyridyle (**1**). Pour déprotoner un groupe méthyle, une base forte telle que le diisopropylamide de lithium (LDA) était nécessaire. Par conséquent, l'ajout d'un excès d'alcane fonctionnalisé avec deux groupements bromés aux extrémités (1,10-dibromodécane ou 1,4-dibromobutane) a entraîné la formation des (4-méthyl-4'-bromoalcane)-2,2'-dipyridyles **2a** et **2b**. L'étape suivante était une autre substitution nucléophile du brome par l'imidazole **3a** (commercial) ou **3b** (pour la synthèse de **3b**, voir la partie expérimentale). L'étape de complexation a été réalisée avec le ruthénium(II)cis-dichlorobis(2,2'-bipyridine) dihydraté et les ligands chélateurs **4a**, **4b**, **4c**.

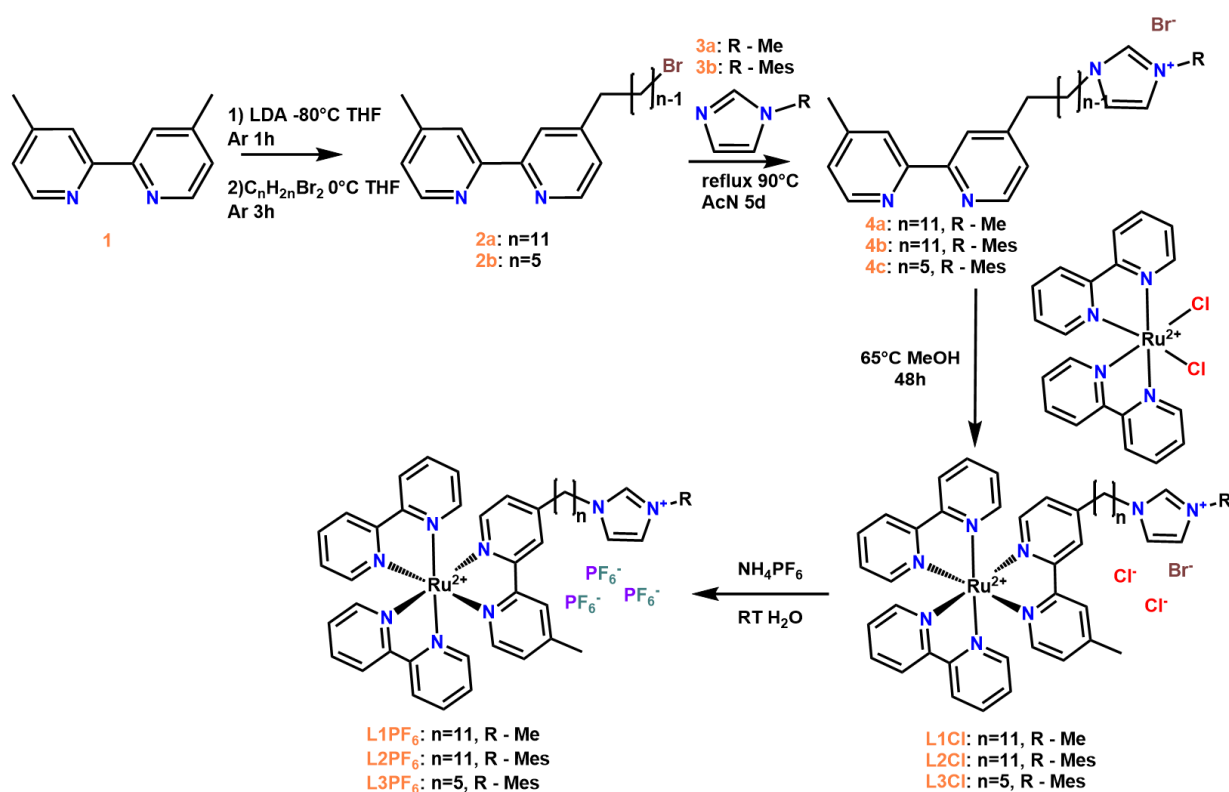


Figure IV.1 Schéma général de la synthèse des complexes de ruthénium utilisés dans l'étude.

Les composés finaux ont été caractérisés par RMN, MS, UV-Vis et PL. Alors que le complexe **L1** était complètement pur, le complexe **L2** contenait des impuretés mineures et le complexe **L3** était encore plus contaminé, de sorte que d'autres expériences ont été réalisées avec le complexe **L1**.

La déprotonation de L1Cl a été suivie par RMN. Nous avons constaté que, sous l'effet de l'addition d'une base t-ButOK, le proton de l'imidazolium disparaissait du spectre de **L1Cl**. Cependant, après avoir laissé le tube à l'air pendant un certain temps, nous avons pu constater la réapparition d'un proton. Ces résultats ont confirmé la déprotonation de **L1Cl** et ont permis de l'utiliser dans la synthèse de Pt NP. La synthèse a été réalisée par une approche organométallique avec la décomposition du précurseur Pt dba₂₃ sous 3 bar de H₂ en présence de **L1Cl** déprotoné (0,1 eq par rapport à la quantité de Pt), un lavage conséquent avec AcN/THF=1/30 et un séchage. Les résultats TEM ont montré des US NP de 1,4 nm avec une petite distribution de taille. Les NP ont été trouvées à la fois à l'état dispersé et en tant que grappes denses (Figure IV.2). Les spectres d'absorption et d'émission de **L1Cl** et de **Pt-L1Cl** sont indiqués sur la Figure IV.3. Les spectres **Pt-L1Cl** sont similaires aux spectres **L1Cl** avec de légers déplacements bathochromiques dans l'absorption (455 nm à 460 nm) et dans les maximums d'émission (628 à 640 nm). L'émission du complexe attaché aux NP a été considérablement réduite, ce qui devrait provenir du transfert d'énergie vers le Pt, conformément aux rapports de la littérature.²⁷⁶. Cette hypothèse reste à confirmer.

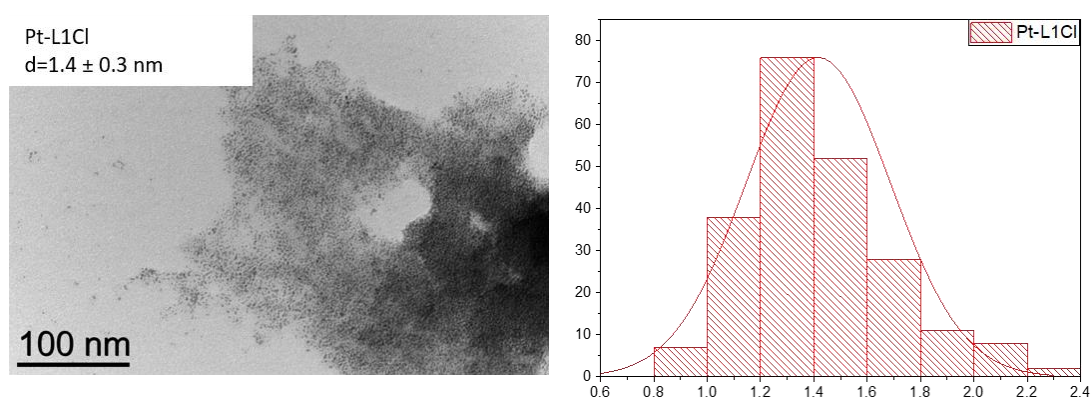


Figure IV.2 Image TEM et diagramme de distribution de taille des NP de **Pt-L1Cl**.

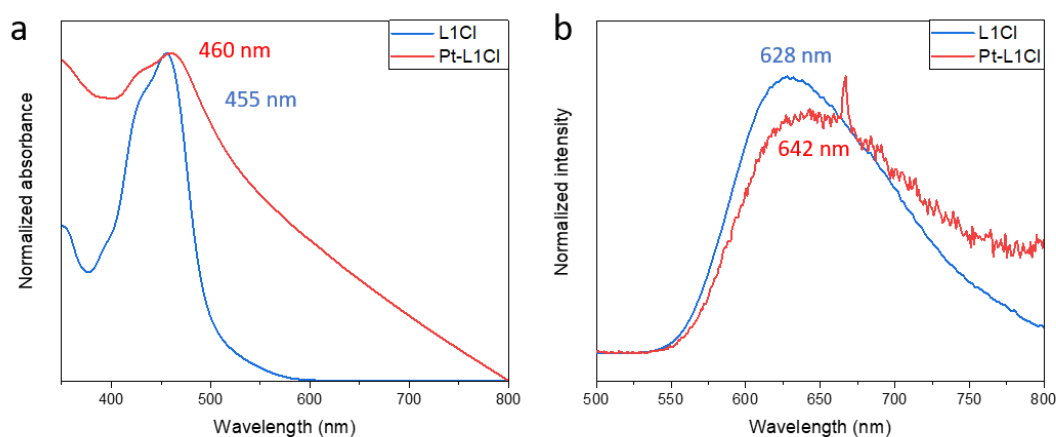


Figure IV.3 a) Spectres d'absorption et b) d'émission de **L1Cl** (bleu) et de **Pt-L1Cl** NP (rouge). Notez que la concentration du complexe n'est pas la même dans les solutions de **L1Cl** et de **Pt-L1Cl** NP. Un pic net sur le spectre d'émission de **Pt-L1Cl** est un artefact expérimental.

En résumé, nous avons présenté ici une synthèse de complexes de ruthénium modifiés par un fragment d'imidazolium. Les complexes ont été caractérisés et le complexe **L1** a été appliqué avec succès dans la synthèse de NP de Pt.

V Conclusions

En résumé, cette thèse présente les résultats de quatre projets axés sur l'étude de l'effet de ligand sur les propriétés des NP. L'originalité de ce travail de thèse réside dans le fait qu'en utilisant les mêmes nano-objets et des techniques de caractérisation similaires, l'influence directe des ligands sur les propriétés d'auto-assemblage, électroniques et catalytiques des NP a pu être étudiée. Les travaux actuels indiquent que l'agent stabilisateur peut servir d'instrument supplémentaire dans la boîte à outils des spécialistes des nanosciences pour concevoir des nanosystèmes très performants pour des applications spécifiques. Les résultats et les tendances décrits dans cette thèse peuvent être utilisés par d'autres chercheurs qui travaillent avec des ligands similaires ou par ceux qui sont intéressés par l'ajustement des propriétés des petites NP métalliques par des ligands.

Reference list

1. Lu, L., Zou, S. & Fang, B. The Critical Impacts of Ligands on Heterogeneous Nanocatalysis: A Review. *ACS Catal.* **11**, 6020–6058 (2021).
2. Zhang, P., Wang, J., Huang, H., Yu, B., Qiu, K., Huang, J., Wang, S., Jiang, L., Gasser, G., Ji, L. & Chao, H. Unexpected high photothematic conversion efficiency of gold nanospheres upon grafting with two-photon luminescent ruthenium(II) complexes: A way towards cancer therapy? *Biomaterials* **63**, 102–114 (2015).
3. Nakanishi, H., Bishop, K. J. M., Kowalczyk, B., Nitzan, A., Weiss, E. A., Tretiakov, K. V., Apodaca, M. M., Klajn, R., Stoddart, J. F. & Grzybowski, B. A. Photoconductance and inverse photoconductance in films of functionalized metal nanoparticles. *Nature* **460**, 371–375 (2009).
4. Calixto, G. M. F., Bernegossi, J., De Freitas, L. M., Fontana, C. R., Chorilli, M. & Grumezescu, A. M. Nanotechnology-based drug delivery systems for photodynamic therapy of cancer: A review. *Molecules* **21**, 1–18 (2016).
5. Chakraborty, I. N., Roy, P., Rao, A., Devatha, G., Roy, S. & Pillai, P. P. The unconventional role of surface ligands in dictating the light harvesting properties of quantum dots. *J. Mater. Chem. A* **9**, 7422–7457 (2021).
6. Gómez-Jiménez-Aberasturi, O. Eco-friendly Materials for Chemical Products Manufacturing: Adhesives Derived from Biomass and Renewable Resources. in *Handbook of Ecomaterials* vol. 3 1937–1952 (Springer International Publishing, 2019).
7. Yaqoob, L., Noor, T. & Iqbal, N. Recent progress in development of efficient electrocatalyst for methanol oxidation reaction in direct methanol fuel cell. *Int. J. Energy Res.* **45**, 6550–6583 (2021).
8. Zhou, Y. & Guo, S. Recent advances in cathode catalyst architecture for lithium–oxygen batteries. *eScience* 100123 (2023) doi:10.1016/j.esci.2023.100123.
9. Abed, A., Derakhshan, M., Karimi, M., Shirazinia, M., Mahjoubin-Tehran, M., Homayonfal, M., Hamblin, M. R., Mirzaei, S. A., Soleimanpour, H., Dehghani, S., Dehkordi, F. F. & Mirzaei, H. Platinum Nanoparticles in Biomedicine: Preparation, Anti-Cancer Activity, and Drug Delivery Vehicles. *Front. Pharmacol.* **13**, 1–23 (2022).
10. Pedone, D., Moglianetti, M., De Luca, E., Bardi, G. & Pompa, P. P. Platinum nanoparticles in nanobiomedicine. *Chem. Soc. Rev.* **46**, 4951–4975 (2017).
11. Gentili, D. & Ori, G. Reversible assembly of nanoparticles: theory, strategies and computational simulations. *Nanoscale* **14**, 14385–14432 (2022).
12. Brust, M., Walker, M., Bethell, D., Schiffrin, D. J. & Whyman, R. Synthesis of Thiol-derivatised Gold Nanoparticles in. 801–802 (2000).
13. Turkevich, J., Stevenson, P. C. & Hillier, J. A study of the nucleation and growth processes in the synthesis of colloidal gold. *Discuss. Faraday Soc.* **11**, 55 (1951).
14. FRENS, G. Controlled Nucleation for the Regulation of the Particle Size in Monodisperse Gold Suspensions. *Nat. Phys. Sci.* **241**, 20–22 (1973).
15. Hussain, I., Graham, S., Wang, Z., Tan, B., Sherrington, D. C., Rannard, S. P., Cooper, A. I. & Brust, M. Size-Controlled Synthesis of Near-Monodisperse Gold Nanoparticles in the 1–4 nm Range Using Polymeric Stabilizers. *J. Am. Chem. Soc.* **127**, 16398–16399 (2005).
16. Xian, J., Hua, Q., Jiang, Z., Ma, Y. & Huang, W. Size-dependent interaction of the poly(N-vinyl-2-pyrrolidone) capping ligand with Pd nanocrystals. *Langmuir* **28**, 6736–6741 (2012).
17. Zeng, J., Zheng, Y., Rycenga, M., Tao, J., Li, Z. Y., Zhang, Q., Zhu, Y. & Xia, Y. Controlling the shapes of silver nanocrystals with different capping agents. *J. Am. Chem. Soc.* **132**, 8552–8553 (2010).
18. Xia, Y., Xia, X. & Peng, H. C. Shape-Controlled Synthesis of Colloidal Metal Nanocrystals: Thermodynamic versus Kinetic Products. *Journal of the American Chemical Society* vol. 137 7947–7966 at <https://doi.org/10.1021/jacs.5b04641> (2015).
19. Lim, B., Xiong, Y. & Xia, Y. A water-based synthesis of octahedral, decahedral, and icosahedral Pd nanocrystals. *Angew. Chemie - Int. Ed.* **46**, 9279–9282 (2007).
20. Yang, T. H., Shi, Y., Janssen, A. & Xia, Y. Surface Capping Agents and Their Roles in Shape-Controlled Synthesis

- of Colloidal Metal Nanocrystals. *Angew. Chemie - Int. Ed.* **59**, 15378–15401 (2020).
21. Pellas, V., Hu, D., Mazouzi, Y., Mimoun, Y., Blanchard, J., Guibert, C., Salmain, M. & Boujday, S. Gold Nanorods for LSPR Biosensing: Synthesis, Coating by Silica, and Bioanalytical Applications. *Biosensors* **10**, (2020).
 22. Gentili, D., Ori, G., Ortolani, L., Morandi, V. & Cavallini, M. Cooperative and Reversible Anisotropic Assembly of Gold Nanoparticles by Modulation of Noncovalent Interparticle Interactions. *ChemNanoMat* **3**, 874–878 (2017).
 23. Park, J. E., Seo, M., Jang, E., Kim, H., Kim, J. S. & Park, S. J. Vesicle-like assemblies of ligand-stabilized nanoparticles with controllable membrane composition and properties. *Nanoscale* **11**, 1837–1846 (2019).
 24. Sánchez-Iglesias, A., Grzelczak, M., Altantzis, T., Goris, B., Pérez-Juste, J., Bals, S., Van Tendeloo, G., Donaldson, S. H., Chmelka, B. F., Israelachvili, J. N. & Liz-Marzán, L. M. Hydrophobic interactions modulate self-assembly of nanoparticles. *ACS Nano* **6**, 11059–11065 (2012).
 25. Nie, Z., Fava, D., Kumacheva, E., Zou, S., Walker, G. C. & Rubinstein, M. Self-assembly of metal-polymer analogues of amphiphilic triblock copolymers. *Nat. Mater.* **6**, 609–614 (2007).
 26. Quintana, C., Cifuentes, M. P. & Humphrey, M. G. Transition metal complex/gold nanoparticle hybrid materials. *Chem. Soc. Rev.* **49**, 2316–2341 (2020).
 27. Nasrallah, H. O., Min, Y., Lerayer, E., Nguyen, T. A., Poinot, D., Roger, J., Brandès, S., Heintz, O., Roblin, P., Jolibois, F., Poteau, R., Coppel, Y., Kahn, M. L., Gerber, I. C., Axet, M. R., Serp, P. & Hierso, J.-C. Nanocatalysts for High Selectivity Enyne Cyclization: Oxidative Surface Reorganization of Gold Sub-2-nm Nanoparticle Networks. *JACS Au* **1**, 187–200 (2021).
 28. Klajn, R., Bishop, K. J. M. & Grzybowski, B. A. Light-controlled self-assembly of reversible and irreversible nanoparticle suprastructures. *Proc. Natl. Acad. Sci. U. S. A.* **104**, 10305–10309 (2007).
 29. Klajn, R., Wesson, P. J., Bishop, K. J. M. & Grzybowski, B. A. Writing self-erasing images using metastable nanoparticle ‘inks’. *Angew. Chemie - Int. Ed.* **48**, 7035–7039 (2009).
 30. Zhao, H., Sen, S., Udayabhaskararao, T., Sawczyk, M., Kučanda, K., Manna, D., Kundu, P. K., Lee, J., Král, P. & Klajn, R. Reversible trapping and reaction acceleration within dynamically self-assembling nanoflasks. *Nat. Nanotechnol.* **11**, 82–88 (2016).
 31. Shiraishi, Y., Shirakawa, E., Tanaka, K., Sakamoto, H., Ichikawa, S. & Hirai, T. Spiropyran-modified gold nanoparticles: Reversible size control of aggregates by UV and visible light irradiations. *ACS Appl. Mater. Interfaces* **6**, 7554–7562 (2014).
 32. Fan, C., Bian, T., Shang, L., Shi, R., Wu, L. Z., Tung, C. H. & Zhang, T. PH-Responsive reversible self-assembly of gold nanoparticles into nanovesicles. *Nanoscale* **8**, 3923–3925 (2016).
 33. He, H., Ostwaldt, J., Hirschhäuser, C., Schmuck, C. & Niemeyer, J. Dual pH-Induced Reversible Self-Assembly of Gold Nanoparticles by Surface Functionalization with Zwitterionic Ligands. *Small* **16**, 2001044 (2020).
 34. Balasubramaniam, S., Pothayee, N., Lin, Y., House, M., Woodward, R. C., St. Pierre, T. G., Davis, R. M. & Riffle, J. S. Poly(N -isopropylacrylamide)-coated superparamagnetic iron oxide nanoparticles: Relaxometric and fluorescence behavior correlate to temperature-dependent aggregation. *Chem. Mater.* **23**, 3348–3356 (2011).
 35. Fava, D., Winnik, M. A. & Kumacheva, E. Photothermally-triggered self-assembly of gold nanorods. *Chem. Commun.* 2571–2573 (2009) doi:10.1039/b901412h.
 36. Zhao, Y., Huang, Y., Zhu, H., Zhu, Q. & Xia, Y. Three-in-One: Sensing, Self-Assembly, and Cascade Catalysis of Cyclodextrin Modified Gold Nanoparticles. *J. Am. Chem. Soc.* **138**, 16645–16654 (2016).
 37. Qu, D. H., Wang, Q. C., Zhang, Q. W., Ma, X. & Tian, H. Photoresponsive Host-Guest Functional Systems. *Chem. Rev.* **115**, 7543–7588 (2015).
 38. Liu, Z. & Jiang, M. Reversible aggregation of gold nanoparticles driven by inclusion complexation. *J. Mater. Chem.* **17**, 4249–4254 (2007).
 39. Shirman, T., Arad, T. & Van Der Boom, M. E. Halogen bonding: A supramolecular entry for assembling nanoparticles. *Angew. Chemie - Int. Ed.* **49**, 926–929 (2010).
 40. Chen, G., Xu, C., Huang, X., Ye, J., Gu, L., Li, G., Tang, Z., Wu, B., Yang, H., Zhao, Z., Zhou, Z., Fu, G. & Zheng, N. Interfacial electronic effects control the reaction selectivity of platinum catalysts. *Nat. Mater.* **15**, 564–569 (2016).
 41. Kwon, S. G., Krylova, G., Sumer, A., Schwartz, M. M., Bunel, E. E., Marshall, C. L., Chattopadhyay, S., Lee, B.,

- Jellinek, J. & Shevchenko, E. V. Capping Ligands as Selectivity Switchers in Hydrogenation Reactions. *Nano Lett.* **12**, 5382–5388 (2012).
42. Kaefffer, N., Larmier, K., Fedorov, A. & Copéret, C. Origin of ligand-driven selectivity in alkyne semihydrogenation over silica-supported copper nanoparticles. *J. Catal.* **364**, 437–445 (2018).
43. Koy, M., Bellotti, P., Das, M. & Glorius, F. N-Heterocyclic carbenes as tunable ligands for catalytic metal surfaces. *Nat. Catal.* **4**, 352–363 (2021).
44. Lara, P., Rivada-Wheelaghan, O., Conejero, S., Poteau, R., Philippot, K. & Chaudret, B. Ruthenium nanoparticles stabilized by N-heterocyclic carbenes: Ligand location and influence on reactivity. *Angew. Chemie - Int. Ed.* **50**, 12080–12084 (2011).
45. Martínez-Prieto, L. M., Rakers, L., López-Vinasco, A. M., Cano, I., Coppel, Y., Philippot, K., Glorius, F., Chaudret, B. & van Leeuwen, P. W. N. M. Soluble Platinum Nanoparticles Ligated by Long-Chain N-Heterocyclic Carbenes as Catalysts. *Chem. - A Eur. J.* **23**, 12779–12786 (2017).
46. Baquero, E. A., Tricard, S., Coppel, Y., Flores, J. C., Chaudret, B. & De Jesús, E. Water-soluble platinum nanoparticles stabilized by sulfonated N-heterocyclic carbenes: Influence of the synthetic approach. *Dalt. Trans.* **47**, 4093–4104 (2018).
47. Martínez-Prieto, L. M., Ferry, A., Rakers, L., Richter, C., Lecante, P., Philippot, K., Chaudret, B. & Glorius, F. Long-chain NHC-stabilized RuNPs as versatile catalysts for one-pot oxidation/hydrogenation reactions. *Chem. Commun.* **52**, 4768–4771 (2016).
48. Bouzouita, D., Lippens, G., Baquero, E. A., Fazzini, P. F., Pieters, G., Coppel, Y., Lecante, P., Tricard, S., Martínez-Prieto, L. M. & Chaudret, B. Tuning the catalytic activity and selectivity of water-soluble bimetallic RuPt nanoparticles by modifying their surface metal distribution. *Nanoscale* **11**, 16544–16552 (2019).
49. Suárez-Riaño, O., Mencia, G., Tricard, S., Esvan, J., Fazzini, P. F., Chaudret, B. & Baquero, E. A. Water-soluble NHC Pd/Ni bimetallic nanoparticles for H/D exchange in aromatic amino-acids. *Chem. Commun.* **59**, 1062–1065 (2022).
50. Zuluaga-Villamil, A., Mencia, G., Asensio, J. M., Fazzini, P. F., Baquero, E. A. & Chaudret, B. N-Heterocyclic Carbene-Based Iridium and Ruthenium/Iridium Nanoparticles for the Hydrogen Isotope Exchange Reaction through C-H Bond Activations. *Organometallics* **41**, 3313–3319 (2022).
51. Ernst, J. B., Schwermann, C., Yokota, G. I., Tada, M., Muratsugu, S., Doltsinis, N. L. & Glorius, F. Molecular Adsorbates Switch on Heterogeneous Catalysis: Induction of Reactivity by N-Heterocyclic Carbenes. *J. Am. Chem. Soc.* **139**, 9144–9147 (2017).
52. Zhang, L., Wei, Z., Thanneeru, S., Meng, M., Kruzyk, M., Ung, G., Liu, B. & He, J. A Polymer Solution To Prevent Nanoclustering and Improve the Selectivity of Metal Nanoparticles for Electrocatalytic CO₂ Reduction. *Angew. Chemie - Int. Ed.* **58**, 15834–15840 (2019).
53. Ansar, S. M. & Kitchens, C. L. Impact of Gold Nanoparticle Stabilizing Ligands on the Colloidal Catalytic Reduction of 4-Nitrophenol. *ACS Catal.* **6**, 5553–5560 (2016).
54. Mori, A., Mizusaki, T., Kawase, M., Maegawa, T., Monguchi, Y., Takao, S., Takagi, Y. & Sajikia, H. Novel palladium-on-carbon/diphenyl sulfide complex for chemoselective hydrogenation: Preparation, characterization, and application. *Adv. Synth. Catal.* **350**, 406–410 (2008).
55. McKenna, F. M. & Anderson, J. A. Selectivity enhancement in acetylene hydrogenation over diphenyl sulphide-modified Pd/TiO₂ catalysts. *J. Catal.* **281**, 231–240 (2011).
56. Marshall, S. T., O'Brien, M., Oetter, B., Corpuz, A., Richards, R. M., Schwartz, D. K. & Medlin, J. W. Controlled selectivity for palladium catalysts using self-assembled monolayers. *Nat. Mater.* **9**, 853–858 (2010).
57. Wu, B., Huang, H., Yang, J., Zheng, N. & Fu, G. Selective Hydrogenation of α,β -Unsaturated Aldehydes Catalyzed by Amine-Capped Platinum-Cobalt Nanocrystals. *Angew. Chemie Int. Ed.* **51**, 3440–3443 (2012).
58. Almora-barrios, N., Verel, R. & Pérez-ramírez, J. Ligand ordering determines the catalytic response of hybrid palladium nanoparticles in hydrogenation. *Catal. Sci. Technol.* (2015) doi:10.1039/C5CY01921D.
59. Makosch, M., Lin, W. I., Bumbálek, V., Sá, J., Medlin, J. W., Hungerbühler, K. & Van Bokhoven, J. A. Organic thiol modified Pt/TiO₂ catalysts to control chemoselective hydrogenation of substituted nitroarenes. *ACS Catal.* **2**, 2079–2081 (2012).
60. Schröder, C., Schmidt, M. C., Hugg, P. A., Baumann, A., Smyczek, J. & Schaueremann, S. Understanding Ligand-

- Directed Heterogeneous Catalysis: When the Dynamically Changing Nature of the Ligand Layer Controls the Hydrogenation Selectivity. *Angew. Chemie Int. Ed.* **60**, 16349–16354 (2021).
61. Pang, S. H., Schoenbaum, C. A., Schwartz, D. K. & Medlin, J. W. Directing reaction pathways by catalyst active-site selection using self-assembled monolayers. *Nat. Commun.* **4**, 1–6 (2013).
 62. Campisi, S., Ferri, D., Villa, A., Wang, W., Wang, D., Kröcher, O. & Prati, L. Selectivity Control in Palladium-Catalyzed Alcohol Oxidation through Selective Blocking of Active Sites. *J. Phys. Chem. C* **120**, 14027–14033 (2016).
 63. Kahsar, K. R., Schwartz, D. K. & Medlin, J. W. Control of metal catalyst selectivity through specific noncovalent molecular interactions. *J. Am. Chem. Soc.* **136**, 520–526 (2014).
 64. Coan, P. D., Farberow, C. A., Griffin, M. B. & Medlin, J. W. Organic modifiers promote furfuryl alcohol ring hydrogenation via surface hydrogen-bonding interactions. *ACS Catal.* **11**, 3730–3739 (2021).
 65. Schrader, I., Warneke, J., Backenköhler, J. & Kunz, S. Functionalization of Platinum Nanoparticles with L-Proline: Simultaneous Enhancements of Catalytic Activity and Selectivity. *J. Am. Chem. Soc.* **137**, 905–912 (2015).
 66. Blaser, H. U. & Studer, M. Cinchona-modified platinum catalysts: From ligand acceleration to technical processes. *Acc. Chem. Res.* **40**, 1348–1356 (2007).
 67. Zaera, F. Chiral modification of solid surfaces: A molecular view. *J. Phys. Chem. C* **112**, 16196–16203 (2008).
 68. Bürgi, T. & Baiker, A. Heterogeneous enantioselective hydrogenation over cinchona alkaloid modified platinum: Mechanistic insights into a complex reaction. *Acc. Chem. Res.* **37**, 909–917 (2004).
 69. Lavoie, S., Laliberté, M. A., Temprano, I. & McBreen, P. H. A generalized two-point H-bonding model for catalytic stereoselective hydrogenation of activated ketones on chirally modified platinum. *J. Am. Chem. Soc.* **128**, 7588–7593 (2006).
 70. Zeng, Y., Lemay, J. C., Dong, Y., Garcia, J., Groves, M. N. & McBreen, P. H. Ligand-Assisted Carbonyl Bond Activation in Single Diastereomeric Complexes on Platinum. *ACS Catal.* **12**, 12186–12194 (2022).
 71. Schrader, I., Neumann, S., Šulce, A., Schmidt, F., Azov, V. & Kunz, S. Asymmetric Heterogeneous Catalysis: Transfer of Molecular Principles to Nanoparticles by Ligand Functionalization. *ACS Catal.* **7**, 3979–3987 (2017).
 72. LeBlond, C., Wang, J., Liu, J., Andrews, A. T. & Sun, Y. K. Highly enantioselective heterogeneously catalyzed hydrogenation of α -ketoesters under mild conditions [15]. *J. Am. Chem. Soc.* **121**, 4920–4921 (1999).
 73. Hong, J., Lee, I. & Zaera, F. Correlated bifunctionality in heterogeneous catalysts: Selective tethering of cinchonidine next to supported Pt nanoparticles. *Catal. Sci. Technol.* **5**, 680–689 (2015).
 74. Yasukawa, T., Suzuki, A., Miyamura, H., Nishino, K. & Kobayashi, S. Chiral Metal Nanoparticle Systems as Heterogeneous Catalysts beyond Homogeneous Metal Complex Catalysts for Asymmetric Addition of Arylboronic Acids to α,β -Unsaturated Carbonyl Compounds. *J. Am. Chem. Soc.* **137**, 6616–6623 (2015).
 75. Cano, I., Huertos, M. A., Chapman, A. M., Buntkowsky, G., Gutmann, T., Groszewicz, P. B. & Van Leeuwen, P. W. N. M. Air-Stable Gold Nanoparticles Ligated by Secondary Phosphine Oxides as Catalyst for the Chemoselective Hydrogenation of Substituted Aldehydes: A Remarkable Ligand Effect. *J. Am. Chem. Soc.* **137**, 7718–7727 (2015).
 76. Cano, I., Martínez-Prieto, L. M., Fazzini, P. F., Coppel, Y., Chaudret, B. & Van Leeuwen, P. W. N. M. Characterization of secondary phosphine oxide ligands on the surface of iridium nanoparticles. *Phys. Chem. Chem. Phys.* **19**, 21655–21662 (2017).
 77. Cano, I., Martínez-Prieto, L. M., Chaudret, B. & van Leeuwen, P. W. N. M. Iridium versus Iridium: Nanocluster and Monometallic Catalysts Carrying the Same Ligand Behave Differently. *Chem. - A Eur. J.* **23**, 1444–1450 (2017).
 78. Almora-Barrios, N., Cano, I., Van Leeuwen, P. W. N. M. & López, N. Concerted Chemoselective Hydrogenation of Acrolein on Secondary Phosphine Oxide Decorated Gold Nanoparticles. *ACS Catal.* **7**, 3949–3954 (2017).
 79. Fiorio, J. L., López, N. & Rossi, L. M. Gold-Ligand-Catalyzed Selective Hydrogenation of Alkynes into cis-Alkenes via H₂ Heterolytic Activation by Frustrated Lewis Pairs. *ACS Catal.* **7**, 2973–2980 (2017).
 80. Kim, S., Kwon, E. E., Kim, Y. T., Jung, S., Kim, H. J., Huber, G. W. & Lee, J. Recent advances in hydrodeoxygenation of biomass-derived oxygenates over heterogeneous catalysts. *Green Chem.* **21**, 3715–3743 (2019).
 81. Zhang, J., Ellis, L. D., Wang, B., Dzara, M. J., Sievers, C., Pylypenko, S., Nikolla, E. & Medlin, J. W. Control of interfacial acid-metal catalysis with organic monolayers. *Nat. Catal.* **1**, 148–155 (2018).

-
82. Crini, G., Fourmentin, S., Fenyvesi, É., Torri, G., Fourmentin, M. & Morin-Crini, N. Cyclodextrins, from molecules to applications. *Environ. Chem. Lett.* **16**, 1361–1375 (2018).
83. Morin-Crini, N., Fourmentin, S., Fenyvesi, É., Lichtfouse, E., Torri, G., Fourmentin, M. & Crini, G. *History of Cyclodextrins*. (2020). doi:10.1007/978-3-030-49308-0_1.
84. Guitet, M., Zhang, P., Marcelo, F., Tugny, C., Jiménez-Barbero, J., Buriez, O., Amatore, C., Mouriès-Mansuy, V., Goddard, J.-P., Fensterbank, L., Zhang, Y., Roland, S., Ménand, M. & Sollogoub, M. NHC-Capped Cyclodextrins (ICyDs): Insulated Metal Complexes, Commutable Multicoordination Sphere, and Cavity-Dependent Catalysis. *Angew. Chemie* **125**, 7354–7359 (2013).
85. Jouffroy, M., Gramage-Doria, R., Armspach, D., Sémeril, D., Oberhauser, W., Matt, D. & Toupet, L. Confining Phosphanes Derived from Cyclodextrins for Efficient Regio- and Enantioselective Hydroformylation. *Angew. Chemie Int. Ed.* **53**, 3937–3940 (2014).
86. Mouarrawis, V., Plessius, R., van der Vlugt, J. I. & Reek, J. N. H. Confinement effects in catalysis using well-defined materials and cages. *Front. Chem.* **6**, 1–20 (2018).
87. Komiyama, M. & Hirai, H. Colloidal Rhodium Dispersions Protected by Cyclodextrins. *Bulletin of the Chemical Society of Japan* vol. 56 2833–2834 at <https://doi.org/10.1246/bcsj.56.2833> (1983).
88. Cassez, A., Ponchel, A., Hapiot, F. & Monflier, E. Unexpected multifunctional effects of methylated cyclodextrins in a palladium charcoal-catalyzed Suzuki-Miyaura reaction. *Org. Lett.* **8**, 4823–4826 (2006).
89. Cassez, A., Kania, N., Hapiot, F., Fourmentin, S., Monflier, E. & Ponchel, A. Chemically modified cyclodextrins adsorbed on Pd/C particles: New opportunities to generate highly chemo- and stereoselective catalysts for Heck reaction. *Catal. Commun.* **9**, 1346–1351 (2008).
90. Senra, J. D., Malta, L. F. B., Souza, A. L. F., Aguiar, L. C. S. & Antunesa, O. A. C. Palladium on calcium carbonate combined to 2-hydroxypropyl- α/β - cyclodextrins: A selective catalytic system for aqueous heck coupling and hydroarylation. *Adv. Synth. Catal.* **350**, 2551–2558 (2008).
91. Chau, N. T. T., Handjani, S., Guegan, J. P., Guerrero, M., Monflier, E., Philippot, K., Denicourt-Nowicki, A. & Roucoux, A. Methylated β -Cyclodextrin-Capped Ruthenium Nanoparticles: Synthesis Strategies, Characterization, and Application in Hydrogenation Reactions. *ChemCatChem* **5**, 1497–1503 (2013).
92. Denicourt-Nowicki, A., Ponchel, A., Monflier, E. & Roucoux, A. Methylated cyclodextrins: An efficient protective agent in water for zerovalent ruthenium nanoparticles and a supramolecular shuttle in alkene and arene hydrogenation reactions. *Dalt. Trans.* 5714–5719 (2007) doi:10.1039/b713989f.
93. Chau, N. T. T., Guégan, J. P., Menuel, S., Guerrero, M., Hapiot, F., Monflier, E., Philippot, K., Denicourt-Nowicki, A. & Roucoux, A. β -Cyclodextrins grafted with chiral amino acids: A promising supramolecular stabilizer of nanoparticles for asymmetric hydrogenation? *Appl. Catal. A Gen.* **467**, 497–503 (2013).
94. Noël, S., Caronia, E., Bricout, H., Tichá, I. C., Menuel, S., Ponchel, A., Tilloy, S., Galia, A., Monflier, É., Jindřich, J. & Léger, B. Asymmetric hydrogenation of ethyl pyruvate over aqueous dispersed Pt nanoparticles stabilized by a cinchonidine-functionalized β -cyclodextrin. *Catal. Commun.* **150**, 0–6 (2021).
95. Bricout, H., Hapiot, F., Ponchel, A., Tilloy, S. & Monflier, E. Cyclodextrins as Mass Transfer Additives in Aqueous Organometallic Catalysis. *Curr. Org. Chem.* **14**, 1296–1307 (2010).
96. Ran, X., Yang, L., Qu, Q., Li, S., Chen, Y., Zuo, L. & Li, L. Synthesis of well-dispersive 2.0 nm Pd-Pt bimetallic nanoclusters supported on β -cyclodextrin functionalized graphene with excellent electrocatalytic activity. *RSC Adv.* **7**, 1947–1955 (2017).
97. Sadjadi, S. & Koohestani, F. Composite of β -cyclodextrin and bentonite clay: a promising support for Pd immobilization and developing a catalyst for hydrogenation of nitroarenes under mild reaction condition. *J. Phys. Chem. Solids* **151**, 109894 (2021).
98. Cocq, A., Bricout, H., Djedaini-Pilard, F., Tilloy, S. & Monflier, E. Rhodium-catalyzed aqueous biphasic olefin hydroformylation promoted by amphiphilic cyclodextrins. *Catalysts* **10**, 1–9 (2020).
99. Sadjadi, S. & Koohestani, F. Palladated composite of MOF and cyclodextrin nanosponge: A novel catalyst for hydrogenation reaction. *J. Mol. Struct.* **1245**, 131068 (2021).
100. Zhang, Q., Zhang, S. & Deng, Y. Recent advances in ionic liquid catalysis. *Green Chem.* **13**, 2619–2637 (2011).
101. Vekariya, R. L. A review of ionic liquids: Applications towards catalytic organic transformations. *J. Mol. Liq.* **227**, 44 (2017).

102. Prechtel, M. H. G., Scholten, J. D. & Dupont, J. Tuning the selectivity of ruthenium nanoscale catalysts with functionalised ionic liquids: Hydrogenation of nitriles. *J. Mol. Catal. A Chem.* **313**, 74–78 (2009).
103. Karakulina, A., Gopakumar, A., Akçok, İ., Roulier, B. L., LaGrange, T., Katsyuba, S. A., Das, S. & Dyson, P. J. A Rhodium Nanoparticle-Lewis Acidic Ionic Liquid Catalyst for the Chemoselective Reduction of Heteroarenes. *Angew. Chemie* **128**, 300–304 (2016).
104. Steinrück, H. P. & Wasserscheid, P. Ionic liquids in catalysis. *Catal. Letters* **145**, 380–397 (2015).
105. Díaz, U., Brunel, D. & Corma, A. Catalysis using multifunctional organosiliceous hybrid materials. *Chem. Soc. Rev.* **42**, 4083–4097 (2013).
106. Kacem, S., Emondts, M., Bordet, A. & Leitner, W. Selective hydrogenation of fluorinated arenes using rhodium nanoparticles on molecularly modified silica. *Catal. Sci. Technol.* **10**, 8120–8126 (2020).
107. Bordet, A., El Sayed, S., Sanger, M., Boniface, K. J., Kalsi, D., Luska, K. L., Jessop, P. G. & Leitner, W. Selectivity control in hydrogenation through adaptive catalysis using ruthenium nanoparticles on a CO₂-responsive support. *Nat. Chem.* **13**, 916–922 (2021).
108. Steinrück, H. P., Libuda, J., Wasserscheid, P., Cremer, T., Kolbeck, C., Laurin, M., Maier, F., Sobota, M., Schulz, P. S. & Stark, M. Surface science and model catalysis with ionic liquid-modified materials. *Adv. Mater.* **23**, 2571–2587 (2011).
109. Bordet, A. & Leitner, W. Metal Nanoparticles Immobilized on Molecularly Modified Surfaces: Versatile Catalytic Systems for Controlled Hydrogenation and Hydrogenolysis. *Acc. Chem. Res.* **54**, 2144–2157 (2021).
110. Jess, A. & Korth, W. Solid Catalyst with Ionic Liquid Layer (SCILL) - A concept to improve the selectivity of selective hydrogenations. *DGMK Int. Conf. Catal. - Innov. Appl. Petrochemistry Refin.* 81–92 (2011).
111. Friedrich, M. F., Lucas, M. & Claus, P. Selective hydrogenation of propyne on a solid Pd/Al₂O₃ catalyst modified with ionic liquid layer (SCILL). *Catal. Commun.* **88**, 73–76 (2017).
112. Arras, J., Paki, E., Roth, C., Radnik, J., Lucas, M. & Claus, P. How a supported metal is influenced by an ionic liquid: In-depth characterization of SCILL-type palladium catalysts and their hydrogen adsorption. *J. Phys. Chem. C* **114**, 10520–10526 (2010).
113. Arras, J., Steffan, M., Shayeghi, Y., Ruppert, D. & Claus, P. Regioselective catalytic hydrogenation of citral with ionic liquids as reaction modifiers. *Green Chem.* **11**, 716–72 (2009).
114. Miller, S. F., Friedrich, H. B. & Holzappel, C. W. The Effects of SCILL Catalyst Modification on the Competitive Hydrogenation of 1-Octyne and 1,7-Octadiene versus 1-Octene. *ChemCatChem* **4**, 1337–1344 (2012).
115. Barth, T., Korth, W. & Jess, A. Selectivity-Enhancing Effect of a SCILL Catalyst in Butadiene Hydrogenation. *Chem. Eng. Technol.* **40**, 395–404 (2017).
116. Xin, B. & Hao, J. Imidazolium-based ionic liquids grafted on solid surfaces. *Chem. Soc. Rev.* **43**, 7171–7187 (2014).
117. Mehnert, C. P., Cook, R. A., Dispenziere, N. C. & Afeworki, M. Supported ionic liquid catalysis - A new concept for homogeneous hydroformylation catalysis. *J. Am. Chem. Soc.* **124**, 12932–12933 (2002).
118. Fehrmann, R., Riisager, A. & Haumann, M. *Supported Ionic liquids fundamentals and application*. Wiley-VCH (2014).
119. Bordet, A., Moos, G., Welsh, C., Licence, P., Luska, K. L. & Leitner, W. Molecular Control of the Catalytic Properties of Rhodium Nanoparticles in Supported Ionic Liquid Phase (SILP) Systems. *ACS Catal.* **10**, 13904–13912 (2020).
120. Moos, G., Emondts, M., Bordet, A. & Leitner, W. Selective Hydrogenation and Hydrodeoxygenation of Aromatic Ketones to Cyclohexane Derivatives Using a Rh@SILP Catalyst. *Angew. Chemie - Int. Ed.* **59**, 11977–11983 (2020).
121. Abu-Reziq, R., Wang, D., Post, M. & Alper, H. Platinum nanoparticles supported on ionic liquid-modified magnetic nanoparticles: Selective hydrogenation catalysts. *Adv. Synth. Catal.* **349**, 2145–2150 (2007).
122. Luska, K. L., Julis, J., Stavitski, E., Zakharov, D. N., Adams, A. & Leitner, W. Bifunctional nanoparticle-SILP catalysts (NPs@SILP) for the selective deoxygenation of biomass substrates. *Chem. Sci.* **5**, 4895–4905 (2014).
123. Offner-Marko, L., Bordet, A., Moos, G., Tricard, S., Rengshausen, S., Chaudret, B., Luska, K. L. & Leitner, W. Bimetallic Nanoparticles in Supported Ionic Liquid Phases as Multifunctional Catalysts for the Selective Hydrodeoxygenation of Aromatic Substrates. *Angew. Chemie - Int. Ed.* **57**, 12721–12726 (2018).

-
124. Liu, Y., Guo, H., Yu, M., Shen, C. & Xu, A.-W. Structure-Dependent Surface Molecule-Modified Semiconductor Photocatalysts: Recent Progress and Future Challenges. *ACS Sustain. Chem. Eng.* **10**, 16476–16502 (2022).
125. Gao, C., Wang, J., Xu, H. & Xiong, Y. Coordination chemistry in the design of heterogeneous photocatalysts. *Chem. Soc. Rev.* **46**, 2799–2823 (2017).
126. Ibrahim, M., Wei, M. M., Deydier, E., Manoury, E., Poli, R., Lecante, P. & Philippot, K. Rhodium nanoparticles stabilized by ferrocenyl-phosphine ligands: Synthesis and catalytic styrene hydrogenation. *Dalt. Trans.* **48**, 6777–6786 (2019).
127. Robson, J. A., González De Rivera, F., Jantan, K. A., Wenzel, M. N., White, A. J. P., Rossell, O. & Wilton-Ely, J. D. E. T. Bifunctional Chalcogen Linkers for the Stepwise Generation of Multimetallic Assemblies and Functionalized Nanoparticles. *Inorg. Chem.* **55**, 12982–12996 (2016).
128. Friederici, M., Angurell, I., Rossell, O., Seco, M., Divins, N. J. & Llorca, J. Facile synthesis of palladium nanoparticles protected with alkanethiolates functionalized with organometallic fragments. *Organometallics* **31**, 722–728 (2012).
129. Bonomi, R., Selvestrel, F., Lombardo, V., Sissi, C., Polizzi, S., Mancin, F., Tonellato, U. & Scrimin, P. Phosphate diester and DNA hydrolysis by a multivalent, nanoparticle-based catalyst. *J. Am. Chem. Soc.* **130**, 15744–15745 (2008).
130. Sheet, D., Halder, P. & Paine, T. K. Enhanced reactivity of a biomimetic iron(II) α -keto acid complex through immobilization on functionalized gold nanoparticles. *Angew. Chemie - Int. Ed.* **52**, 13314–13318 (2013).
131. Materna, K. L., Crabtree, R. H. & Brudvig, G. W. Anchoring groups for photocatalytic water oxidation on metal oxide surfaces. *Chem. Soc. Rev.* 5–7 (2017) doi:10.1039/C7CS00314E.
132. Alea-Reyes, M. E., Soriano, J., Mora-Espí, I., Rodrigues, M., Russell, D. A., Barrios, L. & Pérez-García, L. Amphiphilic gemini pyridinium-mediated incorporation of Zn(II)meso-tetrakis(4-carboxyphenyl)porphyrin into water-soluble gold nanoparticles for photodynamic therapy. *Colloids Surfaces B Biointerfaces* **158**, 602–609 (2017).
133. Arcudi, F., Đorđević, L., Nagasing, B., Stupp, S. I. & Weiss, E. A. Quantum Dot-Sensitized Photoreduction of CO₂ in Water with Turnover Number > 80,000. *J. Am. Chem. Soc.* **143**, 18131–18138 (2021).
134. Mayer, C. R., Dumas, E. & Sécheresse, F. Size controlled formation of silver nanoparticles by direct bonding of ruthenium complexes bearing a terminal mono- or bi-pyridyl group. *Chem. Commun.* 345–347 (2005) doi:10.1039/b415309j.
135. Mayer, C. R., Dumas, E., Miomandre, F., Méallet-Renault, R., Warmont, F., Vigneron, J., Pansu, R., Etcheberry, A. & Sécheresse, F. Polypyridyl ruthenium complexes as coating agent for the formation of gold and silver nanocomposites in different media. Preliminary luminescence and electrochemical studies. *New J. Chem.* **30**, 1628–1637 (2006).
136. Martín Morales, E., Coppel, Y., Lecante, P., Del Rosal, I., Poteau, R., Esvan, J., Sutra, P., Philippot, K. & Igau, A. When organophosphorus ruthenium complexes covalently bind to ruthenium nanoparticles to form nanoscale hybrid materials. *Chem. Commun.* **56**, 4059–4062 (2020).
137. Zhang, X., Li, D. & Zhou, X. P. From large 3D assembly to highly dispersed spherical assembly: Weak and strong coordination mediated self-aggregation of Au colloids. *New J. Chem.* **30**, 706–711 (2006).
138. Zhu, L., Xue, D. & Wang, Z. Metallic cation induced one-dimensional assembly of poly(acrylic acid)-1-dodecanethiol-stabilized gold nanoparticles. *Langmuir* **24**, 11385–11389 (2008).
139. Rao, A., Roy, S., Unnikrishnan, M., Bhosale, S. S., Devatha, G. & Pillai, P. P. Regulation of Interparticle Forces Reveals Controlled Aggregation in Charged Nanoparticles. *Chem. Mater.* **28**, 2348–2355 (2016).
140. Su, J., Huang, X. & Yang, M. Self-Limiting Assembly of Au Nanoparticles Induced by Localized Dynamic Metal-Phenolic Interactions. *Eur. J. Inorg. Chem.* **2020**, 4477–4482 (2020).
141. Liu, D., Chen, W., Sun, K., Deng, K., Zhang, W., Wang, Z. & Jiang, X. Resettable, multi-readout logic gates based on controllably reversible aggregation of gold nanoparticles. *Angew. Chemie - Int. Ed.* **50**, 4103–4107 (2011).
142. Wang, J., Peled, T. S. & Klajn, R. Photocleavable Anionic Glues for Light-Responsive Nanoparticle Aggregates. *J. Am. Chem. Soc.* (2022) doi:10.1021/jacs.2c11973.
143. Goodeve, C. F. & Kitchener, J. A. The mechanism of photosensitisation by solids. *Trans. Faraday Soc.* **34**, 902 (1938).

144. Ben-Shahar, Y., Stone, D. & Banin, U. Rich Landscape of Colloidal Semiconductor-Metal Hybrid Nanostructures: Synthesis, Synergetic Characteristics, and Emerging Applications. *Chem. Rev.* **123**, 3790–3851 (2023).
145. Maeda, K. & Domen, K. Photocatalytic water splitting: Recent progress and future challenges. *J. Phys. Chem. Lett.* **1**, 2655–2661 (2010).
146. GERISCHER, H. Electrochemical Techniques for the Study of Photosensitization. *Photochem. Photobiol.* **16**, 243–260 (1972).
147. Maeda, K., Sahara, G., Eguchi, M. & Ishitani, O. Hybrids of a ruthenium(II) polypyridyl complex and a metal oxide nanosheet for dye-sensitized hydrogen evolution with visible light: Effects of the energy structure on photocatalytic activity. *ACS Catal.* **5**, 1700–1707 (2015).
148. Li, S., Wijethunga, U. K., Davis, A. H., Kim, S., Zheng, W., Sherman, B. D., Yoo, C. G. & Leem, G. Ru(II) Polypyridyl-Modified TiO₂ Nanoparticles for Photocatalytic C–C/C–O Bond Cleavage at Room Temperature. *ACS Appl. Nano Mater.* **5**, 948–956 (2022).
149. Romero, N., Guerra, R. B., Gil, L., Drouet, S., Salmeron-Sánchez, I., Illa, O., Philippot, K., Natali, M., García-Antón, J. & Sala, X. TiO₂-mediated visible-light-driven hydrogen evolution by ligand-capped Ru nanoparticles. *Sustain. Energy Fuels* **4**, 4170–4178 (2020).
150. De Tovar, J., Romero, N., Denisov, S. A., Bofill, R., Gimbert-Suriñach, C., Ciuculescu-Pradines, D., Drouet, S., Llobet, A., Lecante, P., Colliere, V., Freixa, Z., McClenaghan, N., Amiens, C., García-Antón, J., Philippot, K. & Sala, X. Light-driven water oxidation using hybrid photosensitizer-decorated Co₃O₄ nanoparticles. *Mater. Today Energy* **9**, 506–515 (2018).
151. Song, L., Liu, X., Xie, Z., Luo, F. & Song, H. Synthesis and Structural Characterization of Some New Porphyrin-Fullerene Dyads and Their Application in Photoinduced H₂ Evolution. **12**, 11162–11172 (2011).
152. Zhu, M., Lu, Y., Du, Y., Li, J., Wang, X. & Yang, P. Photocatalytic hydrogen evolution without an electron mediator using a porphyrin e pyrene conjugate functionalized Pt nanocomposite as a photocatalyst. *Int. J. Hydrogen Energy* **36**, 4298–4304 (2011).
153. Zhu, M., Dong, Y., Du, Y., Mou, Z. & Liu, J. Photocatalytic Hydrogen Evolution Based on Efficient Energy and Electron Transfers in Donor – Bridge – Acceptor Multibranching-Porphyrin-. *Chem. Eur. J* 4367–4374 (2012) doi:10.1002/chem.201102595.
154. Nikolaou, V., Charalambidis, G., Landrou, G., Nikoloudakis, E., Tsalameni, R., Junghans, K., Kahnt, A., Odobel, F. & Coutsolelos, A. G. Antenna Effect in BODIPY-(Zn)Porphyrin Entities Promotes H₂ Evolution in Dye-Sensitized Photocatalytic Systems. (2021) doi:10.1021/acsaem.1c01975.
155. Wang, L., Duan, S., Jin, P., She, H., Huang, J., Lei, Z., Zhang, T. & Wang, Q. Anchored Cu(II) tetra(4-carboxylphenyl)porphyrin to P25 (TiO₂) for efficient photocatalytic ability in CO₂ reduction. *Appl. Catal. B Environ.* **239**, 599–608 (2018).
156. Kuriki, R., Matsunaga, H., Nakashima, T., Wada, K., Yamakata, A., Ishitani, O. & Maeda, K. Nature-Inspired, Highly Durable CO₂ Reduction System Consisting of a Binuclear Ruthenium(II) Complex and an Organic Semiconductor Using Visible Light. *JACS* **138**, 5159–5170 (2016).
157. Kuehnel, M. F., Orchard, K. L., Dalle, K. E. & Reisner, E. Selective Photocatalytic CO₂ Reduction in Water through Anchoring of a Molecular Ni Catalyst on CdS Nanocrystals. *JACS* **139**, 7217–7223 (2017).
158. Huang, J., Mulfort, K. L., Du, P. & Chen, L. X. Photodriven charge separation dynamics in CdSe/ZnS core/shell quantum dot/cobaloxime hybrid for efficient hydrogen production. *J. Am. Chem. Soc.* **134**, 16472–16475 (2012).
159. Li, X., Lei, H., Liu, J., Zhao, X., Ding, S., Zhang, Z., Tao, X., Zhang, W., Wang, W., Zheng, X. & Cao, R. Carbon Nanotubes with Cobalt Corroles for Hydrogen and Oxygen Evolution in pH 0–14 Solutions. *Angew. Chemie - Int. Ed.* **57**, 15070–15075 (2018).
160. Hijazi, I., Bourgeteau, T., Cornut, R., Morozan, A., Filoramo, A., Leroy, J., Derycke, V., Jusselme, B. & Campidelli, S. Carbon nanotube-templated synthesis of covalent porphyrin network for oxygen reduction reaction. *J. Am. Chem. Soc.* **136**, 6348–6354 (2014).
161. Belser, T., Stöhr, M. & Pfaltz, A. Immobilization of rhodium complexes at thiolate monolayers on gold surfaces: Catalytic and structural studies. *J. Am. Chem. Soc.* **127**, 8720–8731 (2005).
162. Ono, F., Kanemasa, S. & Tanaka, J. Reusable nano-sized chiral bisoxazoline catalysts. *Tetrahedron Lett.* **46**, 7623–7626 (2005).

163. Belser, T. & Jacobsen, E. N. Cooperative Catalysis in the Hydrolytic Kinetic Resolution of Epoxides by Chiral [(salen)Co(III)] Complexes Immobilized on Gold Colloids. *Adv. Synth. Catal.* **350**, 967–971 (2008).
164. Kalsi, D., Louis Anandaraj, S. J., Durai, M., Weidenthaler, C., Emondts, M., Nolan, S. P., Bordet, A. & Leitner, W. One-Pot Multicomponent Synthesis of Allyl and Alkylamines Using a Catalytic System Composed of Ruthenium Nanoparticles on Copper N-Heterocyclic Carbene-Modified Silica. *ACS Catal.* **12**, 14902–14910 (2022).
165. Bailón-García, E., Maldonado-Hódar, F. J., Pérez-Cadenas, A. F. & Carrasco-Marín, F. Catalysts supported on carbon materials for the selective hydrogenation of citral. *Catalysts* **3**, 853–877 (2013).
166. Concepción, P., Corma, A., Silvestre-Albero, J., Franco, V. & Chane-Ching, J. Y. Chemoselective Hydrogenation Catalysts: Pt on Mesostructured CeO₂ Nanoparticles Embedded within Ultrathin Layers of SiO₂ Binder. *J. Am. Chem. Soc.* **126**, 5523–5532 (2004).
167. Kennedy, G., Baker, L. R. & Somorjai, G. A. Selective amplification of C=O bond hydrogenation on Pt/TiO₂: Catalytic reaction and sum-frequency generation vibrational spectroscopy studies of crotonaldehyde hydrogenation. *Angew. Chemie - Int. Ed.* **53**, 3405–3408 (2014).
168. Wei, S., Zhao, Y., Fan, G., Yang, L. & Li, F. Structure-dependent selective hydrogenation of cinnamaldehyde over high-surface-area CeO₂-ZrO₂ composites supported Pt nanoparticles. *Chem. Eng. J.* **322**, 234–245 (2017).
169. Jia, A., Zhang, Y., Song, T., Zhang, Z., Tang, C., Hu, Y., Zheng, W., Luo, M., Lu, J. & Huang, W. Crystal-plane effects of anatase TiO₂ on the selective hydrogenation of crotonaldehyde over Ir/TiO₂ catalysts. *J. Catal.* **395**, 10–22 (2021).
170. Stassi, J. P., Zgolicz, P. D., De Miguel, S. R. & Scelza, O. A. Formation of different promoted metallic phases in PtFe and PtSn catalysts supported on carbonaceous materials used for selective hydrogenation. *J. Catal.* **306**, 11–29 (2013).
171. Wang, G., Xin, H., Wang, Q., Wu, P. & Li, X. Efficient liquid-phase hydrogenation of cinnamaldehyde to cinnamyl alcohol with a robust PtFe/HPZSM-5 catalyst. *J. Catal.* **382**, 1–12 (2020).
172. Luneau, M., Lim, J. S., Patel, D. A., Sykes, E. C. H., Friend, C. M. & Sautet, P. Guidelines to Achieving High Selectivity for the Hydrogenation of α,β -Unsaturated Aldehydes with Bimetallic and Dilute Alloy Catalysts: A Review. *Chem. Rev.* **120**, 12834–12872 (2020).
173. Guo, Z., Xiao, C., Maligal-Ganesh, R. V., Zhou, L., Goh, T. W., Li, X., Tesfagaber, D., Thiel, A. & Huang, W. Pt nanoclusters confined within metal-organic framework cavities for chemoselective cinnamaldehyde hydrogenation. *ACS Catal.* **4**, 1340–1348 (2014).
174. Yuan, K., Song, T., Wang, D., Zhang, X., Gao, X., Zou, Y., Dong, H., Tang, Z. & Hu, W. Effective and Selective Catalysts for Cinnamaldehyde Hydrogenation: Hydrophobic Hybrids of Metal–Organic Frameworks, Metal Nanoparticles, and Micro- and Mesoporous Polymers. *Angew. Chemie - Int. Ed.* **57**, 5708–5713 (2018).
175. Liu, C., Zhu, P., Wang, J., Liu, H. & Zhang, X. Geometrically embedding dispersive Pt nanoparticles within silicalite-1 framework for highly selective α, β -unsaturated aldehydes hydrogenation via oriented C = O adsorption configuration. *Chem. Eng. J.* **446**, 137064 (2022).
176. Zhao, M., Yuan, K., Wang, Y., Li, G., Guo, J., Gu, L., Hu, W., Zhao, H. & Tang, Z. Metal-organic frameworks as selectivity regulators for hydrogenation reactions. *Nature* **539**, 76–80 (2016).
177. Vu, K. B., Bukhryakov, K. V., Anjum, D. H. & Rodionov, V. O. Surface-Bound Ligands Modulate Chemoselectivity and Activity of a Bimetallic Nanoparticle Catalyst. *ACS Catal.* **5**, 2529–2533 (2015).
178. Liu, J., Mendoza, S., Román, E., Lynn, M. J., Xu, R. & Kaifer, A. E. Cyclodextrin-Modified Gold Nanospheres. Host–Guest Interactions at Work to Control Colloidal Properties. *J. Am. Chem. Soc.* **121**, 4304–4305 (1999).
179. Liu, J., Ong, W., Román, E., Lynn, M. J. & Kaifer, A. E. Cyclodextrin-modified gold nanospheres. *Langmuir* **16**, 3000–3002 (2000).
180. Alvarez, J., Liu, J., Román, E. & Kaifer, A. E. Water-soluble platinum and palladium nanoparticles modified with thiolated β -cyclodextrin. *Chem. Commun.* 1151–1152 (2000) doi:10.1039/b002423f.
181. Strimbu, L., Liu, J. & Kaifer, A. E. Cyclodextrin-Capped Palladium Nanoparticles as Catalysts for the Suzuki Reaction. *Langmuir* **19**, 483–485 (2003).
182. Xue, C., Palaniappan, K., Arumugam, G., Hackney, S. A., Liu, J. & Liu, H. Sonogashira reactions catalyzed by water-soluble, β -cyclodextrin-capped palladium nanoparticles. *Catal. Letters* **116**, 94–100 (2007).

183. Mhadgut, S. C., Palaniappan, K., Thimmaiah, M., Hackney, S. A., Török, B. & Liu, J. A metal nanoparticle-based supramolecular approach for aqueous biphasic reactions. *Chem. Commun.* 3207–3209 (2005) doi:10.1039/b502181b.
184. Perl, A., Kumprecht, L., Kraus, T., Armspach, D., Matt, D., Reinhoudt, D. N. & Huskens, J. Self-assembled monolayers of α -cyclodextrin derivatives on gold and their host-guest behavior. *Langmuir* **25**, 1534–1539 (2009).
185. Kumprecht, L., Buděšínský, M., Bouř, P. & Kraus, T. α -Cyclodextrins reversibly capped with disulfide bonds. *New J. Chem.* **34**, 2254–2260 (2010).
186. López-Vinasco, A. M., Martínez-Prieto, L. M., Asensio, J. M., Lecante, P., Chaudret, B., Cámpora, J. & Van Leeuwen, P. W. N. M. Novel nickel nanoparticles stabilized by imidazolium-amidinate ligands for selective hydrogenation of alkynes. *Catal. Sci. Technol.* **10**, 342–350 (2020).
187. Yang, L., Yu, S., Peng, C., Fang, X., Cheng, Z. & Zhou, Z. Semihydrogenation of phenylacetylene over nonprecious Ni-based catalysts supported on AISBA-15. *J. Catal.* **370**, 310–320 (2019).
188. Wand, P., Kratzer, E., Heiz, U., Cokoja, M. & Tschurl, M. High stability of thiol-protected colloidal platinum nanoparticles with reduced ligand coverages in the hydrogenation of 3-hexyne. *Catal. Commun.* **100**, 85–88 (2017).
189. Min, Y., Nasrallah, H., Poinot, D., Lecante, P., Tison, Y., Martinez, H., Roblin, P., Falqui, A., Poteau, R., Del Rosal, I., Gerber, I. C., Hierso, J.-C., Axet, M. R. & Serp, P. 3D Ruthenium Nanoparticle Covalent Assemblies from Polymantane Ligands for Confined Catalysis. *Chem. Mater.* **32**, 2365–2378 (2020).
190. Gillet, A., Cher, S., Tassé, M., Blon, T., Alves, S., Izzet, G., Chaudret, B., Proust, A., Demont, P., Volatron, F. & Tricard, S. Polarizability is a key parameter for molecular electronics. *Nanoscale Horizons* **6**, 271–276 (2021).
191. Aleksandrov, H. A., Neyman, K. M., Hadjiivanov, K. I. & Vayssilov, G. N. Can the state of platinum species be unambiguously determined by the stretching frequency of an adsorbed CO probe molecule? *Phys. Chem. Chem. Phys.* **18**, 22108–22121 (2016).
192. Sisodiya-Amrute, S., Van Stappen, C., Rengshausen, S., Han, C., Sodreau, A., Weidenthaler, C., Tricard, S., DeBeer, S., Chaudret, B., Bordet, A. & Leitner, W. Bimetallic MxRu100-x nanoparticles (M = Fe, Co) on supported ionic liquid phases (MxRu100-x@SILP) as hydrogenation catalysts: Influence of M and M:Ru ratio on activity and selectivity. *J. Catal.* **407**, 141–148 (2022).
193. Sadrerafi, K., Moore, E. E. & Lee, M. W. Association constant of β -cyclodextrin with carboranes, adamantane, and their derivatives using displacement binding technique. *J. Incl. Phenom. Macrocycl. Chem.* **83**, 159–166 (2015).
194. Manai, G., Houimel, H., Rigoulet, M., Gillet, A., Fazzini, P. F., Ibarra, A., Balor, S., Roblin, P., Esvan, J., Coppel, Y., Chaudret, B., Bonduelle, C. & Tricard, S. Bidimensional lamellar assembly by coordination of peptidic homopolymers to platinum nanoparticles. *Nat. Commun.* **11**, 1–7 (2020).
195. Zhao, D., Xie, S., Wang, Y., Zhu, H., Chen, L., Sun, Q. & Zhang, D. W. Synthesis of large-scale few-layer PtS₂ films by chemical vapor deposition. *AIP Adv.* **9**, (2019).
196. Marinkovic, N. S., Sasaki, K. & Adzic, R. R. Determination of Single- and Multi-Component Nanoparticle Sizes by X-ray Absorption Spectroscopy. *J. Electrochem. Soc.* **165**, J3222–J3230 (2018).
197. Benfield, R. E. Mean coordination numbers and the non-metal-metal transition in clusters. *J. Chem. Soc. Faraday Trans.* **88**, 1107–1110 (1992).
198. Gallen, A., Riera, A., Verdaguer, X. & Grabulosa, A. Coordination chemistry and catalysis with secondary phosphine oxides. *Catal. Sci. Technol.* **9**, 5504–5561 (2019).
199. van Leeuwen, P. W. N. M., Cano, I. & Freixa, Z. Secondary Phosphine Oxides: Bifunctional Ligands in Catalysis. *ChemCatChem* **12**, 3982–3994 (2020).
200. Bigeault, J., Giordano, L., De Raggi, I., Gimbert, Y. & Buono, G. Platinum(II)-coordinated phosphinous acid-catalyzed alkylidenecyclopropanation of bicyclic alkenes with terminal alkynes. *Org. Lett.* **9**, 3567–3570 (2007).
201. Achard, T., Giordano, L., Tenaglia, A., Gimbert, Y. & Buono, G. Steric control in the synthesis of phosphinous acid-coordinated mono- and binuclear platinum(II) complexes. *Organometallics* **29**, 3936–3950 (2010).
202. Baquero, E. A., Tricard, S., Flores, J. C., De Jesffls, E. & Chaudret, B. Highly stable water-soluble platinum nanoparticles stabilized by hydrophilic N-heterocyclic carbenes. *Angew. Chemie - Int. Ed.* **53**, 13220–13224

(2014).

203. Anand, S., Pinheiro, D. & Sunaja Devi, K. R. Recent Advances in Hydrogenation Reactions Using Bimetallic Nanocatalysts: A Review. *Asian J. Org. Chem.* **10**, 3068–3100 (2021).
204. Liu, L. & Corma, A. Bimetallic Sites for Catalysis: From Binuclear Metal Sites to Bimetallic Nanoclusters and Nanoparticles. *Chem. Rev.* (2023) doi:10.1021/acs.chemrev.2c00733.
205. Asensio, J. M., Miguel, A. B., Fazzini, P., van Leeuwen, P. W. N. M. & Chaudret, B. Hydrodeoxygenation Using Magnetic Induction: High-Temperature Heterogeneous Catalysis in Solution. *Angew. Chemie* 11428–11432 (2019) doi:10.1002/ange.201904366.
206. Rengshausen, S., Van Stappen, C., Levin, N., Tricard, S., Luska, K. L., DeBeer, S., Chaudret, B., Bordet, A. & Leitner, W. Organometallic Synthesis of Bimetallic Cobalt-Rhodium Nanoparticles in Supported Ionic Liquid Phases (CoxRh100-x@SILP) as Catalysts for the Selective Hydrogenation of Multifunctional Aromatic Substrates. *Small* **17**, 1–10 (2021).
207. Goclik, L., Offner-Marko, L., Bordet, A. & Leitner, W. Selective hydrodeoxygenation of hydroxyacetophenones to ethyl-substituted phenol derivatives using a FeRu@SILP catalyst. *Chem. Commun.* **56**, 9509–9512 (2020).
208. Yu, W., Porosoff, M. D. & Chen, J. G. Review of Pt-Based Bimetallic Catalysis: From Model Surfaces to Supported Catalysts. *Chem. Rev.* **112**, 5780–5817 (2012).
209. Shao, Q., Wang, P., Zhu, T. & Huang, X. Low Dimensional Platinum-Based Bimetallic Nanostructures for Advanced Catalysis. *Acc. Chem. Res.* **52**, 3384–3396 (2019).
210. Jiang, Z., Wan, W., Lin, Z., Xie, J. & Chen, J. G. Understanding the Role of M / Pt (111) (M = Fe , Co , Ni , Cu) Bimetallic Surfaces for Selective Hydrodeoxygenation of Furfural Understanding the Role of M / Pt (111) (M = Fe , Co , Ni , Cu) Bimetallic Surfaces for Selective Hydrodeoxygenation of . (2017) doi:10.1021/acscatal.7b01682.
211. Gong, X., Shi, Q., Zhang, X., Li, J., Ping, G., Xu, H., Ding, H. & Li, G. Synergistic effects of PtFe/CeO₂ catalyst afford high catalytic performance in selective hydrogenation of cinnamaldehyde. *J. Rare Earths* (2022) doi:10.1016/j.jre.2022.02.010.
212. Zhang, Y., Su, J., Chen, J., Dai, C. & Zhang, B. Insight into the role of iron in platinum-based bimetallic catalysts for selective hydrogenation of cinnamaldehyde. *Chinese Chem. Lett.* **33**, 3757–3761 (2022).
213. Ning, L., Zhang, M., Liao, S., Zhang, Y., Jia, D., Yan, Y., Gu, W. & Liu, X. Differentiation of Pt–Fe and Pt–Ni₃ Surface Catalytic Mechanisms towards Contrasting Products in Chemoselective Hydrogenation of α,β -Unsaturated Aldehydes. *ChemCatChem* **13**, 704–711 (2021).
214. Zhang, W., Xin, H., Zhang, Y., Jin, X., Wu, P., Xie, W. & Li, X. Bimetallic Pt-Fe catalysts supported on mesoporous TS-1 microspheres for the liquid-phase selective hydrogenation of cinnamaldehyde. *J. Catal.* **395**, 375–386 (2021).
215. Siani, A., Alexeev, O. S., Lafaye, G. & Amiridis, M. D. The effect of Fe on SiO₂-supported Pt catalysts: Structure, chemisorptive, and catalytic properties. *J. Catal.* **266**, 26–38 (2009).
216. Zanuttini, M. S., Gross, M., Marchetti, G. & Querini, C. Furfural hydrodeoxygenation on iron and platinum catalysts. *Appl. Catal. A Gen.* **587**, 117217 (2019).
217. Gao, X., Tian, S., Jin, Y., Wan, X., Zhou, C., Chen, R., Dai, Y. & Yang, Y. Bimetallic PtFe-Catalyzed Selective Hydrogenation of Furfural to Furfuryl Alcohol: Solvent Effect of Isopropanol and Hydrogen Activation. *ACS Sustain. Chem. Eng.* **8**, 12722–12730 (2020).
218. Geng, Y., Chen, C., Gao, Z., Feng, X., Liu, W., Li, Y., Jin, T., Shi, Y., Zhang, W. & Bao, M. Unsupported Nanoporous Platinum-Iron Bimetallic Catalyst for the Chemoselective Hydrogenation of Halonitrobenzenes to Haloanilines. *ACS Appl. Mater. Interfaces* **13**, 23655–23661 (2021).
219. Wang, Y., Qin, R., Wang, Y., Ren, J., Zhou, W., Li, L., Ming, J., Zhang, W., Fu, G. & Zheng, N. Chemoselective Hydrogenation of Nitroaromatics at the Nanoscale Iron(III)–OH–Platinum Interface. *Angew. Chemie - Int. Ed.* **59**, 12736–12740 (2020).
220. Guo, S., Li, D., Zhu, H., Zhang, S., Markovic, N. M., Stamenkovic, V. R. & Sun, S. FePt and CoPt nanowires as efficient catalysts for the oxygen reduction reaction. *Angew. Chemie - Int. Ed.* **52**, 3465–3468 (2013).
221. Pousthomis, M., Garnero, C., Marcelot, C. G., Blon, T., Cayez, S., Cassagnol, C., Du, V. A., Krispin, M., Arenal, R., Soulantica, K., Viau, G. & Lacroix, L. M. On the advantages of spring magnets compared to pure FePt: Strategy for rare-earth free permanent magnets following a bottom-up approach. *J. Magn. Magn. Mater.* **424**, 304–313

- (2017).
222. Schladt, T. D., Graf, T., Köhler, O., Bauer, H., Dietzsch, M., Mertins, J., Branscheid, R., Kolb, U. & Tremel, W. Synthesis and Magnetic Properties of FePt@MnO Nano-heteroparticles. *Chem. Mater.* **24**, 525–535 (2012).
223. Kim, J., Rong, C., Ping Liu, J. & Sun, S. Dispersible ferromagnetic FePt nanoparticles. *Adv. Mater.* **21**, 906–909 (2009).
224. Bai, S., Bu, L., Shao, Q., Zhu, X. & Huang, X. Multicomponent Pt-Based Zigzag Nanowires as Selectivity Controllers for Selective Hydrogenation Reactions. *J. Am. Chem. Soc.* **140**, 8384–8387 (2018).
225. Luska, K. L., Bordet, A., Tricard, S., Sinev, I., Grünert, W., Chaudret, B. & Leitner, W. Enhancing the Catalytic Properties of Ruthenium Nanoparticle-SILP Catalysts by Dilution with Iron. *ACS Catal.* **6**, 3719–3726 (2016).
226. Goclik, L., Walschus, H., Bordet, A. & Leitner, W. Selective hydrodeoxygenation of acetophenone derivatives using a Fe 25 Ru 75 @SILP catalyst: a practical approach to the synthesis of alkyl phenols and anilines. *Green Chem.* **24**, 2937–2945 (2022).
227. Elgayyar, T., Atwi, R., Tuel, A. & Meunier, F. C. Contributions and limitations of IR spectroscopy of CO adsorption to the characterization of bimetallic and nanoalloy catalysts. *Catal. Today* **373**, 59–68 (2021).
228. Seenivasan, K., Gallo, E., Piovano, A., Vitillo, J. G., Sommazzi, A., Bordiga, S., Lamberti, C., Glatzel, P. & Groppo, E. Silica-supported Ti chloride tetrahydrofuranates, precursors of Ziegler-Natta catalysts. *Dalt. Trans.* **42**, 12706–12713 (2013).
229. Siani, A., Alexeev, O. S., Captain, B., Lafaye, G., Marécot, P., Adams, R. D. & Amiridis, M. D. Synthesis of cluster-derived PtFe/SiO₂ catalysts for the oxidation of CO. *J. Catal.* **255**, 162–179 (2008).
230. Gao, X., Tian, S., Jin, Y., Wan, X., Zhou, C., Chen, R., Dai, Y., Yang, Y., Tian, S., Jin, Y., Wan, X., Zhou, C., Chen, R., Dai, Y. & Yang, Y. Bimetallic PtFe-Catalyzed Selective Hydrogenation of Furfural to Furfuryl Alcohol: Solvent Effect of Isopropanol and Hydrogen Activation. (2020) doi:10.1021/acssuschemeng.0c04891.
231. Nguyen, T. S., Laurenti, D., Afanasiev, P., Konuspayeva, Z. & Piccolo, L. Titania-supported gold-based nanoparticles efficiently catalyze the hydrodeoxygenation of guaiacol. *J. Catal.* **344**, 136–140 (2016).
232. Sakoda, K., Yamaguchi, S., Mitsudome, T. & Mizugaki, T. Selective Hydrodeoxygenation of Esters to Unsymmetrical Ethers over a Zirconium Oxide-Supported Pt-Mo Catalyst. *J. Am. Chem. Soc.* **2**, 665–672 (2022).
233. Shimizu, K. I., Onodera, W., Touchy, A. S., Siddiki, S. M. A. H., Toyao, T. & Kon, K. Lewis Acid-Promoted Heterogeneous Platinum Catalysts for Hydrogenation of Amides to Amines. *ChemistrySelect* **1**, 736–740 (2016).
234. Jin, X., Tsukimura, R., Aihara, T., Miura, H., Shishido, T. & Nozaki, K. Metal-support cooperation in Al(PO₃)₃-supported platinum nanoparticles for the selective hydrogenolysis of phenols to arenes. *Nat. Catal.* **4**, 312–321 (2021).
235. Luska, K. L., Migowski, P., El Sayed, S. & Leitner, W. Bifunctional ruthenium nanoparticle-SILP catalysts (RuNPs@SILP) for the hydrodeoxygenation of eucalyptol under batch and continuous flow conditions. *ACS Sustain. Chem. Eng.* **4**, 6186–6192 (2016).
236. Bordet, A., Moos, G., Welsh, C., Licence, P., Luska, K. L. & Leitner, W. Molecular Control of the Catalytic Properties of Rhodium Nanoparticles in Supported Ionic Liquid Phase (SILP) Systems. *ACS Catal.* **10**, 13904–13912 (2020).
237. Mitsudome, T., Miyagawa, K., Maeno, Z., Mizugaki, T., Jitsukawa, K., Yamasaki, J., Kitagawa, Y. & Kaneda, K. Mild Hydrogenation of Amides to Amines over a Platinum-Vanadium Bimetallic Catalyst. *Angew. Chemie - Int. Ed.* **56**, 9381–9385 (2017).
238. Surburg, H. & Panten, J. *Common fragrance and flavor materials. Phytochemistry* (VCH Weinheim, 2006). doi:10.1002/3527608214.
239. Chen, W. & Viljoen, A. M. Geraniol - A review of a commercially important fragrance material. *South African J. Bot.* **76**, 643–651 (2010).
240. Saudan, L. A. Hydrogenation processes in the synthesis of perfumery ingredients. *Acc. Chem. Res.* **40**, 1309–1319 (2007).
241. Weissmehl, K. & Arpe, H.-J. *Industrial organic chemistry.* (VCH Weinheim, 1997).
242. Neri, G., Arrigo, I., Corigliano, F., De Luca, L. & Donato, A. Selective hydrogenation of cinnamaldehyde on Pt and Pt-Fe catalysts supported on zeolite P. *Catal. Letters* **141**, 1590–1597 (2011).

-
243. Dai, Y., Gao, X., Chu, X., Jiang, C., Yao, Y., Guo, Z., Zhou, C., Wang, C., Wang, H. & Yang, Y. On the role of water in selective hydrogenation of cinnamaldehyde to cinnamyl alcohol on PtFe catalysts. *J. Catal.* **364**, 192–203 (2018).
244. Lan, X. & Wang, T. Highly Selective Catalysts for the Hydrogenation of Unsaturated Aldehydes: A Review. *ACS Catal.* **10**, 2764–2790 (2020).
245. Bai, S., Bu, L., Shao, Q., Zhu, X. & Huang, X. Multicomponent Pt-Based Zigzag Nanowires as Selectivity Controllers for Selective Hydrogenation Reactions. *J. Am. Chem. Soc.* **140**, 8384–8387 (2018).
246. Li, Y., Zhu, P. F. & Zhou, R. X. Selective hydrogenation of cinnamaldehyde to cinnamyl alcohol with carbon nanotubes supported Pt-Co catalysts. *Appl. Surf. Sci.* **254**, 2609–2614 (2008).
247. Xue, Y., Xin, H., Xie, W., Wu, P. & Li, X. Pt nanoparticles supported on $\text{YCo}_x\text{Fe}_{1-x}\text{O}_3$ perovskite oxides: Highly efficient catalysts for liquid-phase hydrogenation of cinnamaldehyde. *Chem. Commun.* **55**, 3363–3366 (2019).
248. Pan, H., Li, J., Lu, J., Wang, G., Xie, W., Wu, P. & Li, X. Selective hydrogenation of cinnamaldehyde with $\text{PtFe}_x/\text{Al}_2\text{O}_3@ \text{SBA-15}$ catalyst: Enhancement in activity and selectivity to unsaturated alcohol by Pt-FeO_x and Pt-Al₂O₃@SBA-15 interaction. *J. Catal.* **354**, 24–36 (2017).
249. Jess, A., Korth, W. & Etzold, B. United States Patent : 3871965 POROUS HETEROGENEOUS CATALYST COATED WITH AN IONIC LIQUID. (2012).
250. Cardona-Farreny, M., Lecante, P., Esvan, J., Dinoi, C., Del Rosal, I., Poteau, R., Philippot, K. & Axet, M. R. Bimetallic RuNi nanoparticles as catalysts for upgrading biomass: Metal dilution and solvent effects on selectivity shifts. *Green Chem.* **23**, 8480–8500 (2021).
251. Hájek, J., Kumar, N., Mäki-Arvela, P., Salmi, T., Murzin, D. Y., Paseka, I., Heikkilä, T., Laine, E., Laukkanen, P. & Väyrynen, J. Ruthenium-modified MCM-41 mesoporous molecular sieve and Y zeolite catalysts for selective hydrogenation of cinnamaldehyde. *Appl. Catal. A Gen.* **251**, 385–396 (2003).
252. Leng, F., Gerber, I. C., Axet, M. R. & Serp, P. Selectivity shifts in hydrogenation of cinnamaldehyde on electron-deficient ruthenium nanoparticles. *Comptes Rendus Chim.* **21**, 346–353 (2018).
253. Hidalgo-Carrillo, J., Aramendía, M. A., Marinas, A., Marinas, J. M. & Urbano, F. J. Support and solvent effects on the liquid-phase chemoselective hydrogenation of crotonaldehyde over Pt catalysts. *Appl. Catal. A Gen.* **385**, 190–200 (2010).
254. Lakowicz R., *J. Principles of Fluorescence Spectroscopy*. (Springer, 1999). doi:10.1007/BF02629943.
255. Zeng, J., Yang, W., Shi, D., Li, X., Zhang, H. & Chen, M. Porphyrin Derivative Conjugated with Gold Nanoparticles for Dual-Modality Photodynamic and Photothermal Therapies in Vitro. *ACS Biomater. Sci. Eng.* **4**, 963–972 (2018).
256. Mineo, P., Abbadessa, A., Mazzaglia, A., Gulino, A., Villari, V., Micali, N., Millesi, S., Satriano, C. & Scamporrino, E. Gold nanoparticles functionalized with PEGylate uncharged porphyrins. *Dye. Pigment.* **141**, 225–234 (2017).
257. Penon, O., Marín, M. J., Russell, D. A. & Pérez-García, L. Water soluble, multifunctional antibody-porphyrin gold nanoparticles for targeted photodynamic therapy. *J. Colloid Interface Sci.* **496**, 100–110 (2017).
258. Zhu, M., Du, Y., Yang, P. & Wang, X. Donor–acceptor porphyrin functionalized Pt nano-assemblies for artificial photosynthesis: a simple and efficient homogeneous photocatalytic hydrogen production system. *Catal. Sci. Technol.* **3**, 2295 (2013).
259. Usmani, S., Mikolasek, M., Gillet, A., Sanchez Costa, J., Rigoulet, M., Chaudret, B., Bousseksou, A., Lassalle-Kaiser, B., Demont, P., Molnár, G., Salmon, L., Carrey, J. & Tricard, S. Spin crossover in Fe(triazole)-Pt nanoparticle self-assembly structured at the sub-5 nm scale. *Nanoscale* **12**, 8180–8187 (2020).
260. Tricard, S., Said-Aizpuru, O., Bouzouita, D., Usmani, S., Gillet, A., Tassé, M., Poteau, R., Viau, G., Demont, P., Carrey, J. & Chaudret, B. Chemical tuning of Coulomb blockade at room-temperature in ultra-small platinum nanoparticle self-assemblies. *Mater. Horizons* **4**, 487–492 (2017).
261. Tricard, S. *Supraparticular chemistry oriented by chemical and physico-chemical methods*. (2019).
262. Nurhayati, Suendo, V., Alni, A., Nugroho, A. A., Majima, Y., Lee, S., Nugraha, Y. P. & Uekusa, H. Revealing the Real Size of a Porphyrin Molecule with Quantum Confinement Probing via Temperature-Dependent Photoluminescence Spectroscopy. *J. Phys. Chem. A* **124**, 2672–2682 (2020).
263. Zhong, Y., Wang, J., Zhang, R., Wei, W., Wang, H., Lü, X., Bai, F., Wu, H., Haddad, R. & Fan, H. Morphology-

- controlled self-assembly and synthesis of photocatalytic nanocrystals. *Nano Lett.* **14**, 7175–7179 (2014).
264. Bera, R., Chakraborty, S., Nayak, S. K., Jana, B. & Patra, A. Structural Insight and Ultrafast Dynamics of 2D Porphyrin Nanostructures. *J. Phys. Chem. C* (2019) doi:10.1021/acs.jpcc.9b03112.
265. Wang, J., Zhong, Y., Wang, L., Zhang, N., Cao, R., Bian, K., Alarid, L., Haddad, R. E., Bai, F. & Fan, H. Morphology-Controlled Synthesis and Metalation of Porphyrin Nanoparticles with Enhanced Photocatalytic Performance. *Nano Lett.* **16**, 6523–6528 (2016).
266. Jiang, Y. B. & Sun, Z. Self-Assembled porphyrin and macrocycle derivatives: From synthesis to function. *MRS Bull.* **44**, 167–171 (2019).
267. Yang, P., Arfaoui, I., Cren, T., Goubet, N. & Pileni, M. P. Electronic properties probed by scanning tunneling spectroscopy: From isolated gold nanocrystal to well-defined supracrystals. *Phys. Rev. B - Condens. Matter Mater. Phys.* **86**, 1–6 (2012).
268. Tan, R. P., Carrey, J., Desvaux, C., Lacroix, L. M., Renaud, P., Chaudret, B. & Respaud, M. Magnetoresistance and collective Coulomb blockade in superlattices of ferromagnetic CoFe nanoparticles. *Phys. Rev. B - Condens. Matter Mater. Phys.* **79**, 1–12 (2009).
269. Martínez-Calvo, M., Orange, K. N., Elmes, R. B. P., La Cour Poulsen, B., Williams, D. C. & Gunnlaugsson, T. Ru(II)-polypyridyl surface functionalised gold nanoparticles as DNA targeting supramolecular structures and luminescent cellular imaging agents. *Nanoscale* **8**, 563–574 (2016).
270. McAtee, R. C., McClain, E. J. & Stephenson, C. R. J. Illuminating Photoredox Catalysis. *Trends Chem.* **1**, 111–125 (2019).
271. Zhang, Y., Judkins, E. C., McMillin, D. R., Mehta, D. & Ren, T. Mesoporous silica-supported ruthenium oxide nanoparticulates as efficient catalysts for photoinduced water oxidation. *ACS Catal.* **3**, 2474–2478 (2013).
272. Lu, Y., Zhu, D., Le, Q., Wang, Y. & Wang, W. Ruthenium-based antitumor drugs and delivery systems from monotherapy to combination therapy. *Nanoscale* **14**, 16339–16375 (2022).
273. Moreau, J., Lux, F., Four, M., Olesiak-Banska, J., Matczyszyn, K., Perriat, P., Frochot, C., Arnoux, P., Tillement, O., Samoc, M., Ponterini, G., Roux, S. & Lemercier, G. A 5-(difluorenyl)-1,10-phenanthroline-based Ru(II) complex as a coating agent for potential multifunctional gold nanoparticles. *Phys. Chem. Chem. Phys.* **16**, 14826–14833 (2014).
274. Thi, T., Thoa, T., Minagawa, N., Aigaki, T. & Ito, Y. Regulation of photosensitisation processes by an RNA aptamer. *Sci. Rep.* 1–9 (2017) doi:10.1038/srep43272.
275. Pramod, P., Sudeep, P. K., Thomas, K. G. & Kamat, P. V. Photochemistry of ruthenium trisbipyridine functionalized on gold nanoparticles. *J. Phys. Chem. B* **110**, 20737–20741 (2006).
276. Estalayo-Adrián, S., McManus, G. J., Dalton, H. L., Savyasachi, A. J., Kelly, J. M. & Gunnlaugsson, T. Functionalisation of gold nanoparticles with ruthenium(II) polypyridyl complexes for their application in cellular imaging. *Dalt. Trans.* **49**, 14158–14168 (2020).

